FACULTY OF SCIENCE
UNIVERSITY OF COPENHAGEN

Deterministic quantum photonic devices based on self-assembled quantum dots

Tommaso PREGNOLATO

PhD Thesis,
September 2019

Niels Bohr Institute

Deterministic quantum photonic devices based on self-assembled quantum dots

This thesis was prepared by
Tommaso Pregnolato

Supervisors
Professor Peter Lodahl
Assistant Professor Nir Rotenberg

Release date: September 9, 2019

Comments: This thesis has been submitted to the PhD School of The Faculty of Science, University of Copenhagen, in partial fulfilment of the requirements for the degree of philosophiæ doctor

Quantum Photonics Group
Niels Bohr Institute
University of Copenhagen
Blegdamsvej 17
DK-2100 Copenhagen
Denmark

http://quantum-photonics.nbi.ku.dk/

Abstract

In this thesis we present our recent progress towards the creation of complex quantum photonic circuits. These devices would integrate on the same chip efficient single-photons sources and photonic components that guide light and interface it with quantum emitters. Such a quantum circuit would constitute the ideal solid-state platform to process quantum states and would play a key role in large-scale quantum networks.

Self-assembled InAs quantum dots (QDs) embedded in GaAs photonic nanostructures are particularly promising candidates for these applications since they have been shown to have good coherence properties and the ability to emit single photons at very high rates. However, major challenges still hinder the implementation of advanced quantum photonic experiments on this platform. For example, structural imperfections on the fabricated devices introduce optical losses that reduce the overall performances. Furthermore, QDs grow at random positions and emit photons at different frequencies due to their large range of sizes. The resulting lack of spatial and spectral knowledge makes the coupling between emitters and photonic devices less efficient and precludes the production of large-scale quantum photonic circuits.

In this thesis, we first describe the protocols we developed to produce complex nanostructures such as electrically contacted nanobeam and photonic crystal waveguides. These techniques allowed for the fabrication of devices in which appealing quantum effects such as single-photon nonlinearities and spin-photon interactions could be observed.

In the second part we overcome the problem of randomly distributed QDs, presenting a method to pre-locate QDs and subsequently fabricate photonic nanostructures about their positions. This photoluminescence-based protocol allowed us to fabricate photonic nanostructures aligned to the pre-selected QDs with final accuracy better than 50 nm.

The newly acquired knowledge over the QD locations lets us explore for the first time the effects of nanofabrication on the spectral properties of InAs QDs in suspended nanostructures. We registered average spectral shifts of up to $\approx 1\,\text{nm}$, which we were able to correct for by applying an electric field across the sample. Furthermore, we also characterised the effects of fabrication on different excitonic complexes.

Finally, to demonstrate for the first time the potential of combining all these capabilities, we deterministically interface QDs with photonic crystal waveguides, which we carefully position both in space and spectrally close to the optical bandgap. Time-resolved measurements allowed us to probe the emission properties of these QDs, revealing a dramatic improvement to their quantum efficiencies. In total, these results constitute an important step towards the fully deterministic spatial and spectral interfacing of quantum emitters with photonic nanostructures, a key requisite to the development of complex quantum circuits.

Resumé

I denne afhandling præsenteres vores seneste fremskridt mod fremstillingen af komplekse fotoniske kredsløb. Med disse kredsløb, kan effektive enkelt-foton-kilder og fotoniske komponenter der leder lys, integreres med kvanteemittere på den samme chip. Et sådant kvante-kredsløb ville udgøre den ideelle fasstofplatform til forarbejdning af kvantetilstande og vil være et centralt element i stor-skala kvantemekaniske netværk.

Selv-sammensatte InAs kvantepunkter, indlejret i GaAs fotoniske nanostrukturer er særligt lovende kandidater for disse anvendelser, da de har vist sig at have gode kohærensegenskaber samt evnen til at emittere enkelte fotoner med en meget høj rate. Dog er der stadig store udfordringer som forhindrer implementeringen af avancerede kvantefotoniske eksperimenter med denne platform. For eksempel vil strukturelle urenheder i de fabrikerede kredsløb introducere optiske tab som vil reducere den overordnede ydeevne. Ydermere, bliver kvantepunkterne groet tilfældige steder, og de emitterer fotoner med forskellige frekvenser som konsekvens af deres varierende størrelse. Denne manglende forhåndsviden om de rummelige og spektrale egenskaber, gør koblingen mellem emitter og fotoniske komponenter mindre effektiv og udelukker stor-skala produktion af kvantefotoniske kredsløb.

I denne afhandling vil vi først beskrive de protokoller vi har udviklet til at producere komplekse nanostrukturer, såsom elektrisk kontaktede nanobeam og fotonisk krystal-bølgeledere. Disse teknikker har muliggjort fabrikation af kredsløb hvor attraktive kvanteeffekter såsom enkeltfoton-ikke-linerariteter og spin-foton-interaktioner kan observeres.
I anden del viser vi hvordan vi løser problemet med den tilfældige placering af kvantepunkterne, ved en metode hvor vi pre-lokaliserer kvantepunkterne og efterfølgende fabrikerer de fotoniske nanostrukturer rundt om udvalgte kvantepunkter med en endelig præcision der er bedre end 50 nm.

Denne nye viden om kvantepunkternes placering, tillader os for første gang at udforske nanofabrikationens effekt på de spektrale egenskaber af InAs kvantepunkter i hængende nanostrukturer. Vi har registreret en spektral ændring på op til $\approx 1\,\text{nm}$, hvilket vi kunne kompensere for, ved at tilføje et elektrisk felt hen over prøven. Ydermere, har vi også karakteriseret fabrikationens effekt på forskellige excitoniske tilstande. Til sidst, for at demonstrere potentialet af kombinationen af alle disse teknikker for første gang, viser vi deterministisk integration af kvantepunkter i fotonisk krystal-bølgeledere, som vi nænsomt placerer både rummeligt og spektralt tæt på det optiske båndgab. Tidsopløste målinger gjorde det muligt at undersøge emissionsegenskaberne ved disse kvantepunkter, hvilket har afsløret dramatiske forbedringer af deres kvanteeffektivitet. Overordnet set, udgør disse resultater et vigtigt skridt mod en fuldstændigt deterministisk rummelig og spektral integration af kvanteemittere med fotoniske nanostrukturer, et nøgleelement for at udvikle komplekse kvantemekaniske kredsløb.

Preface

This thesis presents the results of the research carried out in the Quantum Photonics group led by Prof. Peter Lodahl, at the Niels Bohr Institute, University of Copenhagen, from February 2016 to September 2019. During this period, I was enrolled as a PhD student under the supervision of Professor Peter Lodahl and Assistant Professor Nir Rotenberg, who replaced Associate Professor Søren Stobbe as co-supervisor.

I would like to thank many people, who helped me during this project and contributed to make it such a great experience. The first acknowledgement goes to Professor Peter Lodahl, who welcomed me in the Quantum Photonics group 6 years ago and gave me the opportunity to get involved in and contribute to so many fascinating experiments, which have nourished my fascination with the quantum properties of light.

I would like to thank my co-supervisor Dr. Nir Rotenberg for all the support during this PhD project and for always having time for discussions. A special thanks goes also to Dr. Xiao-Liu Chu, who helped me in the optical measurements during this project and who gave a fundamental contribution on the optimisation of the optical setup used during the work described in this thesis. The exciting achievements on the localisation technique presented in this report would not have been possible without all the meetings and hours spent together with Nir and Liu and I am very grateful they wanted to share their enthusiasm for physics with me. I would also like to acknowledge Sandra Helena Øder Madsen, Dr. Tim Schröder and Dr. Søren Stobbe for their help in the initial stages of the project on quantum dot localisation.

The central part of my work in the Quantum Photonics group has been focused on the fabrication of nanodevices for quantum photonics applications. I spent a lot of the time in the cleanroom facilities at the H. C. Ørsted Institute, University of Copenhagen, where I learnt and mastered all the main fabrication procedures used for the production of nanostructures on GaAs/AlGaAs heterostructures. It has been a pleasure to share that time with the great Fab Team, with whom I developed the recipes for fabricating the samples used in several experiments run in the Quantum Photonic group. And so I thank Dr. Leonardo Midolo, Camille Papon, Asli Dilara Ugurlu, Zhe Liu and Ying Wang for sharing with me all the exciting moments that nanofabrication creates.

I have been part of the Quantum Photonic group for the last 6 years, during which I had the pleasure to meet many people and great colleagues. I would like to thank all the former and current members of the group: in addition to those already mentioned, in random order, Dr. Henri Thyrrestrup Nielsen, Dr. Dapeng Ding, Dr. Claudéric Ouellet-Plamondon, Dr. Xiaoyan Zhou, Dr. Hanna Le Jeannic, Dr. Ravitej Uppu, Dr. Thomas Hummel, Freja Thilde Pedersen, Martin Hayhurst Appel. The nice atmosphere in the Quantum Photonic group is the product of the lovely people who are part of it and I am glad I got to meet all of you. A special acknowledgement to Peter, Nir, Liu, Leonardo, Camille and Asli for proof-reading this thesis and providing helpful feedbacks.

During my PhD project I had the pleasure to spend a couple of weeks in the research group led by Prof. Andreas D. Wieck at the Ruhr-University of Bochum, Germany. Under the supervision

of Dr. Arne Ludwig and in close collaboration with Marcel Schmidt, I had the chance to have a closer look to the epitaxial growth of self-assembled quantum dots. I am very grateful for the welcoming atmosphere and the interesting scientific experience, and for this I would like to thank Andreas and all the members of his group.

The Quantum Optics section at the Niels Bohr Institute has always been a very cheerful place, where both great science and fascinating discussions takes place. I wish to thank all the members of the QUANTOP and the Hy-Q groups for making these years at the NBI a very entertaining experience.

Last but not the least, I wish to thank my family, who always supported me and cheered me up during these past years away from home.

Tommaso Pregnolato
September 9, 2019

List of publications

The work performed during this PhD project has resulted in the publications listed below:

- **T. Pregnolato**, X.-L. Chu, T. Schröder, R. Schott, A. D. Wieck, A. Ludwig, P. Lodahl, N. Rotenberg, "Deterministic positioning of quantum dots in nanophotonic waveguides", arXiv:1907.01426 (2019).

- D. Ding, M.H. Appel, A. Javadi, X. Zhou, M.C. Löbl, I. Söllner, R. Schott, C. Papon, **T. Pregnolato**, L. Midolo, A.D. Wieck, A. Ludwig, R.J. Warburton, T. Schröder, P. Lodahl, "Coherent optical control of a quantum-dot spin-qubit in a waveguide-based spin-photon interface", Phys. Rev. Appl. 11, 031002 (2018).

- A. Javadi, D. Ding, M.H. Appel, S. Mahmoodian, M.C. Löbl, I. Söllner, R. Schott, C. Papon, **T. Pregnolato**, S. Stobbe, L. Midolo, T. Schröder, A.D. Wieck, A. Ludwig, R.J. Warburton, P. Lodahl, "Spin-photon interface and spin-controlled photon switching in a nanobeam waveguide", Nat. Nanotechnol. 13, 398403 (2018).

- H. Thyrrestrup, G. Kiršanskė, H. Le Jeannic, **T. Pregnolato**, L. Zhai, L. Raahauge, L. Midolo, N. Rotenberg, A. Javadi, R. Schott, A.D. Wieck, A. Ludwig, M.C. Löbl, I. Söllner, R.J. Warburton, P. Lodahl, "Quantum Optics with Near-Lifetime-Limited Quantum-Dot Transitions in a Nanophotonic Waveguide", Nano Lett. 18, 18011806 (2018).

- G. Kiršanskė, H. Thyrrestrup, R.S. Daveau, C.L. Dreeßen, **T. Pregnolato**, L. Midolo, P. Tighineanu, A. Javadi, S. Stobbe, R. Schott, A. Ludwig, A.D. Wieck, S.I. Park, J.D. Song, A. V. Kuhlmann, I. Söllner, M.C. Löbl, R.J. Warburton, P. Lodahl, "Indistinguishable and efficient single photons from a quantum dot in a planar nanobeam waveguide", Phys. Rev. B. 96, 165306 (2017).

- M. C. Löbl, I. Söllner, A. Javadi, **T. Pregnolato**, R. Schott, L. Midolo, A. V. Kuhlmann, S. Stobbe, A.D. Wieck, P. Lodahl, A. Ludwig, R.J. Warburton, "Narrow optical linewidths and spin pumping on charge-tunable close-to-surface self-assembled quantum dots in an ultrathin diode", Phys. Rev. B. 96, 165440 (2017).

- R. S. Daveau, K. C. Balram, **T. Pregnolato**, J. Liu, E. H. Lee, J. D. Song, V. Verma, R. Mirin, S. W. Nam, L. Midolo, S. Stobbe, K. Srinivasan and P. Lodahl, "Efficient fiber-coupled single-photon source based on quantum dots in a photonic-crystal waveguide", Optica 4, 178 (2017).

Contents

Chapter 1

Introduction

One of the major scientific landmarks of the 20th century was the discovery of the wave-particle duality of light, an idea so fundamental that caused a complete paradigm change in the study of the nanoscopic world and triggered the birth of the new course of science known as quantum physics. The new description of the laws of nature enabled a deeper understanding of light and matter and unlocked a number of new inventions that constitute the cornerstones of current technologies such as the laser and the transistor. Owing to the large impact that such a progress had on the scientific development of the century, many nowadays refer to it as *the first quantum revolution*.

The advances enabled by those technologies have matured to such a point that we are now able to make one step further and start exploiting all the concepts introduced by quantum physics. Phenomena such as energy quantisation or quantum superposition are now better understood and can be used in a variety of new applications, like quantum simulations or secure quantum communication. Furthermore, more complex quantum experiments such as entanglement generation over long distances [1] or the reduction of the back-action effects on the measurements of the motion of oscillating macroscopic objects [2] are also becoming more common. These exciting results suggest we are now witnessing the dawn of a *second quantum revolution*, a new era characterised by the implementation of the discoveries introduced by quantum physics for the development of new quantum technologies [3].

Quantum photonics is one of several new fields leading the way in this revolution. This platform exploits the quantum properties of the coupling between light and matter in order to build large networks of solid-state quantum systems for applications such as quantum information or quantum cryptography. A number of functionalities are therefore required, which are schematically illustrated in Fig. 1.1: for example, photonic chips must integrate highly efficient sources of single photons, along with structures that provide the ability to propagate and control them with low optical losses [4]. Moreover, at the nodes of such quantum networks, light has to be coherently interfaced with the emitters in order to perform operations with the high fidelity necessary for the processing of quantum states [5].

Self-assembled InAs quantum dots (QDs) embedded in GaAs photonic nanostructures have the potential to provide all the functionalities just described. These emitters have been proven to be near-optimal sources, as they are able to emit single quanta of light with high efficiency and good levels of coherence [6, 7]. The GaAs platform facilitates the engineering of the photonic environment around the QDs by the fabrication of nanophotonic devices, e.g. photonic-crystal waveguides. In these systems, the emitter is shielded from free-space modes and coupling efficiencies $> 98.4\%$ have been demonstrated [8], thus showing that such a platform has the potential to offer the optimal interface between photons and emitters.

Performing advanced quantum experiments on photonic chips with embedded QDs remains

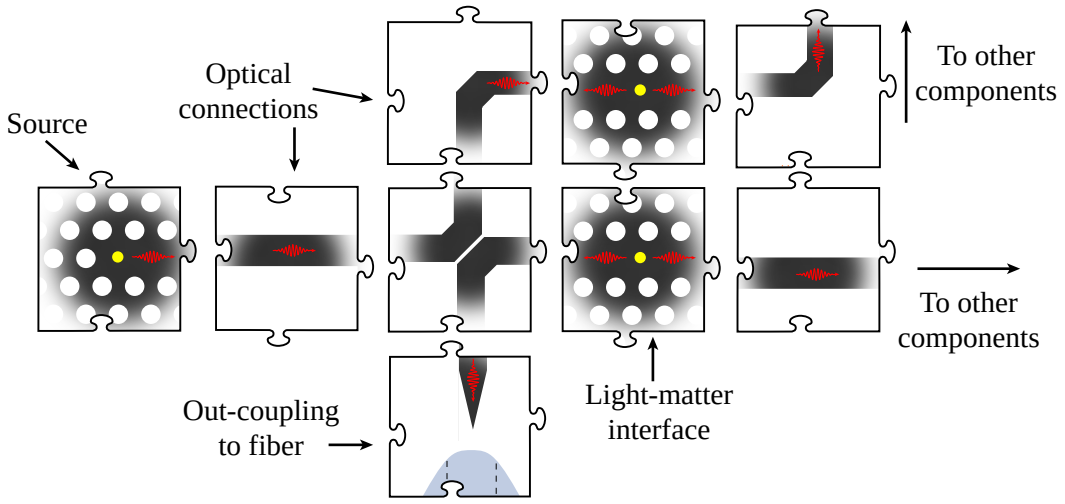

Figure 1.1: Conceptual illustration of a quantum photonic circuit. Components with different functionalities (e.g. sources, light-matter interfaces, out-couplers) are integrated on the same chip and optically connected together by waveguides.

a demanding task, as the fabrication of these circuits is highly non-trivial and precise control of each integrated optical components is required to reduce structural imperfections and hence optical losses due to scattering or disorder [6]. Moreover, QDs grow randomly on the sample and present a large distribution of sizes that results in a broad range of emission frequencies [9]. These factors must be overcome as the spatial and spectral coupling between the photonic nanostructures and the emitters directly influences the efficiency of the light-matter interaction. Typical samples therefore contain several copies of the same device and a post-selection of the ones showing higher performances is carried out in order to find the few nanostructures that present optimal conditions for the experiment under consideration. Although this approach may still enable simple investigations, it clearly prevents the fabrication of large and complex architectures and hence hinders the scaling of the platform towards more advance applications. In this thesis we address these issues and develop fabrication protocols to overcome such challenges.

The outline of this thesis is as follows. In Chap. 2 a theoretical introduction of the system investigated during this PhD project is given. We first introduce the electronic properties of semiconductors, with main focus on GaAs as it is the material of all the presented samples. The main features of bulk and interfaces are described, with particular interest on how the energy bands respond to different configurations. We then move on to the optical properties of the system under study and we introduce why self-assembled quantum dots are optimal emitters of single photons for solid-state devices. Finally, two types of photonic nanostructures are introduced, i.e. photonic crystal and nanobeam waveguides, along with a description of their ability to control the emission properties of embedded quantum dots.

Chap. 3 overviews the fabrication techniques employed for the production of the studied samples. Starting from the common lithographic methods, we then describe the main etching methods for GaAs-based system, with particular interest on the relationship between energy bands and the electrochemistry processes behind the wet etching of III-V semiconductors. Finally, the main procedure for metal deposition is presented.

In Chap. 4 we describe the nanofabrication protocols developed for the different types of devices prepared during this PhD project and constituting some of the building blocks of the quantum photonic platform. The developed fabrication procedures for ohmic contacts, suspended

photonic crystal waveguides and tapered out-couplers are discussed along with the results of their characterisation.

The problem of the QD random positions is tackled in Chap. 5. After an introduction to the state-of-the-art localisation techniques, the chapter continues with the detailed description of the approach we developed during this project. A thorough statistical analysis reported at the end of the chapter demonstrates the final alignment error between pre-selected QD and nanostructures fabricated about their positions.

The first implementations of the developed localisation technique are presented in Chap. 6. In the first part of the chapter we make use of the ability to reliably map the QD locations on the sample to investigate the nanofabrication-induced changes on the spectral emission of self-assembled QDs embedded in planar nanostructures. In the second part, we present our results on the integration of the emitters in photonic-crystal waveguides to deterministically control the emission properties of the QDs.

Finally, conclusions and outlook are presented in Chap. 7

Chapter 2

Theoretical background for photonic experiments with self-assembled quantum dots

In this chapter we present an overview of the theoretical background of self-assembled quantum dots (QDs) embedded in gallium arsenide (GaAs) photonic nanostructures. In the first part of the chapter we will focus on the electronic properties of GaAs as a semiconductor material, describing the concepts of doping, interfaces and junctions, which are the fundamental properties constituting the core of the material system we use in our experiments. In the second part the discussion will move on to self-assembled QDs and we will introduce the basic optical properties that have granted them the name of "solid-state atoms". Finally, the basic features of nanophotonic waveguides will be presented and we will demonstrate how they can be used to modify the emission properties of embedded QDs, showing some of the reasons why they constitute a promising platform for quantum photonic experiments.

2.1 Basics of semiconductors physics

Gallium arsenide is a crystalline material formed by a face-centred cubic (FCC) lattice of Ga^{3+} and As^{3-} and presents the typical zinc blend structure (Fig. 2.1a), where every As^{3-} is bonded to 4 ions of Ga. In solids, the overlap of the valence electron orbitals causes the electronic states to hybridise and form bands of allowed energy rather than the discrete levels that characterise single atoms [10]. However, not all values of energies are allowed and gaps between different bands hence appear. The last populated band before a band gap is usually called the valence band (VB) and it is followed by the first empty one called the conduction band (CB). Solids can be categorised based on the properties of such bands and their populations: if, at temperature $T = 0\,\mathrm{K}$, the VB is partially occupied by electrons, then the material behaves like a metal; that is to say, the electrons can freely move and are responsive to an applied electric field F. On the contrary, if the valence band is fully occupied, the charge carriers are not affected by F and the solid is therefore an insulator. However, if the energy difference between the edges of the two bands $E_g = E_C - E_V$ (for CB and VB, respectively) is of the order of few eV [11, 12], small amounts of energy provided by, for example, a thermal or optical excitation are enough to promote some electrons to the CB, while leaving behind a positively-charged vacancy in the valence band called a "hole". This behaviour is typical of the category of materials called semiconductors, to which GaAs belongs as $E_g\,(T = 0\,\mathrm{K}) = 1.519\,\mathrm{eV}$ [13].

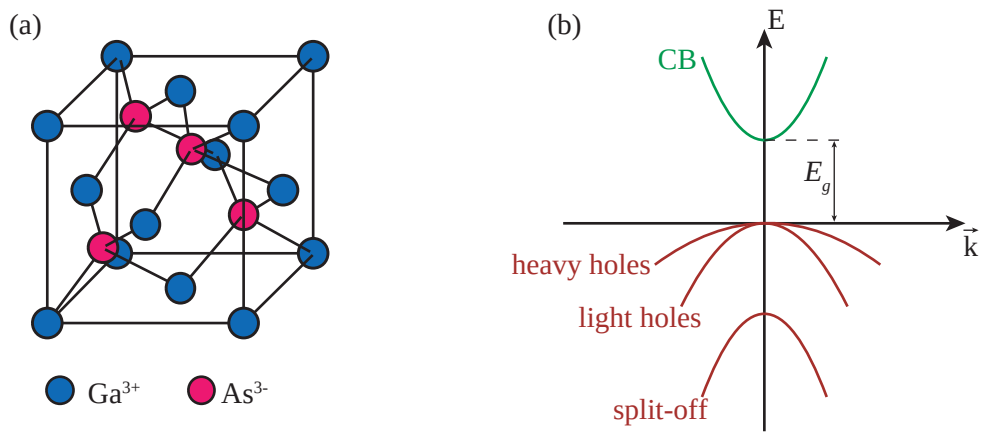

Figure 2.1: Material properties of GaAs. (a) Model of the zinc blend crystallographic structure of GaAs. (b) Sketch of the GaAs band structure depicted around the center of the first Brillouin zone. Both the conduction band (CB, green) and the three valence bands (red) are shown.

The band structure of semiconductors can be visualised by plotting the dispersion relation $E = E(\mathbf{k})$, which explains how the energy of electrons varies as a function of the momentum $\mathbf{k}$ and provides the necessary information to understand both the electronic and optical properties of a semiconductor. Fig. 2.1b illustrates such relation at the center of the first Brillouin zone, at the point of highest symmetry. Here, the minimum of the CB and the maximum of the VB appear at the same position in the k-space, i.e. the bandgap is direct. This property of GaAs makes it an optimal material for optical applications, because electronic transitions between CB and VB can be activated by the absorption or emission of photons, without any change in the momentum of the electrons.

GaAs consists of only one CB (green in Fig. 2.1b) and three different sub-bands of the VB (red in Fig. 2.1b); the top-most two are degenerate and normally called "heavy holes" and "light holes", while the third one (denominated "split-off" band) appears less energetic. Another important feature of the dispersion relation illustrated in Fig. 2.1b is the almost-parabolic shape of the bands for the shown range of momenta. Since electrons moving in free space have energy with a similar functional form, the same electron model can be used also for the case of semiconductors, with the only difference that an effective mass m^* for the charges has to be used. Such a parameter is defined as the inverse of the curvature of the energy band, calculated at its extreme (i.e. at the maximum in the VB or at the minimum for the CB) [10]. The three curvatures of the sub-bands in the GaAs valence band thus result in different values of m^*, hence the terminology "heavy" and "light holes".

2.1.1 Different categories of semiconductor

GaAs, like any other semiconductor material, is classified by the type and density of its majority charge carriers. Intrinsic semiconductors constitute the simplest case, where conduction electrons e^- are generated by thermal excitation from the valence band. Their density in the CB is a function of the number of available states in the band and of the probability of the electron occupancy at a given energy E, which can be calculated by Fermi-Dirac statistic. The final equations for the

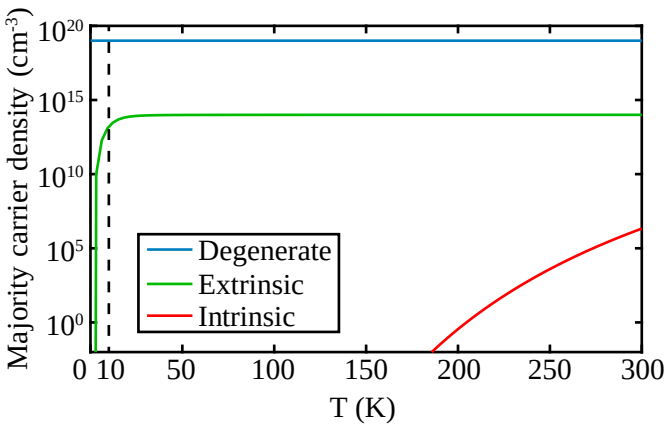

Figure 2.2: Temperature dependence of the majority carrier density for three different levels of dopants in GaAs for the range of T of interest for the applications described in this work: intrinsic (red), non-degenerate extrinsic (impurities density $N_D = 5 \times 10^{13}\,\mathrm{cm}^{-3}$, green) and degenerate extrinsic ($N_D = 10^{19}\mathrm{cm}^{-3}$, blue). The dashed line indicates the temperature used for most of the results presented in this work.

densities of electrons n and holes p read [14]

$$n = N_C \exp\left(\frac{E_{f,i} - E_C}{k_B T}\right) \tag{2.1a}$$

$$p = N_V \exp\left(-\frac{E_{f,i} - E_V}{k_B T}\right), \tag{2.1b}$$

where N_C (N_V) is the effective density of states in the conduction (valence) band and k_B is the Boltzmann constant. As one hole h^+ is generated when one e^- is excited to the CB, in intrinsic semiconductors $p = n = n_i$. The term $E_{f,i}$ is the intrinsic Fermi level, which is a very important physical parameter that describes the energy of the outermost electrons in the bands of the material at a finite temperature.

Eqs. (2.1) show that the carrier densities increase for $E_{f,i}$ approaching the relevant band. In the intrinsic case, $E_{f,i}$ is generally situated in the middle of the bandgap, resulting in a relatively small concentration of carriers at room temperature, which rapidly decreases for lower values of T (cf. Fig. 2.2). As the conductive properties of semiconductors are functions of n and p [14], such temperature dependence causes intrinsic GaAs to behave like an insulator at cryo T ($T < 10\,\mathrm{K}$). In the case of applications where such a change is detrimental, semiconductors can be doped with impurities that increase the level of carriers; these materials are called extrinsic. Two types of doping exist, based on the nature of the dopant atoms: when donors are used, the concentration of electrons in the material increases and the semiconductor is denoted as n-type. The presence of new charges creates new energy states closer to the CB, which shift the Fermi level $E_{f,n}$ close to E_C. Conversely, the introduction of acceptor atoms results in higher densities of h^+ and the Fermi level $E_{f,p}$ moves closer to the valence band; this type of material is referred to as p-doped.

The new carriers provided by the impurities increase the conductivity of GaAs and high densities can be maintained also below room temperature (Fig. 2.2). Nonetheless, the generation of free charges from the dopant atoms is still a thermally activated process, which fails for $T \to 0\,\mathrm{K}$ causing a drop in the major carrier density at cryogenic temperatures (the so-called "freezing-out" of the carriers), as shown in Fig. 2.2. Such an issue can be circumvented by increasing the density

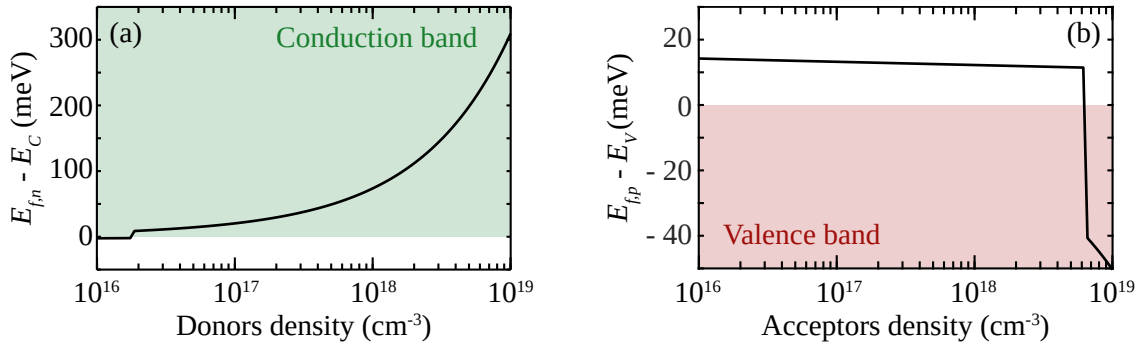

Figure 2.3: (a) Position of Fermi levels $F_{f,n}$ with respect to the edge of the conduction band E_C for different values of donors densities. (b) Position of Fermi levels $F_{f,p}$ with respect to the edge of the valence band E_V for different values of acceptors densities. The sharp change in both curves indicates the transition of the material to degenerate doping, i.e. the Fermi levels move inside the closest band, shown as shaded areas. All the values are calculated at $T = 10\,\mathrm{K}$.

of dopants in the materials, which hence become degenerately doped [14]. In GaAs, the concentration of impurities necessary to reach such status is about $10^{16} - 10^{17}\mathrm{cm}^{-3}$ for n-type and $10^{18} - 10^{19}\mathrm{cm}^{-3}$ for p-type [15, 16]. This high level of doping heavily changes the structure of the material and profoundly modifies its properties and the energy bands [15, 17]. One of the most relevant changes is the reduction of the energy necessary to ionise the dopants and the subsequent shift of the impurities states towards and across the closest band. This new configuration has the effect of moving the Fermi level inside the band (i.e. $E_{f,n} \geq E_C$ and $E_{f,p} \leq E_V$, as shown in Fig. 2.3), which is a configuration similar to metallic materials and which causes the majority carrier density to be independent of the temperature. A summary of the effects of T for different types of semiconductors is presented in Fig. 2.2, which reports the total density of majority carriers for intrinsic GaAs (i-GaAs, red curve) and n-GaAs doped with an impurities concentration of $N_D = 5 \times 10^{13}\,\mathrm{cm}^{-3}$ (non-degenerate extrinsic, green curve) and $N_D = 10^{19}\mathrm{cm}^{-3}$ (degenerate extrinsic, blue curve).

2.1.2 Effects at the interfaces

Surfaces

The concepts overviewed in the previous section describe the main characteristics of bulk semiconductors, that is when they are considered as indefinitely extending in space. Real materials are of course finite and have edges that locally modify their properties. At these positions the crystalline structure is abruptly interrupted and surface atoms present dangling bonds formed by unused valence electrons. The presence of these free charges generate a surface potential ϕ_0 that penetrates into the material and causes a rearrangement of the carriers in the first layer of the semiconductor, which is often referred to as space-charge (SC) layer and has width w_{sc} that varies for different boundary conditions. The effects on the energy bands caused by the position-dependent carrier density $\rho(z)$ can be studied by solving Poisson's equation [18]

$$\frac{d^2\phi(z)}{dz^2} = -\frac{\rho(z)}{\varepsilon_s}, \tag{2.2}$$

where ε_s is the semiconductor permittivity and the coordinate z indicates the direction normal to the surface of the material. The potential $\phi(z)$ causes a spatial-dependent change in the values

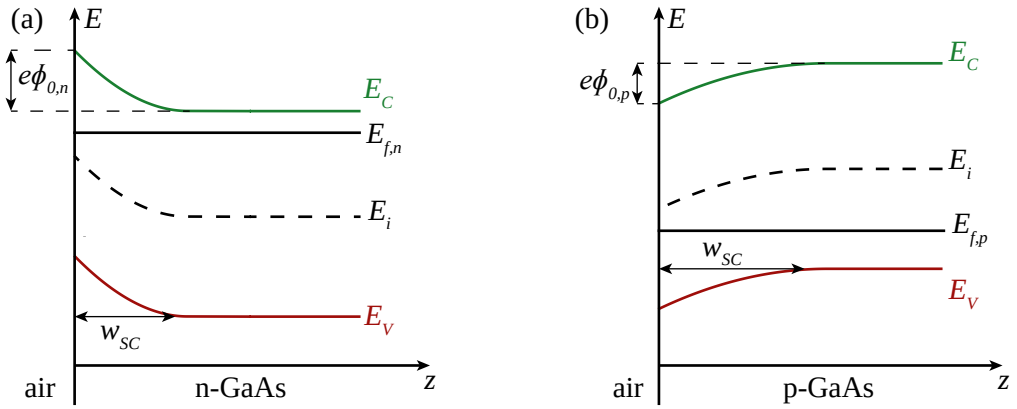

Figure 2.4: Band bending at the surface of two different type of GaAs: (a) n-doped GaAs and (b) p-GaAs. In both cases, the relevant energy levels are shown: the minimum of the conduction band E_C and the maximum of the valence band E_V, together with the Fermi levels generated by the intrinsic carriers E_i and those related to the introduction of dopants $E_{f,n}$ and $E_{f,p}$, respectively. Space-charge layers of width w_{SC}, caused by the surface potentials in the two materials ($\phi_{0,n}$ and $\phi_{0,p}$, respectively), are visible.

of E_C and E_V and generates the bending of the energy bands at the surface. Fig. 2.4 depicts a schematic representation of the band diagram for both n- and p-GaAs and illustrates how the relevant energy levels of the material (i.e. E_C, E_V and E_f) vary as a function of the position. Here, ϕ_0 is shown to affect differently the two types of semiconductors, as it produces energy barriers of different heights and shapes: in n-GaAs the increased density of electrons at the surface repels the majority carrier in the space-charge layer and the energy bands hence bend upwards [12]. In p-type materials the reconfiguration of the superficial atoms depletes the majority carriers too, but in this case it results in a downward bending [18, 19]. Such effects are confirmed by the height of the energy barriers measured on as-grown n- and p-GaAs, as it has been reported that $|e\phi_{0,n}| = 0.61\,\text{eV}$ and $|e\phi_{0,p}| = 0.33\,\text{eV}$, respectively [20].

Similarly to the carriers introduced in the material by the dopants, the new energy states generated at the surface fix E_f at a specific position in the band diagram. This effect is denominated "pinning of the Fermi level" [18] and it is an important phenomenon for understanding the behaviour of the carriers in the space-charge layer. The relative distance between the Fermi level at the surface $E_{f,s}$ and the edges of the energy bands in fact modifies the density of charges in the SC layer in the way illustrated in Fig. 2.5: at thermal equilibrium, the concentrations at the surface of electrons in the CB n_s and of holes in the VB p_s can be expressed as [14, 18, 21]

$$n_s = n \exp\left(\frac{e\phi_{0,n}}{k_B T}\right) = N_C \exp\left(\frac{E_{f,s} - E_C + e\phi_{0,n}}{k_B T}\right) = N_C \exp\left(\frac{E_{f,s} - E_{C,s}}{k_B T}\right) \tag{2.3a}$$

$$p_s = p \exp\left(-\frac{e\phi_{0,p}}{k_B T}\right) = N_V \exp\left(\frac{-E_{f,s} + E_V - e\phi_{0,p}}{k_B T}\right) = N_V \exp\left(-\frac{E_{f,s} - E_{V,s}}{k_B T}\right), \tag{2.3b}$$

where e is the electron charge, n and p are the densities in bulk introduced in eqs. (2.1) and the variables $E_{C,s}$ and $E_{V,s}$ are respectively the minimum of the CB and the maximum of the VB at the surface. Eqs.(2.3) describe three regimes for different sign of ϕ_0 (Fig. 2.5): in the case of an n-type semiconductor, a negative ϕ_0 bends the bands upwards, increasing the depletion of carriers from the SC layer. Conversely, $\phi_0 > 0\,\text{V}$ indicates a downward bending, which in n-doped material causes the accumulation of electrons at the surface. Finally, $\phi_0 = 0\,\text{V}$ constitutes the condition for

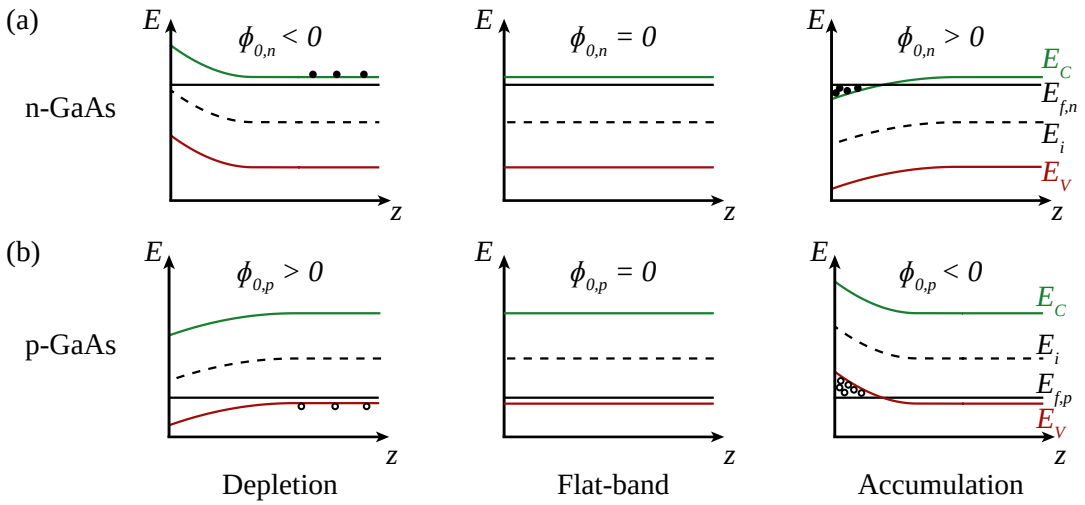

Figure 2.5: Schematic band diagrams that show the possible regimes for different values of the surface potential ϕ_0 for different types of GaAs: (a) n-doped and (b) p-doped.

the flat-band configuration, where any effect due to surface states is inhibited [14, 18]. The same three regimes happen in p-type semiconductors as well, but at values of ϕ_0 with opposite sign. Interestingly, a bias voltage V applied across the material modifies the position of the bulk Fermi level and can therefore be used to switch between the three aforementioned conditions. A more general form of eqs. (2.3) hence reads

$$n_s = n \exp\left(\frac{e\,(\phi_{0,n} + V)}{k_B T}\right) \tag{2.4a}$$

$$p_s = p \exp\left(-\frac{e\,(\phi_{0,p} + V)}{k_B T}\right), \tag{2.4b}$$

and it shows that an applied V can be used to control the total density of charges in the SC layer, which is of high importance in devices based on metal-insulator-semiconductor interfaces like metal-oxide-semiconductor field effect transistors (MOSFET) [12, 14].

Metal on semiconductor

The deposition of a metal on the surface of GaAs produces a different type of interface between the two materials, which can still be described by the formalism employed thus far for the surface states. The main difference consists of the origin of the band bending at the surface, which is now related to the work function of the deposited metal $e\phi_m$ [14]. In fact, during the formation of the contact, the different positions of the Fermi levels between both parts of the junction produce an electric field at the interface which initiates the migration of the electrons towards the side with lower E_f. As a result, while the energy level in the metal $E_{f,metal}$ is almost unaffected due to the large number of charges in it, the Fermi level in the semiconductor effectively shifts towards $E_{f,metal}$. Eventually, when the equilibrium state is reached, the levels on both sides of the junction will line-up, causing the pinning of semiconductor E_f at the position of $E_{f,metal}$. Furthermore, similarly to the accumulation of charges at the surface, the rearrangement of carrier densities produces the bending of the bands at the interface, as schematically sketched in Fig. 2.6. The energy barriers $e\phi_B$ formed are often referred to as Schottky barriers and, in the ideal case, are

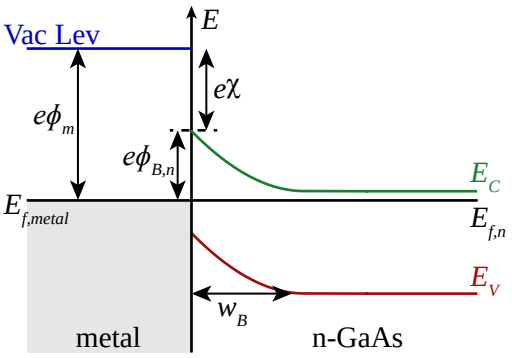

Figure 2.6: Schematic representation of the Schottky barrier in n-GaAs. When the Fermi levels on both sides of the interface align, an energetic barrier is formed with height $e\phi_B = e(\phi_m - \chi)$ and thickness w_B.

defined as

$$e\phi_{B,n} = e(\phi_m - \chi) \qquad \text{for n-type,} \tag{2.5a}$$

$$e\phi_{B,p} = E_g - e(\phi_m - \chi) \qquad \text{for p-type,} \tag{2.5b}$$

where $e\chi$ is the semiconductor electron affinity, which is defined as the energy difference between the conduction band minimum and the vacuum level (which is, by definition, infinitely far away from the solid and has energy $E_{\text{VacLev}} = 0\,\text{eV}$). Solving Poisson's equation eq.(2.2) provides all the relevant parameters for the system under study [14], such as the spatial dependence of the band edges E_C and E_V and the width of the barrier w_B, which is found to vary as [14]

$$w_B \propto \sqrt{\frac{1}{n}} \tag{2.6}$$

for a n-doped material (but a similar relationship holds for p-type semiconductors too).

The main purpose of the deposition of metals on semiconductors is to provide electrical control over the properties and energy levels of these materials. When a bias voltage is applied across the interface, charge carriers move across the barrier and shift the energy level upwards (for $V > 0\,\text{V}$) or downwards (for $V < 0\,\text{V}$). Several processes may describe the electronic transport and the most relevant for the applications reported in this work are based on (i) thermionic emission, when electrons with high enough thermal energy can cross the interface above $e\phi_B$, and (ii) tunnelling through the Schottky barrier [14]. Whilst the former regime is dominant at room T, the latter constitutes the main process in cryogenic applications. In both cases, however, the parameters that control the current density J generated by the metal contact are the aforementioned height $e\phi_B$ and width w_B, since, for example, higher and/or larger barriers results in lower values of J.

As previously discussed, the variables $e\phi_B$ and w_B depend on the work function of the deposited metal and on the majority carrier density of the semiconductor. Different materials therefore have specific effects on J. Two different categories of contacts can be defined based on their behaviours and effects on the charges flow. Schottky contacts are formed by metals that cause a high potential barriers at the semiconductor interface and therefore limit the current across it [14]. This type of contact is usually employed as a capacitive input to the device, which allows for the accumulation or depletion of charges in specific areas of the sample. Ohmic contacts, instead, provide a current flow across the metal-semiconductor interface that linearly increases with the applied voltage. The resistance of this type of junction results negligible compared to the total

resistance of the device and currents are produced already at low voltages, with no perturbation of the energy levels in the sample [14]. For this reasons ohmic contacts provide the optimal way to electrically contact electronic chips. These type of contacts are usually fabricated by depositing metals with low work functions on degenerately doped semiconductors in order to form energy barriers as low and as thin as possible [12]. The relevant figure-of-merit for ohmic contacts is their specific contact resistance R_c, defined as

$$R_c = \left(\frac{\mathrm{d}J}{\mathrm{d}V}\right)^{-1}_{V=0}. \tag{2.7}$$

However, advanced integrated circuits require the miniaturisation of the several devices they host and this causes an increase of the density current flowing in them. In this situation, a better parameter for comparing different ohmic contacts is the total resistance $R = R_c/A$, with A being the contact area.

Heterostructures

Semiconductor technology exploits one more type of interface, that is the junction between layers of different materials in contact with each other. These structures are usually referred to as heterostructures and are formed already during the production of the semiconductor material, when several layers with different doping levels and types, or even different compounds, are grown sequentially. One of the famous examples of this type of interface is the so-called p-n junction, which is formed by the combination of a p- and n-doped semiconductor. Regardless of the nature of the involved materials, heterostructures are characterised by an interface where the Fermi levels on either sides are initially at different positions. Similarly to what has been previously discussed, in this situation an electric potential $\phi_{bi} = (E_{f,n} - E_{f,p})/e$ is generated, which is known as "built-in potential" and which forces the carriers to move towards the oppositely charged side of the junction. The result is once again the alignment of the Fermi levels across the junctions and the formation of band bending at the interface, which can be studied by following the same approach used for surface states and metal contacts [14].

Different combinations of materials provide different levels of complexity on the engineering of the band diagram of the device. For example, the addition of an intrinsic layer in the middle of a p-n junction allows us to separate the two doped materials, thus reducing the electric field generated between them. The band diagram of the resulting heterostructures, also know as p-i-n diode, calculated for GaAs layers is reported in Fig. 2.7a, where the intrinsic layer is shown inclined for its full width. Such an effect is caused by the low density of carriers available in the i-region, which results in a depletion region extending over the entire layer, as expected from eq. (2.6). Another important feature of this heterostructure is the fact that the built-in field is constant throughout the middle region, which causes the separation of any carriers situated there. The intensity of this electric field can be controlled by applying a bias voltage across the p-i-n diode, which affects the separation between $E_{f,n}$ and $E_{f,p}$. For forward bias (i.e. $V > 0\,\mathrm{V}$) and $V < \phi_{bi}$, the difference between the Fermi levels of both doped layers decreases as the voltage increases, thus lowering the effect of ϕ_{bi} on the carriers and hence reducing their separation. At $V = \phi_{bi}$ a flat-band configuration is reached and any effect of the built-in field is nullified. For higher values of bias, the electrons in the n-type materials start flowing towards the p-doped side of the junction and an increasing current can be detected. On the other hand, in reverse bias ($V < 0\,\mathrm{V}$) the levels $E_{f,n}$ and $E_{f,p}$ move further apart as the built-in field is enhanced by the applied voltage. No current flow can be measured for a large range of negative V, until the energy barrier formed by the intrinsic layer becomes so thin that suddenly carriers are able to cross through it,

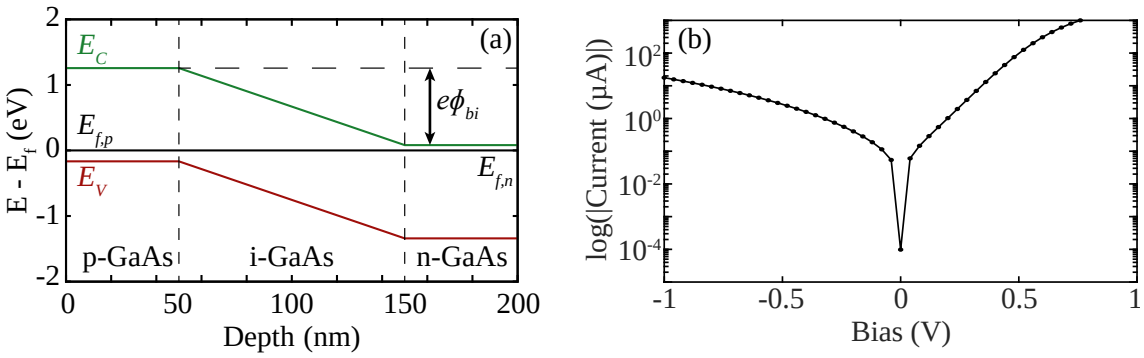

Figure 2.7: Properties of a p-i-n GaAs diode. (a) Calculated band diagram of a p-i-n GaAs diode. When the Fermi levels $E_{f,p}$ and $E_{f,n}$ are aligned, a built-in potential ϕ_{bi} causes the complete depletion of the carriers in the intrinsic region, which results completely bent. The calculation is performed by setting the level of impurities for both doped layers at $N_D = 10^{16}\,\mathrm{cm}^{-3}$ and for $T = 298\,\mathrm{K}$. (b) Example of the voltage dependence of the current measured on a p-i-n GaAs diode at room temperature. The increasing values in reverse bias regime are a signature of leakage currents possibly due to surface states and small structural defects introduced during the fabrication process.

causing a sharp increase in J that is known as breakdown current. In the ideal case, the relationship between applied voltage V and current density J can be described by the Shockley equation, which reads [14]

$$J = J_0 \left[\exp\left(\frac{eV}{k_B T} \right) - 1 \right], \tag{2.8}$$

where J_0 is called saturation current and it is a function of the carrier densities n and p. Eq. (2.8) shows the exponential nature of current detected across an ideal p-i-n diode. In real devices, however, some deviations may appear in the measured signal, like a slow increase in J measured for reverse bias, as visible in the Fig. 2.7b. Possible causes for this non-ideal behaviour may be related to parasitic effects caused by surface currents or defects in the device structure.

2.2 Single-photon emitters in solid state: self-assembled QDs

2.2.1 Epitaxial growth of heterostructures

In the previous section we introduced some of the properties that characterise the heterostructures, which are formed by several layers of semiconductor material grown on top of each other. In the following pages we will elaborate on the production of such structures, focusing mainly on the method employed for the samples used for the work of this PhD project.

Gallium arsenide production is based on so-called bottom-up approaches, where materials are grown atomic layer after atomic layer. The process employed for the samples used during this work is called molecular beam epitaxy (MBE), which is one of the most advanced growth methods for semiconductors [11]. It is based on the evaporation of the solid Ga and As into a chamber that is kept at ultra high vacuum (i.e. $10^{-10} - 10^{-11}$ mbar [11, 12]), where a substrate wafer is mounted. Owing to the high process temperature (500-600 °C), the atoms directed towards the sample diffuse around its surface until they reach energetically favourable locations. Different solid precursors may be used during the growth and their amount and relative concentrations can be controlled by operating the shutters of the effusion cells that host them. The high level of precision possible

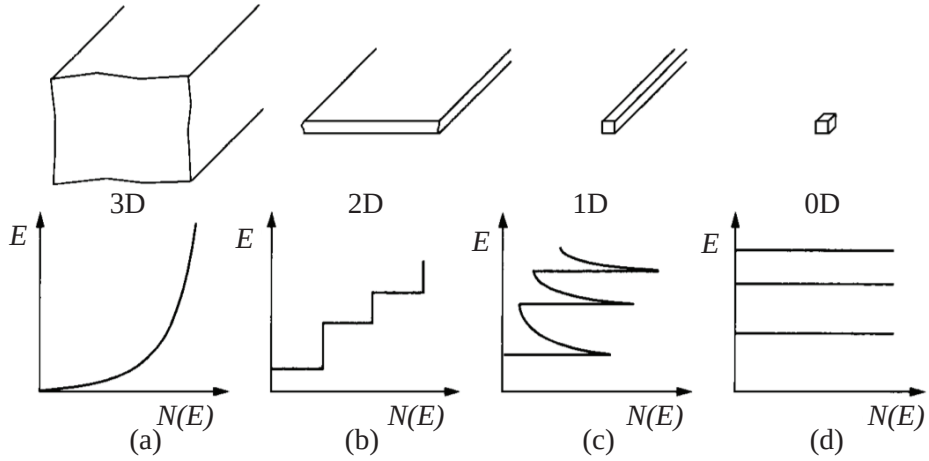

Figure 2.8: Schematic plots of densities of states for systems with different dimensionalities: (a) bulk material, (b) quantum well, (c) quantum wire and (d) quantum dot. Adapted from [14].

during the process enables the growth of semiconductor materials with atomic-layer precision. Furthermore, different elements can be introduced in the chamber at the same time, thus allowing for the addition of dopant impurities such as Si (n-type) or C (p-type) or for the production of ternary or more complex alloys.

Epitaxial growth is routinely employed for the production heterostructures, owing to the high material quality achievable. However, not all the combinations of semiconductors are possible, as only crystals with similar structure and lattice constants can be combined. In fact, if this condition is not matched, stacking defects and dislocations are generated in the solid that lower the overall quality of the samples. A well-known example of semiconductors with similar properties is the GaAs/AlAs system, which have lattice constants that differ by less than 0.1 Å [11]. An important feature of this type of heterostructure is the energy gap difference between the two materials, which enables interesting levels of band-structure engineering. In fact, when a thin layer of GaAs is grown between two layers of AlAs, the energy bands align in such a way that a potential well for the electrons is formed, since $E_g^{GaAs} < E_g^{AlAs}$. When the thickness of GaAs becomes smaller than the electronic de Broglie wavelength, i.e. $d_{\mathrm{GaAs}} \leq h/\sqrt{2m^* k_B T}$ (corresponding to about 10-20 nm [14]), the charge carriers are fully confined along the growth dimension. This type of heterostructure is called a quantum well.

The confinement of electrons along one direction is not the only available option. As schematically illustrated in Fig. 2.8, systems with other dimensionalities exist: in addition to bulk (3D) and quantum wells (2D), higher degrees of confinement produce quantum wires (1D) and quantum dots (0D). The density of electronic states $N(E)$, i.e. the number of available states per unit volume and within an energy interval, is severely affected by the change of dimensionality of each system (Fig. 2.8), resulting in a variation of the specific electronic and optical properties.

2.2.2 Self-assembled QDs

Among all the structures presented in Fig. 2.8, quantum dots (QDs) are the system of interest for the work of this PhD project. Owing to the confinement in all three spatial directions, the density of states of each sub-band n reads [14]

$$N_n(E) = 2\,\delta\,(E - E_n)\,, \tag{2.9}$$

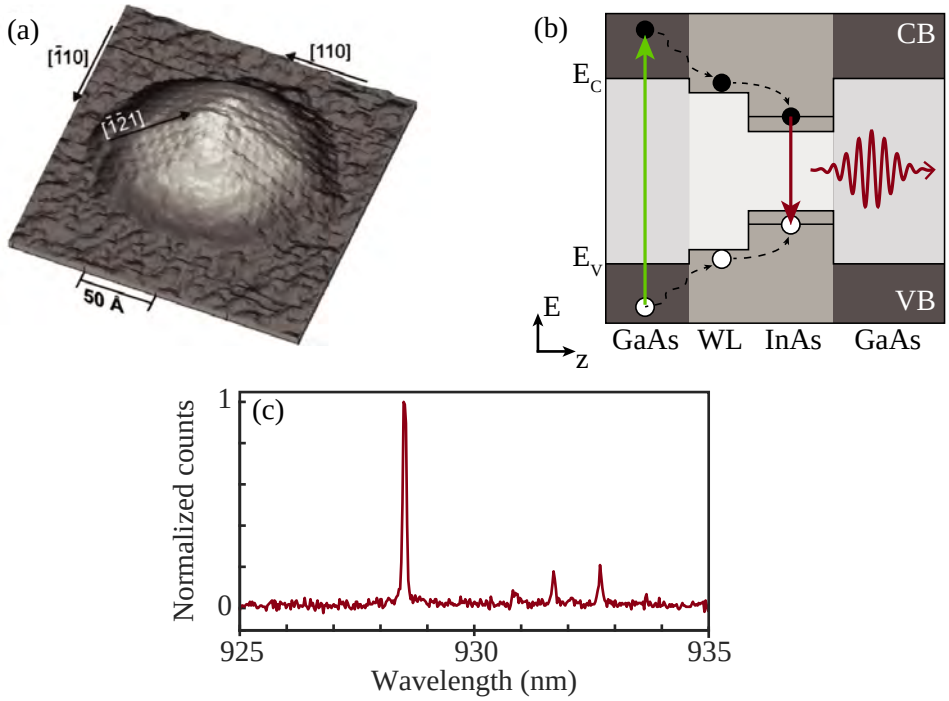

Figure 2.9: Self-assembled QDs. (a) Scanning tunnelling microscope (STM) image of an uncapped QD. Adapted from [22]. (b) Band diagram of an InAs QD embedded in a GaAs matrix. The full 3D energy confinement generate discrete states in the QD. After an above-band excitation (green arrow) excites an electron (black circle) into the CB of GaAs, a hole (white circle) is left in the VB. Fast, non-radiative processes (black dashed arrows) transfer the carriers into the WL and eventually to the QD, where they recombine by emitting a single photon (red arrow). (c) Typical spectrum collected from a self-assembled QD embedded in bulk GaAs.

where the factor 2 is due to the spin degeneracy and δ is the delta function. QDs are therefore characterised by discrete energy states, thus resembling the electronic and optical properties of single atoms. Such a feature has granted them the name "artificial atoms" and make them well-suited for the generation of single photons for application based on solid-state devices [6, 7].

Self-assembled QDs consist of nanometer-sized island of InAs embedded in a matrix of GaAs and they are epitaxially grown by means of the Stranski-Krastanov (SK) method [9]. The drive of such a process is the mismatch between the lattice constants of the two semiconductors: since InAs has a lattice parameter that is 7% larger than GaAs, an accumulation of strain occurs in the material when InAs is grown on a GaAs substrate. After about 1.5 monolayers of InAs [23], which form the so-called wetting layer (WL), the strain in the structure is reduced by rearranging the deposited atoms in such a way that a local energy minimum is reached and individual island are formed. A scanning tunnelling microscope (STM) image of the resulting structure is shown in Fig. 2.9a. Since the strain relaxation is an elastic process, very few defects are created during the formation of QDs [9, 24] and this ensures bright optical transitions with linewidths of the order of few μeV [6, 7]. A capping layer of GaAs is subsequently grown to complete the full 3D confinement, since $E_g^{InAs} < E_g^{GaAs}$. This, in combination with the direct bandgap of both semiconductors, ensures the emission of single photons when the electrons in the CB recombine with the holes in the VB, as schematically illustrated in Fig. 2.9b. A typical spectrum of such an emission event presents single lines, as reported in Fig. 2.9c, demonstrating the discrete nature of the QD energy states.

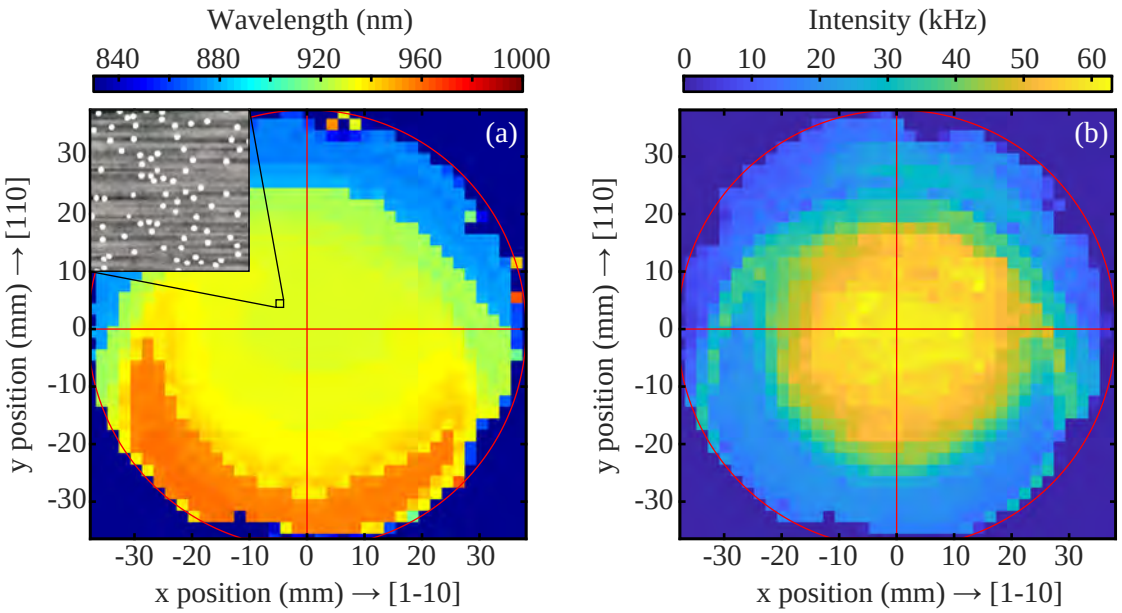

Figure 2.10: Side-effects of Stranski-Krastanov growth. (a) Photoluminescence map, collected at $T = 77\,\mathrm{K}$, reporting the spatial dependence of the brightest emission peak. Higher concentrations of In shift the signal towards longer wavelengths. Inset: atomic force microscope image of epitaxially grown QDs. The nucleation process starts at positions where the adatoms have less energy, resulting in QDs randomly placed on the surface of the wafer. The lateral size of the image is 1 µm. Adapted from ref. [9]. (b) Detected intensity of the peaks analysed in (a). In both maps, the 3-inch wafer is indicated by a straight red line. The relevant crystallographic directions are also shown.

The benefits of the self-assembly process, however, come with a price to pay; the lack of control over the spatial position and spectral property of the resulting emitters. The strain reduction is in fact a process that happens locally and the nucleation of the InAs islands occurs at random positions on the surface of the sample [9, 24, 25], as clearly shown by the atomic force microscope (AFM) image in the inset of Fig. 2.10a. Moreover, the final size and shape of the QDs are difficult to control precisely as they are very sensitive to the growth parameters, causing each quantum dot to emit at a different wavelength [24–27]. This results in a large distribution of emission wavelengths and intensities over the full area of the substrate, as shown in Fig. 2.10, which reports photoluminescence (PL) maps of an as-grown wafer collected at $T = 77\,\mathrm{K}$. The emission wavelength λ of the brightest peak shown in Fig. 2.10a clearly varies as a function of the position, from $\lambda \approx 960\,\mathrm{nm}$ at the bottom of the layer (where the In concentration is higher) down to $\lambda \approx 900\,\mathrm{nm}$ on the topmost area. The intensity of the peak changes with the position as well, as visible in Fig. 2.10b, suggesting a spatial-dependent variation of the QD sizes.

2.2.3 QDs as two-level systems

The similarities between single atoms and QDs allow them to be described as solid-state based two-levels systems, where an optical excitation causes the transition from a ground state $|g\rangle$ to an excited state $|e\rangle$, as schematically shown in Fig. 2.9b. Such a system can subsequently relax and release energy by the spontaneous emission of a single photon, which is a purely quantum effect since it is triggered by the interaction between the system and the electromagnetic vacuum

field [28].

Self-assembled QDs have sizes much smaller than the wavelength of the light they emit, which is a condition that allows the use of the dipole approximation for the description of the interaction between them and the electromagnetic field. The interaction Hamiltonian $\hat{H}_I$ reads

$$\hat{H}_I = -\hat{\mathbf{d}} \cdot \hat{\mathbf{E}}, \tag{2.10}$$

where $\hat{\mathbf{E}}$ is the electric field operator and $\hat{\mathbf{d}}$ the dipole moment operator. The spontaneous decay rate γ_r of a two-level system is calculated according to Fermi's golden rule as [28]

$$\gamma_r = \frac{2\pi}{\hbar^2} \sum_f \left| \langle f | \hat{H}_I | i \rangle \right|^2 \delta(\omega_f - \omega_i), \tag{2.11}$$

with $|i\rangle$ and $|f\rangle$ are the respective initial and final state of the system and the delta function $\delta(\omega_f - \omega_i)$ shows that the decay process results in the emission of a photon with frequency that matches the energy separation between the two states, thus ensuring the energy conservation. From eqs.(2.10) and (2.11), it can be shown that the radiative decay rate γ_r of a QD can be written as [6]

$$\gamma_r(\mathbf{r_0}, \omega_0, \mathbf{d}) = \frac{\pi \omega_0}{\hbar \varepsilon_0} |\mathbf{d}|^2 \rho_{LDOS}(\mathbf{r_0}, \omega_0, \hat{\mathbf{e}}_\mathbf{d}). \tag{2.12}$$

Eq.(2.12) demonstrates that γ_r of a self-assembled QD is a function of the position $\mathbf{r_0}$, the emission frequency ω_0 and the dipole $\mathbf{d} = |\mathbf{d}|\hat{\mathbf{e}}_\mathbf{d}$ of the emitter. Furthermore, the term $\rho_{LDOS}(\mathbf{r_0}, \omega_0, \hat{\mathbf{e}}_\mathbf{d})$ is the so-called local density of optical states (LDOS), which is a parameter that describes the number of available optical modes per volume and energy experienced by the dipole $\mathbf{d}$ when vibrating at frequency ω_0 and positioned in $\mathbf{r_0}$. The LDOS provides information about the electromagnetic environment around the emitter and eq.(2.12) demonstrates how any modification of it may affect the decay dynamics of QDs (as we will see in Sec. 2.3).

2.2.4 Excitonic states in QDs

Every optical excitation generates one electron in the conduction band and one hole in the valence band of a QD (cf. Fig. 2.9b). In fact, the degeneracy between light-hole and heavy-hole sub-bands is lifted due to strain accumulated during the growth; as the latter is the closest one to the CB, the heavy holes are the most relevant carriers during the radiative recombination and we will focus on these ones from now on.

Instead of analysing the charge carriers separately, a more convenient basis can be introduced to facilitate the study of the decay dynamics in a QD and it is based on the exciton, which is a quasi-particle defined as an electron-hole pair bound by exchange and Coulomb interactions, with the latter included only perturbatively due to the strong confinement achieved in self-assembled QDs [6]. In this new picture, whilst the ground state $|g\rangle$ still corresponds to an emitter with no excitation (i.e. $|0\rangle$), the first excited state $|e\rangle = |X\rangle$ consists in an electron in the CB and a hole in the VB, as shown in Fig. 2.11a and Fig. 2.11b, respectively.

Fig. 2.11 displays the simplest configurations possible for different excitonic states. Here, electrons and holes are shown along with their pseudospins, which describe their total angular momentum $j = l + s$. Being fermions, both carriers have $s_{e/h} = 1/2$, while the value of l is given by the symmetry of the hosting band: spherical symmetry for CB ($l_e = 0$) and p-like symmetry for VB ($l_h = 1$). Four different spin-states are thus possible: electrons have $m_j = \pm 1/2$, represented as $|\uparrow\rangle$ and $|\downarrow\rangle$, while heavy holes show $m_j = \pm 3/2$, i.e. $|\Uparrow\rangle$ and $|\Downarrow\rangle$. An exciton can therefore be formed by the combinations $|\Uparrow\uparrow\rangle$, $|\Downarrow\downarrow\rangle$, $|\Uparrow\downarrow\rangle$ and $|\Downarrow\uparrow\rangle$. Due to the conservation of total angular

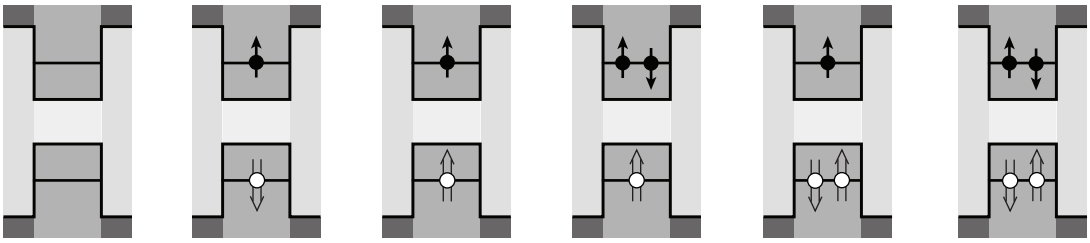

Figure 2.11: Schematic illustration of the lowest-energy excitonic states: (a) ground state $|0\rangle$, (b) bright neutral exciton $|X_b^0\rangle$, (c) dark neutral exciton $|X_d^0\rangle$, (d) negatively charged trion $|X^-\rangle$, (e) positively charged trion $|X^+\rangle$ and (f) biexciton $|XX\rangle$.

momentum, only the last two transitions generate a photon and they are therefore said to represent bright excitons $|X_b\rangle$ (Fig. 2.11b). Following the same reasoning, the first two combinations are typical of dark excitons $|X_d\rangle$ (Fig. 2.11c).

As visible from the STM image in Fig. 2.9a, InAs QDs are slightly elongated along the [110] direction and this asymmetry breaks the degeneracy between the bright states, resulting in two orthogonal dipoles $|X_b^0\rangle = \left(1/\sqrt{2}\right)(|\Uparrow\downarrow\rangle - |\Downarrow\uparrow\rangle)$ and $|Y_b^0\rangle = \left(1/\sqrt{2}\right)(|\Uparrow\downarrow\rangle + |\Downarrow\uparrow\rangle)$; similar relationships exist for the respective dark states. The energy difference between the two bright states is referred to as fine-structure splitting ΔE_{fss} and is typically of the order of 10-100 µeV [6].

Other excitonic states are possible, based on the initial conditions of the emitter when the optical excitation occurs: for example, structural defects or impurities may trap an electron or a hole inside the QD, resulting in excitons with an additional negative (Fig. 2.11d) or positive charge (Fig. 2.11e), respectively. States of this type are named trions ($|X^-\rangle$ and $|X^+\rangle$, respectively), as opposed to simpler neutral exciton $|X_{b/d}^0\rangle$, where no net charge exists. Finally, high-energy excitation schemes may result in the generation of two e^--h^+ pairs in the QD, which form the so-called biexciton $|XX\rangle$. Each charge configuration of the excitonic states generates different exchange and Coulomb interactions between the carriers, which result in emitted photons with different energies that appear at different wavelengths in the QD emission spectrum [29, 30].

Deterministic control over the number of charges hosted in a single QD is possible by exploiting the properties of heterostructures presented in Sec. 2.1.2. In fact, when QDs are grown in the intrinsic region of a p-i-n diode as illustrated in Fig. 2.12a, the ability to change the position of the energy bands in the structures via an applied bias voltage allows for the control over the width of the energy barriers around the emitter, thus enabling or preventing the tunnelling of electron into the QD. High quality contacts and properly engineered heterostructures allow for fine tuning of the field at the QD position, unlocking the control at the single-charge level [29–33].

The shift of the energy levels operated by the external bias has one more effect on the photons emitted from the QDs, which is to tune the wavelength for different values of V, as reported in the photoluminescence map in Fig. 2.12b. Such behaviour is know as the quantum-confined Stark effect [34] and it has often been used to investigate the properties of different excitonic states. In fact, the relationship between emission energy and applied electric field F can be modelled as [35–37]

$$E(F) = E_0 - p \cdot F + \alpha \cdot F^2, \tag{2.13}$$

where E_0 is the emission energy for $F = 0\,\mathrm{V/m}$, p is the excitonic permanent dipole parallel to the direction of the applied field and α is the polarizability of the investigated state and provides information on how F affects the extension of the excitonic wavefunction. The overall effects of

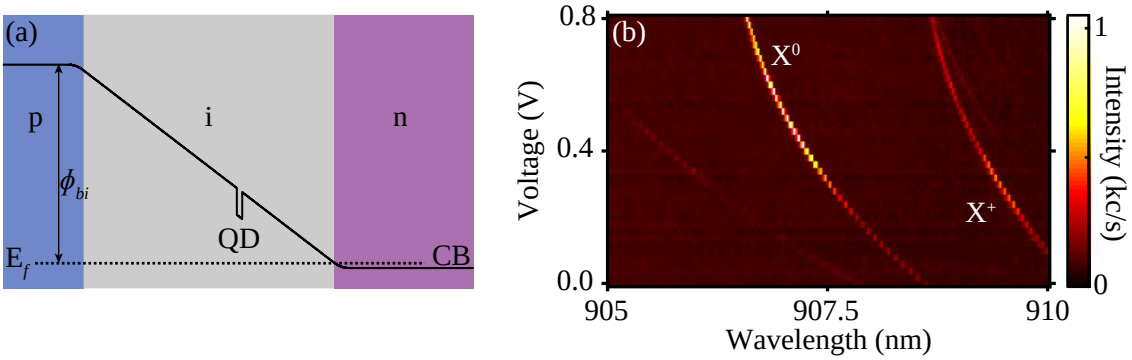

Figure 2.12: Deterministic control of the excitonic population via applied voltage. (a) Schematic conduction band profile at zero bias voltage for a p-i-n, where QDs are grown in the intrinsic layer. Adapted from ref. [31]. (b) Photoluminescence of a QD embedded in a p-i-n diode as a function of the applied voltage. The two lines are visible and they most likely shows the X^0 and X^+ transitions. Adapted from ref. [32].

the external electric field can be adjusted by properly engineering the band structure of the sample and tuning ranges as broad as 25 meV (corresponding to about 18 nm) were demonstrated when tunnelling barriers were employed [37]. These results show that the electrical control enabled by doped heterostructures constitutes an appealing tool for the manipulation of the spectral properties of self-assembled QDs, which is key for several application in quantum photonics.

2.2.5 Decay dynamics in QDs

Although the presence of several excitonic states paints a rather complicated picture for the possible energy states in QDs, the system can still be described in terms of two states, one excited and one ground state, where eq. (2.12) still applies. As the neutral exciton is the most relevant state for the application described in this work, this will be the main focus when describing the decay dynamics for InAs QDs.

Fig. 2.13 shows a level scheme depicting the typical transitions in a neutral exciton $|X^0\rangle$ for a QD embedded in a homogeneous medium. A more complete approach should also include the states of the second dipole $|Y^0\rangle$; however, any transition between $|X^0\rangle$ and $|Y^0\rangle$ requires the spin flip of both carriers at the same time and can be omitted compared to the other relevant decay rates of the neutral exciton. For this reason, we can assume that the two orthogonal dipoles are decoupled and therefore safely omit the second one.

After the excitation of an electron to the CB, the generated bright state $|X_b\rangle$ can decay down to the ground state $|0\rangle$ either radiatively, with rate $\gamma_{b,r}$, or by thermal relaxation of the charge to the VB with non-radiative rate $\gamma_{b,nr}$. Before the decay, spin-flip processes may occur at rate γ_{bd} that convert the bright state into a dark state $|X_d\rangle$, which can only decay non-radiatively with rate $\gamma_{d,nr}$. The same processes may also result in the opposite situation, that is the transition $|X_d\rangle \rightarrow |X_b\rangle$ may also take place. The dynamics just described results in a double exponential decay for the population $\rho_b(t)$ of the bright exciton [38]

$$\rho_b(t) = A_f \exp(-\Gamma_f t) + A_s \exp(-\Gamma_s t), \tag{2.14}$$

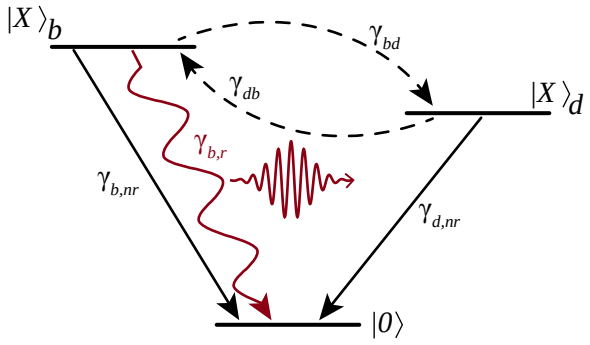

Figure 2.13: Schematic representation of the level scheme for a neutral exciton. The bright state $|X_b\rangle$ can decay down to the ground state $|0\rangle$ either radiatively or non-radiatively with rates $\gamma_{b,r}$ and $\gamma_{b,nr}$, respectively. Only non-radiative recombinations are allowed for the dark state $|X_d\rangle$. Coupling between the two excitonic state are possible and occur at rates $\gamma_{db} = \gamma_{bd}$.

where the fast and slow decay rates respectively read

$$\Gamma_f = \frac{\gamma_{b,r}}{2} + \gamma_{b,nr} + \gamma_{db} + \sqrt{\frac{\gamma_{b,r}^2}{4} + \gamma_{db}^2} \tag{2.15a}$$

$$\Gamma_s = \frac{\gamma_{b,r}}{2} + \gamma_{b,nr} + \gamma_{db} - \sqrt{\frac{\gamma_{b,r}^2}{4} + \gamma_{db}^2} \tag{2.15b}$$

and the terms A_f and A_s are the relative amplitudes of the respective decay component. In order to obtain the eqs. (2.15), a few assumptions have been made [38]: (i) for weak non-resonant regimes, the initial populations of the two excited states can be set to be $\rho_b(t=0) = \rho_d(t=0) = 0.5$; (ii) at the usual operational temperatures for our experiments (i.e. $T \approx 10\,\mathrm{K}$), the thermal energy is much larger than the energy splitting between $|X_b\rangle$ and $|X_d\rangle$, thus $\gamma_{bd} \approx \gamma_{db}$; (iii) $\gamma_{b,nr} \approx \gamma_{d,nr}$ based on experimental findings [39]. By fitting experimental decay curves acquired during lifetime measurements performed on single QDs with the model in eq. (2.14), the values of both radiative and non-radiative decay rates can be evaluated. These parameters can be used to calculate the quantum efficiency of the investigated emitter, which is an important figure-of-merit that quantifies the probability of emitting photons after excitation and it is defined as [6]

$$QE_b = \frac{\gamma_{b,r}}{\gamma_{b,r} + \gamma_{b,nr}}. \tag{2.16}$$

As the decay rates $\gamma_{b,r}$ and $\gamma_{b,nr}$ vary from one QD to another due to differences occurring during their growth, large ranges of QE_b can be found on the same sample, with $QE_b \approx 1$ being the most desirable values for photonic applications [6].

2.2.6 Decoherence in self-assembled QDs

Radiative decay rates of $\gamma_r \approx 1 - 1.3\,\mathrm{ns}^{-1}$ have been reported for QDs embedded in a homogeneous medium [8, 30, 40], which correspond to optical linewidths of about $\Gamma_0 = \gamma_r/2\pi \approx 160 - 200\,\mathrm{MHz}$ [41, 42]. In typical experiments, however, linewidths much broader than the lifetime-limited values are often measured due to the presence of decoherence mechanisms that affect the emission of photons. The causes of such detrimental effects are due to the solid-state

nature of self-assembled QDs and the unavoidable interactions between the emitters and the surrounding material. The three main sources of decoherence that have been identified are phonons, spin noise and charge fluctuations.

As illustrated in Fig. 2.9b, after the above-band excitation of an electron into the conduction band, the carriers undergo fast and non-radiative processes that transfer them into the QD, where they eventually recombine. These transitions occurs on a picosecond time scale and are the results of interactions between the generated charges and the phonons, i.e. the acoustic vibrations of the GaAs crystalline lattice. Such energy exchange causes dephasing in the system, which both generates side-bands and broaden the zero-phonon line in the emission spectrum. Whilst the former constitute only 5-10% of the total emitted light and can therefore be removed by spectral filtering, the latter effect depends on the dimensionality of the system and is more difficult to deal with. Recent works have studied this effect and proposed possible approaches to address this issue, based on the fabrication of photonic nanostructures encapsulated inside polymeric materials [43, 44].

Spin fluctuations have been shown to affect the overall coherence of self-assembled QDs [41] and they are caused by the coupling between the photo-generated electrons and the oscillating Overhauser field, which is an effective magnetic field generated by the nuclear spins of the atoms forming the QD. The resulting spin noise usually oscillates with frequency between 1 kHz and 100 kHz and produces a broadening of the emission spectrum due to Zeeman splitting of the excitonic energy states [41]. Such an effect is detrimental for quantum applications based on the electron spins, where long coherence times are essential [45]. A number of studies, reviewed in [7, 46], have presented possible solutions to this problem, like the use of the hole spin as a viable qubit owing to its reduced interaction with the Overhauser field.

The third source of decoherence in systems based on self-assembled QDs comes from the Coulomb interaction between the emitters and mobile charge carriers present in their proximity, which are introduced by defects or surface states. This interaction induces a fluctuating shift in the optical transition energy of the two-level system and hence causes a broadening in the optical linewidth of the QD. Typical frequencies for this charge noise have been reported between 1 Hz and 1 kHz [41]. The common approach to counteract this effect is the use of p-i-n diodes, where the static electric field across the QDs can stabilise the charges. Narrow optical linewidths [33, 42] and high levels of indistinguishability [32, 47] have proven the efficacy of this method.

2.3 Photonic nanostructures

The radiative decay rate for a two-level system has been presented in the previous section and eq. (2.12) demonstrates that its final value is strongly dependent on the LDOS, which means that an emitter will have a shorter or longer lifetime based on the number of states it is allowed to decay into. Any modification of the material around the QDs affects the LDOS and thus enables the enhancement or the suppression of the QD decay rate and, more generally, provides the ability to tailor the strength of the local light-matter interaction. Several different types of photonic nanostructures have been proposed to this end [6]; in this work we will mainly focus on photonic crystals waveguides and nanobeam waveguides.

2.3.1 Photonic crystal waveguides

Photonic crystals (PhCs) can be defined as inhomogeneous dielectric materials where the refractive index varies periodically in space with a length scale comparable to the optical wavelength [48]. Similarly to their electronic counterparts, the propagation of photons in this type of structure is

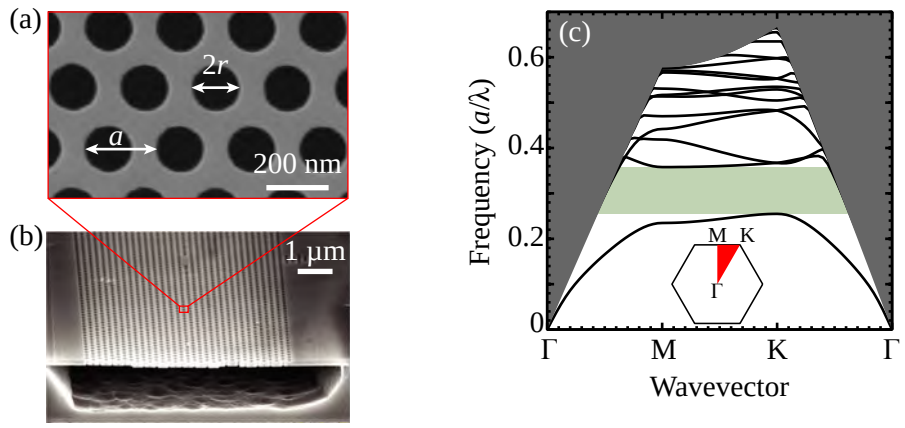

Figure 2.14: Photonic crystal membranes. (a) Top-view SEM image of photonic crystal constituted by triangular lattice, with period a, of air holes with diameter $2r$ etched into a GaAs membrane. (b) Side-view SEM image of a PhC membrane. The removal of the layer of material underneath the membrane enables the confinement along the out-of-plane direction due to total internal reflection. (c) Band structure of a PhC membrane with triangular lattice. The solid black lines represent the eigenfrequencies of the system. An range of frequencies are not allowed and forms the photonic bandgap shown in green. The dark grey area correspond to the modes that are not bound to the GaAs slab and escape from it. The inset report the hexagonal Brillouin zone of the PhC lattice, where the relevant wavevectors are indicated.

controlled by the Bragg scattering, which forbids the propagation of some optical modes. Therefore, photonic bandgaps exist in the band structure, which is now calculated as the dependence of the angular frequency on the Bloch vector $\mathbf{k}$ of the lattice, i.e. $\omega = \omega(\mathbf{k})$.

In general, PhCs can be obtained by alternating materials with different dielectric constants and full photonic bandgaps are formed when such repetition occurs in all three dimensions, thus blocking the propagation of light in all direction. However, fabricating this type of structures is quite demanding and other simpler solutions have been developed instead. One of these is the so-called photonic crystal membranes, which are 2D PhCs fabricated on thin slabs of a dielectric sandwiched in between two layers of a second material with lower refractive index. In this way, while the propagation along the plane is suppressed by the presence of the photonic bandgap, the out-of-plane emission is controlled by the total internal reflection at the interface, thus creating a quasi 3D-confinement of light [48]. In the specific case of the samples presented in this work, PhCs are formed by a GaAs membrane with thickness of 160-180 nm where a regular lattice of air-holes have been fabricated. An example of such a structure is shown in Fig. 2.14a, which reports a scanning electron microscope (SEM) image of a PhC with a triangular lattice of holes with radius $r = 73\,\text{nm}$ and lattice constant $a = 240\,\text{nm}$. The total internal reflection is achieved by removing the layer of material underneath the GaAs layer, thus completely suspending the membrane in air as demonstrated in Fig. 2.14b. An example of band structure for PhCs of this type is shown in Fig. 2.14c, where the photonic bandgap is shown in green. For a fixed value of thickness, varying the parameters a and r causes a shift of the central position of the bandgap. The grey area illustrates all the modes that are not bound to the membrane and escape from it, and is often referred to as light cone. The existence of a range of forbidden frequencies in PhC membranes translates into a reduction of the LDOS for QDs embedded in the middle of these nanostructures and emitting photons at the corresponding wavelengths. This phenomenon has been demonstrated experimentally in [38], where the spontaneous emission of several InAs QDs

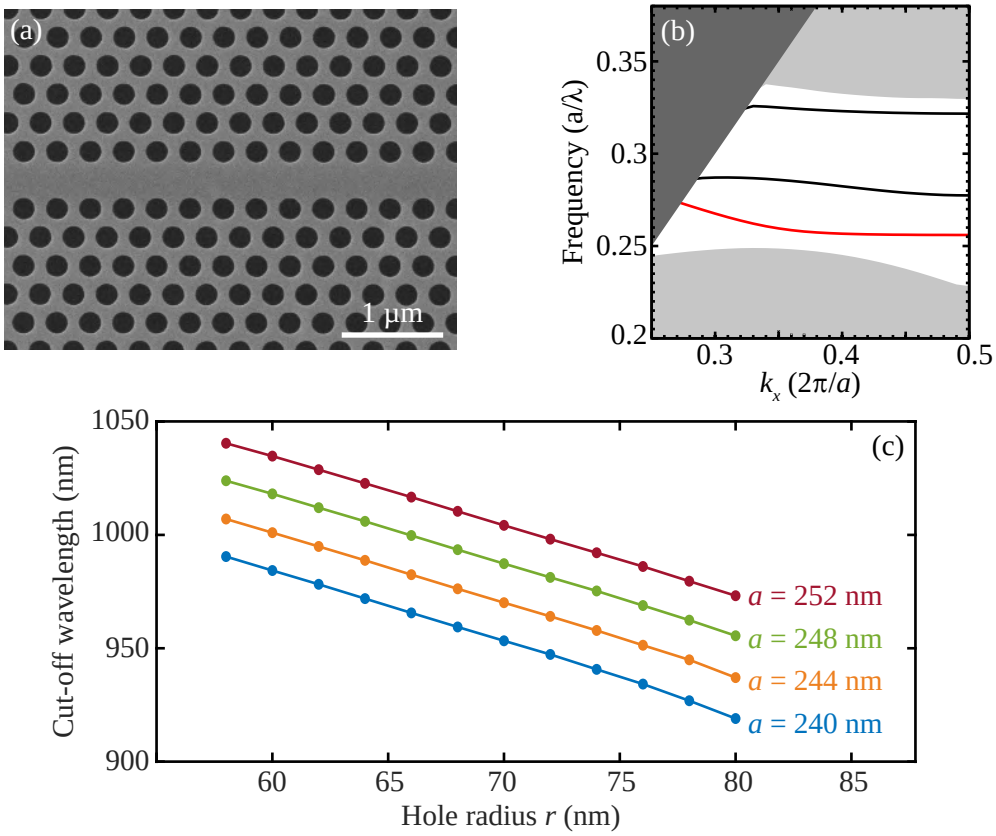

Figure 2.15: Photonic crystal waveguides. (a) Top-view SEM image of a PhCW obtained by the removal of one row of holes from a PhC with triangular lattice. (b) Band structure of the PhCW shown in (a). The dark grey area represents the light cone, whereas the light grey regions correspond to the range of frequencies propagating through the GaAs slab. Three modes appear in the photonic bandgap (solid lines), with the fundamental one marked in red.

have been suppressed by factors up to 70.

In analogy with the electronic crystals, defects can be introduced into PhCs in order to modify their properties. For example, removing a row of holes from the PhC in Fig. 2.14a produces a line defect denominated photonic crystal waveguide (PhCW). Fig. 2.15a shows a SEM image of such nanostructure, while Fig. 2.15b presents an example of its typical band structure, where the normalised angular frequency ω is plotted as a function of the wavevector parallel to the propagation direction k_x. Three new curves appear in the photonic bandgap, which indicate modes that are allowed to propagate only along the line defect. Hereafter we will referred to the lowest energetic one as "fundamental mode" (shown in red in Fig. 2.15b). The values of the corresponding frequencies can be calculated by the dispersion relation and are functions of the parameters a and r of the PhC. In fact, the fundamental mode shifts to lower frequencies when the hole radius becomes smaller or the lattice constant a gets larger. This relationship is demonstrated in Fig. 2.15c, where the wavelength calculated at the edge of the Brillouin zone is plotted as a function of r for PhCWs with different values of a. As shown by these results, a reduction of only 1 nm in r causes an increase of about 4 nm in the cut-off wavelength.

The dispersion relation can also be used to extract another important parameter, i.e. the group

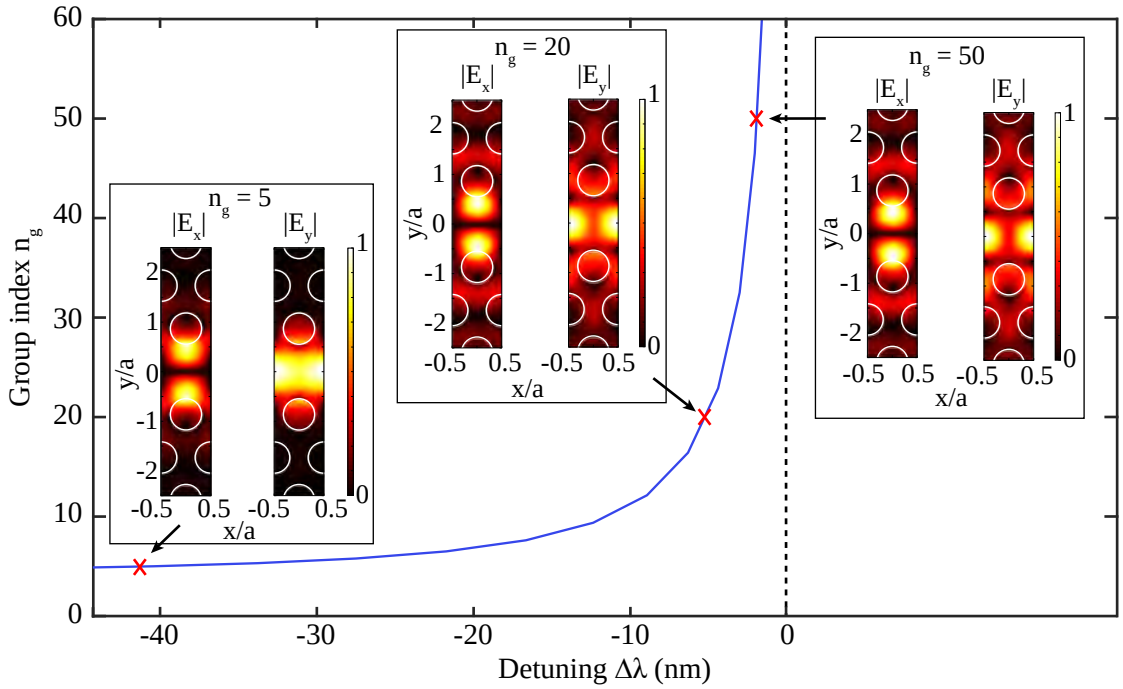

Figure 2.16: Spatial and wavelength dependent properties of a propagating mode in a PhCW ($a = 245\,\text{nm}$ and $r = 78\,\text{nm}$). The calculated values of the group index n_g rapidly increases for decreasing detuning $\Delta\lambda$. The normalised amplitudes of the in-plane electric field distribution in the unit cell and for three different detunings from the band edge are also reported and show that only minor changes appear for $\Delta\lambda \to 0$. All the values were obtained from finite-elements simulations.

index n_g

$$n_g(\omega) = \frac{c}{v_g} = \frac{c}{\frac{\partial\omega}{\partial k_x}}, \tag{2.17}$$

where c is the speed of light in vacuum and v_g is the group velocity of the guided mode. The group index is inversely proportional to the slope of the dispersion relation and therefore diverges for values of k_x approaching the edge of the Brillouin zone, as shown in Fig. 2.16 where the calculated values of n_g are plotted as a function of the detuning $\Delta\lambda$ from the cut-off of the fundamental mode. Since at the same time $v_g \to 0$, the increase of the group index is colloquially defined "light slow-down" and it manifests as a stronger confinement of the propagating mode, as illustrated by the normalised amplitudes of the in-plane electric field distributions for three different values of n_g presented in Fig. 2.16. It is worth noting that the main features of the propagating mode do not vary considerably for different detunings $\Delta\lambda$, which is expected since they are defined mainly by the parameters a and r of the PhCW.

The introduction of new modes in the photonic bandgap largely enhances the LDOS and hence the radiative decay rate of embedded QDs on resonance with those frequencies. The parameter that quantifies such effects is the Purcell factor F_p, which is defined as the ratio between the radiative decay rate in the PhCW $\gamma_{\text{wg,r}}$ and the value obtained in a homogeneous medium $\gamma_{\text{B,r}}$ [6]. In a PhCW it can be written in the form [49]

$$F_p(\omega, \mathbf{r}) = \frac{\gamma_{\text{wg,r}}}{\gamma_{\text{B,r}}} = \frac{3\pi a c^2}{\omega^2 \sqrt{\varepsilon(\mathbf{r})}} n_g(\omega) \left|\hat{\mathbf{e}}(\omega, \mathbf{r}) \cdot \hat{\mathbf{e}}_{\mathbf{d}}\right|^2, \tag{2.18}$$

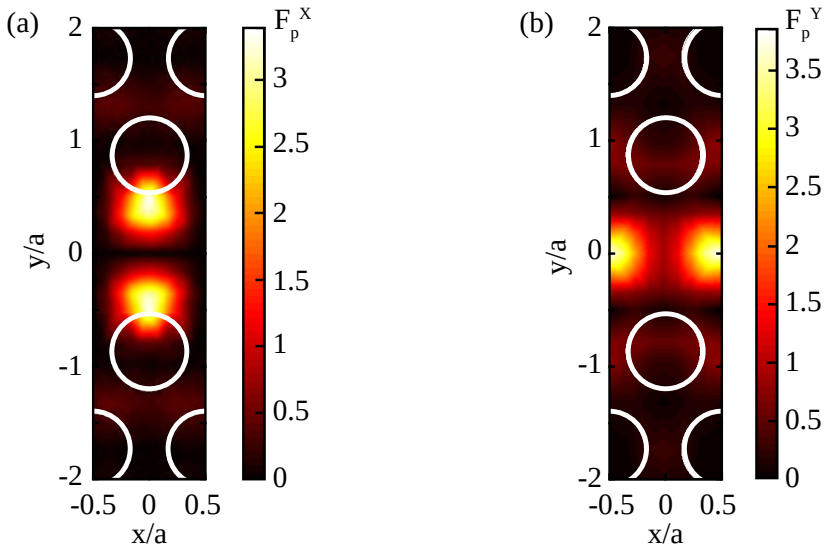

Figure 2.17: Spatial dependence of the Purcell factor F_p in the unit cell of a PhCW, calculated for $n_g = 20$, for dipoles oriented (a) along and (b) transversal to the propagation direction. The white circles represent the air holes. High values of F_p can be found only in relative small regions of the device. Adapted from [50].

with $\varepsilon(\mathbf{r})$ the spatially periodic permittivity of the semiconductor, where any dependence on the frequency can be neglected due to the small range of interest for the quantum photonics applications we are considering here [6]. The term $\hat{\mathbf{e}}(\omega,\mathbf{r})$ is the unity vector of the propagating electric field, with frequency ω and at the position $\mathbf{r}$. All the other parameters have been already defined. Eq.(2.18) demonstrates that, for a given photonic crystal waveguide, F_p is a function not only of the confinement strength quantified by the frequency dependent $n_g(\omega)$, but it is also affected by the position of the emitter dipole and its orientation with respect to the electric field components. Such relationship thus results in values that drastically vary over different positions of the PhCW unit cell, following the spatial distributions of the in-plane electric field shown in Fig. 2.16. The values of $F_p(\omega,\mathbf{r})$ can be simulated via a finite-element method [50] and an example of the results obtained for $n_g = 20$, for both dipole orientations, are reported in Fig 2.17. Here, it is visible that only relative small areas of the unit cell show $F_p \gg 1$: for example, with a lattice constant of $a = 250\,\text{nm}$, which is a typical value for the samples investigated in this work, the dipole transversely oriented with respect to the propagation direction (that is, y-oriented) can experienced an enhancement of $F_p^Y > 3$ only in regions with a radius of about 50 nm.

The enhancement of the decay rate into the waveguide mode, obtained from the engineered environment that a PhCW provides, has the important effect of improving the coupling efficiency of the light into the nanostructures. The figure-of-merit in this case is the so-called β-factor, which is defined as ratio between $\gamma_{\text{wg,r}}$ and the total decay rate of the emitter into all the available modes γ_{tot} [50]

$$\beta = \frac{\gamma_{\text{wg,r}}}{\gamma_{tot}} = \frac{\gamma_{\text{wg,r}}}{\gamma_{\text{wg,r}} + \gamma_{ng} + \gamma_{\text{wg,nr}}}, \tag{2.19}$$

where γ_{ng} and $\gamma_{\text{wg,nr}}$ are the rates of, respectively, the decay into non-guided modes and of the non-radiative recombinations that may occur in a QD (see previous section). Large values of β can therefore be achieved by enhancing the decay of the emitter into the waveguide mode of interest. Following this approach, $\beta \geq 98.4\%$ have been achieved experimentally [8].

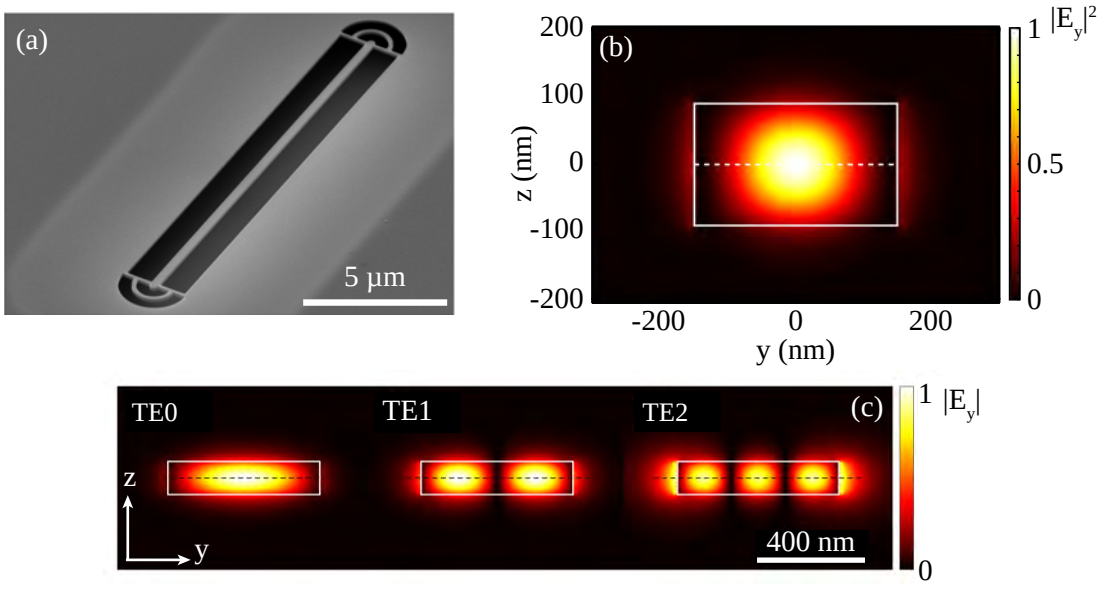

Figure 2.18: Nanobeam waveguides. (a) Tilted-view SEM image of a suspended nanobeam waveguide that connects to circular gratings. (b) Finite-element simulations of the guided mode supported by a suspended GaAs NBW with width of 300 nm and 180 nm thick. (c) Same as (b), but for a NBW that is 600 nm wide. Three modes are supported in the larger NBW and are clearly confined in the high index region. (b) Adapted from [51], (c) adapted from the supporting material of [33].

2.3.2 Nanobeam waveguides

Another nanostructure with functionalities that are useful for quantum photonic technologies is the so-called nanobeam waveguide (NBW), which is illustrated in Fig. 2.18a. A NBW consists of a suspended strip of GaAs, with widths that could vary based on the specific applications. The number of modes supported by these nanostructures depends on the size of the cross-section, as in these devices the light is confined only by the total internal reflection that occurs at the four interfaces. For example, only one mode is supported inside NBWs that are 300 nm wide and with a thickness of 180 nm (cf. Fig. 2.18b), whereas up to three modes can be confined in NBWs with width of 600 nm, as demonstrated in Fig. 2.18c.

The lack of a photonic bandgap in these structures reduces the maximum confinement achievable. Nonetheless, modest values of β and F_p can still be obtained in fairly large NBWs, as illustrated in Fig. 2.19a and Fig. 2.19b, respectively. Here, the coupling efficiencies and Purcell factor for the simulated modes shown in Fig. 2.18c are plotted as a function of the distance d between emitter and central axis of the nanostructure. The multi-mode nature of the 600 nm-wide NBW clearly limits the maximum β of the fundamental mode. Narrower waveguides are therefore more suitable for quantum photonic applications, as they support only one mode and higher coupling efficiencies are therefore possible. Fig. 2.19c reports the calculated values of β for the mode shown in Fig. 2.18b and demonstrates that coupling efficiencies as high as 95% can be achieved. However, the values of β vary with the position of the emitter and quickly drops to below $\approx 80\%$ for $d > 50\,\text{nm}$, which reveals that QDs located in the central region of a NBW are better coupled to the propagating mode.

The ease of fabricating such nanostructures makes this type of waveguide the optimal choice to optically connect different devices, as shown in the SEM image in Fig. 2.19d. Here, a NBW

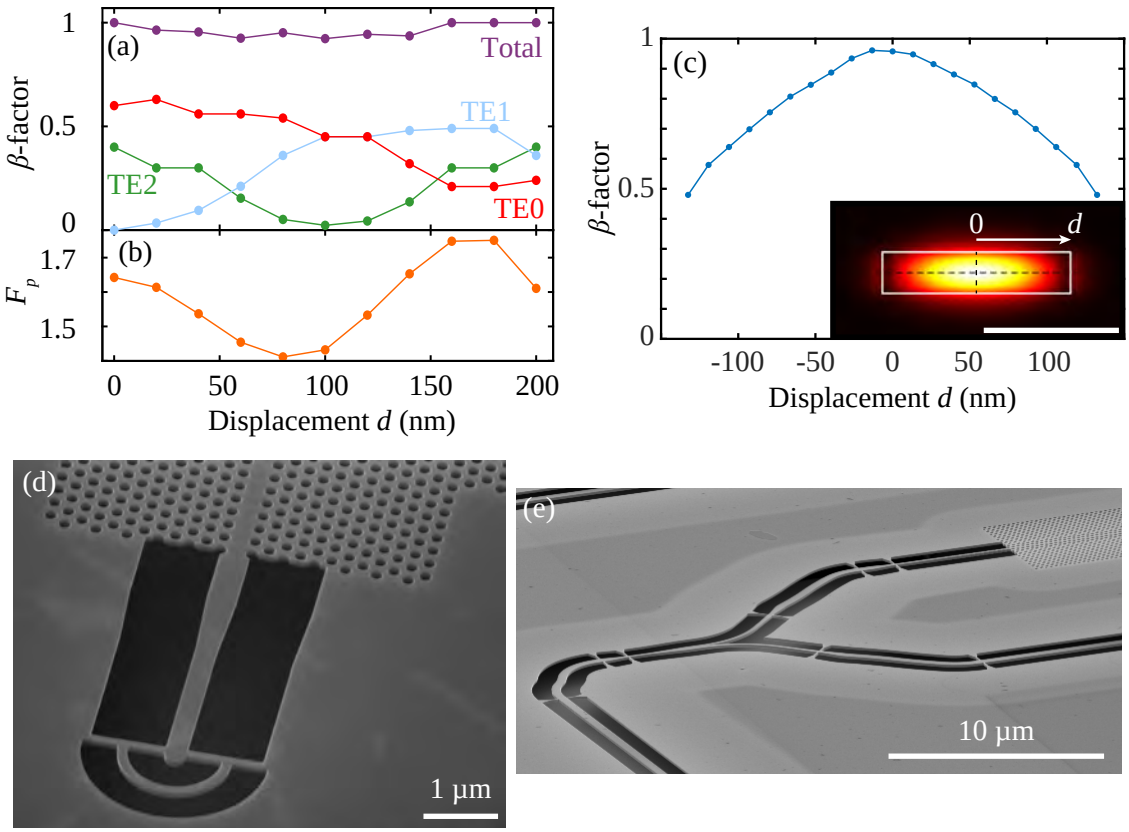

Figure 2.19: Applications of NBWs. (a) Position dependent β-factor for the guided mode of a 600 nm-wide NBW. The sum of the β-factors for each mode is also shown. (b) Total Purcell factor F_p as a function of the QD position in the NBW of (a). The complex lineshape is related to the multi-mode nature of the waveguide. (c) Same as in (a), but for a waveguide with width of 300 nm. Inset: all the presented values are obtained by moving the emitter location from the central axis (d = 0 nm) towards the edge of the NBW. The scale bar is 400 nm. All the values in (a), (b) and (c) are calculated for a dipole transversely oriented with respect to the propagation direction. (a) and (b) Adapted from the supporting material of [33], (c) adapted from [51]. (d) Tilted-view SEM image of a NBW used to optically connect a PhCW to a circular grating, which functions as out-coupler for the light propagating from the waveguide. (e) Tilted-view SEM image of a suspended bean-splitter to couple light both into both a PhCW and a second NBW.

is used to couple the light propagating in a PhCW to a circular grating, which will send the photons vertically out of plane into a microscope objective for detection. More complex designs are also possible, as demonstrated in Fig. 2.19e, where a suspended NBW forms a beam-splitter that couples light into both a PhCW and a second NBW, thus connecting components with different functionalities and forming more intricate quantum photonics circuits.

Chapter 3

Nanofabrication techniques for photonic devices in GaAs

The electronic and optical properties of self-assembled InAs QDs embedded in GaAs presented in the previous chapter make them a promising choice for quantum optics experiments on a solid-state platform. The direct bandgap of the semiconductors and the 3D energy confinement achieved in this system enable the production of single photons via spontaneous emission. The possibility to control such process by applying electric fields across the samples or by the engineering of the photonic environment around the emitters has been an important aspect for the proliferation of this quantum photonic system. Another important factor is the access to the large existing library of fabrication procedures available for nanotechnologies based on III-V semiconductors. In this chapter we will present three of the main techniques, namely lithography, etching and metal deposition, which constitute the backbone of all the fabrication procedures developed during this project.

3.1 Lithography

Lithography is the fabrication process where a geometrical pattern is transferred to a polymeric layer called resist. A schematic illustration of the process flow is depicted in Fig. 3.1, where a p-i-n GaAs diode with embedded QDs is used as an example. After coating the sample (panel I), its surface is exposed by a beam of either photons or electrons, which interact with the polymeric chains of the resist and transfer part of their energy during multiple scattering events (panel II). The nature of the beam used for a lithographic process defines the two big categories of lithography: if light is used, then the technique is denominated photolithography; on the other hand, electro-beam (or e-beam) lithography employs electrons to transfer energy to the polymeric chains.

The chemical reactions initiate during the exposure may be of two opposite kinds, based on the chemical nature of the polymer. In one case, the chemical bonds between the molecules break, making the exposed areas more soluble to solutions called developers. On the other hand, if the deposited energy generates new bonds between the chains, the exposed regions will become insoluble in developers. The first type of resist is denominated positive-tone, while the second type is called negative-tone, as the inverted image of the chosen design will remain after the development. Such a difference is illustrated in panels IIIa and IIIb of Fig. 3.1, respectively, along with a top-view optical microscope image of a lithographic mask prepared on a positive resist.

Among other features, the opposite chemical response to the beam results in a fundamental difference between the profile of the resulting sidewalls on the resist. Positive resists generally

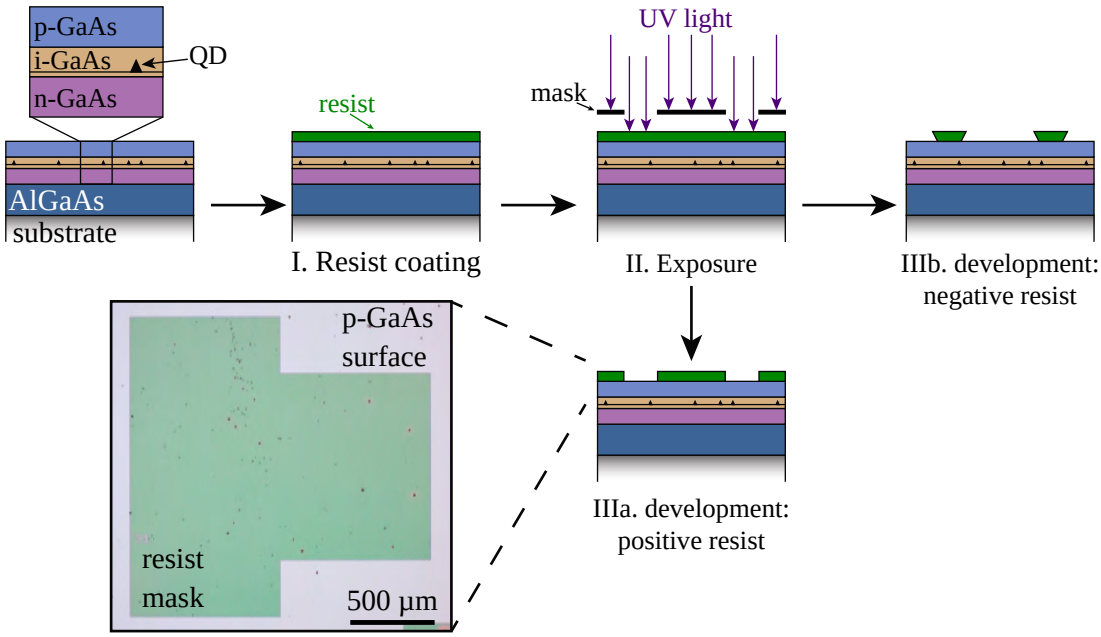

Figure 3.1: Schematic representation of the photolithography process flow. After preparing the sample by spin coating a layer of resist (panel I), the sample is irradiated by UV light. A solid mask blocks some parts of the beam of light, which exposes only the areas that composed the desired design (panel II). During the development, the transferred pattern is revealed by the dissolution of either the exposed areas, in the case of positive resist (panel IIIa), or the shadowed ones, in the case of negative resists (panel IIIb). An exemplary microscope image of a successful exposure of a mesa structure on a positive resist is shown in the inset.

present exposed areas with steeper edges (i.e. high contrast) and higher resolutions are hence achievable, making them an optimal choice for the fabrication of, for example, fine optical structures. Conversely, negative-tone resists normally show a re-entrant profile and are therefore employed mainly for the exposure of large areas like, e.g., contacts pads or mesa-like structures similar to the one shown in Fig. 3.1.

While the main features of the techniques are common to both photolithography and e-beam lithography, specific properties may make one type of lithography more favourable than the other for some applications. We will briefly discuss this in the following, with special focus to the processes used during the work for this project.

Photolithography

Two main approaches exist in photolithography for patterning a layer of photoresist: one can either shine light through a metallic mask that casts a shadow on the resist-coated sample underneath to define the exposed area (as illustrated in panel II of Fig. 3.1); or write the patterns directly on the polymer by means of a focused laser. In the first method, a lamp is used as light source and a shutter placed in front of it controls the amount of energy deposited on the sample. This approach is often used for large masks. In the second approach, more precise control can be achieved by controlling how long the laser stays on each individual spot and by adjusting its output intensity and focus. While the processing time may be longer than in the previous case, a more complex set of patterns can be produced.

Irrespective of the light source, a common limitation affects both approaches: the employed wavelength sets the smallest feature that can be patterned via photolithography due to the diffraction limit. For this reason, common microfabrication techniques use UV light ($\lambda \approx 350 - 440$ nm [12, chap. 4]) in order to achieve features of at least 1 µm in size. In the specific case of the samples prepared during this PhD project, for example, UV lithography has been used to pattern large structures, with dimensions ranging from few hundreds of µm to a few millimetres, like the one shown in Fig. 3.1.

Electron-beam lithography

When the size of the fabricated structures decreases below a few hundreds of nanometers, UV lithography cannot be used anymore and e-beam lithography is employed instead. Nanometer-sized features can be easily patterned with this technique due to the nature of the particles constituting the beam: when electrons are accelerated by voltages of just a few tens of kV – a value that is easily achievable by modern common electro-lithographic systems – their de Broglie wavelength $\lambda_e = h/\sqrt{2m_e eV} < 1$ nm [52]. However, the finite size of the beam and aberrations present in the system still limit the final resolution of this technique. Spot diameters of a few nm are readily achievable in state-of-the-art machines, thanks to the high level of control they provide; the e-beam lithography system used during this project is a Elionix ELS-F125, which can produce a beam diameter as small as 1.8 nm [a].

The amount of electrons deposited by the beam per unit of area is another important factor that affects the quality of the exposed patterns. Such a parameter is referred to as dose and quantifies the energy transferred to the polymeric chains. Every electrosensitive resist has a specific threshold dose D_0 that fully dissolves it during the development process. Generally, polymers that have high contrast and sensitivity to the electron beam are preferred in order to obtain lithographic masks patterned with a higher resolution and vertical sidewalls. The resist of choice for all the samples fabricated during this project is ZEP520A, which is widely used and known not only because it fulfils the aforementioned requirements [53–55], but also for its stability and resistance against dry-etching processes, an utterly important feature for the success of our fabrication processes (as it will be discussed in Sec. 3.2).

Typical chips for nanophotonics applications include several devices with features of a few hundreds of nm in size that are often close to patterns with areas ranging from 10 to 50 µm^2. In these situations, higher control over the spatial distribution of the deposited energy is necessary. In fact, the effective lateral extension of the scattering events during the lithographic process is much larger than the actual size of the electron beam. Fig. 3.2a shows a Monte Carlo simulation of the trajectories of primary (blue lines) and backscattered electrons (red lines) when a beam accelerated by a voltage of 100 kV passes through 550 nm of ZEP520A coating on a GaAs substrate. Despite an initial beam diameter of a few nm, the final interaction volume covers a region of about 10 µm in diameter. Regions of the lithographic mask with high density of exposed patterns hence get an effective dose larger than expected, thus lowering the final resolution and compromising the successful production of complex chips. Such a phenomenon is well-know in the nanofabrication community and is referred to as the proximity effect.

Advanced lithographic techniques can adjust the value of the electron-beam dwelling time at each position of the pattern in such a way that a spatially uniform dose is eventually deposited during the exposure. This procedure is denominated proximity effect correction (PEC) and it is based on the analysis of the energy point spread function (PSF) for the electrons of the beam.

[a] http://www.sts-elionix.com/node/25

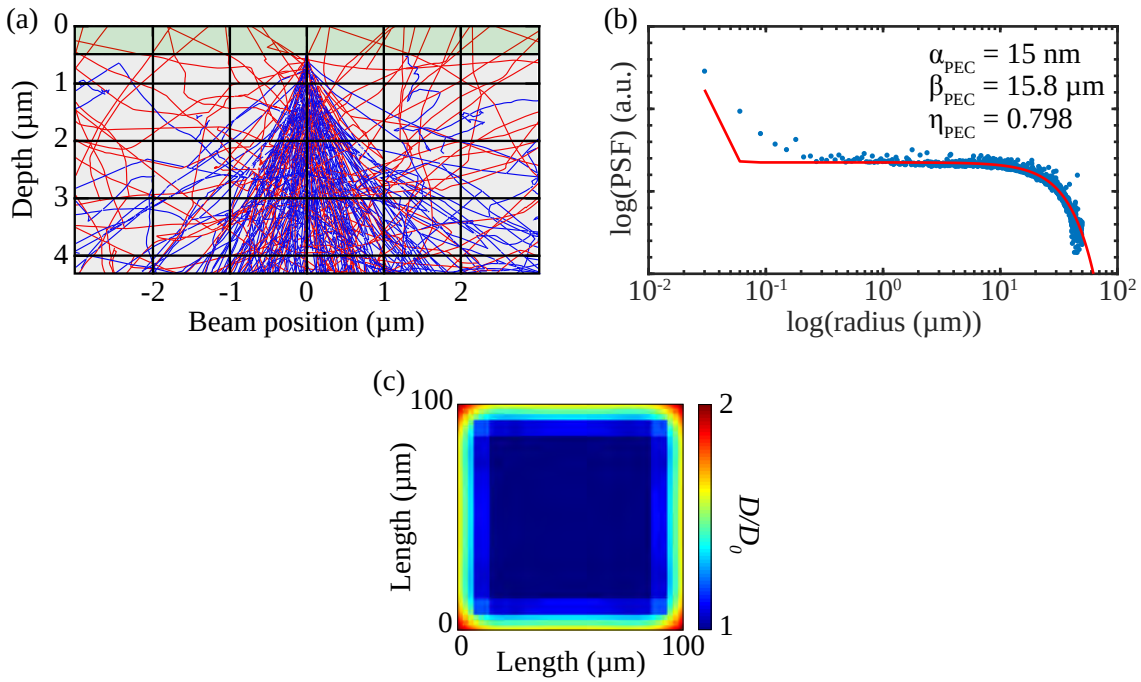

Figure 3.2: Proximity effect correction. (a) Monte Carlo simulation of the trajectories of primary (blue lines) and backscattered electrons (red lines). The simulated sample is formed by a 550-nm thick layer of ZEP520A (green area) coated on a substrate of GaAs (grey area). The acceleration voltage for electrons in the beam is set to 100 kV. (b) Normalised values of the point spread function obtained from Monte Carlo simulations (blue dots). The corresponding fitting function is also plotted (red line). The chosen functional shape is a sum of two Gaussians and the fitting parameters are shown. (c) Result of PEC on a square with edge length of 100 μm. The different colours indicate different level of deposited dose D, normalised to the value D_0 need to completely clear the center of the square. Due to the proximity effect, the lowest doses are used in the central areas of the geometry due to the large number of contributions from the neighbouring regions.

Several models have been proposed to replicate the non-trivial functional form of the PSF [56–59], but the most commonly used is to approximate the distribution as a sum of two Gaussian functions

$$\mathrm{PSF}(r) \approx \frac{1}{\pi\,(\eta_{PEC}+1)}\left[\frac{1}{\alpha_{PEC}^2}\exp\left(-\frac{r^2}{\alpha_{PEC}^2}\right)+\frac{\eta_{PEC}}{\beta_{PEC}^2}\exp\left(-\frac{r^2}{\beta_{PEC}^2}\right)\right]. \tag{3.1}$$

The first (second) term in eq. (3.1) describes the contribution of the forward (back) scattering to the total energy, with α_{PEC} (β_{PEC}) defining the radius of the corresponding interaction area. The coefficient η_{PEC} is the ratio between the two components and similarly to α_{PEC} and β_{PEC}, can be estimated either by calibration or by fitting the values obtained by Monte Carlo simulations of the spatial dependence of energy deposited after each scattering event. Fig. 3.2b presents an example of the latter approach, where the normalised PSF for the system illustrated in Fig. 3.2a is shown for an acceleration voltage of the e-beam of 125 kV (corresponding to the voltage provided by the system used during this PhD project). The evaluated fitting parameters demonstrate that the backscattered electrons are the main contribution to the overall deposited energy and, more importantly, have effects covering an area as large as $2\beta_{PEC} \approx 32\,\mu$m.

Commercially available software packages exist that provide tools for simulating and fitting

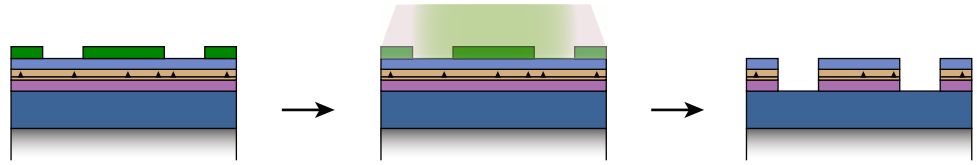

Figure 3.3: Schematic representation of the dry etching process. After defining a lithographic mask (panel I), the exposed areas are dissolved due to interaction with the gaseous reagents (panel II). The polymeric layer is then removed in organic solvents, revealing the designed pattern successfully transferred to the sample surface (panel III).

PSF's for different combinations of resist and substrates; during this project, we use the one developed by Beamfox Technologies ApS[b], which outputs the values presented in Fig. 3.2b. This software performs a 2D convolution of the fitted PSF with the geometries in the mask to obtain the distribution of the energy deposited on the resist during the exposure. Based on this information, all the dose contributions for each polygon of the patterns are calculated and the dwelling time is adjusted accordingly. An example of the PEC performed on a square with edge length of 100 µm is reported in Fig. 3.2c. The coloured map indicates the different estimated doses D normalised to the value D_0 necessary to completely clear the center of the geometry. As expected, the ratio D/D_0 decreases when moving from the edges to the central region of the square, where the total energy absorbed by the resist is the sum of all the contributions from the adjacent areas.

3.2 Etching

The etching process enables the transfer of the exposed patterns from the resist mask to the underneath material. This is achieved by dissolving the areas of the sample's surface that are not covered by the undeveloped polymer. A schematic representation of the process flow is depicted in Fig. 3.3 and Fig. 3.5. Based on the phase of the chosen reactants, two main classes of etching can be defined: the process is denominated "dry" when the used etchants are gaseous (panel II in Fig. 3.3), whereas the term "wet etching" indicates a process performed in liquid solutions. In the following pages, both types will be described and both advantages and limitations of each technique will be overviewed. The discussion will focus mainly on processes and chemicals used in the fabrication of GaAs-based devices, but it can be easily expanded to other types of systems (e.g. other III-V semiconductors or Si) as the main considerations will still hold.

Dry etching

Dry etching techniques exploit both chemical and physical processes to remove material from the sample [12, chap. 5]. The chemical reactions control the selectivity of the etching process, as different material compositions react differently in the presence of the same reactant. This allows for the dissolution of the exposed areas while keeping the resist layer unaltered. Such a process, however, is quite isotropic and then non-optimal when small features (for example, the holes of a photonic crystal) need to be fabricated. The physical part of the dry etching compensates for this lack of directionality, as the particles forming the gaseous solutions are accelerated towards the sample surface and the resulting sputtering process produces vertical and sharp features. The high energy of this process, necessary to facilitate the etching of even very small patterns, causes a lot

[b] https://www.beamfox.dk

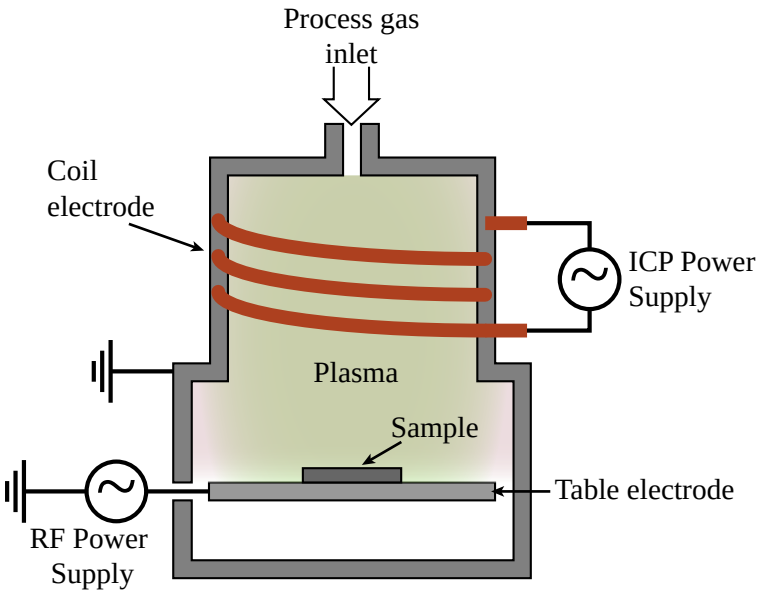

Figure 3.4: Schematic illustration of the plasma etcher used during this PhD project. The sample sits on a table electrode that forms a capacitor together with the metallic walls of the chamber. By controlling the RF power between these two plates, the energy of the plasma can be controlled during RIE processes. When a coil electrode is also used, the same system can be employed to perform ICP etching.

of damage to the surface of the chip; this is especially problematic when a resist mask is used, as it can quickly get removed, thus exposing areas of the sample that were supposed to be protected. A good balance between selectivity and anisotropy is then essential and it can be achieved by using durable lithographic masks (like inert dielectric materials or, as already mentioned, highly resistant polymeric resists like ZEP520A) and by calibrating the parameters of the machines used to perform the etching.

Several dry etching techniques exist [12, chap. 5], but here we will focus on two of them that were used for the works reported in this thesis: reactive ion etching and inductively coupled plasma etching, both performed in the same system (Plasmalab System 100, Oxford Instruments, with ICP 65 source), sketched in Fig. 3.4. In common dry etching processes, highly reactive particles are generated by a plasma. Different methods exist to produce and control the plasma, which define the technique that is used [12, chap. 5]. Reactive ion etching (RIE) is a well-established technique, where the radio frequency (RF) plasma is formed by applying an alternating current between a table electrode, where the sample is positioned, and the metal walls of the reaction chamber (Fig. 3.4). The same RF source is also used to generate the bias potential (DC bias) that accelerates the energetic particles towards the sample surface. In order to limit the damage caused by the physical sputtering during the etching process, low RF powers are usually used. Etch rates and achievable anisotropy are therefore limited, but high levels of selectivity can be reached due to the reduced erosion of the resist mask.

The system used during this PhD project also hosts a second RF power source (cf. Fig. 3.4), which is inductively coupled to the first RF circuit. When operated, it allows for independent control of the plasma energy and the accelerating DC bias. Higher etching rates and improved anisotropy are thus achievable, to the expense of a reduced selectivity. This new configuration is referred to as inductively coupled plasma (ICP)

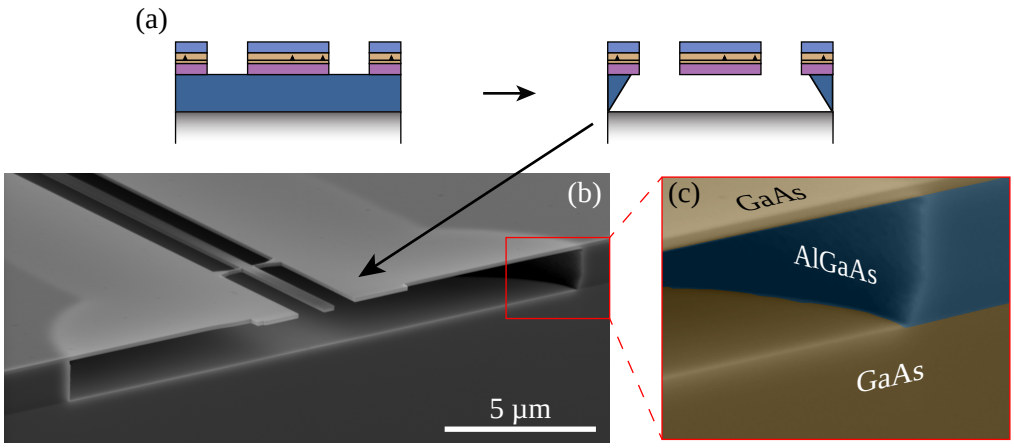

Figure 3.5: (a) Schematic representation of the selective wet etching. The material-dependent reactivity of chemical reactions allows for the dissolution of only specific layers of the heterostructure, while leaving others unaltered. (b) Tilted-view SEM image of a cleaved suspended nanobeam waveguide obtained by etching the sample in a dilute HF solution, which selectively dissolved $Al_{0.75}Ga_{0.25}As$ while leaving the GaAs layers unaffected. (c) Close-up false-colour SEM image of the undercut resulting from the selective dissolution.

Regardless of the employed configuration, the chemical reactions of the process can be controlled by the composition of the gaseous mixture introduced in the chamber, which is set by controlling the flow of each component by means of a mass-flow controller. For the GaAs/AlGaAs system both alkane-based and halogen-based mixture have been reported as etchants [60, 61]. During this PhD project different combinations of boron trichloride (BCl_3), chlorine (CL_2) and argon (Ar) have been used for the fabrication of nanostructures. The chlorinated compounds act as main etchants, with BCl_3 also having a passivating function on the etched sidewalls. Ar is instead added to dilute the mixture and thus control the selectivity of the etching [60]. Varying the relative concentrations of these gasses enables the tuning of the process selectivity, while the total pressure inside the chamber affects the nature of the dry etching, which results more (less) chemical for higher (lower) values of that parameter.

Wet etching

When devices are to be fabricated in heterostructures, some steps may involve the selective removal of one layer while keeping all the others unaffected, as schematically depicted in Fig. 3.5a. Although some selectivity can be achieved in dry-etching processes, the results are nevertheless limited by the high energy of the plasma. In these situations, wet etching is chosen instead due to its chemistry-based nature. The high reactivity between the layer that has to be removed and specific reagents is advantageous to achieve processes with high selectivity, which enable the fabrication of structures similar to the one presented in Fig. 3.5b. Here, a tilted-view SEM image shows a sample formed by a GaAs membrane grown on top of a layer of $Al_{0.75}Ga_{0.25}As$ and selectively etched in a dilute solution of hydrofluoric acid (HF). This type of etchant can easily dissolve AlGaAs with Al content above 70% without damaging GaAs, as shown in Fig. 3.5c. This process is commonly used in the production of devices based on the GaAs/AlAs system, when suspended nanostructures like the one in Fig. 3.5b are necessary [60, 62] or to perform a complete epitaxial lift-off of the GaAs layer from the substrate [63–65]. Conversely, wet etching is not the optimal choice for the fabrication of devices with small features and vertical sidewalls (like

photonic crystals), as the strong correlation between chemical reactions and material composition makes the wet etching isotropic and hence hinders the control of the nanostructures profile.

After decades of development, a large selection of etchant solutions exists for the fabrication of GaAs-based technologies, as reviewed in [12, 66]. Despite the variety of compounds and parameters that define each specific chemical reaction, all the different wet etching processes can be analysed from a common electrochemical point of view. In fact, the dissolution of GaAs can generally be described in terms of redox reactions, where an oxidising agent Ox_2 exchanges electrons with the semiconductor material, which hence acts as a reductant Red_1. The general form of the resulting reaction reads

$$a\mathrm{Red}_1 + b\mathrm{Ox}_2 \rightarrow c\mathrm{Ox}_1 + d\mathrm{Red}_2\,, \tag{3.2}$$

where the subscripts of both reagents and products identify different chemical species and the factors a, b, c, and d are the stoichiometric coefficients. Reaction (3.2) can be further decomposed as the sum of two semi-reactions

$$a\mathrm{Red}_1 - n\,e^- \rightarrow c\mathrm{Ox}_1 \tag{3.3a}$$

$$b\mathrm{Ox}_2 + n\,e^- \rightarrow d\mathrm{Red}_2\,, \tag{3.3b}$$

which explicitly state the number n of electrons e^- exchanged between the reagents. Reaction (3.3a) describes the oxidation of the chemical species 1, while reaction (3.3b) shows the concurrent reduction of species 2. The etching of GaAs will occur only if the redox processes are energetically favourable and will proceed with a rate that depends on the concentration of the reagents and the temperature of the reactions.

In Chap. 2 we have discussed how energy levels and interfaces affect the density of carriers in semiconductors and how accumulation or depletion regions may appear at their surfaces. Such effects need to be taken into consideration when the mechanisms of wet etching are studied, since they may modify the effective concentrations of reactants and therefore affect the exchange of electrons between reductants and oxidants. Extensive work on this topic has been done by Gerischer and Mindt [67, 68] and detailed explanations can be found in literature [21]. Here we will present an overview of the processes that are relevant for the etching of the samples prepared during this PhD project.

For this analysis, the interface of interest is the one formed by (i) the surface of GaAs and (ii) the portion of etchant solution in contact with it. The properties of (i) have been already described in Chap. 2, where we presented their dependence on doping type and density of surface states. The features of (ii) are instead affected by the nature and the concentration of the chemicals dissolved in solution. Although different phases are involved, many similarities may be drawn between the two parts of the system: for example, the components of a redox couple are also characterised by energy states, which are populated based on their position with respect to the Fermi level of the solution $E_{f,liq}$. Since the concept of a Fermi level for a liquid might seem a little odd, this parameter can be related to the more familiar standard potential of the related semi-reaction $E^\circ_{Ox/Red}$. This parameter quantifies the electromotive force involved in the chemical process and measured at pressure $p = 1\,\mathrm{bar}$ with respect to the standard hydrogen electrode [69]. The relationship between $E_{f,liq}$ and $E^\circ_{Ox/Red}$ reads [68]

$$E_{f,liq} = E^\circ_{SHE} - e\,E^\circ_{Ox/Red} = -4.5\,\mathrm{eV} - e\,E^\circ_{Ox/Red}\,, \tag{3.4}$$

where $E^\circ_{SHE} = -4.5\,\mathrm{eV}$ is the absolute electrode potential of the standard hydrogen electrode. The parameter $E_{f,liq}$ can then be seen as the energy necessary for transferring one electron from the reductant to the oxidant.

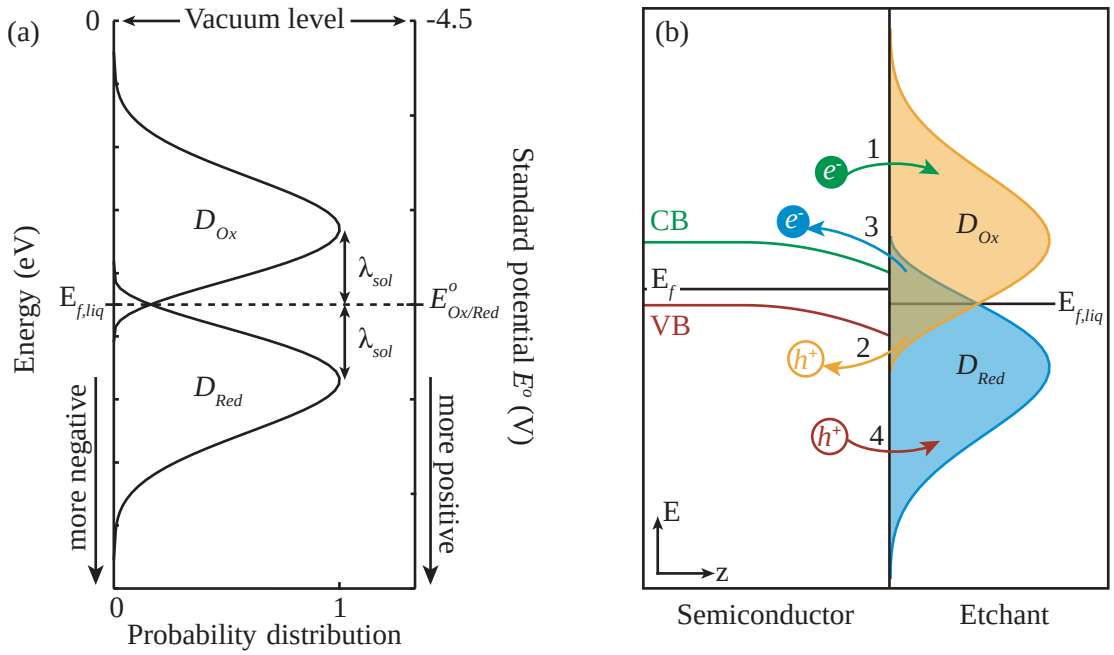

Figure 3.6: (a) Energy band diagram of a generic redox couple. Both the absolute scale (left axis) and the standard potential scale (right axis) are shown. (b) Schematic representation of the possible charge transfer mechanisms when a semiconductor is in contact with an electrolytic solution. The numbers of each arrow correspond to the case described in the main text, while the colour scheme helps to identify the source of the exchanged carriers: electrons transferred from CB are green, holes from VB are red, electrons supplied by the reductant are blue and holes moving from the oxidant to the semiconductor are coloured in orange.

The interaction between the molecules of the redox couple and the solvent generates a distribution of energy states for the oxidised (D_{ox}) and the reduced species (D_{red}) [21]. A schematic illustration of such distributions for a generic redox couple is presented in Fig. 3.6a. Here, in analogy with the solids, we note the formation of bands for oxidant and reductant, which are distributed around $E_{f,liq}$ and have their maxima separated by the amount $2\lambda_{sol}$. This parameter corresponds to the reorientation energy necessary to modify the solvation shell of ions surrounding the molecules of each component of the redox couple when an electron is transferred from *Red* to *Ox*. The values of λ_{sol} depend on the nature of the solvent and have been shown to vary over a broad range, between 0.3 and 1.6 eV [21].

When the two parts of the system are brought into contact during the wet etching process, the energy difference between the solid and liquid Fermi levels initiates a transfer of carriers across the interface. As charges can freely move only between levels at the same energy, four possible mechanisms may occur at the interface based on the overlap between the solid and etchant bands. These processes are illustrated in Fig. 3.6b, where only one carrier is considered for simplicity:

1. electrons are transferred from the conduction band (CB) of the semiconductor to the oxidised reagent:
$$Ox^+ + e^- \rightarrow Red\,;$$
2. holes move from the oxidant to the valence band (VB):
$$Ox^+ - h^+ \rightarrow Red\,;$$

3. electrons move from the reductant to the conduction band:

$$Red - e^- \rightarrow Ox^+ ;$$

4. holes are transferred from the valence band to the reduced component:

$$Red + \mathrm{h}^+ \rightarrow Ox^+ .$$

The first two processes describe the reduction of the oxidised component of the electrolytic solution, while the remaining two show the oxidation of the reductant. Unsurprisingly, cases 1 and 3 correspond to the same semi-reactions obtained by the more general approach previously discussed (cf. reactions (3.3a) and (3.3b)). In addition to those, though, two new processes are now introduced due to the presence of holes, which are a type of carriers relevant only for semiconductors. When the Fermi levels of both sides of the junction align, the system reaches the equilibrium state and the transfer of charges stops.

The charge transfer rates can be described in terms of current densities, with cases 1 and 2 generating the cathodic currents i^c_{CB} and i^c_{VB}, respectively, and oxidations producing anodic currents instead (i^a_{CB} and i^a_{VB} in case 3 and 4, respectively). These rates are found to be functions of the concentration of the employed reagents, along with the overlap between the distribution of energy levels in the solution and the available states in the bands of the semiconductor. Specifically, i^c_{CB} and i^a_{VB} are dependent on the carrier densities at the surface of the solid, a variable that is a function of the applied voltage (see Chap. 2), while i^c_{VB} and i^a_{CB} are bias independent and are determined mainly by the overlap between the bands of the two phases, i.e. valence band vs. D_{ox} and conduction band vs. D_{red}, respectively. The intensity of each of these currents determines which of the four processes is the dominant one and provide information about the selectivity and the rate of a specific wet etching process. Importantly, the explicit dependence of these rates on the carrier and bands positions at the surface explain the differences between different doping types that have been found for several etchants [12, 66], but that was not explicitly visible from the reaction (3.2).

The changes in carrier densities caused by the exchange between phases redistribute the charges at the interface of both semiconductor and liquid. In the solid, this results in a modification of the space-charge layer as introduced in Chap. 2. A similar effect happens in electrolytic solutions, where a compact layer of ions (i.e. the Helmholtz layer [68]) is formed, followed by a diffuse layer of particles with opposite sign. Since the concentration of ions in the solution is generally higher than the carrier density in the semiconductor, one can assume to a first approximation that the charge transfer will mainly affect the energy levels in the solid, while the total charge of the Helmholtz layer will remain approximately constant if the concentrations in the solutions are not altered. Therefore, similarly to what happens in the case of metal-semiconductors junctions (cf. Chap. 2), the conduction and valence bands edges of the semiconductor are pinned at the solid-liquid interface.

Depending on the relative alignment between the bands in the semiconductor and in the etchant solution, the wet etching of GaAs may occur by two main mechanisms: (i) anodic or (ii) electroless dissolution. Fig. 3.7 schematically illustrates both of them. As described by Gerischer and Mindt [67], the requirement for the anodic dissolution is the presence of holes in the valence band of the semiconductor, which positively charge the surface. The negative ions in the electrolytic solution are attracted to the atoms of the solid and create new bonds with them by breaking the superficial molecules. In the case of GaAs, for example, 3, 6 or 8 holes per molecule are necessary to break all the bonds at the surface, depending on the reaction parameters [70–72]. As shown in Fig. 3.7a, owing to the reduced overlap between VB and Ox, h^+ are not provided by the solution but their concentration is rather a function of the properties of the space-charge layer at

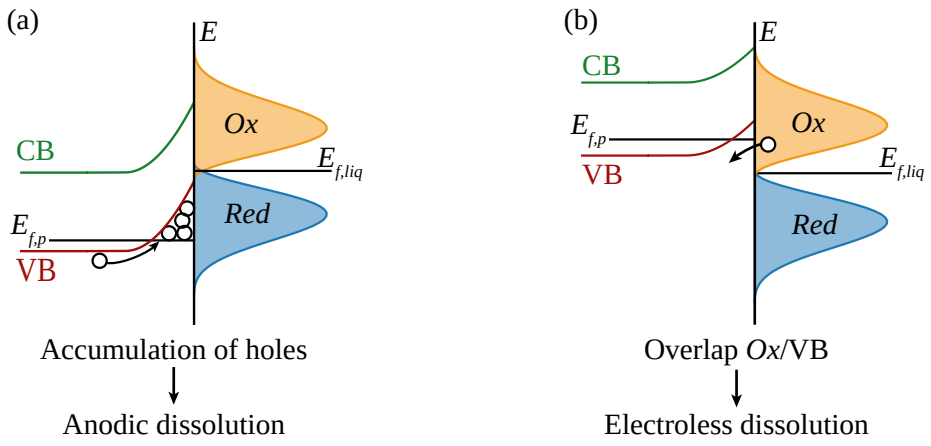

Figure 3.7: Dissolution processes in p-GaAs. (a) Anodic dissolution: the accumulation of holes at the surface forms a positive space-charge layer that attracts the negative ions in solution. The resulting chemical bonds break the superficial molecules. (b) Electroless dissolution: the large overlap between the oxidant band *Ox* and the valence band VB allows for the transfer of holes into the surface of p-GaAs, initiating the dissolution of the material.

the surface. The dominant current density hence is i^a_{VB} (i.e. case 4) and the anodic dissolution a voltage-dependent process. Furthermore, following the same argument, this etching mechanism can easily occur in p-doped materials; photo-generation of holes is however necessary in n-type semiconductors to initiate this process. It is worth noting that the anodic dissolution just requires etching solutions that contain negatively charged ions, like the acidic or basic deoxidant solutions used to remove the native oxide from the surface of GaAs.

When a strong oxidiser is present in the solution, the process to provide h^+ to the valence band changes: as depicted in Fig. 3.7b, the positive $E^\circ_{Ox/Red}$ of this type of chemical species results in an increase of the overlap between VB and D_{ox}. The dominant charge transfer mechanism is now described by case 2 and the current density i^c_{VB}, which is independent of the applied voltage. After that, in a similar way as discussed above, the accumulated holes at the surface attract negative ions in the solution and bond with them, thus finalising the dissolution of the solid. If the oxidiser is strong enough, the transfer of holes to the valence band is always possible, independently on the doping of the material or on the illumination (even though photo-generation of carriers may increase the etching rate). An example of this type of reagent is hydrogen peroxide (H_2O_2), a commonly known oxidant for GaAs with $E^0_{H_2O_2} = 1.776\,\text{V}$ [73]. From eq. (3.4), $E_{f,liq} = -6.276\,\text{eV}$ that is way below the edge of the GaAs valence band, which at room temperature can be estimated at $E_C = -(e\chi + E_g) \approx -5.49\,\text{eV}$ from the vacuum level [14].

3.3 Metal deposition

The technology of metal deposition is one of the pillars of the fabrication of micro- and nano-devices in semiconductors, as it can be used for a large number of different applications: for example, metal contacts are prepared on p-i-n diodes in order to apply a bias voltage and hence control of the electrical properties of heterostructures and QDs (cf. Chap. 2). Alternatively, metallic alignment markers can be deposited on a sample to facilitate the exposure of multiple lithographic layers or to act as a reference frame for an easier detection of nanostructures on the chip (cf. Chap. 5).

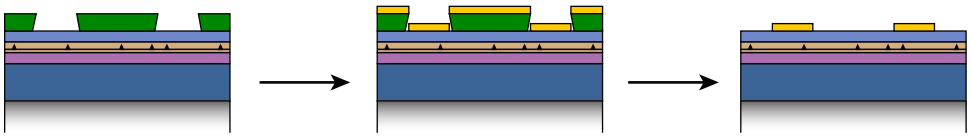

Figure 3.8: Schematic representation of the workflow for the metal deposition. After the preparation of a lithographic mask (panel I), the layer of metal is uniformly deposited on the surface of the sample (panel II). Finally, the polymeric mask is removed during a lift-off process, along with the unwanted metal (panel III).

Despite the variety of possible uses, the deposition procedure can be summarised in a few simple steps; a schematic representation of the workflow is depicted in Fig. 3.8. After the preparation of a lithographic mask with the pattern of choice (panel I), the deposition is performed in an electron-beam evaporator, where crucibles containing the chosen metals are heated by bombardment with energetic electrons. This process produces atomic vapours that uniformly deposit the material on the sample surface (panel II). Finally, the polymeric mask is removed via a lift-off process (panel III): the sample is dipped in organic solvents that remove the polymer along with metal deposited on it, leaving on the sample surface only the patterns exposed to the metallic vapours. Re-entrant sidewalls increase the contact area between solvent and lithographic mask and hence facilitate the lift-off process; as negative resists readily present this type of profile, they are commonly used in the metal deposition protocols.

Chapter 4

Building the components of quantum photonic chips

Nanophotonic devices in GaAs provide the necessary building blocks for the fabrication of advanced quantum photonics chips. Fig. 4.1 shows some examples of the variety of devices prepared throughout this PhD project. Nanobeam waveguides (Fig. 4.1a) can be used to guide the light and optically connect several devices to build large scale networks. Photonic crystal waveguides like the one in Fig. 4.1b may constitute the nodes of this system, as they strongly confine light and enable highly efficient light-matter interactions. Conversely, tapered nanobeams (Fig. 4.1c) can be used to couple the photons out of the chip and into optical fibers with negligible losses, thus allowing for the interconnection of multiple quantum chips and scaling the photonic platform even further. All this operations can be performed with high level of coherence by using electrical contacts (Fig. 4.1d) to control and reduce the charge noise that the solid-state environment generates.

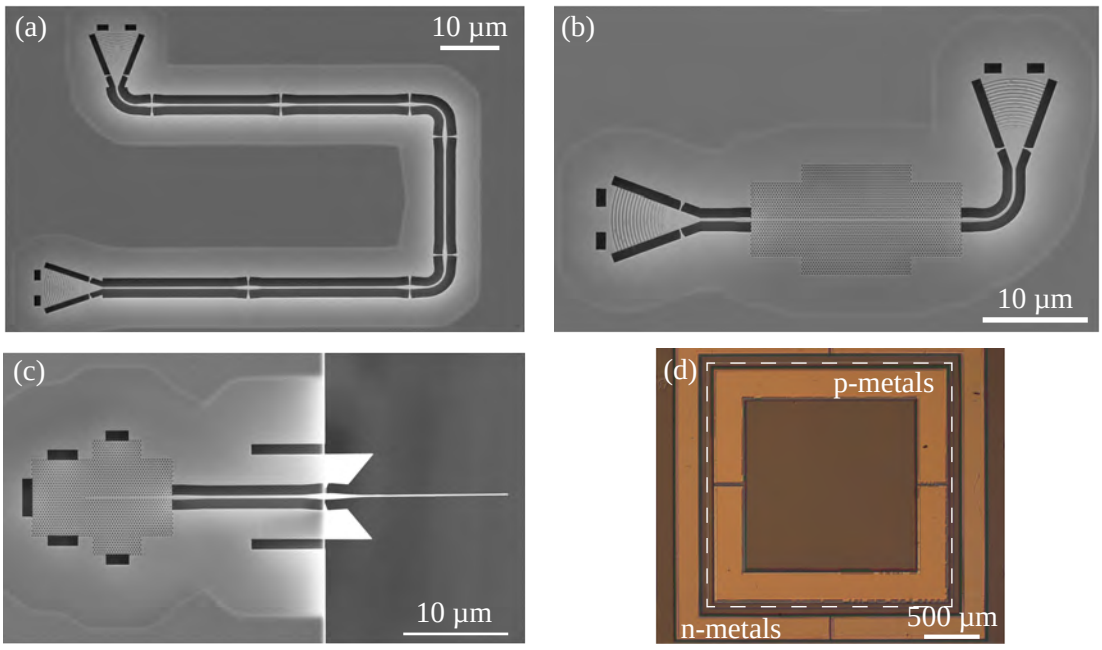

Figure 4.1: Examples of the nanodevices that constitute the building blocks of quantum photonic chips: (a) nanobeam waveguide, (b) photonics crystal waveguide, (c) taper out-coupler and (d) mesa structures (defined by the white dashed line) with metal contacts.

The µm-size footprint that each of these nanostructures have suggests the vision of few-mm large chips hosting a few hundreds of these photonic components. The main challenge that has to be overcome to reach such a goal is the development of processes that enable the fabrication of high quality quantum photonic devices in a reliable and reproducible way. Most importantly, the compatibility between different fabrication processes is key for the production of working devices with a high yield. In the following pages we present the methods we developed for the fabrication of the devices shown in Fig. 4.1 and describe how we combined the techniques presented in Chap. 3 to produce high quality quantum photonic chips based on self-assembled QDs in GaAs nanostructures.

4.1 Protocols for the fabrication of photonic nanostructures

The fabrication procedure we developed for the photonic devices presented in this work is based on a soft-mask process. This method consists in exposing the nanostructures by e-beam lithography on a polymeric resist directly coated on top of the GaAs membrane. RIE-ICP and wet etching techniques are subsequently used to transfer the pattern to the semiconductor material. The nanofabrication workflow is illustrated in Fig. 4.2. This process does not require the deposition of dielectric (e.g. Si_3N_4 or SiO_2) or metallic layers necessary for the formation of the so-called hard-mask [74–77] and therefore involves fewer fabrication steps. However, the highly energetic plasma used during the dry etching process (cf. Chap. 3) erodes the soft polymeric resist, thus damaging its surface and the exposed patterns. The main challenge therefore consists in reducing these detrimental effects in order to fabricate nanostructures with negligible levels of defects and surface roughness. The main concepts of the techniques used in each step have been already presented in Chap. 3. Here we will focus on the specific processes and parameters that we optimised to overcome such issues. Detailed recipes of the developed process are described in appendix B.

Fig. 4.1 shows a few examples of the nanostructures we routinely fabricate, i.e. NBWs (Fig. 4.1a) and PhCWs (Fig. 4.1b) that present grating out-couplers at both ends. These devices cover quite large areas (up to a few thousands of μm^2) and are formed by many parts with sizes ranging from about 50 nm up to a few µm. Lithographic masks of this type require proximity effects correction for successful exposures of the patterns (cf. Chap 3). We therefore set out to investigate the correct base dose D_0 necessary to completely clear a layer of ZEP520A with thickness of about 550 nm, which is the amount commonly coated on our samples (Fig. 4.2, panel

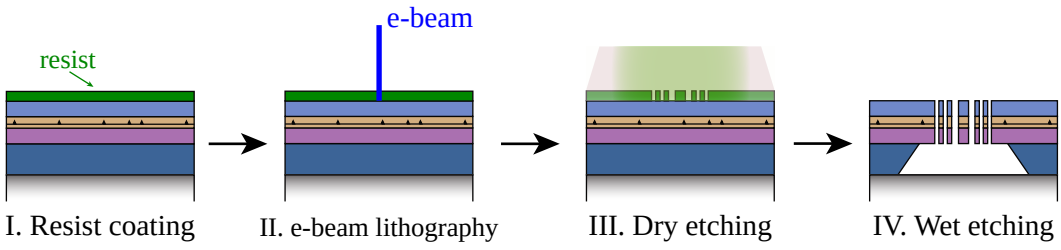

Figure 4.2: Fabrication workflow for suspended nanostructures in GaAs. The procedure is based on a soft-mask process, where the patterns are exposed by e-beam lithography on a layer of resist coated on the sample surface (panels I and II). A dry etching process is subsequently used to transfer mask designs into the GaAs membrane (panel III). After removing the polymeric layer, the sacrificial AlGaAs layer is dissolved by selective wet etching, thus achieving the full suspension of the nanostructures.

I)

Every resist has a specific energy threshold that results in successfully open patterns. The exact value is influenced by the development steps, where different variables (e.g. developer composition [53], temperature of the solution or duration of the step [55]) may lower or increase such a limit. It is therefore important to use the same parameters for every exposure in order to achieve high reproducibility of the process. All the samples presented in this work have been developed in n-amylacetate for 1 min, while the solution was kept at $T = -5\,^{\circ}\mathrm{C}$ to achieve better contrast [55]. In this conditions, we found $D_0 = 336\,\mu\mathrm{C/cm^2}$. By using this value in combination with the parameters of the PSF function shown in Fig. 3.2, we corrected each of the masks designed throughout this project with the PEC software provided by Beamfox Technologies ApS. In this way we could obtain the dose distribution for optimal exposures (Fig. 4.2, panel II).

After the development of the lithographic mask, the patterns were transferred to the GaAs substrate via dry etching (Fig. 4.2, panel III). Calibration tests were run by monitoring the thickness of the resist during the process by real-time interferometric measurements. Comparing this value with the SEM inspection of the device cross-sections allowed us to evaluate the optimal end-point of the process [17]. We observed that the etched features tend to show eroded and distorted edges when the thickness of the unexposed resist is reduced to less than 200 nm [60].

Two different dry-etching recipes were developed: (i) a slow RIE process that allows for a good control of the etched depth of large features. This aspect makes it optimal for the fabrication of shallow-etched gratings like the ones shown in Figs. 4.1a and b. However, the prevalently chemical nature of this process makes it quite isotropic and hence not suitable for small patterns like the holes of PhCs (cf. Chap 2). (ii) A ICP etching was then developed to achieve the anisotropy required for vertical sidewalls. Using this recipe we obtained a selectivity of GaAs over resist of about 2:1 for features larger than 1 µm and about 2:3 for smaller ones [60]. The latter unfavourable ratio was compensated by coating a resist layer thicker than the etched depth into the material; with a thickness of ZEP520A of about 550-570 nm, we were able to etch holes about 180 nm deep. The real-time interferometric measurements were employed to monitor the erosion rate of the polymeric layer during the entire process, which was stopped when the predefined value was reached. Table 4.1 presents a summary of the parameters chosen for each dry etching process.

Process type	Mixture composition (flow settings in sccm)	Chamber pressure (mTorr)	DC bias (V)	ICP power (W)	Table T (°C)
RIE	BCl_3/Ar (5/10)	10	210 ± 10	0	15
ICP	BCl_3/Cl_2/Ar (3/4/25)	4.7	310 ± 5	300	0

Table 4.1: Parameters of the dry etching recipes used in this project.

A wet etching process is subsequently used to selectively dissolve the AlGaAs sacrificial layer and hence completely suspend the nanostructures (Fig. 4.2, panel IV). After the removal of the resist mask in a warm organic solvent (N-Methyl-2-pyrrolidone, or NMP, kept at $T = 70\,^{\circ}\mathrm{C}$), the samples were dipped in a dilute solution of HF, with concentration of 10% w/w. As a result of the chemical reactions involved in the process, several residues are usually produced, which accumulate on the surface of the devices and may lower the final quality of the samples. In order to remove them, a cleaning procedure based on the chemical nature of these side-products was used on every sample [17, 60, 78]. It is worth noting that all the steps just described must be performed while keeping the samples inside the liquid: in fact, thin nanostructures like the NBW shown in Fig 4.1a are not robust against capillary forces created when the sample is removed from

the solutions and may therefore collapse. For this reason, the processed chips were finally dipped in isopropyl alcohol (IPA) and then the liquid was removed by a critical point drying process, where the alcohol evaporates without any abrupt phase transition.

4.1.1 Additional steps for the fabrication of suspended tapers

The fabrication of tapers like the one shown in Fig 4.1c presents additional challenges. This type of nanostructures is employed to out-couple the light from the chip to an optical lensed fiber positioned on its side, as sketched in Fig. 4.3a. This configuration requires lateral access to the device, which can be achieved by cleaving the sample at the position of the taper to free it from the surrounding material. Full separation between the two parts is possible if the long tapered section is fabricated completely free-standing, i.e. without any connections to the rest of the sample (except of course for its input). Furthermore, optimal coupling necessitates the expansion of the waveguide mode diameter (about 300 nm) to match that supported by the optical fiber, which is $\approx 2.5\,\mu m$ for the lensed fibers used in this project. This value is much larger than the thickness of the sacrificial AlGaAs layer in our samples, which amounts to about $1.37\,\mu m$[a], and reflections from the exposed substrate may distort the pattern of the emitted light and hence reduce the out-coupling efficiency. In order to avoid this detrimental effect, we decided to fabricate the tapered coupler protruding from the edge of the sample (as sketched in Fig. 4.3b) and we developed an approach to precisely cleave the chip at the input of the taper without breaking the suspended nanostructure.

Fig. 4.3c demonstrates the final mask design of the coupler. After two tethers functioning as support for the suspended nanostructure, the taper section is formed by slowly reducing the width w of the taper from 300 nm to about 118 nm over a length of $\approx 15\,\mu m$ to allow for an adiabatic conversion between the mode diameters. A straight tether of width $w = 50\,nm$ is added to connect the tip of the out-coupler to the bulk, as shown in the inset of Fig. 4.3c. Its purpose is to prevent any distortions in the polymeric mask during the development step. In fact, the extreme aspect ratio of the nanostructure reduces the contact surface between the resist layer and the GaAs underneath, thus negatively affecting the overall adhesion of the polymer. Turbulences that may generate in the developer solution during the related step can then move the narrow features around and bend the exposed tapers. The narrow tether avoids this outcome. Furthermore, its small size does not withstand the energetic sputtering process during the dry etching step and hence this feature is not transferred to the GaAs membrane, keeping the taper completely separated from the surrounding parts of the sample and can be safely cleaved.

The solution developed for the successful cleaving of nanostructures protruding from the edge of the sample consists in the addition of two trenches on both sides of the tapered section (shows in green in Fig. 4.3c). Generally, the cleaving of crystals like GaAs is performed by first producing a defect at the desired position of the edge of the chip (either by scratching or indenting the surface) and by subsequently applying a small pressure on the sample to propagate the dislocation just created. A crack as deep as the sample thickness will open by following the most favourable crystallographic direction and the chip will then be separated into two pieces. If no defects are present, the dislocation will continue to propagate in a straight line. This behaviour is clearly detrimental for the protruding taper we want to fabricate. The additional trenches allow for a complete separation of the parts that will be cleaved already in the mask. In this way, as illustrated in Fig. 4.3c, if the dislocation is initiated along the optimal cleaving line (red dashed line), the crack will not propagated across the nanostructure but rather on the substrate *under* the suspended waveguide and will finally continue again on the surface on the opposite side. The length of the

[a] We refer the reader to appendix A for the detailed layer structures of the wafers used in this project.

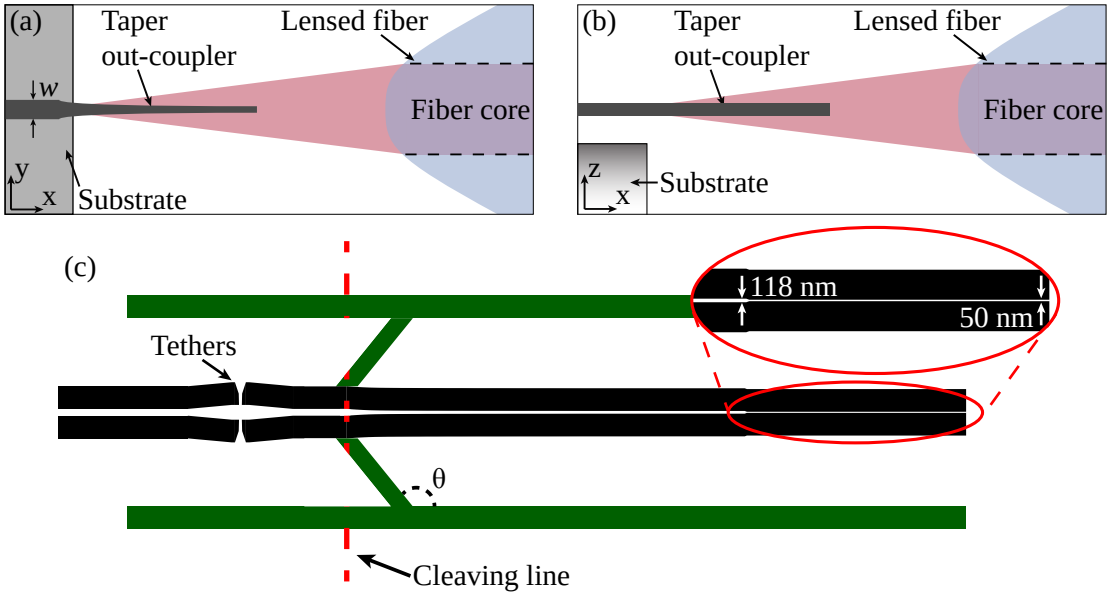

Figure 4.3: Design of suspended taper for efficient side-coupling between a NBW and an optical fiber. Schematic illustration of the side-coupling approach: (a) top-view and (b) side-view. A slow reduction of the taper width allows for the adiabatic conversion of the mode-field diameters, necessary for the optimal overlap between the mode confined in the nanostructure and the one supported by the optical fiber core. In order to avoid reflections from the substrate, the taper needs to be fabricated protruding from the edge of the sample. (c) Example of the lithographic mask for the suspended structures used for side coupling. The red dashed line indicates the optimal cleaving line, along which the dislocation propagates. The crack will then continue on the substrate when it encounters the additional trenches (shown in green). The angle $\theta = 130°$ reduces the scattering of the laser light into the coupled optical fiber. The inset shows a clearer view of the tether used to keep the long taper in place on the resist mask.

additional patterns compensate for not accurate positioning of the initial scratch. Furthermore, the angle θ helps re-directing the scattering of the laser light from the cleaved edge of the sample and hence reduces the noise collected by the optical fiber; its value can be optimised by simulations and in the fabricated structures is set to $\theta = 130°$.

The developed technique, enabled the fabrication of structures like the one reported in Fig. 4.1c. It is worth noting that the shown nanostructure is fully suspended and presents a taper that is approximatively 13 µm long.

4.2 Protocols for the fabrication of ohmic contacts

As seen in Chap.2, metal contacts can be used to apply a voltage across a p-i-n diode and hence allow for the control of the electrical properties of heterostructures and QDs. In this work we mainly focus on ohmic contacts since their properties are more suitable for quantum-photonics applications.

The main parameter defining the height of the Schottky barrier is the difference between the metal work function $e\phi_m$ and the electron affinity $e\chi$ of the semiconductor (see Chap .2). These variables are material dependent and hence some alloys are more suitable than others for the preparation of ohmic contacts. After several years of research and development, a large number of

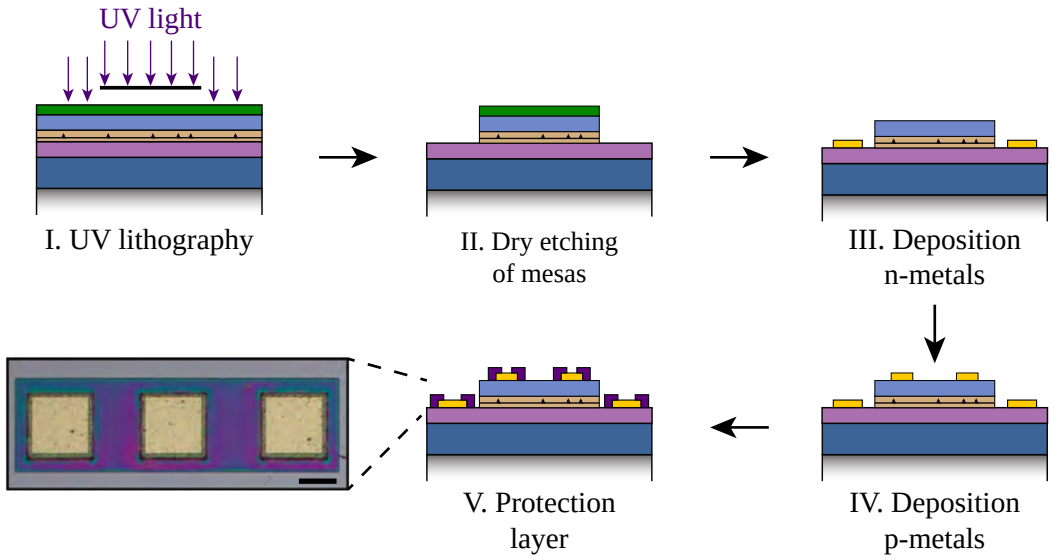

Figure 4.4: Workflow for the deposition of ohmic contacts. First, the UV mask to define the mesa structure is exposed (panel I), followed by the RIE etching necessary to transfer the patterns into the GaAs membrane (panel II). Ohmic contacts on n-GaAs a formed by depositing a mixture of Ni/Ge/Au, followed by a rapid thermal annealing (panel III). Finally, p-type metal are prepared by depositing Ti and Au (panel IV). A protection layer formed by an hard-baked epoxy-based photoresist if then prepared to isolate the edge of the contacts from the electrolytic solutions used during wet etching (panels V). Inset: optical microscope image of the polymeric protection layer. The scale bar is 100 µm long.

options have been found for optimal contacts on p-type and n-type semiconductors [12, 79–81]. Despite this variety, the most commonly used alloy for the fabrication of ohmic contact on n-GaAs is based on an alloy of nickel/germanium/gold (Ni/Ge/Au), developed for the first time by Braslau *et al.* in 1967 [82]. The mechanism behind the performance of this mixture is quite complex, but it can be summarised as a local increase in the carrier concentration at the semiconductor surface due to the diffusion of Ge [12, chap. 6]. Such a process is activated during an annealing step, which has also the effect of improving the adhesion of the metals on GaAs. Layers of Ni can be added to the aforementioned stack to control the diffusive rate of the metals. This is especially important for Au as it tends to create long spikes throughout the diode, which may results in short-circuits if layers with opposite doping are reached. This type of contacts has been proven to be quite robust to fabrication imperfections and low values of contact resistance ($R_c \cdot A_c \approx 10^{-6}\,\Omega\,\mathrm{cm}^2$, where A_c is the contact area) have been achieved over a wide range of parameters [80–86].

The production of ohmic contacts on p-GaAs is more complicated, as low Schottky barriers are obtained by introducing holes at the surface of the semiconductor, but not many materials that are sources of this type of dopants exist. Zn and Be have been reported as possible options for p-type metals on GaAs [87–89], but they have the tendency to contaminate low-pressure systems and their use is often avoided. Furthermore, Zn can diffuse very easily into the material and therefore increase the chance of generating defects in the structures. If the impurities level is high enough (i.e. above $10^{18} - 10^{19}\,\mathrm{cm}^{-3}$), non-alloyed TiAu contacts have shown good conduction properties [79]. In this case, the layer of gold acts as a bonding pad, while the layer of titanium is used as an adhesion promoter between Au and GaAs. Chromium can also be used instead of Ti, with no loss in conductivity or adhesion strength.

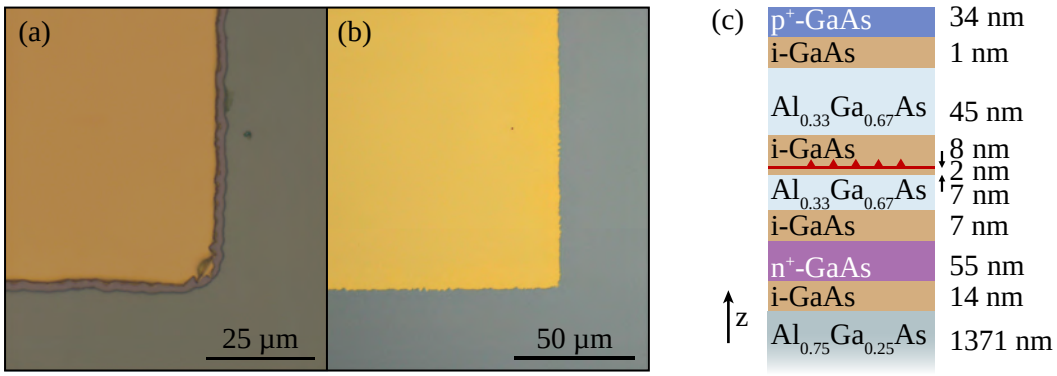

Figure 4.5: Effect of the electrochemical etching. Optical microscope images of (a) a sample affected by corrosion around the fabricated metal contacts and (b) a sample fabricated following the developed recipe. In the latter case, no trench can be spotted around the deposited metal. (c) Layer structure of the p-i-n diode used in the sample prepared during this project. The thickness of each layer is not in scale.

Fig. 4.4 schematically illustrates the main steps for the fabrication of ohmic contacts on p- and n-doped GaAs[b]. Following this procedure, structures like the one shown in the optical microscope image in Fig. 4.1d were routinely prepared.

The first step consists in exposing the embedded n-doped layer. To do so, a UV lithography mask is prepared to cover squared areas of about 2.5 mm x 2.5 mm and protect them during the subsequent RIE process (panels I and II in Fig. 4.4). The resulting structures are commonly called mesas and define the area of the p-i-n diode where photonic nanostructures will be fabricated. UV lithography is employed again for patterning the mask used for the deposition of n-type contacts (panel III in Fig. 4.4).

GaAs is know to be easily oxidised when exposed to air [90] and such thin layer of native oxide may lower the conduction at the contact interface. For this reason, a deoxidation step is usually performed before the metal deposition, where the sample is dipped in an acidic solution for short time to dissolve the layer of GaAs-oxide from the surface. The chip is then moved to an e-beam evaporator where the metals are deposited following the order Ni/Ge/Au/Ni/Au, with respective thicknesses of 5/40/60/27/150 nm. After a lift-off process (cf. Chap 3), the sample is mounted in a rapid thermal annealer, where it is treated at 420 °C for 10 s in order to form the ohmic contact.

The final step of the deposition procedure is the fabrication of the p-metals (panel IV in Fig. 4.4), which are formed by depositing first 50 nm of Ti and then 150 nm of Au. Surprisingly, following the same steps employed for the n-metals does not result in working p-type contacts. In fact, as demonstrated by the comparison in Figs. 4.5a and b, all samples prepared in that way reported trenches around the contact pads. This is a major issue on the diodes we typically use, where the p-doped layer is very thin (cf. Fig. 4.5c) and even a corrosion of 10-20 nm may result in complete isolation from the rest of the sample. This was proved by electrical characterisation of the mesas, which resulted in no detected current between any of the p-type pads for any value of applied voltage. This behaviour is not acceptable for large-scale experiments, where several devices have to be contacted at once on the same chip. We note that contacts on n-GaAs were however fully functional.

[b] In this chapter we focus on the main steps of the process and we refer the reader to appendix B for detailed recipes of the developed process.

The reported behaviour suggests that some uncontrolled etching process has occurred during the fabrication of the p-type contacts. Similar results have been already demonstrated in the literature [12, 71, 91, 92] and are usually described as galvanic corrosion. This etching process occurs when two materials with different standard potentials $E^{\circ}_{Ox/Red}$ are put in contact in the presence of an electrolytic solution [68]. This type of erosion is however unlikely to happen on our samples, as no steps involving ionic solutions takes place after the deposition of the metals. Furthermore, the fact that the n-type contacts showed no effects due to corrosion suggests the idea that a doping-dependent process may be involved.

We set out to pinpoint the causes of this unknown process by testing the effects of each step for the fabrication of metals. All the investigated samples were cleaved from the same wafer and prepared by following the workflow presented above up to a certain step, after which different fabrication procedures were tested:

(I) different combinations of p-metals were deposited at the final stage, in order to study the effect of different metal work functions and the metallisation processes;

(II) the lithographic mask for the p-contacts layer was prepared and then removed in two different ways;

(III) reference samples were also prepared, where the lithographic process for the p-layer was done right after the preparation of the mesa structures (i.e. no n-metals were deposited);

(IV) the order of the metal depositions was reversed and the p-type contacts were deposited before their n-type counterparts.

Table 4.2 reports an overview of the results we obtained and it shows that different metals and different metallisation processes did not affect the final result, as found in test (I). Test (II) had an unexpected outcome since it showed that corroded areas on the p-GaAs, corresponding to the exposed patterns of the lithographic mask (Fig 4.6), were formed already before the p-metal deposition. Test (III) resulted in no corrosion around the pads, independently from the cleaning procedure used. Interestingly, no n-type metals were deposited on both samples, which suggested that the presence of n-metals could be the possible trigger for the etching of p-GaAs. This speculation was confirmed in test (IV), where the fabrication procedure was reversed and p-type metals were deposited before their n-type counterpart.

Test	First deposited metal	p-metal	mask cleaned	trenches
(I)	n-metal	AuZn	hot NMP	yes
	n-metal	TiAu	hot NMP	yes
(II)	n-metal	-	hot NMP	yes
	n-metal	-	O_2 descum/deox/hot NMP	yes
(III)	-	-	O_2 descum/deox/hot NMP	no
	-	-	O_2 descum/hot NMP	no
(IV)	p-metal	AuZn	hot NMP	no

Table 4.2: Overview of the tests performed in order to investigate the causes of the formation of trenches around the p-metal pads.

The results of our tests indicate that the uncontrolled etching process affects layers with opposite doping differently and, most importantly, it is triggered by the presence of fully-processed

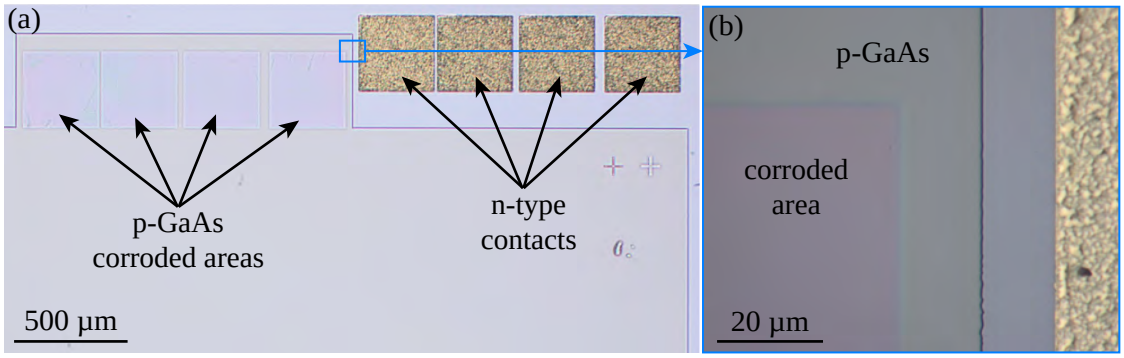

Figure 4.6: Optical microscope images of the corroded p-GaAs layer visible after removal of lithographic mask. (a) Overview of the mesa structure and the deposited n-type contacts. The rough surface of the metals is the result of the annealing step. (b) Close-up image of the area indicated by the blue rectangle in (a).

n-type pads. Based on the electrochemical approach to the etching of III-V semiconductors described in Chap. 3, we propose a possible explanation for the unexpected corrosion we found on our samples. The main concepts are schematically outlined in Fig. 4.7.

Fig. 4.7a shows a sketch of the band diagram of the p-i-n diode that constitutes our samples before the formation of the contact and at the equilibrium state, i.e. when the Fermi levels E_f of both doped layers are aligned. In this situation, the surface potentials $\phi_{0,n}$ and $\phi_{0,p}$ pin the bands at specific positions, upwards for the n-GaAs and downwards for p-GaAs [19, 20]. When the n-metal is deposited and the contact is formed, the E_f moves to lower energies and aligns to the metal Fermi level $E_{f,m}$ and narrows the energy barrier at the semiconductor surface. This change has an effect on the carriers densities in the heterostructure, which rearrange in order to recover the equilibrium state. Since the metal $E_{f,m}$ pins the Fermi level on the n-side of the junction, E_f on the p-side will eventually set on this level too. Such effect is the same as a negative voltage applied to p-GaAs that produces the accumulation of holes at its surface, as described by eq. (2.4b) and illustrated in Fig. 4.7b. During the development of the lithography mask for the p-metals, then, the exposed areas of the sample surface are exposed to the developer, which is an alkaline solution and therefore initiates the anodic dissolution of GaAs. In fact, such process may be also enhanced by the basic nature of the liquid, since high pH is known for shifting the GaAs band-edges upwards [21, 93]. If no n-type contact is formed, the redistribution of charges and subsequent holes accumulation on the surface of p-GaAs do not occur, hence no corrosion takes place, as found in test (III).

When the fabrication procedure is reversed and p-type contacts are prepared first, a similar process as the one just described happens in the bands of the diode (Figs. 4.7c and d). In this case, however, two important distinctions take place: firstly, during the contact formation, electrons are transferred from metal to p-GaAs and E_f then moves upwards. In this way, an effective *positive* voltage is applied to the n-side of the junction and the charge depletion at the surface decreases. Secondly, holes are the minor carriers in n-doped semiconductors; for this reason, their concentration at the surface of n-GaAs is extremely low and anodic dissolution does not spontaneously occur. Therefore, the unexpected etching on n-GaAs is strongly suppressed, as also confirmed by test (IV) (Tab. 4.2).

The found ability to inhibit the anodic dissolution by reversing the fabrication process and depositing the n-type metal at the end of it has however a disadvantage: it moves the annealing step after the deposition of p-type metals. As mentioned above, AuZn alloy may be an option for annealed contacts, but it is often avoided for the high diffusion of Zn. On the other hand,

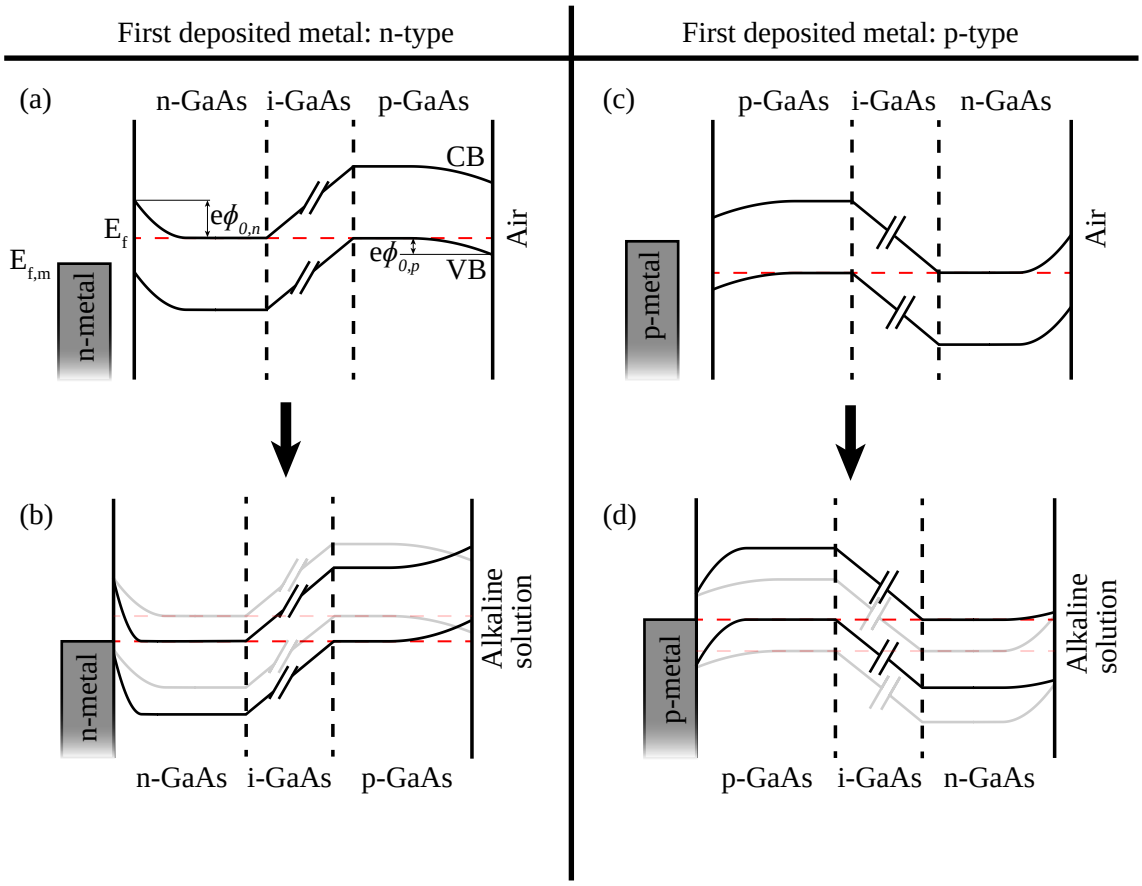

Figure 4.7: Schematic illustration of the proposed mechanism causing the corrosion of the p-GaAs layer. (a) Band diagram of the p-i-n diode at the equilibrium state, before the formation of the metal contact. The Fermi levels on both sides of the junction are aligned and energy barriers on the n-side and the p-side are shown ($e\phi_{0,n}$ and $e\phi_{0,p}$, respectively). The metal energy band is filled by electrons up to its Fermi level $E_{f,m}$. (b) When the contact is formed, the semiconductor Fermi level move downwards and align to its metal counterpart. This causes a shift in the bands of the entire diode and an effective negative voltage is felt by the p-doped layer. This effect initiates the anodic dissolution of p-GaAs when the sample is dipped in the alkaline developer solution. (c) and (d) Same as (a) and (b), but with the metal contact formed on the p-doped layer first. The anodic dissolution of n-GaAs is inhibited by the reduced bending of the bands at its surface and by the low concentration of holes in extrinsic semiconductors of this type.

however, the performances of non-alloyed TiAu contacts decreases when they undergo annealing treatments and this forces us to keep the initial order of the depositions, i.e. first n-type and then p-type. We solved this problematic situation by reducing the photo-generation of carrier during the development step, when the anodic corrosion takes place. Ambient light (even the UV-filtered light of cleanrooms) can indeed excite electrons from the valence to the conduction band, thus increasing the density of holes at the surface and therefore also the etching rate of the material. By developing the lithographic mask of p-type contacts in the dark, we are able to slow the etch rate down to a level that does not heavily affect the final performances of the fabricated contacts. No trenches were visible under the optical microscope when this procedure was followed, as demonstrated by the comparison between Fig. 4.5a and Fig. 4.5b.

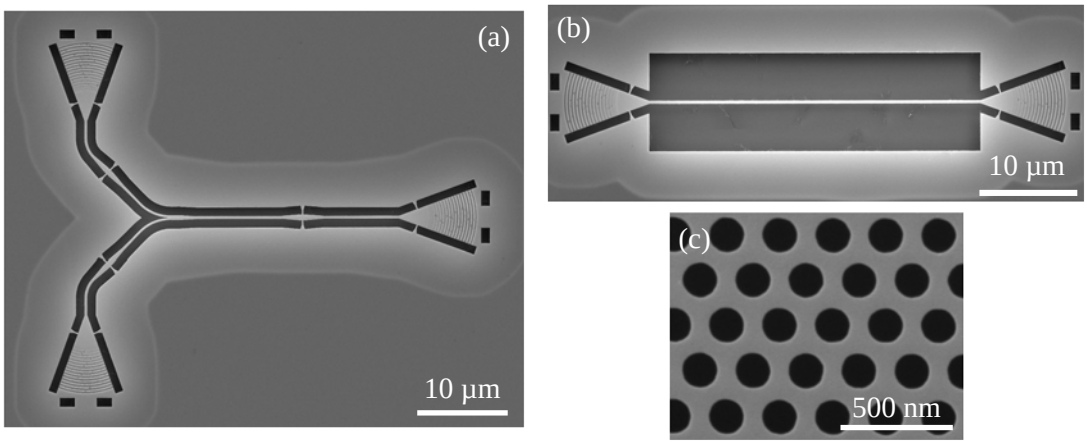

Figure 4.8: SEM images of typical photonic nanostructures fabricated with the developed protocol. (a) Three shallow-etched gratings are optically connected by a suspended NBW that presents a beam-splitter section to guide light to both the couplers on the left hand-side. (b) Straight suspended NBW connecting to shallow-etched out-couplers. The trenches on both side of the nanobeam have width of 5 µm and are 35 µm long. (c) Photonic crystal with air holes patterned in a triangular lattice, with $a = 235\,\text{nm}$ and $r = 72\,\text{nm}$.

After both n- and p-metals are successfully deposited on the mesa, the fabrication of suspended nanostructures takes place. As described in Sec. 4.1, strong reagents are used for the etching of the devices that may damaged the contacts and lower their performance. The wet etching step is especially troublesome for the deposited pads as they get exposed to electrolytic solutions that may initiate a galvanic corrosion around the metal. Furthermore, the Ti layer in the p-metals may get dissolved by HF, resulting in the lift-off of the full pad. To prevent this, we introduced one last step at the end of the fabrication of the mesa structures, consisting in the preparation of a polymeric layer covering the edges of the contacts (panel V). By means of UV lithography, frames around the pads were exposed on an epoxy-based resist, which was than hard-baked at $T = 140\,^{\circ}\text{C}$ for 20 mins in order to improve its durability. The final result is demonstrated in the inset of Fig. 4.12, which shows the design of the exposed polymeric frame around the metals. The central regions of the contacts are left open to allow the wire bonding of the chips; no risk of damage exists for this area of the pads as it is cover by Au and therefore chemically robust.

4.3 Assessment of the capabilities of the developed protocols

The fabrication procedures we just described allowed us to fabricate a variety of complex suspended nanostructures, as demonstrated in Fig. 4.8. The high level of precision achieved by each protocol reduced the presence of structural imperfections and facilitated the fabrication of devices with demanding requirements, such as the exposure of large geometries next to long and thin features (Fig. 4.8b), or the etching of holes with diameters as small as 144 nm as in Fig. 4.8c.

Building chips for advanced quantum photonic experiments, however, present one more challenge: they demand a fine control over the feature sizes of the fabricated components, as they have a large impact on the final properties of the nanodevices, like the dependence of the propagating mode in a PhCW on the size of the hole radius (cf. Chap. 2). Therefore, the final test for the true capabilities of the developed protocols is based on the success of the experiments run on the fabricated samples.

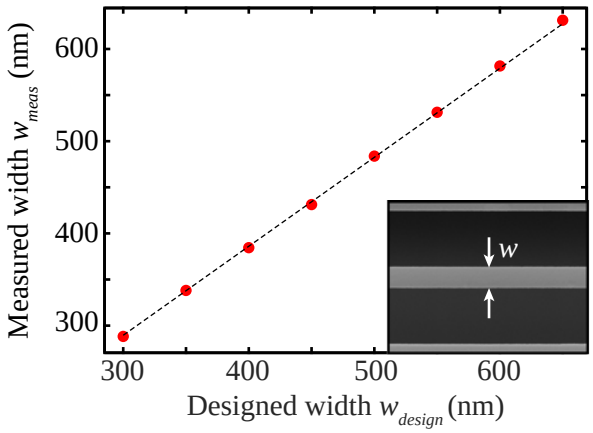

Figure 4.9: Characterisation of the impact of the fabrication process on the width of NBW. The value of the width measured from SEM images w_{meas} is plotted as a function of the corresponding design value w_{design}. The dots show the average of the values measured for 5 NBWs with the same nominal width, whereas the calculated standard deviation results smaller than the marker size and therefore omitted. From a linear fit of the dataset (black dashed line), we found that $w_{meas}/w_{design} = 0.965$.

4.3.1 Fabrication of efficient out-couplers

The light propagation of NBWs is affected by their width (cf. Chap. 2). Therefore, being able to fabricate devices with the desired value of this parameter is essential. We investigated the effects of the nanofabrication process on this type of structures by measuring the width w_{meas} of the fabricated nanostructures from SEM images. Fig. 4.9 reports the results of this study, where the measured widths (averaged over 5 devices) are plots as function of their design values w_{design}. From a linear fit of the data we found that the final w_{meas} is only 3.5% smaller than the initial value.

The characterisation of fabrication-induced changes on NBWs helped the design and fabrication of long tapers employed in [94] for studying the evanescent coupling between photonic nanostructures and optical microfiber with a diameter of about 2 µm. The energy transfer between the parts of such a coupled system is made possible by a slow reduction of the NBW width over long distances. Any defect or edge roughness in the fabricated nanostructures would cause scattering of the light and hence lower the overall coupling efficiency. The use of PEC and the etching process we developed were key to reduce such detrimental effects.

Examples of the fabricated nanostructures are shown in Figs. 4.10a and b. The first SEM image shows a device formed by a 1D photonic-crystal mirror, which is designed to reflect wavelengths ranging from 870 to 1060 nm, and a NBW that is linearly tapered from a width of 300 nm to 140 nm over a length of 30 µm.The second type of tested nanostructures presents a similar taper, although having final width of 160 nm, and with a PhCW that is terminated on one side by a photonic crystal section.

Fig. 4.10c shows the schematics of the optical setup used: a pulled optical fiber is positioned on top of the out-coupler section while the transmitted (T) and reflected (R) signals of the probing light are monitored in order to find the optimal position. The fiber also has a dimple to improve the coupling. The chip-to-fiber efficiency is calculated by measuring the reflected power and comparing it to the known input power. When propagation and insertion losses in the optical setup are accounted for, we calculated a chip-to-fiber coupling efficiency $\eta_{CF,NBW} > 80\%$ for

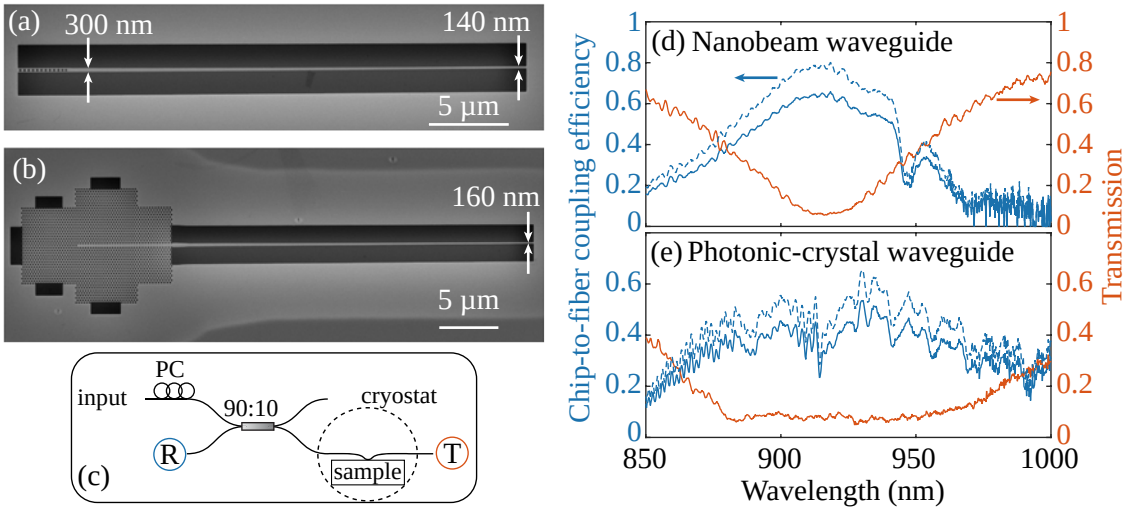

Figure 4.10: Scanning-electron images of the fabricated samples for different coupling methods: (a) suspended 1D photonic-crystal mirror (on the left hand-side) terminated with a 30 µm long tapered waveguide. (b) Photonic-crystal waveguide connected to a 30 µm long tapered nanobeam waveguide. (c) Schematics of the optical setup used to characterised the efficiency of the evanescently coupled system. The input light is coupled, after polarization control (PC), into a 90:10 fiber beam splitter, which transmits the light to the sample sitting in the cryostat. The collected signals are the transmitted light after the coupled system (T) and the reflected one from the sample (R). (d) Chip-to-fiber coupling efficiency η_{CF} for the NBW shown in (a) (solid blue line) obtained from reflection measurement. The values corrected for the propagation losses in the tapered fiber is also reported (dashed blue line). The orange curve shows the transmission through the fiber when coupled to the device relative to the case of the uncoupled system. (e) Similar data for the device containing the PhCW in (b). Adapted from ref. [94].

the nanobeam and $\eta_{CF,PhCW} > 60\%$ for the photonic-crystal waveguide, as shown respectively in Fig. 4.10d and Fig. 4.10e. The lower value registered for the photonic-crystal waveguide may be attributed to the higher number of interfaces in this type of device, which introduce more losses into the system. When the QDs were used as emitters of single photons, count rates of 4.38 MHz and 3.37 MHz were detected on superconducting nanowire single-photon detectors and translated into overall single-photon source efficiency $\eta_{SP,NBW} = 15.5\%$ and $\eta_{SP,PhCW} = 10.9\%$ for nanobeam and photonic-crystal waveguide, respectively.

The efficiency of the suspended taper discussed in Sec. 4.1.1 was also characterised and the results were reported in [32]. Above-band pulsed laser light was used to excited the QDs and the emitted photons were collected by a side-coupled lensed fiber (cf. Fig. 4.3b). The signal is then sent to an avalanche photodiode (APD) to record the total amount of detected single photons. A count rate of about 2 MHz is achieved when the emitters are saturated and corresponds to a single-photon rate of about 1 MHz when corrected for multiphoton probability. When the repetition rate of the excitation laser (76 MHz) and the propagation losses along the optical setup are considered, the aforementioned detection frequency corresponds to a chip-to-fiber efficiency $\eta_{CF} = 16.6\%$ [95], which translates into an overall source efficiency of $\eta_{SP} = 10.3\%$ [32] and is comparable to the values presented above for evanescent coupling.

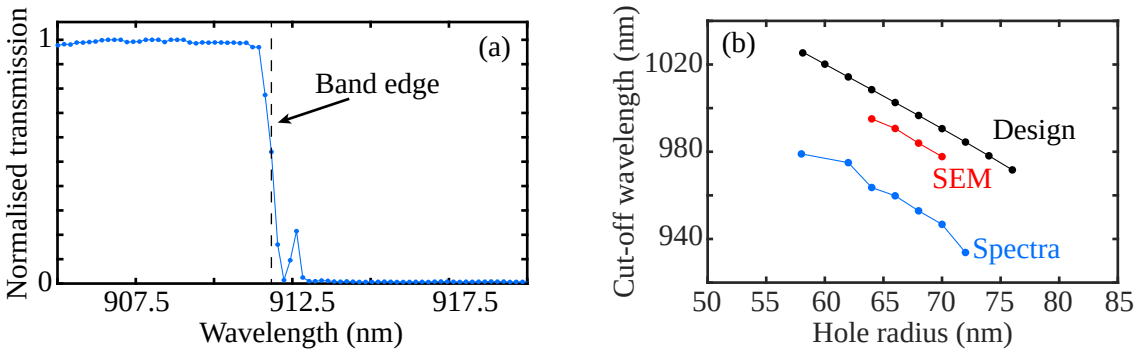

Figure 4.11: Characterisation of the fabrication-induced effects on the hole size in PhCWs. (a) Example of the transmission spectra recorded from the fabricated PhCWs. The typical drop in the signal is shown. The estimated position of the band edge is marked by a black dashed line. The small peak detected about this position is probably originated by Anderson-localised modes. (b) Comparison between nominal spectral position of the cut-off wavelength (black) and those evaluated from SEM images (red) and transmission spectra (blue). A larger shift detected from the optical experiments may suggest that a change in the hole size is not the only cause of the final detuning found on the fabricated PhCWs.

4.3.2 Fabrication of efficient light-matter interfaces

The values of the lattice constant a and hole radius r are the relevant parameters for photonic crystal waveguides, as the spectral properties of the propagating modes strongly depend on them (cf. Chap. 2). Between them, the size of r is the most likely to be affected by the fabrication steps, which can make the holes larger than expected and hence shift the resonances of the PhCWs to lower frequencies. In fact, the value of a is set by the position of the patterns in the lithographic mask and therefore only errors in the hardware employed for the exposure may modify it. We therefore assumed the lattice parameter to be constant throughout the full fabrication procedure and hence focused only on the hole radius for the optimisation of the protocol.

The characterisation of the fabrication induced effects on PhCWs was twofold: (i) SEM images of the holes were analysed to measure the average value of their radius, and (ii) the spectral position of the cut-off wavelength for each nanostructure was measured from transmission spectra. These measurements were performed by coupling laser light into one of the gratings shown in Fig. 4.1b and by monitoring the signal out-coupled from the second of them while tuning the excitation wavelength. The estimated values were then compared with the one obtained from band-structure simulations that were run using the same parameters of the fabricated devices.

Fig. 4.11a reports a typical transmission signal recorded during this analysis, which demonstrates the expected drop when the excitation laser is tuned towards lower frequencies and into the photonic bandgap. The small peak visible in the spectrum probably originates from weak Anderson-localised modes which usually appear about the position of the band edge [78]. Fig. 4.11b reports one example of the final comparison of the obtained values, where the SEM data (red) was extrapolated from simulation results by using the averages of the measured radii. Whilst a spectral shift of only $\approx 15\,\text{nm}$ is visible between the design (black) and the SEM values, a much larger change is detected for the band edge positions obtained from transmission spectra ($\approx 40\,\text{nm}$, in blue). This discrepancy suggests that the small enlargement of the radius measured from SEM images (i.e. about 4 nm) is not the only effect induced by the fabrication processes. For example, the few layers of GaAs native oxide that commonly grows on the surfaces may dissolve during the

wet etching step, thus reducing the overall thickness of the GaAs membrane; further investigations are necessary to pinpoint the possible causes of the detected changes. Nonetheless, we exploited the investigation just described to calibrate the initial design values of the hole radius, which were always set to shorter lengths to compensate for the fabrication-induced modifications. This approach was used for all the photonic crystal waveguides we prepared and enabled the investigation of appealing quantum effects such as single-photons nonlinearities [96] and chiral emission of QDs [97], which are hard to detect in presence of optical losses due to structural defects or when the fundamental mode in fabricated nanostructures is far detuned from the designed value and therefore not spectrally coupled to the embedded QDs.

4.3.3 Electrical control of the properties of QD

Quantum photonic experiments are normally carried out at cryogenic temperatures ($T < 10\,\mathrm{K}$), which is a quite extreme condition for the electrical properties of semiconductors and metals, as we discussed in Chap. 2. The metal deposition protocol we developed must therefore result in contacts that are ohmic at room T and, most importantly, that maintain a low level of resistance also in such demanding environment.

Fig. 4.12a presents examples of I-V curves (i.e. plotting values of current I as a function of applied bias V) that are typically measured at $T = 10\,\mathrm{K}$ for TiAu and NiGeAu contacts deposited on the samples prepared during this project. The collected data demonstrates that both types showed ohmic behaviour at cryogenic temperatures in the tested range of applied voltage. The reported values of resistance have been obtained from a linear fit of the data points and are representative of the values usually measured: a few tens of Ohm for n-type and between 3 and $10\,\mathrm{k\Omega}$ for p-type contacts. The electrical behaviour of the related diode is demonstrated in Fig. 4.12b, where the logarithm of the recorded current is plotted against the applied bias. For $T = 298\,\mathrm{K}$ values smaller than $1\,\mu\mathrm{A}$ were measured for the same voltage range shown in Fig. 4.12a. A decrease by about an order of magnitude was registered at cryogenic temperatures, where the thermal energy of the charge carriers in the sample is reduced.

The measured conductivity for $T < 10\,\mathrm{K}$ confirms not only the successful fabrication of ohmic contacts on the p-i-n diode, but also the good electrical properties of the degenerately doped layer in the sample. An electric potential could therefore be applied across the entire layer, which let us electrically address all the QDs embedded in the large mesa structures and tune them as shown in Fig. 4.12c. Here, the typical Stark tuning of two excitonic lines from the same QD is shown. The peaks are identified as X^0 and X^+ based on how their intensity varies with the applied bias.

Most importantly, the procedure we propose has shown to be compatible with the processing necessary for the etching of nanostructures as it enabled the fabrication of complex samples like the one in Fig. 4.12d, where suspended NBWs and PhCWs (inset of Fig. 4.12d) were successfully prepared on a mesa with both p- and n-type metals. The electrical control possible on this photonic chips allowed us to effectively suppress the decoherence mechanisms related to charge noise in QDs embedded in nanobeam waveguides. This gave us the means to achieve the emission of photons with high indistinguishability as we report in [32], where a Hong-Ou-Mandel (HOM) visibility as high as $V = (94 \pm 1)\%$ was measured when the QDs were excited with a quasi-resonant laser. Furthermore, the used of gated samples improved our abilities in detecting single-photon non-linearities in resonant transmission experiments, as we reported in [33], where a linewidth as small as $\Gamma_{RF} = (0.96 \pm 0.07)$ GHz was evaluated for a QD embedded in a NBW. As the measured decay rate for the same emitter was $\gamma = 5.49\,\mathrm{ns}^{-1}$, the corresponding natural linewidth was $\Gamma = \gamma/2\pi = (0.87 \pm 0.003)$ GHz, showing that the measured interaction between light guided in the planar nanostructure and the QD was near-lifetime-limited.

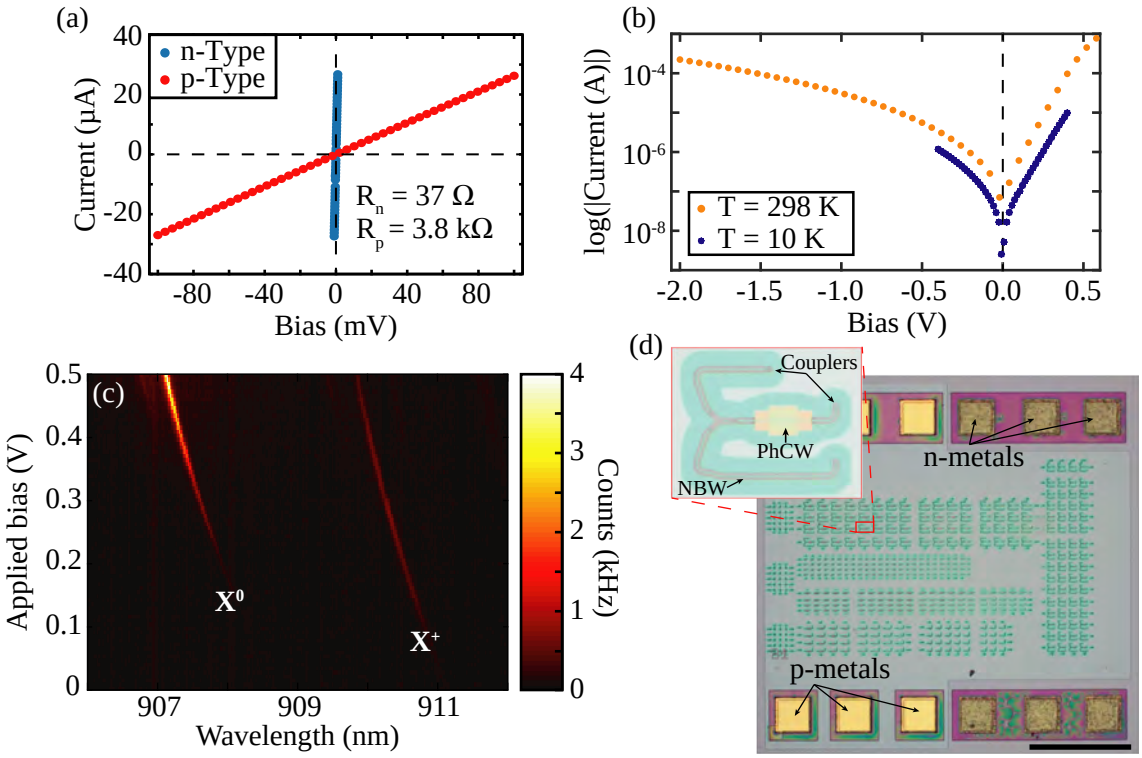

Figure 4.12: Examples of I-V curves measured on fabricated samples. (a) The linear dependence between applied bias and recorded current confirms the ohmic behaviour for both n-type (blue) and p-type contacts (red). The extrapolated values of the resistances of both types of contacts (R_n and R_p, respectively) are also reported. The measurements have been performed at $T = 10$ K. (b) IV curves measured from the corresponding diode of (a). Current values smaller than 1 μA have been measured for a range of applied bias [-0.2 V; 0.2 V], at room temperature. The cryogenic temperature decreases the thermal component of the carriers total energy, thus reducing the detected current by about an order of magnitude. (c) Voltage-wavelength photoluminescence spectra for a QD embedded in a p-i-n diode. The fluorescence plateaus of both neutral (X_0) and positive trion (X^+) are shown. (d) Optical microscope image reporting an example of a full processed sample with electrically contacted NBWs and PhCWs, an example of which is shown in the inset. The green areas around the nanostructures correspond to the undercut resulting from the selective wet etching step. The scale bar is 500 μm.

The developed protocol for the formation of ohmic contact has shown to be reliable and reproducible since it was employed also on more complicated heterostructures, where the QDs are grown in a p-i-n-i-n diode [31]. Such layer structure was proposed to reduce the detrimental effects of the built-in field at the position of the emitters and thus improving the control of the charge population in a QD at the single-electron level. The ability of preparing the electron spin in the ground state with fidelities as high as 96% showed that the fabricated devices can be implemented as spin-controlled switches for integrated quantum photonics applications [98].

4.4 Conclusions

In summary, in this chapter we presented the nanofabrication protocols we developed for the production of the major elements necessary to build quantum photonic circuits. A soft-mask process

for the fabrication of suspended devices has been optimised and employed for the production of nanostructures with low level of losses. This was confirmed by measuring single-photon source efficiencies as high as 15.5% in NBWs [94], which corresponds to a twofold improvement compared to previous reports on similar devices [99].

A procedure to successfully deposit ohmic contacts was also presented. Samples fabricated by following this protocol demonstrated suppressed charge noise and hence improved coherence. This led to the generation of coherent single photons with a HOM visibility of $V = (94 \pm 1)\%$, which approaches the indistinguishability level reported in micropillar cavities, i.e above 98.5% [47, 100].

The improved coherence properties of the gated structures were also shown by the improved quality of the signal detected in resonant transmission measurements, where we managed to measure near-lifetime-limited transitions from a QD embedded in a NBW [33]. This effects were always affected by large spectral diffusion in previous samples fabricated without gates [96].

Finally, the deposited ohmic contacts, in combination with a properly engineered heterostructure [31], have shown to permit the control of the QD spin-state to the single-electron level with fidelity as high as 96% and hence facilitated the production of efficient spin-photon interfaces [98].

The fabricated devices therefore showed to have met all the stringent requirements to perform advanced experiments. In Chap. 6 we will make use of these achievements and show that the developed protocols have also the capabilities to unlock the deterministic control over the emission properties of QDs embedded in photonic crystal waveguides.

Chapter 5

Locating QDs and deterministic fabrication

The different devices presented in the previous chapter are a few examples of the building blocks constituting the quantum photonic platform based on self-assembled QDs embedded in GaAs nanostructures. The achieved exciting results testify that they are promising candidates for the development of next-generation quantum photonic applications. Nevertheless, the lack of *a priori* knowledge of the spatial position and spectral properties of Stranski-Krastanov QDs has forced many experiments based on this type of emitters to rely on the fabrication of multiple devices at once and the subsequent post-selection of the few successful structures with good spatial and spectral coupling between emitters and structures. Whilst interesting results can still be achieved using this approach, it clearly limits the possibility of building complex chips and large-scale experiments.

Two main strategies have been proposed to solve this scalability issue: the first one involves the growth of QDs at pre-defined sites. This method exploits the tendency of InAs dots to nucleate in the proximity of superficial structural defects. The employed substrates are therefore prepared by fabricating regular patterns of holes etched into the material that act as seeds for the QD growth [101]. Nanostructures are subsequently fabricated at the same pre-defined positions [102, 103]. QDs grown by this method have shown emission of single and indistinguishable photons [104, 105], but the initial fabrication steps necessary for the substrate preparation introduce defects and impurities in the material that lower the quantum efficiency of the emitters and cause a broadening of the exciton linewidth, which ranges between 10 and few hundreds of μeV [101, 104, 106].

The second strategy uses a different approach, i.e. the emitters are first grown by the usual Stranski-Krastanov method and then located using localisation techniques. The nanostructures are subsequently fabricated about their positions. This approach does not affect the good optical properties of self-assembled QDs, but requires the use of procedures that detect the locations of QDs with nanometer precision; this is the approach we decided to follow in this PhD project. In this chapter a description of the method we developed will be given and we will show that not only we locate self-assembled QDs with high precision, but we also exploit this knowledge to fabricate nanostructures at the desired positions with accuracy errors lower than 50 nm.

5.1 Literature review of localisation techniques

A variety of localisation techniques have been developed in order to address the challenge posed by the random QD positions. In this section, we present an overview of the principal methods, where we will describe the main concepts of each approach together with the final precision and accuracy that can be achieved. We will furthermore address the strong and weak points with regard to the type of the sample we are interested in, i.e. planar structures with nanometer-size features.

5.1.1 Detection by scanning electron microscope inspection

During the growth of self-assembled QDs, the InAs islands are capped by a layer of GaAs in order to ensure the necessary 3D confinement. The strain that such formations introduce in the material produces a small stacking defect in the crystalline structure of the capping layer, which propagates up to the surface of the grown wafer and results in a small bump (Fig. 5.1a). If this feature is large enough, then it can be spotted by inspecting the sample by means of a scanning electron microscope. This technique was first reported by Badolato *et al.* in [107], where they mapped the position of QDs with respect to a pre-fabricated matrix of gold markers that was used as a reference frame. In order to enhance the signal from the bump, the authors used stacked QDs, i.e. growth in sequence on top of each other, since they produced large surface bumps. They then fabricated a photonic crystal cavity aiming to position the emitter within 25 nm from one of the four electric-field maxima of the cavity defect, as illustrated in Fig. 5.1b. Although a statistical analysis of the final fabrication accuracy was not performed, the authors reported that one device showed emission properties that are in good agreement with the expected theoretical behaviours.

A similar approach was employed by Kuruma *et al.* in more recent years [108], but using a thin GaAs membrane containing only single QDs. The use of very low acceleration voltage (1 kV) in combination with an angled secondary electron detector enabled the detection of the shallow surface bumps (Fig. 5.1c). The final location precision was evaluated from comparing the optical coupling strengths calculated by using the positions detected by SEM and the values obtained from micro-photoluminescence (μPL) measurements for about 30 devices. The authors reported a final spatial error of about 5 nm. It is however worth mentioning that Kuruma and co-workers used the described technique as a characterisation tool to inspect the devices only *after* fabrication,

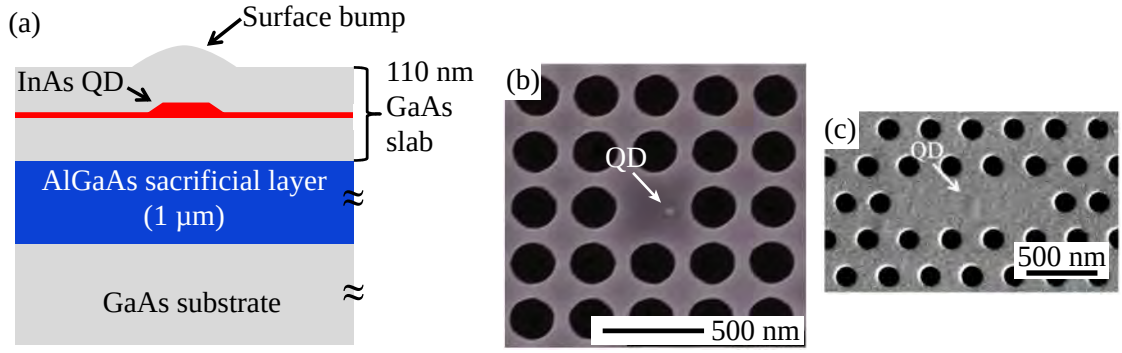

Figure 5.1: Detection of QDs by SEM inspection. (a) Schematic cross-section of the investigated sample with a single QD. (b) SEM image of a fabricated photonic crystal cavity, where the emitter (indicated by the bright spot) is positioned at the desired position inside the cavity defect. (c) SEM image of the fabricated photonic crystal cavities. The white arrow shows the located surface bumps. (a) and (c) adapted from [108], (b) reproduced from [107].

with the main intent of selecting only the nanostructures showing surface bumps located inside the cavities. Nonetheless, the main experimental ideas behind the presented approach may be valuable for finding the QDs positions before the fabrication of nanostructures.

In conclusion, SEM inspection can be used to locate QDs and to map them relative to the position of pre-deposited gold markers. Since a scanning electron microscope is the only necessary tool, no demanding requirements are needed and high location precision can still be achieved. On the other hand, however, the surface bumps may not be spotted with ease, especially when the sample contains non-stacked QDs and if the signal-to-noise ratio of the employed microscope is low. Finally, no spectral information can be acquired in this system and an additional characterisation step is therefore required.

5.1.2 Detection by raster-scan techniques

Reference alignment markers are also used in techniques that are based on the collection of raster images. For example, in the works by Thon *et al.* [109] and by Coles *et al.* [110], samples with pre-fabricated gold structures (see inset of Fig. 5.2a) were mounted in cryostats and μPL setups were employed to collect the emission signals while scanning piezoelectric stages to move the microscope objective. The photons collected at each position were then sent to avalanche photodiodes, which allowed the authors to construct image scans like the ones shown in Figs. 5.2a and b, where the detected counts are plotted as a function of the stage position for each scan. The center of the QD was then found by fitting the recorded signal with a Gaussian function (Figs. 5.2a). Two different approaches were used in the presented works for the location of the alignment structures: Thon and co-workers monitored the emission from the GaAs bandgap and detected a dip when scanning across the gold markers, which blocked the luminescence signal from the substrate (as shown in Fig. 5.2b). Coles and co-authors, on the other hand, collected the reflection of the laser from the metallic structures (plot not reported here). In both cases, however, the statistical analysis built by multiple scans enabled the mapping of the QDs with respect to the markers with errors of about 5 nm [109], which was reduced by an order of magnitude when a solid immersion lens was used [110]. Furthermore, in both works planar nanostructures were fabricated about the desired positions and subsequent optical measurements resulted in a final accuracy of $\approx 50\,\text{nm}$. In the work of Thon *et al.* the success yield was reported to be 70 %.

A second method to acquire raster images is by means of an atomic force microscopy (AFM), as reported by Sapienza *et al.* [111]. In this case, the surface morphology of the sample was investigated by scanning an AFM tip, which could detect the profile of both the shallow surface bumps caused by the QDs (Fig. 5.2c) and the fabricated markers (Fig. 5.2d). After fitting the raster images, the authors were able to correlate the positions of markers and QDs and estimated their relative locations with an error of 13 nm. No nanostructures were fabricated in the reported work.

In conclusion, localisation of self-assembled QDs has been achieved with high precision by means of raster-scanning techniques. Specifically, position errors of 13 nm were obtained when AFM scans were employed [111], while the implementation of statistical analysis has enabled reduction of that value to below 5 nm in photoluminescence experiments [109, 110]. Moreover, in the latter experiments, planar nanostructures were successfully fabricated, with an extrapolated accuracy of approximately 50 nm. It is worth noting that optical setups used for raster-scans may also facilitate the spectral characterisation of the investigated emitters, as they can be easily modified to collect the spectrum of the light emitted from the QDs. The techniques discussed in this subsection are quite time-consuming: not only are raster-scans performed slowly to avoid losing resolution, but several of them are required for each QD in order to decrease the final location error and acquisition times as long as a few hours per image are common. This may be

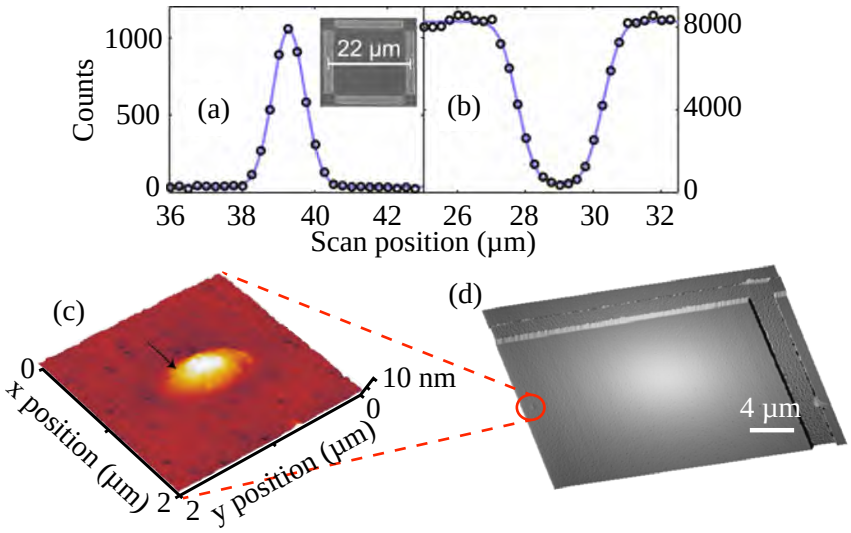

Figure 5.2: Detection of QDs by raster-scanning techniques. (a) Detected counts from the QD signal as a function of the scan position. The empty circles show the experimental data, while the curve represents the Gaussian fit. Inset: SEM image of the gold reference structures. (b) As in (a), but for the gold reference structures. The detection of the markers is manifested as a reduction of the recorded intensity, as the metal shadows the emission from the substrate. (a) and (b) adapted from ref. [109]. (c) AFM image of a surface bump which indicates the position of the QD. (d) AFM image of a region close to the reference markers. (c) and (d) adapted from [111].

disadvantageous when a quick turnaround between different samples is expected.

5.1.3 Localisation by photoluminescence imaging

A third option in literature that exploits pre-fabricated reference markers to map the position of self-assembled QDs is based on photoluminescence imaging of the investigated sample. This method was first proposed by Kojima *et al.* [112] and then improved and developed in several other works [63, 111, 113–117]. The general steps of this technique are the following: after the deposition of a reference frame of gold markers, the sample is mounted in a cryostat and aligned to an imaging setup. Large regions of the sample are illuminated by two light sources (typically LEDs) with different wavelengths. One of these sources provides an above-band excitation for the QDs, whereas the second one uses a broadband spectrum to light up the metallic markers, as they reflect the radiation back. The two sources are kept ON at the same time and a charge coupled device (CCD) camera is used to collect images like the one reported in Fig. 5.3a, where both the reflection from the reference structures and the photoluminescence emitted by the QDs are visible at once. Long-pass filters (LPF) – or other combinations of filters [115] – are used in front of the camera to block any unwanted signal from the illumination sources. The recorded images finally undergo an image analysis procedure that allows for the detection of the centers of both the markers and the QDs. The choice of the employed algorithm seems to be the main factor for the final localisation precision, as the locations of the emitters relative to the reference markers have been found with errors ranging from about 50 nm [112] down to below 5 nm when advanced high-resolution techniques have been used [114]. In terms of final accuracy in fabricating nanostructures at the desired positions, alignment errors as low as 40-50 nm have been inferred from the optical measurements performed on the fabricated devices [112, 113, 116]. An additional laser and a

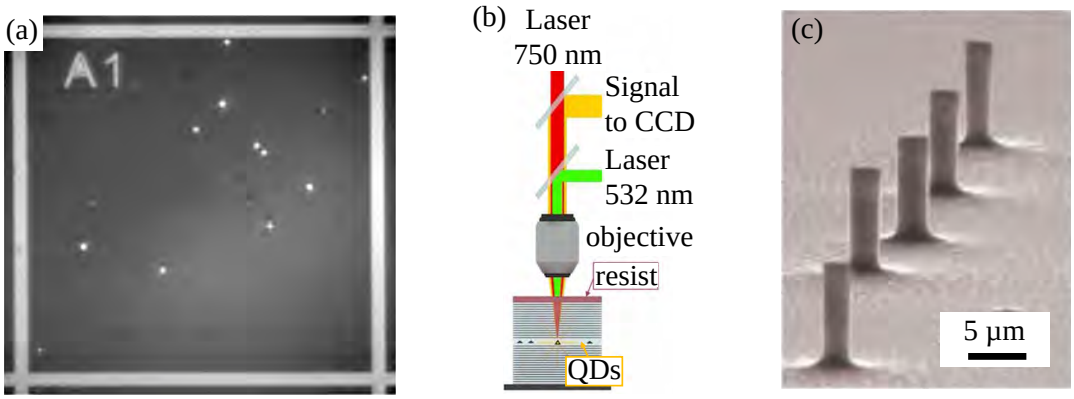

Figure 5.3: (a) Localisation of QDs by photoluminescence imaging: example of the image acquired by the CCD camera. Both the reference markers (bright lines) and the QDs emission (bright spots) are visible. Adapted from [114]. (b) Schematic of the setup for the deterministic fabrication of photonic structures by in-situ photolithography. (c) SEM image of micro-pillars fabricated by in-situ photolithography. (b) and (c) adapted from [118].

spectrometer can also be coupled to the same imaging setup and used to perform spectroscopy on the investigated sample, thus allowing for a full characterisation of the chosen emitters before the fabrication process. The final quality of the collected images is very sensitive to the stability over time of the employed setup. More importantly, distortions and poor signal-to-noise ratios severely affect the overall uncertainties of the detected locations, as reported by Liu and collaborators in their work [114], where the use of an upgraded imaging setup yields a sixfold improvement.

5.1.4 In-situ photolithography

Localisation techniques based on in-situ lithography present an approach that is completely different from the ones described so far, as the detection setup is used not only to locate the emitters and characterise their spectral properties, but also to pattern the structures aligned to them. In the case of in-situ photolithography, the experimental procedure is carried out by focusing two different lasers on the surface of a sample mounted inside a cryostat and coated by a layer of photosensitive negative-tone resist (Fig. 5.3b). The QDs are then excited by the first, above-band laser and the emission signal is monitored as the sample is scanned by piezoelectric stages with few-nm resolution. The investigated QD is aligned to the excitation optical path when the maximal intensity is detected. The second, green laser is then directed on the same spot in order to expose the resist and thus prepare a lithographic mask covering the surface above the chosen QD. The sample is then removed from the optical setup and processed through the remaining fabrication steps. When first proposed [118, 119], the described technique allowed the authors to fabricate only circularly-symmetric micro-pillars (Fig. 5.3c), but it has been improved since then and more complex patterns can now routinely be prepared [47, 120, 121].

The ability to locate QDs without the need for alignment markers enables high levels of localisation precision and values of uncertainties as low as 2 nm have been reported [121]. However, the use of photolithography limits the final size of the exposed features to a few µm due to the diffraction limit (see Sec. 3.1) and it is therefore not suitable for the fabrication of nanodevices. Furthermore, planar geometries prepared by means of in-situ photolithography are yet to be reported.

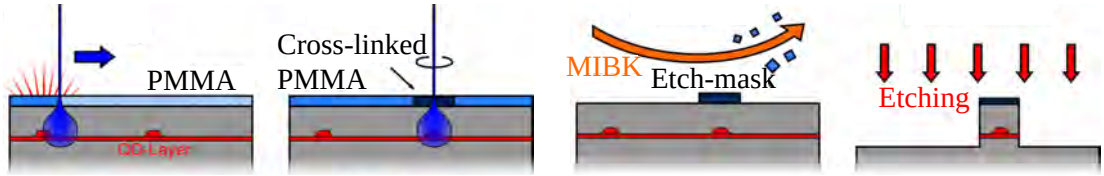

Figure 5.4: Deterministic fabrication of photonic structures by in-situ cathodoluminescence lithography. Sketch of the fabrication process: after mapping the sample by means of cathodoluminescence (panel I), the coated resist is overexposed at the detected position of the chosen QD (panel II). After development (panel III), the overexposed polymer acts as a mask for the subsequent etching step, which transfer the pattern onto the GaAs substrate (panel IV). Adapted from [123].

5.1.5 In-situ cathodoluminescence lithography (CLL)

The resolution limit of photolithography can be overcome by using an electron-beam instead. In this case, the in-situ technique is based on cathodoluminescence (CL), i.e. the luminescence process where emitters are excited by electrons. One of the first experiments where this technique was employed for fabricating photonic devices was reported by Gschrey *et al.* in 2013 [122], where the authors used a modified SEM equipped with a liquid-He cryostat and connected to a spectrometer. As clearly shown by the work flow illustrated in Fig. 5.4, the main difference in the experimental procedure between in-situ photolithography and CLL is the use of an electron-beam for both mapping and exposing the sample. The achieved localisation errors are comparable to the method presented in the previous section, with values between 20 and 30 nm being reported [123–125]. More interestingly, a statistical analysis on the final alignment between QDs and fabricated structures has been reported by Kaganskiy *et al.* in ref. [126], where accuracy levels as low as 34 nm have been demonstrated.

One of the key elements of CLL is the use of different doses for the two steps of the procedure [122]. Low dose is used for the CL mapping in order to excite the QDs without exposing the resist, whereas higher deposited energy is used for the e-beam writing to activate the cross-linking process that produces the negative resist mask. As described in Chap. 3, proximity effects cause reduced resolution of the lithographic process and fine optical structures may result heavily distorted, especially when high electron doses are used. Multiple exposures of an electron-beam on the same area as used for this technique can only accentuate these detrimental effects. As reported by Schnauber and co-workers [127], a thorough calibration process of the experimental parameters helps to achieve some level of proximity correction, but deviations from the designed geometry may still occur and affect the final performances of the fabricated devices.

In conclusion, several techniques exist to locate the positions of self-assembled QDs and fabricate photonic structures at the desired locations. Some of them also offer the possibility to spectrally characterise the emitters, thus enabling the fabrication of tailored devices that show improved optical coupling. Table 5.1 presents a summary of the reported state-of-the-art values of the final uncertainties in detecting the QD positions, along with the alignment error in fabricating devices at the desired locations. Noticeably, Table 5.1 shows that high localisation precision does not always correspond to similar high levels of alignment accuracy between emitters and fabricated structures. Possible causes of this difference may be found in systematic errors introduced during the fabrication process or even in intrinsic limitations of the chosen detection technique. The final alignment accuracy is therefore the relevant figure-of-merit and gives a better comparison between

Technique	Ref.	QD detection uncertainty	Final alignment error
SEM with markers	[107]	n.a.	25 nm (inferred from experiment results)
SEM inspection	[108]	~ 5 nm (post-fabrication)	n.a.
PL raster-scan	[109, 110]	< 5 nm (~ 0.5 nm with SIL)	~ 50 nm (inferred from experiment results)
AFM scan	[111]	13 nm	n.a.
PL imaging	[63, 111–117]	~ 4.5 nm	< 50 nm (inferred from experiment results)
in-situ photolithography	[47, 118–121]	2 nm	> 200 nm (inferred from experiment results)
in-situ CLL	[122–127]	20-30 nm	~ 34 nm (measured)

Table 5.1: Summary of the reported state-of-the-art values of QD position uncertainties and alignment accuracy of the fabricated devices. We note that the value of the final alignment error has been usually inferred from the results of optical experiments performed on the fabricated sample and directly measured only in [123].

the different proposed methods.

5.2 Our approach: modified PL imaging

5.2.1 The developed protocol

For the work presented here, we decided to follow the approach based on photoluminescence imaging [113, 114], since it is a method compatible with our fabrication processes. Also, it can achieve low alignment errors without time-consuming raster-scans and it employs relatively simple optical systems. The workflow we followed is illustrated in Fig. 5.5 and consists of four main steps: first, we prepare a reference frame formed by a regular matrix of metallic crosses, fabricated by means of electron-beam lithography, followed by the deposition of 10 nm of Ti and 90 nm of Au. Fig. 5.6a shows an optical microscope image (in dark-field mode) of the final sample, where two sets of reference markers are visible: the central grid (green box) defines the area investigated for locating QDs, whereas the four large structures that are situated at the corners (orange boxes) are the registration markers needed for aligning the lithographic layers necessary for the fabrication of nanostructures. A close-up view of each of the squares forming the central grid is in the SEM image in Fig. 5.6b, where the reference crosses are visible, along with their

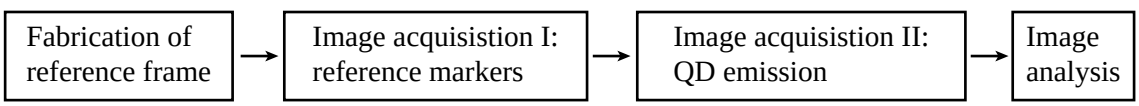

Figure 5.5: Workflow of the localisation technique developed in this work.

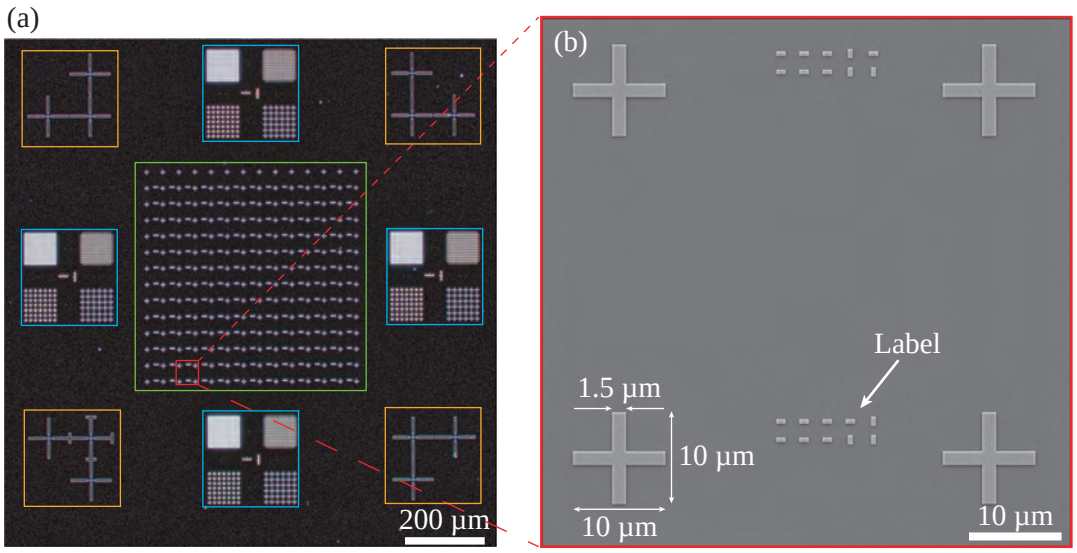

Figure 5.6: Reference frame for the µPL method developed during the work for this PhD project. (a) Optical microscope image, acquired in dark-field configuration, of a typical sample prepared for the localisation technique. The macroscopic features constituting the fabricated mask are visible: the grid of reference markers in the center (green box), the structures used for aligning different layers during e-beam lithography and placed at the corners of the image (orange boxes) and the regular grids used to study the distortion level of the acquired images (light blue boxes). (b) SEM image of one of the areas investigated to locate the QDs. The four reference crosses are visible, together with the binary code used for labelling the square. The dimension of the reference markers are also reported.

dimensions.

The sample is then mounted in a µPL setup (sketched in Fig. 5.7a), which consists of a closed-cycle cryostat (Montana Instrument Cryostation) that contains three piezo-stages (Attocube Systems AG) and a microscope objective (Olympus LCPLN100XIR) inside the vacuum space. The temperature is kept at $T \approx 10\,\mathrm{K}$ in every step of the image acquisition. A 780-nm diode laser (Thorlabs) is coupled to the objective through a 10:90 (reflection:transmission) beam-splitter (BS) and provides the light to illuminate the sample surface. After moving the sample into focus, the collected signal is sent to a CCD camera (Andor iKon-M, with a 13.3 x 13.3 mm^2 sensor formed by 1024 x 1024 active pixels), positioned such that a surface area of about 60 µm x 60 µm is visible, i.e. each pixel corresponds to a region on the sample of about 59 nm in size. Furthermore, a wide-field (WF) lens is used in the excitation path in order to focus the laser onto the back focal plane of the objective and thus achieve a large illumination area covering the whole square shown in Fig. 5.6b.

The acquisition procedure we developed consists of two steps, which are summarised in Fig. 5.7: first, the reference crosses are imaged and pictures like the one in Fig. 5.7b are collected. Then (Fig. 5.7c), a narrow bandpass filter (BP, FWHM = $935\,\mathrm{nm} \pm 0.5\,\mathrm{nm}$) is placed in the collection path to block the signals from both the GaAs ($\lambda_{GaAs} \approx 820\,\mathrm{nm}$) and the wetting layer emission ($\lambda_{WL} \approx 860 - 880\,\mathrm{nm}$, [128]), while letting the light from the QDs through, as depicted in Fig. 5.7d. In fact, the narrow bandwidth of the filter has also the advantage of stopping most of the inhomogeneous emission typical for this type of emitters (see Chap. 2) and hence is used to select just a small part of the full QD ensemble.

Image analysis algorithms are then used on each image to locate the centers of the markers and of the QDs, respectively. The final positions are finally correlated to find the coordinates of the emitters with respect to the reference frame, an operation made possible by the fact that the stage was not moved in between the acquisition of the two images and the employed integration time was short enough to prevent any relevant drift of the system (typically 1 s for the reference frame and 1 to 10 s for the QDs image). Since the relative distance between the e-beam registration markers and reference crosses is defined by the lithography, the locations of the emitters detected in each square can be rigidly translated into absolute coordinates that can be used for the deterministic fabrication of the photonic nanostructures at the QD positions.

The proposed method is in many aspects similar to the typical procedures based on PL imaging reported in literature, but it presents one very important difference: we use photoluminescence, and not reflection, to image the alignment markers. The reason behind this choice is sketched in Fig 5.8 and is related to the fact that the angle at which light is reflected from the golden reference crosses is dependent on the angle of the incoming light. As small misalignment angles are unavoidable, the position of the markers detected on the image plane will likely be misplaced with respect to the real one, thus introducing a detection error that eventually lowers the final alignment accuracy. We tested this by monitoring the positions of 4 QDs over time and after purposely misaligning the LED light source [129]. The results of these tests are presented in Fig. 5.8 and show that offsets of up to $\approx 150\,\text{nm}$ can be detected, especially when the optical setup is aligned again after exchanging the investigated sample (cf. QDs number 3 and 4). In order to avoid such large errors, we implemented an illumination protocol based on the photoluminescence from the substate, corresponding mainly to the emission from the GaAs bandgap.[a] This new illumination method is operationally achieved by placing a 800-nm long-pass filter (LPF) in the collection path, which blocks the reflected radiation from the above-band excitation laser but lets the fluorescence signal from the sample pass through. As sketched in Fig. 5.8b, in this configuration the emission originates from the material, resulting in an illumination that is independent from the angle of the incoming excitation light and, most importantly, always normal to the sample surface. This new implementation therefore ensures that the detected images always coincide with the real positions of the reference markers, which are now formed by dark crosses on a bright background since the metal blocks the GaAs emission (as shown in Fig. 5.7b).

5.2.2 Further considerations on setup and sample designs

Whilst the different choice on the light source is the main distinction and improvement compared to other localisation methods based on PL imaging, other aspects of the employed optical setup and designed samples have been analysed and optimised. The resulting considerations will be discussed in the following pages.

Design of the reference grid

The design of the reference markers is an important part for the correct detection of their position. In terms of shape, the markers have to be easily recognisable in the acquired images and yet present simple geometries to facilitate the analysis algorithm. Furthermore, the size of their features have to be well-above the value d_{DL} set by the diffraction limit

$$d_{DL} = \frac{\lambda}{2 \cdot \text{NA}} \tag{5.1}$$

[a] The contributions from wetting layer and QDs are of course also present, but hidden by the much more intense emission from the GaAs bandgap.

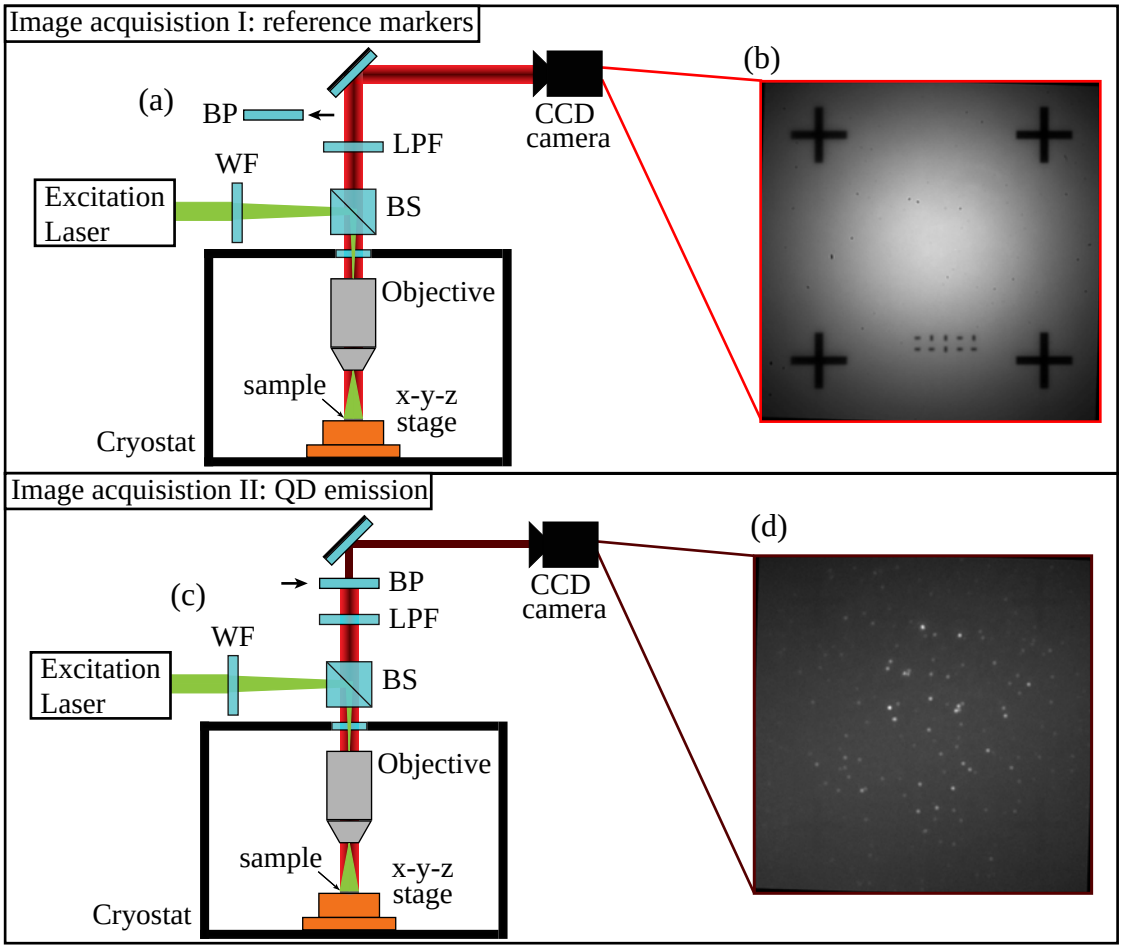

Figure 5.7: Schematic representation of the optical setup and the operational steps of the developed location technique. (a) After fabrication of reference markers, the sample is mounted in a close-cycle cryostat customised with three piezo-stages and a microscope objective mounted inside the vacuum chamber. An above-band excitation laser is coupled via a 10:90 beam-splitter (BS) to the objective, while a wide-field lens (WF) focus the beam onto its back focal plane in order to illuminate a wide area of the sample. The fluorescence from the substrate is then collected into a CCD camera, after passing through a long-pass filter (LPF) that blocks the reflected radiation of the excitation laser. (b) The acquired images of the reference markers, consisting in four dark crosses and a bright background. (c) The imaging of the QDs is performed by placing a narrow band-pass filter (BP) in the collection path, which blocks all the fluorescence signal from the GaAs bandgap while letting through the light emitted from the QDs. (d) In the collected images, the QDs are visible as bright spots on a dark background.

where NA is the numerical aperture of the collection lens. In our experiments, where we used a microscope objective with NA = 0.85 and wavelengths ranging between 820 nm and 950 nm, eq. (5.1) gives values in the range $d_{DL} \approx [482;559]$ nm, which corresponds to about 9 pixels of the field-of-view (FoV). Different designs have been tested, but the simple four-armed crosses shown in Fig. 5.6b resulted in the best choice to easily fulfil the aforementioned requirements. Furthermore, the chosen dimensions (line width = 1.5 µm and total length = 10 µm) offer a good compromise between resolvable features and leaving enough space available for the fabrication of

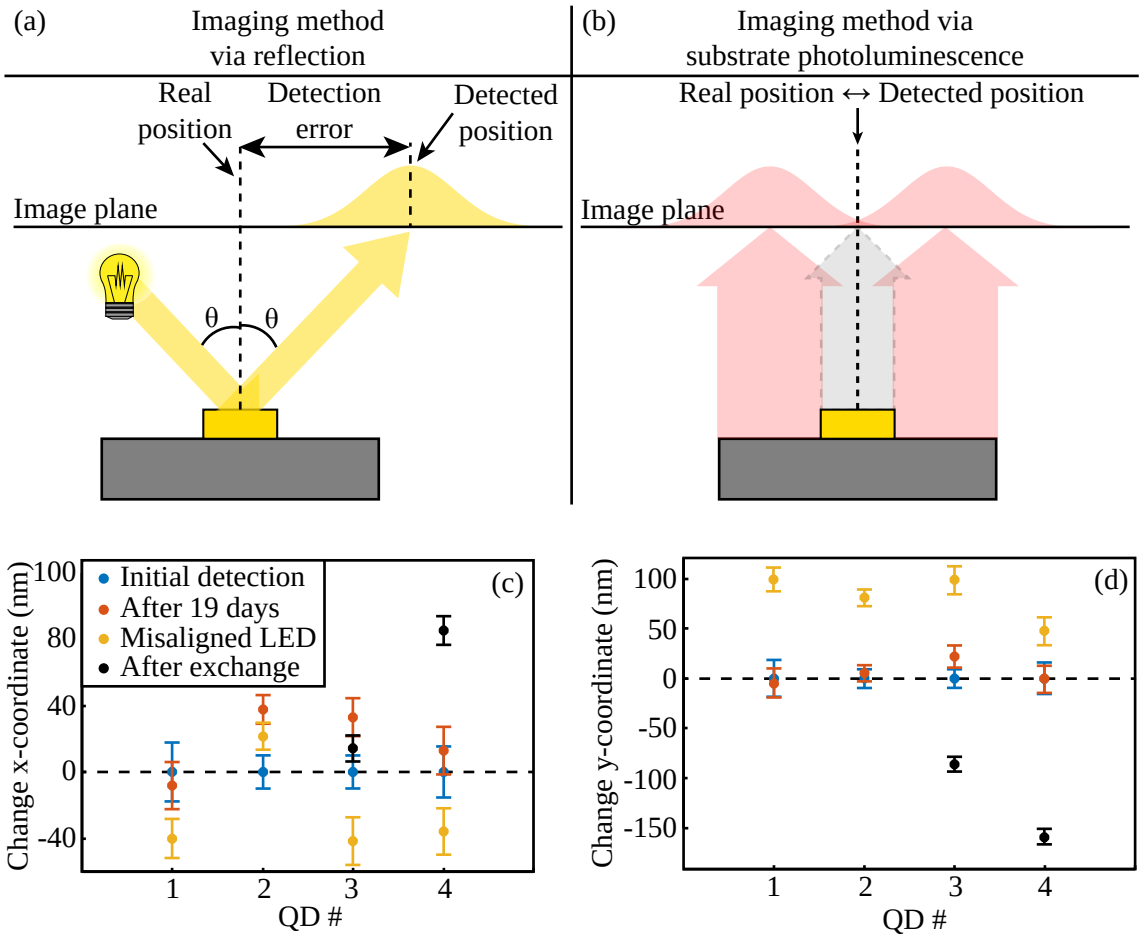

Figure 5.8: Effects of the illumination method on the detected positions. (a) When the acquired image is generated by reflecting the excitation light, small angles θ in the incoming radiation cause a shift in the position of the detected features. (b) In the case when the substrate photoluminescence is used as light source, no detection error is present because the illumination is always normal to the surface of the sample. Change in the (c) x- and (d) y-coordinates of QD locations measured relative to markers for different positions of the light source. (c) and (d) adapted from [129].

nanostructures, especially for the large ones, such as photonic crystal waveguides.

Fig. 5.6a shows an example of the typical grid of reference markers investigated throughout this project, which consists of 13 rows by 13 columns, i.e. 169 squares to analyse for locating QDs. It is therefore important to use labels to avoid mistakes in identifying the area under study at any given time. The considerations for the marker design are of course also valid for the labels. Instead of the alphanumeric name typically used [113–116], we decided to use a binary code to identify the row and column number. An example of the employed labels is visible in Fig. 5.6b and it is formed by a series of golden boxes with dimensions 0.5 µm x 1 µm and oriented along different directions: the rectangles extending horizontally identify the character "0", while the vertical ones correspond to "1". Following these rules, for example, the square shown in Fig. 5.6b is labeled "00001, 00011", corresponding to "Row 01 (upper line of the label), Column 03 (lower line)". Once again, the choice of location and size makes these structures large enough to be easily detectable and identifiable in each acquired image (cf. Fig. 5.7b), without using up too much space on the surface of the sample.

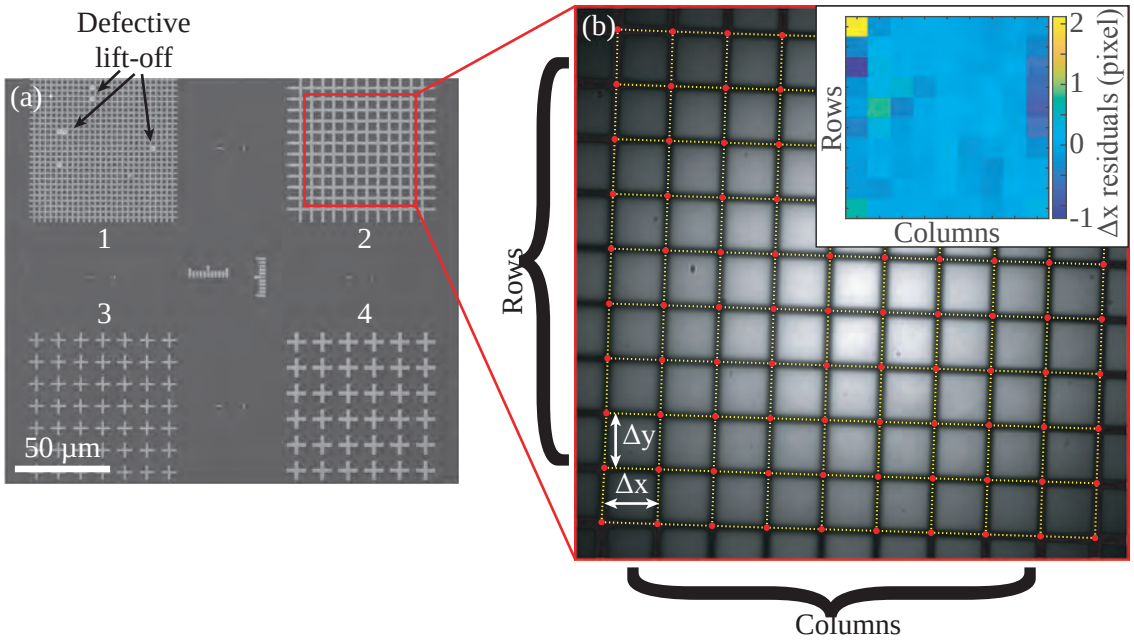

Figure 5.9: Structures used for distortion analysis. (a) Overview of the four different fabricated patterns: structures 1 and 2 consist of regular grid of straight lines, whereas structures 3 and 4 are regular matrices of crosses. The redundancy present in the mask enables the distortion analysis also in presence of debris left from the fabrication process. (b) Analysed image of structure 2. Each intersection between lines has been detected and marked with a red dot. Yellow dotted lines represent linear fits of each row and column of the grid. Inset: Coloured map of the calculated local deviations of the distance Δx from the average value.

Distortions and aberrations

As already mentioned in Sec. 5.1.3, the main source of errors for the type of detection procedure presented in this work consists of the distortions produced by the optical aberrations affecting the optical system. Small surface imperfections in the components of the imaging setup are the main origins of such anomalies, which therefore cannot be completely removed. However, the distortions they cause on the recorded images can be corrected if the real geometry of the depicted structure is known. In order to analyse these effects in our setup, we implemented a series of grids of different shapes, of which four copies were always fabricated on the sample along with the reference grid (light blue boxes in Fig. 5.6a). Fig. 5.9a shows an SEM image of the chosen geometries, which consist of a couple of grids of solid lines (structures 1 and 2) and two regular matrices of crosses (3 and 4). Despite the different constituting elements, each structure can be inscribed in a square with an edge of 80 µm, thus ensuring that they fill completely the FoV of our CCD camera and allowing for a thorough study of the entire imaged area. Moreover, even though we focused on only one of these grids in each investigation, the presence of many copies makes sure that the distortion analysis can also be performed in the presence of imperfections introduced by the fabrication process, like the debris left by a defective lift-off shown in Fig. 5.9a.

The most commonly used grid is that identified by number 2 in Fig. 5.9a. It is formed by lines with a width of 1 µm and separated by 5 µm. The resulting distance between the centers of consecutive lines is $\Delta x = \Delta y = 6\,\mu m$, for both columns and rows respectively. The presence of any distortion in the recorded image can then be detected by locating the center of each intersection to

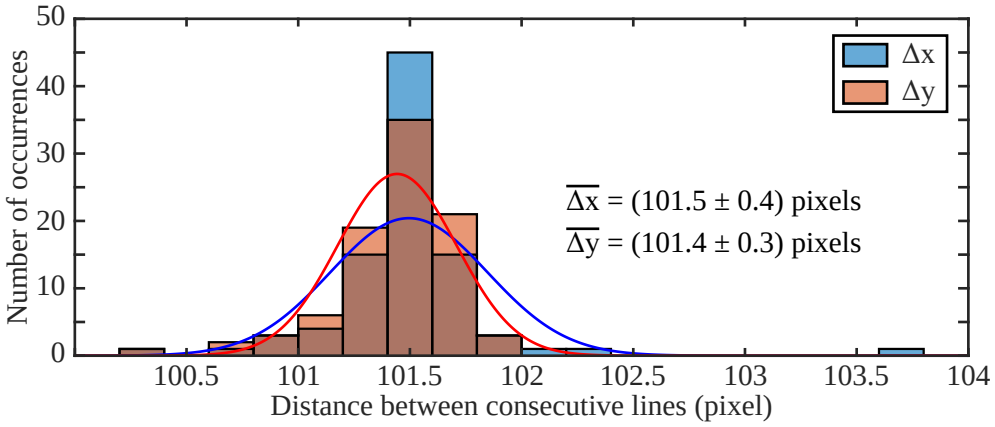

Figure 5.10: Histogram of the calculated distances between consecutive intersections of the lines constituting the grid for distortion analysis. The fitted normal distributions along with the calculated mean values and standard deviations are also shown.

calculate the values of Δx and Δy and compare them with the designed one. Fig. 5.9b shows an example of an image we typically acquire for this study, where each intersection has been located[b] and marked by a red dot. The inset in Fig. 5.9b reports a coloured map of the resulting Δx residuals, i.e. the difference between the average line separation $\overline{\Delta x}$ and each calculated Δx (similar maps can be built for Δy). The plot shows that large deviations from $\overline{\Delta x}$ are mainly found at the edges of the FoV, suggesting that the reference crosses should be positioned towards the central area of the image to ensure higher accuracy. Based on similar findings from other investigated samples, we designed the reference grid with crosses that are 40 µm apart (distance center-to-center), i.e. about 10 µm from each edge of the FoV. We further investigated the effects of aberrations by calculating the mean values and the standard deviation of the calculated values of Δx and Δy. As shown by the histogram plotted in Fig. 5.10, $\overline{\Delta x}$ and $\overline{\Delta y}$ well overlap within the errors and hence we can safely assume that no large spatial distortions can be measured in the images we proceed to acquire for QD localisation purposes.

Effects of the band-pass filter

In the presented localisation method, the acquisition of the two different types of images (i.e. QDs and reference markers) is made possible by flipping a narrow band-pass filter in and out of the collection path. Such a movable component may introduce an offset in the collection path and hence introduce a systematic displacement between the detected position of markers versus emitters. We therefore set out to characterise the effects of the BP filter and we did so by comparing positions of QDs located with and without the optical element placed in the collection path (for this test, a 900-nm long-pass filter was used instead of the 800-nm one in order to block out the intense emission from GaAs bandgap and wetting layer [129]). The histograms of the changes in both x- and y-coordinates of the detected QD positions are shown in Figs. 5.11a and b, respectively, and mean values and standard deviations were extrapolated by fitting a Gaussian distribution to both datasets. As presented in Fig. 5.11, the measured offsets are randomly distributed around zero, with mean values of 0.09 pixels (corresponding to ≈ 5.4 nm) and -0.02 pixels (≈ −1.2 nm) for x- and y-coordinates, respectively. The standard deviations were found to be just below 30 nm (i.e.

[b] We located the center of each intersection by employing the same algorithm that was used to identify the center of the reference markers. We refer the reader to the next section for a detailed description of it.

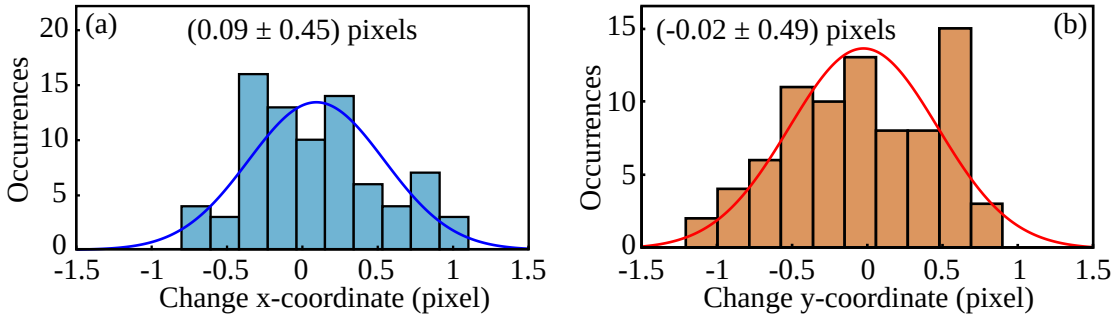

Figure 5.11: Detected change of (a) x- and (b) y-coordinates caused by the presence of the band-pass filter placed in the collection path. The fitting normal distributions along with the calculated mean values and standard deviation are also shown. Adapted from [129].

about 0.5 pixels) for both datasets, which is a value smaller than the alignment errors presented in Table 5.1 and which can therefore be deemed acceptable for our application.

To further improve the final accuracy, we developed another localisation protocol that makes use of the ability to electrically control the photoluminescence of QDs. When embedded in a p-i-n diode, in fact, the QD emission can be "switched ON and OFF" by applying a voltage across the sample. Such an effect is caused by the built-in field across the structure (cf. Chap. 2) that results in high probability for the photo-generated carriers to tunnel out from the QDs, which then produce no emission. By applying a bias voltage to the sample, however, the energy bands can be tilted and the tunnelling rates reduced, thus increasing the radiative recombination probability of the carriers [130]. We exploited this effect to image the references crosses and the QDs independently, without the use of the band-pass filter. The improved protocol is based on the same two-step imaging procedure previously described. A 900-nm long-pass filter is placed in the collection path to block the strong emission from the GaAs bandgap and hence the illumination for the images with reference markers is now provided by the emission from the wetting layer, which presents a tail end at wavelengths longer than the filter cut-off. The switch between the two types of collected images is performed by tuning the applied voltage V, with the reference markers imaged at $V = 0\,\mathrm{V}$ and the QDs becoming visible at $V = 0.5\,\mathrm{V}$. No changes are necessary in the image analysis algorithm. Even though the images collected with the new modified protocol present a slightly lower signal-to-noise ratio that causes a small decrease in the overall detection precision (as we will present in the following pages), the final alignment accuracy may benefit from the removal of a moveable optical element that causes a systematic shift.

5.3 Image analysis procedure

Along with the imaging setup, the core of the localisation protocol developed during this PhD project consists of the algorithm used to perform the image analysis and detect the centers of reference markers and QDs. The code that is at the heart of the localisation method has been written in MATLAB and built in such a way that it can be run to automatically analyse batches of images. Any type of sample can be investigated, given that the requirements previously discussed have been fulfilled. In this section the main parts of the procedure will be described and the final results for the achieved detection precision will be presented for two different samples, one having QDs growth at the center of a membrane of intrinsic GaAs and one with the emitters embedded

in a p-i-n diode (hereafter, these two samples will be denominated undoped and doped sample, respectively).

Step 1: Background and image correction

The first step of the analysis algorithm consists of applying corrections to the acquired images in order to prepare them for the subsequent analysis. Distortion correction is performed at this stage in order to remove any possible artefacts from the images. The analysis on the effects of aberrations in our imaging system has shown that advanced procedures are not necessary, but we can still improve the quality of the images by performing the following steps.

Fig. 5.12a shows a typical example of a camera image of the reference markers. Two main features are noticeable: (i) the spatial non-uniformity of the background intensity and (ii) the wrong orientation of the reference grid, as indicated by the position of the binary label (cf. Fig. 5.6b). Both effects are ascribed to the optical elements in our setup; the Gaussian profile of the excitation

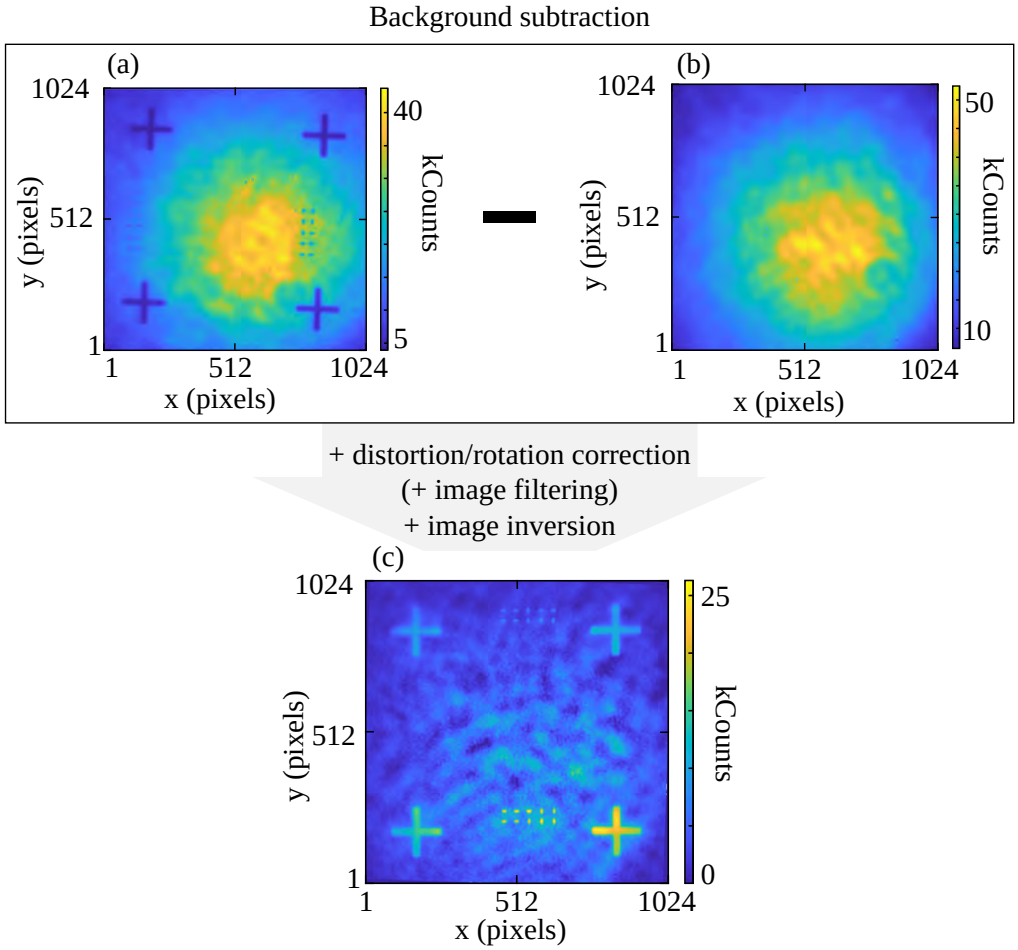

Figure 5.12: Schematic representation of the first step of the analysis algorithm. The acquired raw image (a) presents a background with a non-uniform intensity distribution, which can be corrected for by subtracting the average over 5 images of the sample surface with no visible structures (b). (c) Final intensity map of the square under investigation, after rotation correction and image inversion. If necessary, image filtering can also be performed.

beam results in a Gaussian distribution of photoluminescence intensity of the substrate and the lenses and mirrors placed in the setup flip and rotate the final image collected at the CCD camera. We solve these issues by implementing two different steps in the developed code: first, the background correction is performed by subtracting a background image, obtained by averaging over 4-5 images of different areas of the sample where no fabricated structures are visible (cf. Fig. 5.12b). To achieve the best results, it is important that these reference images are acquired by using the same parameters (e.g. excitation power and integration time) as the ones used for the crosses. The background-corrected images are then mirrored and rotated in order to obtain the real orientation of the reference square. The analysis of the distortion grids provides an estimate of the rotation angle, which is obtained by a linear fit of the detected intersection centers for both rows and columns (indicated as yellow dotted lines in Fig. 5.9b). Finally, the colours of the rotated image are inverted to generate an intensity map with bright features on a darker background, which facilitates the image analysis. The final result of this first main step is shown in Fig. 5.12c. From our experience, a signal-to-background ratio of about 500 is already enough for obtaining nm-level precision in the final detection of the QD locations.

Step 2: Analysis of reference crosses

The corrected image (reproduced again in Fig. 5.13a) is now ready for the analysis to locate the center of the reference markers. Each cross is then cropped from the image and studied independently by following the procedure schematically illustrated in Fig. 5.13. The considerations behind the developed algorithm are similar to the ones used in raster-scanning techniques, i.e. higher final detection precision is possible by performing multiple scans of the same object. This is implemented in the present procedure by fitting multiple cross-sections of each arm of the marker. By doing so, their central axis can be found and therefore also the center of the cross (x_{Xc} , y_{Xc}), calculated as the intersection of each arm.

Fig. 5.13c plots the values of collected intensity along the red line marked in the cropped image shown in Fig. 5.13b and is a typical cross-section for any of the rows or columns. Even though the background correction causes some fluctuations at both ends of the cross-section, the signal corresponding to the arm of the cross is clearly visible as a central wide peak and can be fitted with the function [131]

$$y(x) = A \cdot \frac{\operatorname{erf}\left(\sqrt{\frac{1}{2\sigma}}\left(x_{c,i} - \frac{d}{2} - x\right)\right) - \operatorname{erf}\left(\sqrt{\frac{1}{2\sigma}}\left(x_{c,i} + \frac{d}{2} - x\right)\right)}{\operatorname{erf}\left(\sqrt{\frac{1}{2\sigma}}\left(-\frac{d}{2}\right)\right) - \operatorname{erf}\left(\sqrt{\frac{1}{2\sigma}}\left(\frac{d}{2}\right)\right)} + B \cdot x + C. \tag{5.2}$$

The fitting function in eq. (5.2) is the result of the convolution between a one-dimensional Gaussian $g(x) = \exp\left(-x^2/2\sigma\right)$ and the rectangular function $\Pi(x)$

$$\Pi(x) = \begin{cases} 1, & -\frac{d}{2} \leq x \leq \frac{d}{2} \\ 0, & x > \left|\frac{d}{2}\right|, \end{cases} \tag{5.3}$$

with d the designed value of the arm width. Furthermore, in eq. (5.2), $\operatorname{erf}(x) = \frac{2}{\sqrt{\pi}} \int_0^x e^{-t^2} dt$ is the error function, the parameter A is the amplitude of the fitting function, while the linear term $B \cdot x$ and the constant C account for any spatial-dependent background contribution that was not completely removed during the first step of the analysis procedure. The central position of the arm in the ith cross-section $x_{c,i}$ is evaluated as one of the fit parameters in eq. (5.2) and its uncertainty is calculated as half of the 95.4% confidence interval (i.e. 2 standard deviations) calculated from the fit.

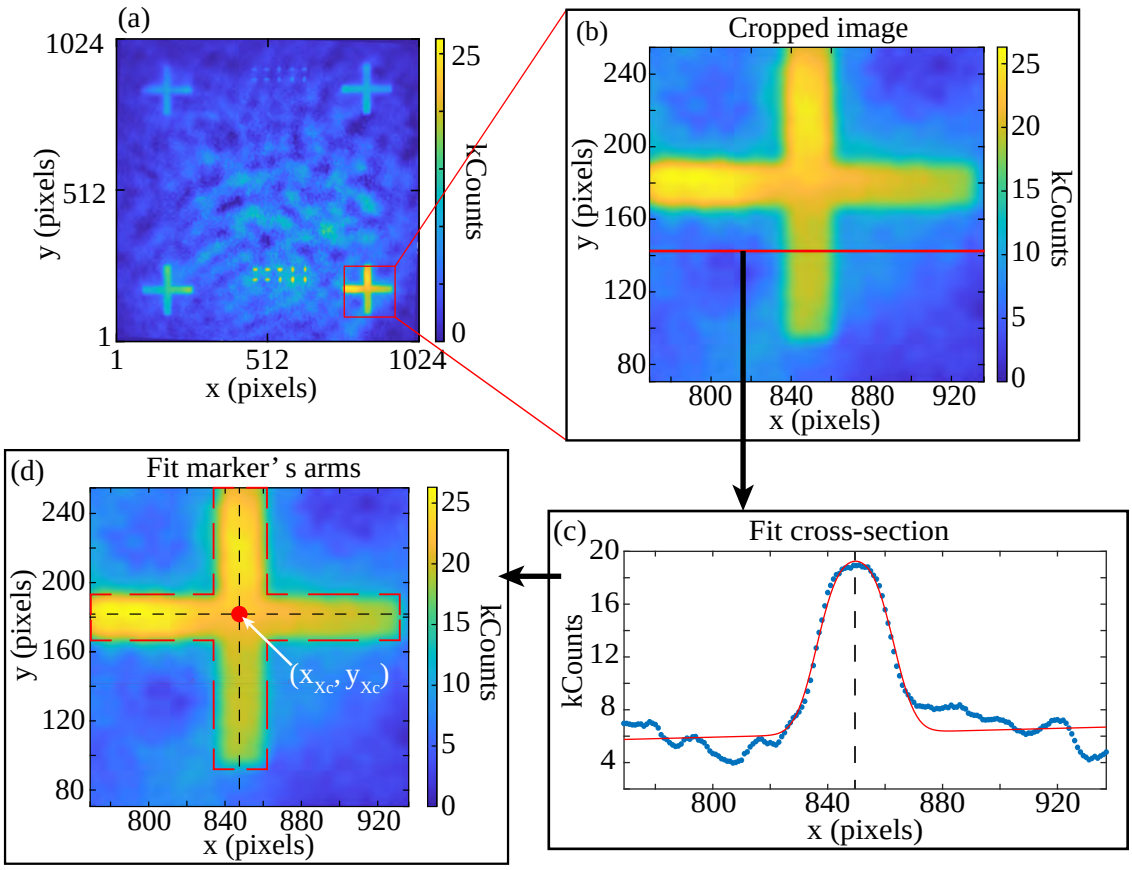

Figure 5.13: Schematic illustration of the procedure to detect the center of the reference markers. (a) Corrected image, starting point of the analysis. (b) Cropped area around one of the reference crosses. The red line marks one of the horizontal cross-sections fitted to find the x-coordinate of the center of the marker. (c) Plot of the detected counts along the pixels marked by a red line in (b). The blue dots show the data, while the red curve indicates the result of the fit performed to extrapolate the value of center $x_{c,i}$ (indicated by the black dashed line). (d) The coordinates (x_{Xc} , y_{Xc}) of the marker center (red dot) are evaluated by linearly-fitting all the values of $x_{c,i}$.

The fitting routine is looped for each cross-section in the selected regions of the cropped image, resulting in a series of different values for $x_{c,i}$. The final coordinates x_{Xc} and y_{Xc} are then obtained from the weighted average of the evaluated $x_{c,i}$, calculated over the analysed rows and columns respectively. Thanks to the initial rotation correction of the image, the reference cross is aligned to the axes of the intensity map and therefore averaging over all the relevant cuts correspond to a linear fit of each of the marker's arm (Fig. 5.13d).

Repeating the full fitting procedure for each of the four markers allows one to find the coordinates of their centers, expressed in terms of pixels of the image. This unit is however not useful for the alignment of different lithographic steps and it is therefore converted into µm, a trivial operation as both designed and imaged values of the markers locations are now known. In the same step, moreover, the origin of the reference frame is translated to the center of the lower-left cross in order to give a more realistic view to each map. The final result for the analysis of the reference crosses is shown in Fig. 5.14a, where the red dot marks the detected center position of the marker, expressed in real units of length.

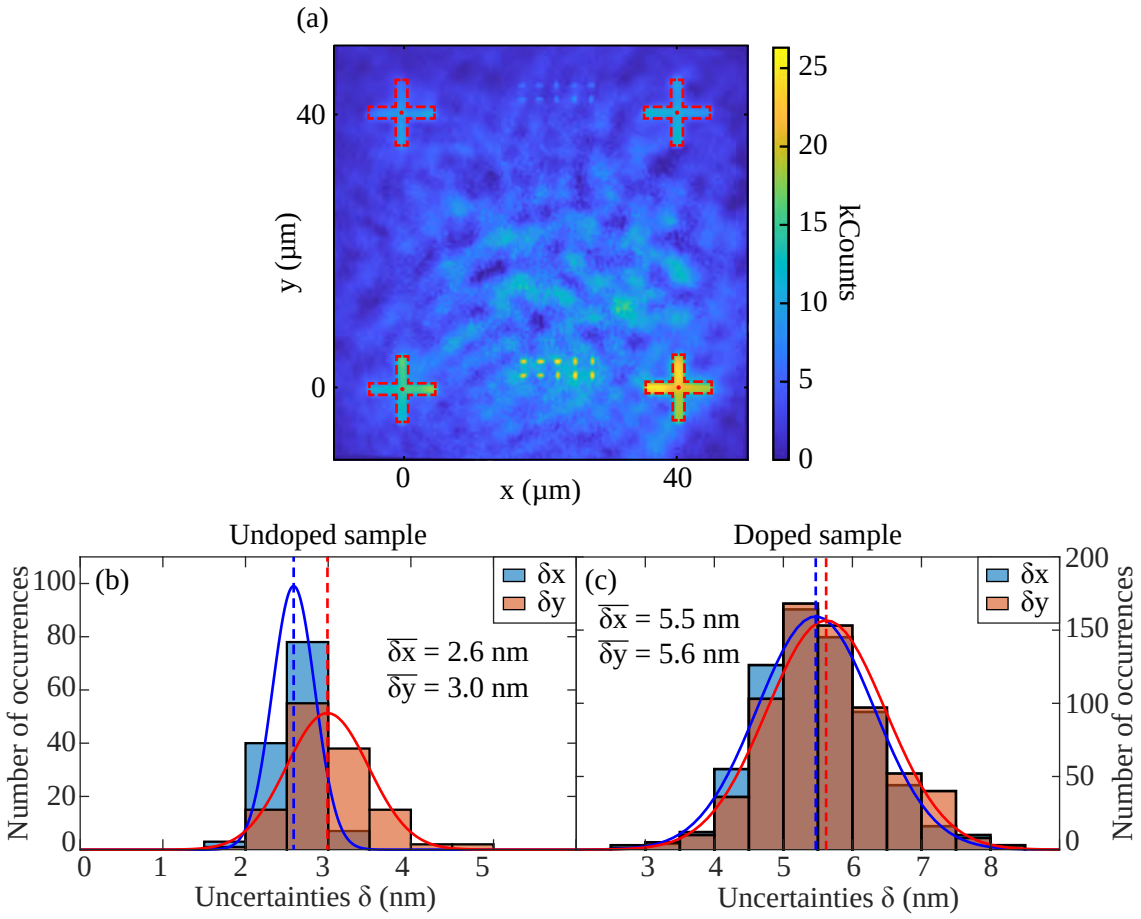

Figure 5.14: Results of the procedure to locate the reference markers. (a) Analysed intensity map with the detected positions of the crosses marked by red dots. (b) Histograms of the evaluated uncertainties of the x- and y-coordinates of the markers positions on the undoped sample. The fitted normal distributions and evaluated mean values are also reported. (c) As in (b), but for the doped sample.

The final uncertainties on the detected positions (δx and δy) are calculated by propagating the values obtained from the cross-section fits. The histograms in Fig. 5.14b and Fig. 5.14c report the distributions we obtained on the two types of sample under investigation. Markers on the undoped sample (Figs. 5.14b) have been located with uncertainties ≤ 3 nm for both x- and y-coordinates, whereas the locations found on the doped sample (Figs. 5.14c) present a slightly lower level of precision. This difference is probably caused by the different illumination method used in the latter case, which results in a lower signal-to-background ratio. Nonetheless, the values of the final detection errors are still comparable with state-of-the-art PL imaging techniques [114].

Step 3: Analysis of QDs

The third main part of the analysis algorithm concerns the QD positions and starts with the correction of any rotation (and, if necessary, also distortion) in the second type of acquired images (Fig. 5.7d). It is important to use the same operations as performed for the analysed image of the corresponding reference markers, in order to maintain spatial overlap between the two maps. No

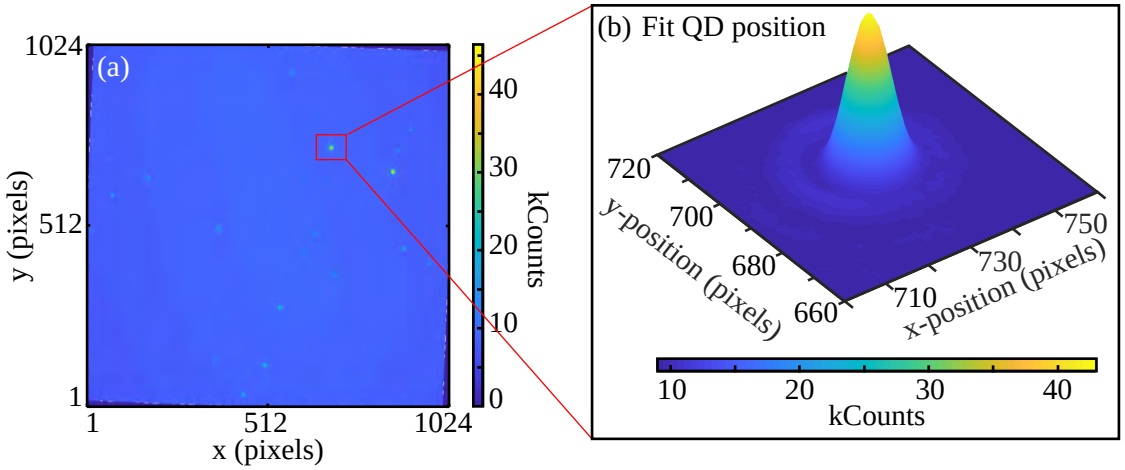

Figure 5.15: Camera images analysed to determine the QD locations. (a) Acquired image after rotation correction. The QDs appear as tiny bright spot on a uniform dark background. (b) Surface plot on one of the cropped region-of-interests fitted to evaluate the coordinates of the emitter center.

background correction is necessary as it is already blocked by the LPF, as visible in the intensity map shown in Fig. 5.15a. The image under analysis is then thresholded[c] and filtered in order to remove QDs that are too dim and too close to the edges of the FoV. A selection of the regions-of-interest (ROIs) is performed to limit the detection analysis to only bright spots that are well separated and have reasonable dimensions when compared to the diffraction limit expressed in pixels (usually, between 10 and 20 pixels in diameter). Each ROI is centred at the centroid of the selected spot.

Fig. 5.15b shows an example of the intensity distribution of the QD luminescence in each ROI. As expected from emitters with dimensions smaller than the diffraction limit, the pattern of the detected emission can be described by an Airy disk and, in the cases of in-plane dipoles parallel to image plane, the location of the point source correspond to the position of the detected maximum [133]. Since these requirements are fulfilled by the QDs in our samples, the coordinates of their location (x_{QD}, y_{QD}) can be found by fitting each ROI with a two-dimensional Gaussian, which approximates the Airy pattern fairly well and has the functional form

$$g_{2D}(x,y) = A \cdot \exp\left(-\left(\frac{(x-\mathrm{x_{QD}})^2}{2\sigma_x^2} + \frac{(y-\mathrm{y_{QD}})^2}{2\sigma_y^2}\right)\right) + B\cdot x + C\cdot y + D, \tag{5.4}$$

where A corresponds to the maximum intensity in the ROI and the two linear terms $B\cdot x$ and $C\cdot y$ and the constant D account for the background. The parameters σ_x^2 and σ_y^2 are the standard deviations of the 2D Gaussian along the x- and y-direction respectively, and are in general considered not equal as small asymmetries may be present.

The uncertainty on the detected location of the QD center can be estimated more precisely than by just halving the confidence interval calculated from the fit, if the point spread function describing the fitted intensity distribution and the pixel width are know, as discussed in [133]. In the reported work, the authors proposed a more reliable formula for the variance of the detected

[c]Thresholding is an operation used in digital image processing where pixels below (above) a set threshold value of intensity are replaced by black (white) pixel [132].

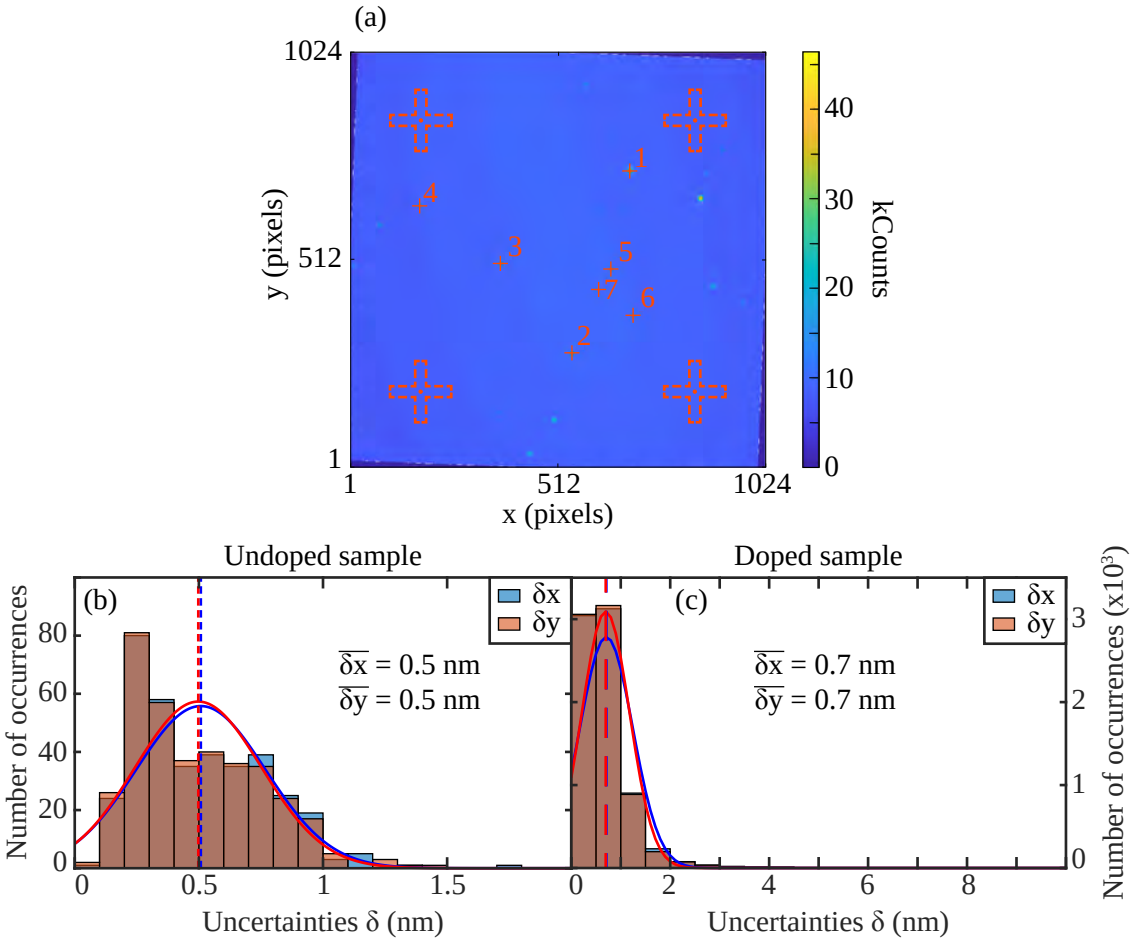

Figure 5.16: Results of the procedure to locate the QDs. (a) Analysed intensity map with the detected QD locations marked with red crosses. The emitters are also numbered from the brightest to the dimmest. (b) Histograms of the evaluated uncertainties of the x- and y-coordinates of the QD locations on the undoped sample. The fitted normal distributions and evaluated mean values are also reported. (c) As in (b), but for the doped sample.

positions of single-molecules, which reads

$$\sigma^2_{tot,x} = \frac{\sigma^2_{a,x}}{N}\left(\frac{16}{9} + \frac{8\pi\sigma^2_{a,x}b^2}{Na^2}\right), \tag{5.5}$$

where the subscript x indicates that it is calculated for the x-coordinate, but the same functional form can be used for the y-coordinate as well. In eq. (5.5), $\sigma^2_{a,x} = \sigma^2_x + a^2/12$, where a^2 is the pixel area. Since the investigated intensity distribution is written in terms of pixels, we set $a^2 = 1$. The parameter N describes the total number of photons emitted by the QD and corresponds to the volume under the 2D Gaussian, i.e. $N = 2\pi A\sigma_x\sigma_y$. Finally, the variable b^2 indicates the background level of the analysed region, which can be set to $b^2 \approx D$ as the linear terms of the fit are usually much smaller than the constant value. As all the parameters in eq. (5.5) are known, the uncertainty on the detected QD location can be calculated as $\delta x = \sqrt{\sigma^2_{tot,x}}$.

The two-dimensional fitting routine is repeated for all the selected ROIs and the coordinates of all the QD centers are thus found and marked on the analysed image, as shown in Fig. 5.16a,

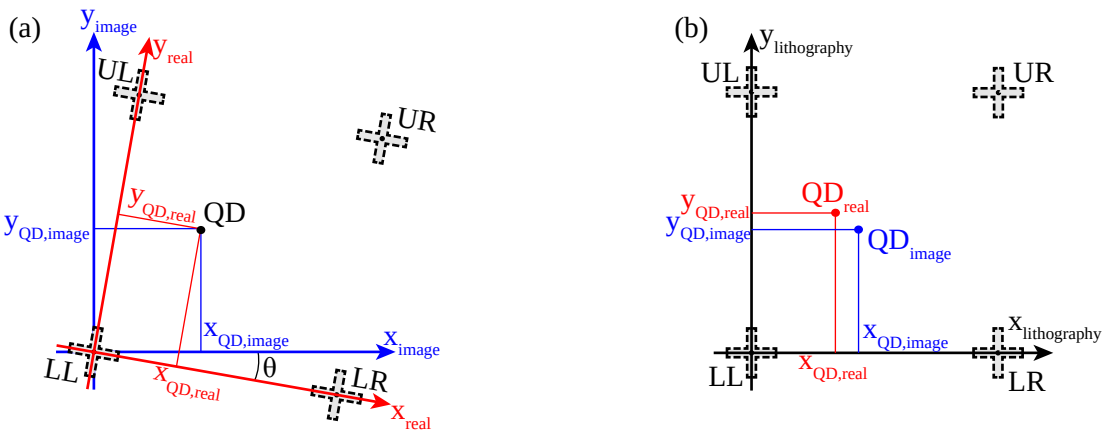

Figure 5.17: Schematic illustration of the effect of rotation angles between the image and the real reference frame. (a) The coordinates of the QD locations evaluated from the 2D Gaussian fits are based on the reference frame of the image (blue). If the real frame formed by the crosses (red) is not aligned to the image, the true coordinates differ from the detected one. (b) The erroneous set of coordinates found from the image analysis leads to the fabrication of the devices at the wrong position. In both images, the labels of the crosses help to identify them: LL = lower-left, LR = lower-right, UL = upper-left and UR = upper-right.

where the located emitters are also numbered from the brightest to the dimmest. A statistical analysis of all the calculated uncertainties shows that the average value is $\leq 0.7\,\text{nm}$ for both doped and undoped samples, as illustrated in Figs. 5.16b and c. Such low error is an order of magnitude smaller than the value reported in current state-of-the-art techniques [114], which can be achieved thanks to the higher signal-to-background ratio possible with the 2-steps acquisition approach we developed.

Step 4: Correlating QD image to reference markers

The coordinates of the QD positions resulting from the fitting routine performed in the previous step are defined in terms of pixels and with respect to the lower-left corner of the FoV. Similar to the markers, a conversion of units is required in order to use the QD locations for the deterministic fabrication of photonic nanostructures. Therefore, the coordinates of the QD centers calculated in the reference frame of the image ($x_{QD,image}$, $y_{QD,image}$) must be translated into the real reference frame of the sample ($x_{QD,real}$, $y_{QD,real}$). Such transformation has to be cautiously performed to avoid any introduction of systematic errors that will lower the final alignment accuracy. In general, simple rigid translations along the x- or y-direction are not enough because small rotation angles may exist that could cause a large final misalignment, as illustrated in Fig. 5.17. In fact, when the two reference systems are rotated by an angle θ, the coordinates found from the fitting routine (in blue in Fig. 5.17a) do not correspond to the ones measured in the frame of the crosses (in red), even when the origins of the two sets of axes overlap. During the preparation of the subsequent lithographic layers (Fig. 5.17b), the erroneously detected locations of the emitters will cause alignment errors with respect to the fabricated devices. For example, with $\theta = 1°$, a QD detected at $x_{QD,image} = 5\,\mu\text{m}$ is actually located at $x_{QD,real} \approx 4.913\,\mu\text{m}$ with respect to the reference cross, an error along the x-direction of $\approx 87\,\text{nm}$.

A rotation correction in the investigated images is already implemented as one of the first steps of the analysis algorithm, but it provides only a coarse adjustment as its main purpose is to

align the arms of the crosses to the axes of the intensity map. A finer correction is subsequently implemented when the coordinates of the QDs are mapped to the fabricated markers and it is operationally achieved by performing the following geometrical transformation

$$\begin{aligned}\begin{pmatrix} \mathrm{x}_{\mathrm{QD,real}} \\ \mathrm{y}_{\mathrm{QD,real}} \end{pmatrix} &= R_\theta \begin{pmatrix} \mathrm{x}_{\mathrm{QD,image}} - \mathrm{x}_{\mathrm{Xc}}^{LL} \\ \mathrm{y}_{\mathrm{QD,image}} - \mathrm{y}_{\mathrm{Xc}}^{LL} \end{pmatrix} \\ &= \begin{pmatrix} \cos\theta & -\sin\theta \\ \sin\theta & \cos\theta \end{pmatrix} \begin{pmatrix} \mathrm{x}_{\mathrm{QD,image}} - \mathrm{x}_{\mathrm{Xc}}^{LL} \\ \mathrm{y}_{\mathrm{QD,image}} - \mathrm{y}_{\mathrm{Xc}}^{LL} \end{pmatrix},\end{aligned} \tag{5.6}$$

where R_θ is the rotation matrix and the coordinates $(\mathrm{x}_{\mathrm{Xc}}^{LL}, \mathrm{y}_{\mathrm{Xc}}^{LL})$ are the coordinates (in pixels) of the lower-left reference marker, labelled LL in Fig. 5.17. Eq. (5.6) describes an initial translation of the origin of the reference frame to the coordinates of LL, followed by a rotation of all the points by an angle θ. The cosine and sine of rotation angle θ can be calculated as

$$\begin{aligned}\cos\theta &= \frac{\mathrm{y}_{\mathrm{Xc}}^{UL} - \mathrm{y}_{\mathrm{Xc}}^{LL}}{\sqrt{\left(\mathrm{x}_{\mathrm{Xc}}^{UL} - \mathrm{x}_{\mathrm{Xc}}^{LL}\right)^2 + \left(\mathrm{y}_{\mathrm{Xc}}^{UL} - \mathrm{y}_{\mathrm{Xc}}^{LL}\right)^2}} \\ \sin\theta &= \frac{\mathrm{x}_{\mathrm{Xc}}^{UL} - \mathrm{x}_{\mathrm{Xc}}^{LL}}{\sqrt{\left(\mathrm{x}_{\mathrm{Xc}}^{UL} - \mathrm{x}_{\mathrm{Xc}}^{LL}\right)^2 + \left(\mathrm{y}_{\mathrm{Xc}}^{UL} - \mathrm{y}_{\mathrm{Xc}}^{LL}\right)^2}},\end{aligned} \tag{5.7}$$

with $(\mathrm{x}_{\mathrm{Xc}}^{UL}, \mathrm{y}_{\mathrm{Xc}}^{UL})$ the coordinates of the center of the upper-left cross (UL in Fig. 5.17). Combining eqs.(5.7) and eq.(5.6) results in a system of equations formed only by values detected from the previous steps of the algorithm and, when solved, provides the correct location of the detected QDs with respect to the fabricated reference frame. Finally, the unit conversion from pixel to μm is used to obtain the coordinates in real-world units. Fig. 5.18a depicts the final result of the localisation algorithm, where the detected locations of the QDs are marked and overlapped with the found positions of the reference markers.

The overall final detection precision is calculated by propagating the uncertainties of all the parameters that appear in eq. (5.6). Although several variables with errors are involved, the initial low uncertainty levels obtained from the detections of crosses and QDs result in an overall high precision, as shown in Figs. 5.18b and c: the average uncertainty obtained for the undoped sample is $\overline{\delta} = 4.9\,\mathrm{nm}$, whereas $\overline{\delta} = 9.2\,\mathrm{nm}$ for the doped one.

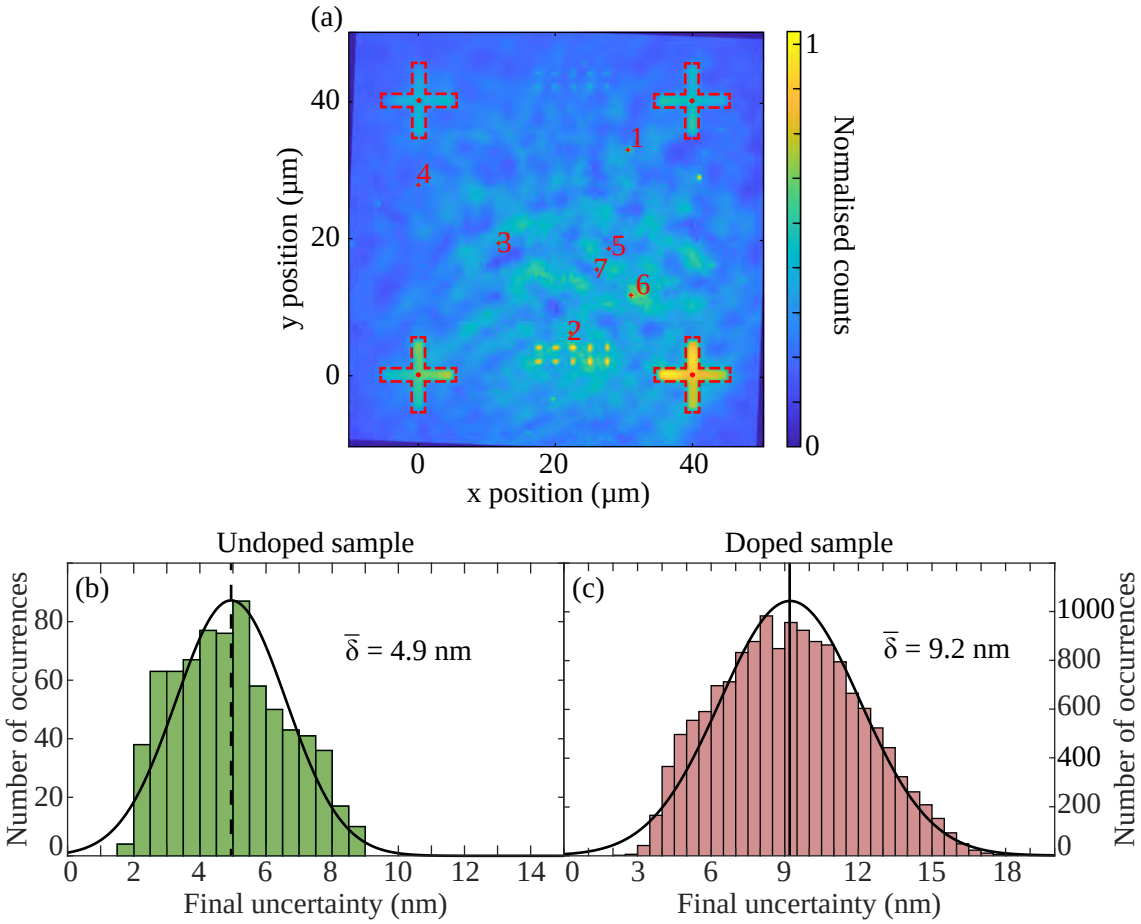

Figure 5.18: Final results of the localisation procedure. (a) Detected location of reference markers and QDs are correlated and overlapped on the same image. (b) Histograms of the final detection uncertainties of the QD location with respect to the reference frame on the undoped sample. The fitted normal distributions and evaluated mean values are also reported. (c) As in (b), but for the doped sample.

5.4 Final characterisation of the alignment accuracy

The uncertainties of the QD locations found via the algorithm developed during this PhD project are comparable to those obtained by current state-of-the-art techniques, as reported in Table 5.1. However, the truly relevant figure-of-merit for the deterministic fabrication of photonic nanostructures about the positions of the QDs is the final alignment accuracy. In order to characterise this parameter for the method we proposed, we fabricated nanobeam waveguides (NBWs) on both undoped and doped samples, centred at pre-selected locations of the emitters and oriented along the x- and the y-direction of the reference grid (as shown in Fig. 5.19a and b). The nanostructures have a rectangular cross-section with widths ranging from 288 nm to 631 nm on the undoped sample and of 300 nm on the doped one. Photonics crystal waveguides (PhCWs) (Fig. 5.19c) were also fabricated on the same chips, by removing one row of holes from photonic crystals with a triangular lattice, hole radii ranging from 71 nm to 76 nm and lattice constants from 233 nm to 247 nm. In this case, however, the devices were placed in such a way that the emitters would sit at different positions within the unit cell and hence at different distances from the nearest surface.

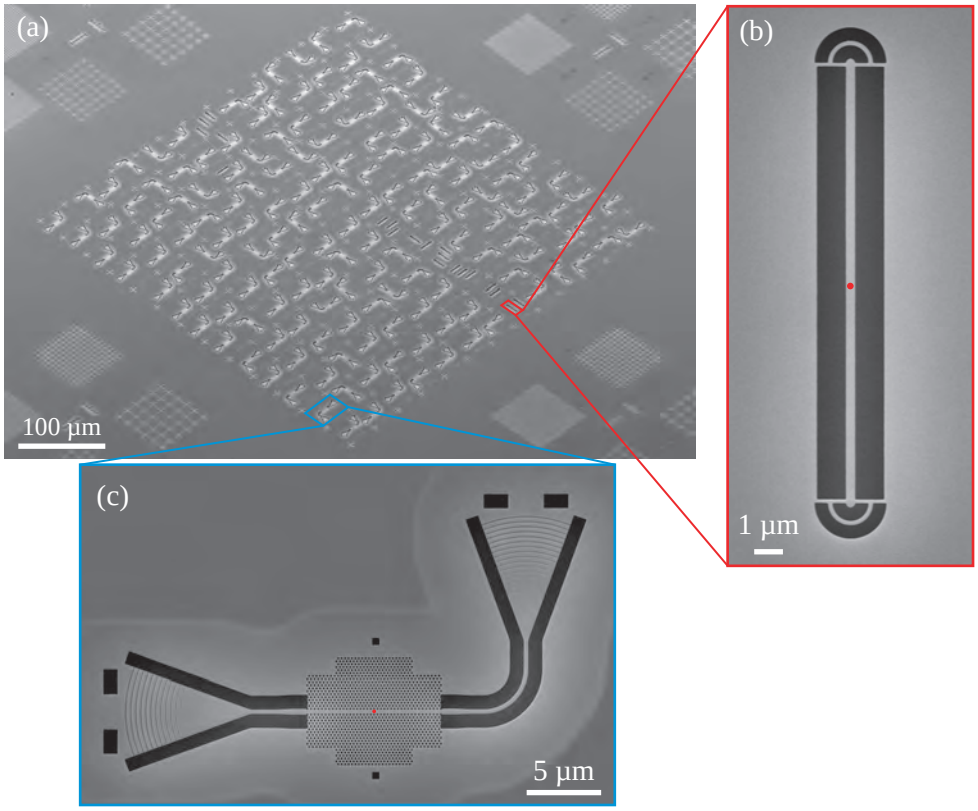

Figure 5.19: Nanophotonic waveguides fabricated about pre-located QDs. (a) A SEM image of the resulting photonic chip with both nanobeam and photonic crystal waveguides containing QDs. (b) Closed-up SEM image of a fabricated nanobeam waveguide, centred about the detected QD position (red dot). (c) SEM image of a fabricated photonic crystal waveguide. The small squares on each side of the photonic crystal section indicate the designed position of the emitters (marked with a red dot).

Using µPL measurements we confirmed that 46 out of 48 NBWs fabricated on the undoped sample contained the pre-selected emitter and thus resulting in a yield of about 96%. The same investigation performed on the doped sample showed 27 successfully fabricated NBWs out of 29 (a yield of 93%). This initial characterisation was also performed on the PhCWs, while also monitoring the distance QD-to-vertical surface to study possible effects due to the higher complexity of the geometry. The results of this investigation are shown in Fig. 5.20 and summarised in Table 5.2. Whilst no QDs were found in only 4 PhCWs (1 on the undoped sample and 3 on the doped one) out of all the structures designed to have one emitters at different positions along the axis parallel to the propagation direction (Fig. 5.20a), some correlation between QD positions in the unit cell and yield appears in Fig. 5.20b. The plot shows that less emitters could be detected in areas close to the holes of the photonic crystal; more specifically, when located closer than 100 nm to the nearest vertical surface, especially on the doped sample (Table 5.2). Such behaviour can be explained by the detrimental effects caused by surface states, which lower the quantum efficiency of the emitters, as discussed in previous chapters. In particular, on the doped sample the presence of a surface potential generates a local depletion of free charges that results in a reduction of the electrical conductivity [134]. The applied voltage is therefore less effective in reducing the built-in field and the radiative recombination stays low [130]. In contrast, no built-in field is present in the

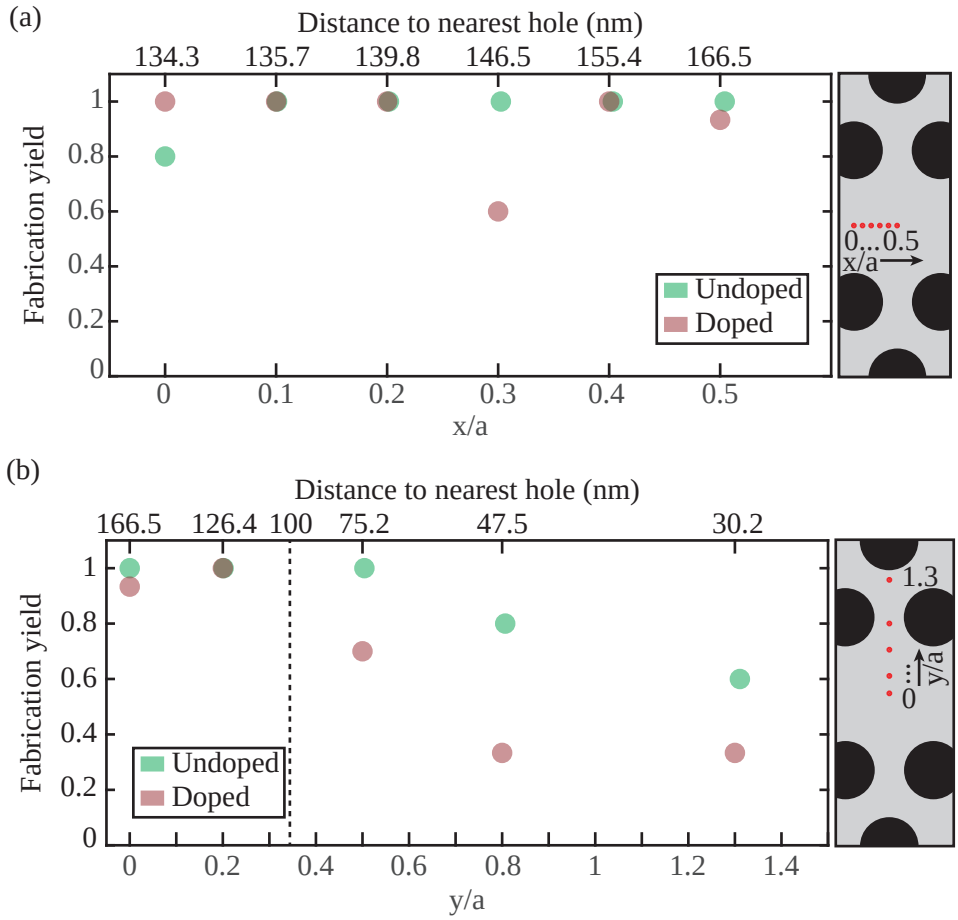

Figure 5.20: Dependence of the fabrication yield on the designed QD position in the unit cell of the PhCWs: (a) along and (b) perpendicular to the propagation direction, as shown in the respective panels on the right. The distance to the nearest hole, calculated for average values of lattice constants and hole radii used, is also shown.

Distance QD vs. nearest surface	**Yield undoped sample (successful/total)**	**Yield doped sample (successful/total)**
> 100 nm	97% (34/35)	94% (47/50)
$\leq$ 100 nm	80% (12/25)	44% (15/34)

Table 5.2: Results of the first characterisation of the deterministic positioning technique. Lower yield is measured for QDs located at less that 100 nm from the nearest surface, especially on the doped sample.

undoped wafer and the embedded QDs are 'always ON' as they do not necessitate any bias, thus explaining the different yields measured in the two types of investigated sample.

A more quantitative characterisation of the alignment error between the QDs and nanostructures was performed by imaging the luminescence generated from the nanobeam waveguides, as shown in Fig. 5.21. We followed the same two-step approach described above and acquired one set of images for the detection of reference markers and centers of the NBWs and another one

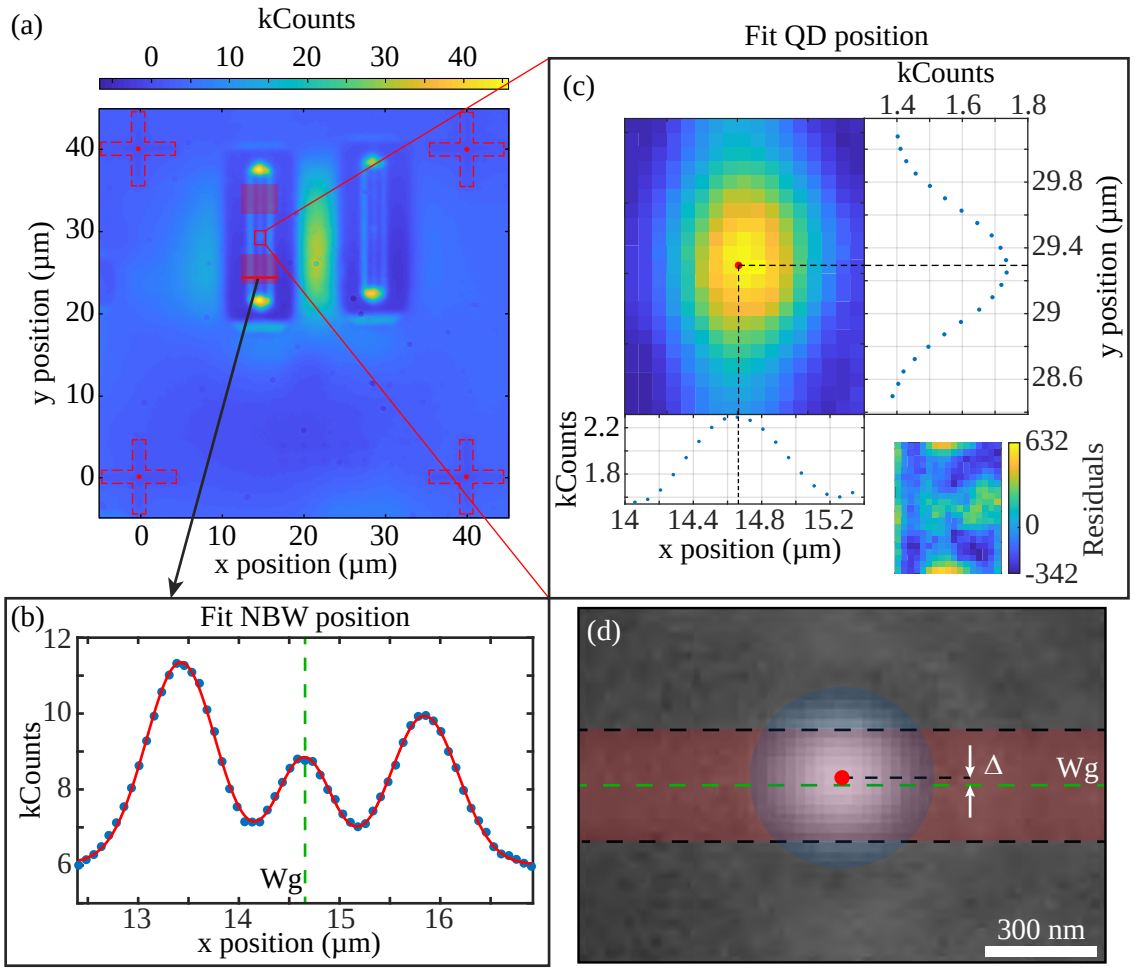

Figure 5.21: Schematic description of the characterisation of the deterministic fabrication of nanostructures. (a) Example of the intensity map analysed for the characterisation of the technique. The positions of the reference markers are detected by following the same localisation steps used before. (b) Cross-section on one of the NBWs displayed in (a), taken along the red line. Only cross-sections in the red-shaded areas marked in (a) are investigated. In the plot, the blue dots are the counts detected at each pixel of the CCD camera, whereas the red curve is the result of the fit. The center of the waveguide Wg is marked by the green dashed line. (c) ROI about the QD embedded in the NBWs. The right and low panels present 1D cut along the coordinates of the located center, marked by the red dot in the 2D map. The inset on the lower right corner shows a 2D plot of the calculated residuals. (d) False-color μPL image of the NBW and embedded QD. The edges and center of the nanobeam Wg are marked by dashed lines (black and green, respectively), whereas the QD emission is shown in blue, with the center marked by the red dot and the relative misalignment indicated by Δ.

for the central position of the QDs. Although the widths of the nanostructures are smaller than the diffraction limit of our optical setup and they appear blurred in the intensity map, they still present a fairly visible Gaussian profile as shown by the central peak in Fig. 5.21b. The two side peaks are caused by the light scattered from the external edges of the trenches next to the suspended nanobeam. As for the markers analysis, a selection of cross-sections (red-shaded areas

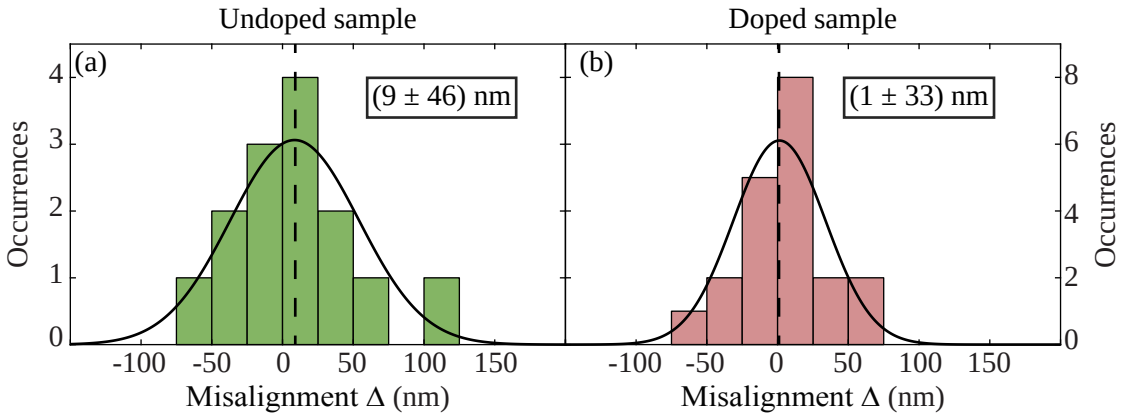

Figure 5.22: Final results of the evaluated alignment accuracy. (a) Measured misalignment distribution between the QDs and the center of a nanobeam waveguide for the undoped sample. The mean and standard deviation are also shown. (b) The same as in (a), but for the doped sample.

in Fig. 5.21a) were fitted with the sum of three Gaussians in order to extrapolate the position of the central peak Wg, with the uncertainties calculated as half of the 95.4% confidence interval from the fit. The weighted average of each position was finally calculated to find the center of the investigated nanostructure. Specifically, only x-coordinates (y-coordinates) were considered for NBWs aligned along the y-direction (x-direction) due to the corresponding orientation of the fitted cross-sections.

The location of the QD centers were found by fitting the intensity distribution of the photoluminescence from a small area around the emitter. A skewed two-dimensional Airy function was used to account for the shape of the emission pattern, which appears somewhat elongated due to the geometry of the hosting nanostructure. An example of the analysed area is reported in Fig 5.21c, where the plot of the residuals confirms that the fitting function describes fairly well the analysed pattern.

The final misalignment Δ between the central axis of the NBWs and the center of the QDs (marked as a red dot in Fig. 5.21d) can then be quantified by subtracting the values of analogous coordinates. Histograms of the obtained Δ, calculated both for undoped and doped sample, are plotted in Fig. 5.22, along with the fitted normal distribution. For the devices fabricated on the undoped sample, we found an average systematic alignment error of 9 nm that we attribute to a rigid shift introduced during the fabrication procedure. We note, however, that this value is well below the overlay alignment accuracy that the employed electron-beam lithography system can achieve (i.e. 15 nm, from specifications). The standard deviation of the distribution represents a more valuable quantity, as it describes the random errors related to the deterministic positioning technique we developed. The value we found for the undoped sample is 46 nm and is comparable with the accuracies reported in Table 5.1. The results of the analysis of the devices fabricated on the doped sample are shown in Fig. 5.22b and reveal a vanishing average systematic shift. More excitingly, the random alignment error obtained on the doped sample is 33 nm, more than 10 nm smaller than what was measured on the other sample. Such result confirms that the absence of the moving band-pass filter improves the final accuracy of the developed method, to a level smaller than what reported in several other works (cf. Table 5.1) and thus proving the effectiveness of the localisation technique developed during this PhD project.

5.5 Conclusions

In the present chapter, the localisation technique developed during the work of this PhD project has been described. It is based on a modified photoluminescence imaging approach that exploits the substrate emission, instead of the reflection of the illumination light, to collect images of the reference markers. The different approach prevents any systematic errors in the detection of the features on the investigated chip. A second image is then acquired, depicting the photoluminescence emission from the QDs as circular bright spots on a dark background. An image analysis algorithm has then been developed for locating the centers of markers and emitters and to correlate them to find the positions of the QDs in the reference frame used for the fabrication of further e-beam lithographic layers. We presented a statistical analysis on the detection precision, where location uncertainties as low as $\approx 5\,\text{nm}$ have been reported. Most importantly, we performed the characterisation of the deterministic positioning of nanostructures about the pre-located QD positions and we discussed the results in this chapter. Excitingly, the statistical analysis of the alignment accuracy of the fabricated devices have shown random errors smaller than 50 nm, which demonstrates that the developed approach enables a reliable and deterministic fabrication of nanophotonic devices based of self-assembled QDs, which is a necessary step towards the integration of advanced quantum optics experiments on solid-state systems.

Chapter 6

First applications of the localisation technique

The two-step photoluminescence protocol we developed allows for precise mapping of the locations of self-assembled QDs onto a reference frame. More importantly, we were able to fabricate photonic nanostructures about pre-selected locations with alignment errors smaller than 50 nm. These results prove we now have the tools to overcome the issue of random growth that affects Stranski-Krastanov QDs and to finally enable a more deterministic implementation of this type of emitters. The newly acquired knowledge over the spatial position, for example, can be exploited to reliably address single QDs and systematically investigate their spectral properties. The ability to collect such information before the fabrication of any device facilitate the fabrication of photonic nanostructures that are spectrally well-coupled to the embedded emitters. In this chapter, we present two studies that constitute our first attempts to make use of these new possibilities: we first monitored how the fabrication procedure affects the spectral properties of QDs (Sec. 6.1) and then we integrate the emitters in PhCWs to deterministically control the light-matter interaction (Sec. 6.2).

6.1 Characterisation of spectral changes due to fabrication

As already discussed in previous chapters, the solid-state nature of self-assembled QDs makes them very sensitive to their immediate environment; their spectral properties for example are strongly affected by the presence of charges or structural defects. The fabrication of nanostructures heavily modifies the region around the emitters, as the etching into the sample produces new surfaces that influence the properties of the QDs. Characterising such effects is therefore necessary in order to design nanostructures that show optimal spectral coupling to the embedded emitters.

Thorough studies of the fabrication-induced effects are usually difficult to perform, because the knowledge of the spatial position of the QD is necessary to reliably address the same emitter both before and after its integration into a photonic nanostructure. To the best of our knowledge, only two works have reported this type of investigation: (i) by means of cathodoluminescence, Kaganskiy and co-workers [126] monitored the emission energy, the fine-structure splitting and the decay times of QDs before and after the fabrication of circular mesa structures with diameter of 2 µm around them; (ii) more recently, Liu *et al.* made use of a luminescence-based imaging technique to investigate the effects of nanofabrication on the linewidth of QDs that were integrated in micropillar cavities [116]. We note that both reported studies focused on µm-size monolithic structures and no investigation on individual QDs in suspended nanostructures has been reported

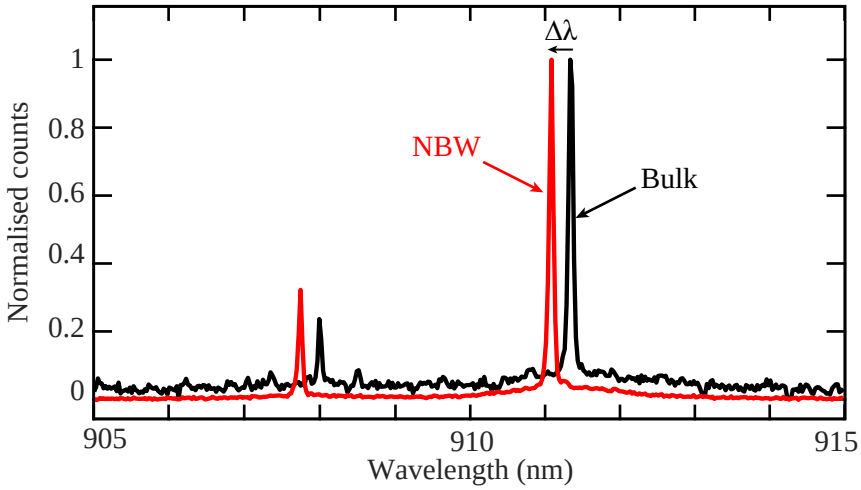

Figure 6.1: Example of the emission spectra collected for a QD before (bulk sample, black) and after (NBW, red) fabrication of photonic nanostructures. The spectral shift $\Delta\lambda$ is marked. The different peaks in each spectrum correspond to different excitonic states, likely X^0 and X^+ as described in the main text.

in the literature.

We set out to characterise the spectral changes induced by the fabrication of suspended nanobeam and photonic crystal waveguides on pre-selected QDs. To do so, we collected photoluminescence spectra from pre-selected QDs both before and after the fabrication of nanostructures on both samples presented in the previous chapter, i.e. doped and undoped (cf. Chap. 5). An advantage of our μPL imaging approach is that spectral information of the located emitters can be easily acquired in the same optical setup. After the collection of images of the reference crosses and QDs and the selection of the brightest emitters in each square, we switched the imaging system to a confocal configuration by removing the wide-field lens placed in the excitation path. The laser was thus focused to a spot on the sample of $\approx 1.5\,\mu$m in diameter. The collected signal was guided via a free-space path to a spectrometer (Andor Shamrock 750), where it was dispersed by a grating with 1200 lines/mm and spectral resolution of 0.03 nm and subsequently collected by a CCD camera (Andor Newton 940). The emitters were excited by the same diode laser employed for the imaging process, which was set to a power well below saturation of the QDs. Finally, for the doped sample, a voltage source (Keithley 2450) was used to apply a constant bias of 0.3 V both before and after nanofabrication.

An example of the collected spectra is shown in Fig. 6.1, where photoluminescence signals are reported for a QD before (black) and after (red) its integration in a suspended nanobeam waveguide (see Fig. 5.19b) on the doped sample. A clear spectral shift $\Delta\lambda \approx -0.3\,$nm is visible. The results of a systematic investigation of such effect performed on both samples and for both types of nanostructures are reported in Fig. 6.2 and show that non-zero shifts have been found in every fabricated sample, although with different magnitude and directions. Specifically, on the undoped sample we calculated a mean shift $\Delta\lambda = 0.8\,$nm on NBWs and a mean shift $\Delta\lambda = 0.1\,$nm on PhCWs, with standard deviations of 0.6 nm and 0.7 nm, respectively. A possible explanation for these values can be found in the release of accumulated stress after the selective etching of the sacrificial layer. In fact, the GaAs membrane grown on top of the $Al_{0.75}Ga_{0.25}As$ layer presents a small intrinsic strain generated by the mismatch of lattice constants of the materials, namely $a_{GaAs} = 5.6420\,$Å and $a_{AlGaAs} = 5.6499\,$Å, for AlGaAs with an aluminium content of 75% [13]

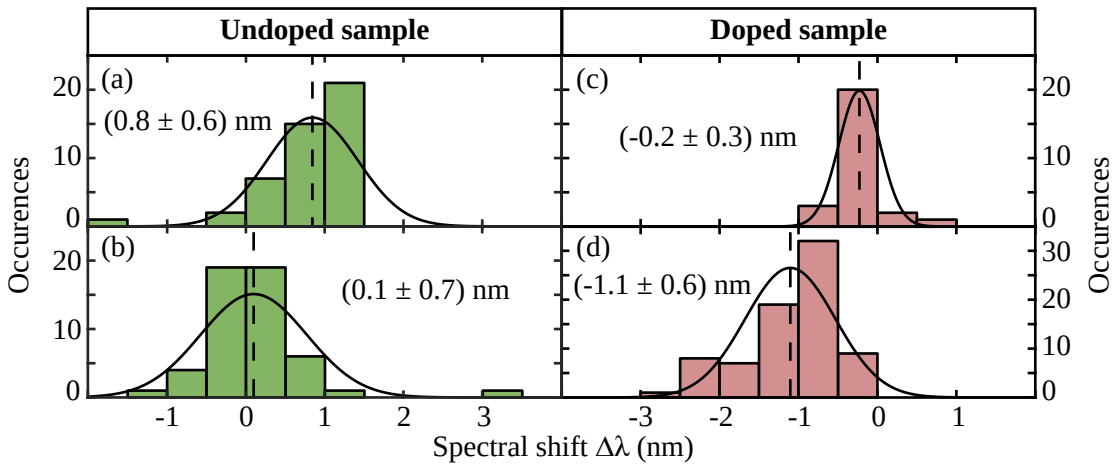

Figure 6.2: The effect of integration in nanostructures on the spectral properties of QDs. (a) and (b) show histograms of spectral shift measured from QDs in undoped samples embedded in NBWs and PhCWs, respectively. The fitted normal distributions and the evaluated vales of mean and standard deviation are also reported. (c) and (d) are the same as in (a) and (b), but for doped samples.

(both values are calculated for T = 10 K). The initial strain then amounts to

$$\frac{(a_{AlGaAs} - a_{GaAs})}{a_{GaAs}} = 1.4\%,$$

where the positive sign indicates a tensile strain. During the HF etching of the samples, the sacrificial AlGaAs layer is dissolved, the membrane thus becomes free-standing and, more importantly, free to release the internal stress by buckling a little. Such effects have already been studied by Nakaoka and co-workers in [135], where they measure spectral shifts on the same order of magnitude in an ensemble of QDs in structures with a geometry similar to the NBWs. The different value of $\Delta\lambda$ extrapolated from the PhCWs may arise from the fact they have a more extensive and "two-dimensional" geometry, which may result in a different strain configuration and therefore a different release mechanism. Finally, the relative large standard deviations found are probably due to the specific response of each QD to the applied stress, which has been shown to depend on the amount of Ga constituting the emitter and is therefore different to each one of them [136].

The analysis performed on the doped sample reveals that the measured spectral shifts are $\Delta\lambda = (-0.2 \pm 0.3)$ nm and (-1.1 ± 0.6) nm for QDs integrated in nanobeam and photonic crystal waveguides, respectively. Even though the magnitude of these spectral changes is similar to that of the doped sample, the shifts are now towards the opposite direction on both types of structures. This finding demonstrates that the fabrication process affects QDs that are embedded in homogenous GaAs and in heterostructures differently. We also note that the values measured for QDs integrated in PhCWs on the doped sample are larger than the ones for the NBWs on the same wafer. This may be due to the different geometries and densities of vertical surfaces in the two types of nanostructures. This may affect the applied voltage differently and hence influence the effective amount of electrical tuning corresponding to the value of bias set on the voltage source. A similar effect was noted between the surface potential and local depletion of charges, which influenced the measured yield in Sec. 5.4.

The measured spectral shifts were also analysed as a function of the NBW width w[a] and with

[a]This study was conducted only for the devices fabricated on the undoped sample.

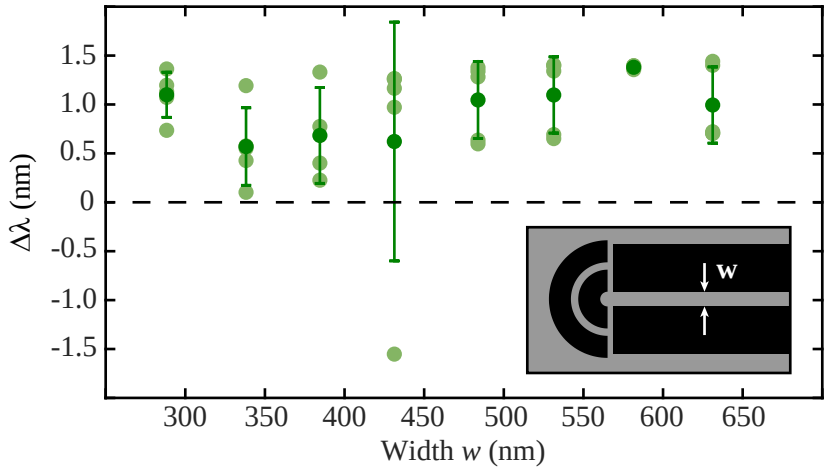

Figure 6.3: Dependence of the measured spectral shift on the width w of the nanobeam waveguides fabricated on the undoped sample. The dark symbols and error bars are the mean and the standard deviations of $\Delta\lambda$ found for each value of the width, which are shown as light coloured circles. The inset shows the design of the fabricated devices, where their width is marked.

respect to the designed QD position in the unit cell of the fabricated PhCWs. The result of the former study is presented in Fig. 6.3 and demonstrates that the measured shifts have no clear dependence on w, as all the calculated mean values overlap within the errors. In other words, varying the distance between QDs and vertical surfaces from 144 nm to about 315.5 nm has no clear correlation with the detected spectral changes. Similarly, no clear effects are detectable when the QDs sit at different positions in the unit cell of PhCWs, regardless of whether their locations change along the x- or the y-direction (Fig. 6.4a and b, respectively). In this case, the separation between QDs and nearest vertical surface varies between about 29 nm and 171 nm. The absence of any trend in Figs. 6.3 and 6.4 supports the conclusion that the main cause of the spectral shifts is the release of internal strain after the selective dissolution of the sacrificial layer rather than other effects such as the trapping of new charges generated by the fabrication of new vertical walls close to the QDs.

An investigation into the effect of nanofabrication on the electrical tuning of the QDs in the doped sample has also been performed. Exemplary voltage-dependent spectra acquired both before and after the integration in PhCWs are shown in Fig. 6.5. Here, the charge plateaus of the neutral exciton (X^0) and positive trion (X^+) are both visible. In particular, the charged exciton has been identified as X^+ based on the fact that it is brighter at larger fields (i.e. lower applied voltages) than the neutral counterpart [30, 32]. As presented already in Fig. 6.2, both excitonic lines blueshift after the fabrication of PhCWs. We also note that part of the fluorescence plateaus show some overlap between the bulk and the PhCWs signals, with amounts that vary among different QDs. For the emitter reported in Fig. 6.5, for example, the bulk emission of X^+ can be recovered for about 0.35 nm by increasing the bias voltage by about 140 mV, whereas the emission peaks of X^0 present a smaller overlap, as 0.15 nm of the initial fluorescence signal could be retrieved over 60 mV. In general, a wide range of bandwidths have been measured for different QDs [137], which is an encouraging result as it shows that the electrical tuning can be employed to correct for the fabrication-induced spectral shifts, especially when using wafers with layer structures engineered to achieve large tuning ranges [37].

We studied the effect of nanofabrication on the emitter dipole by fitting the Stark shifts of the recorded spectra (as indicated by the white dashed line in Fig. 6.5). The quadratic dependence

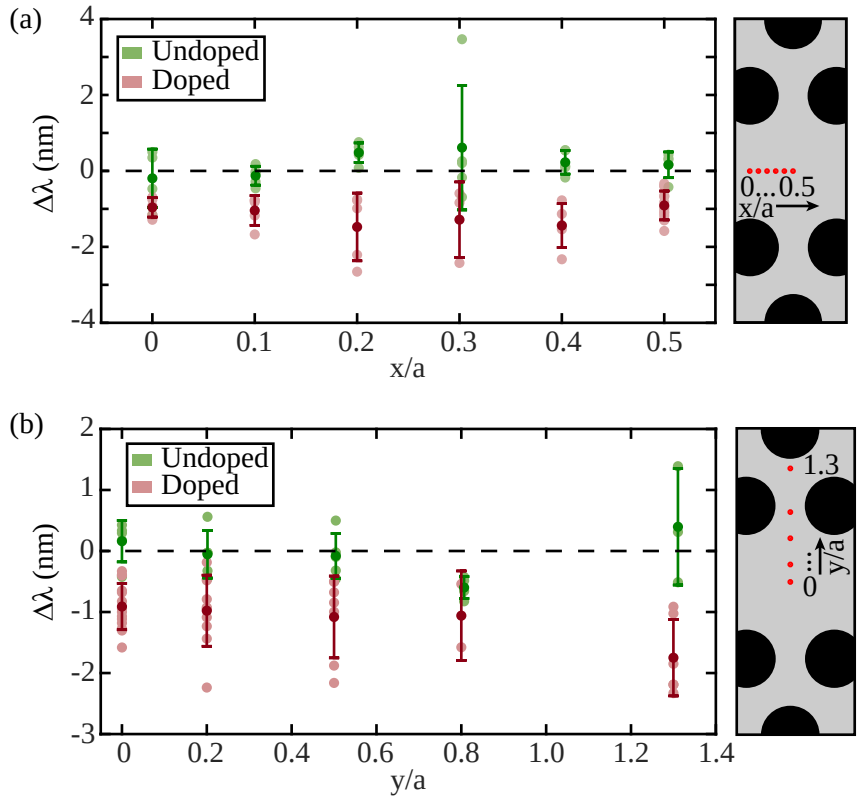

Figure 6.4: Dependence of the measured spectral shift on the QD position inside the unit cell of the PhCWs. The coordinates of the QDs varies both along (a) x- and (b) y-direction, as shown in the respective insets.

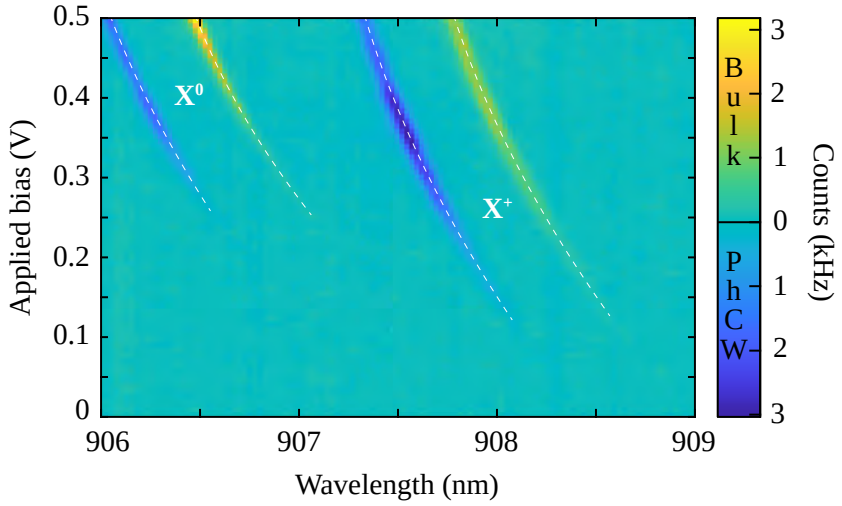

Figure 6.5: Voltage-wavelength PL spectra for a QD located about 129 nm away from the nearest surface in a PhCW. The fluorescence signals of both the neutral (X^0) and charged (X^+) excitons are seen in the maps and, in this case, both blue shift by about 0.5 nm with applied bias. The Stark shift parameters can be evaluated by a quadratic fit (dashed line), as discussed in the main text.

of the transition energy with respect to the applied field F [35–37], written in terms of emission

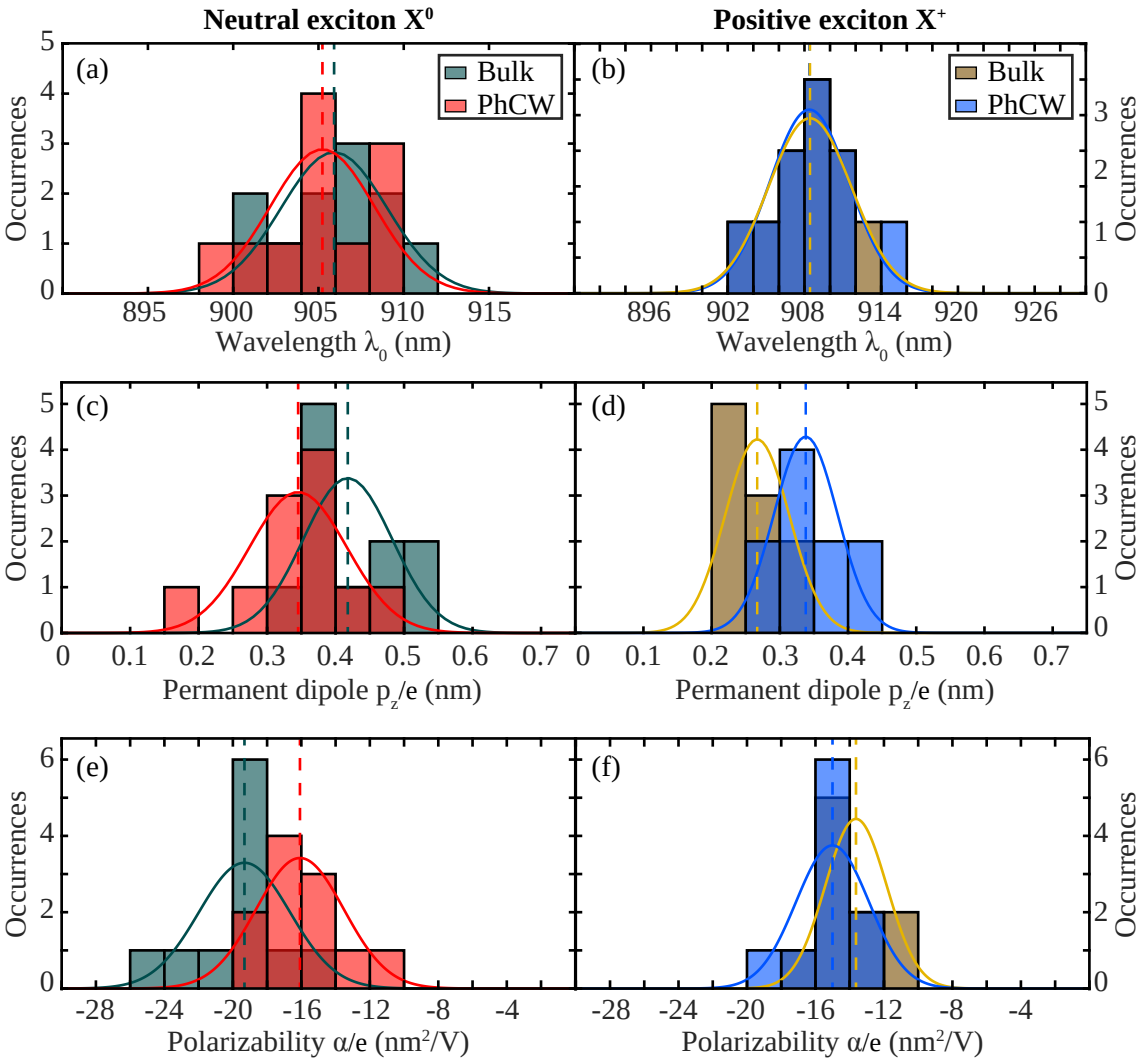

Figure 6.6: Histograms of the fit parameters of the detected Stark shifts for both the neutral exciton X^0 and the positively charged trion X^+: (a) and (b) emission wavelength at vanishing applied field λ_0, (c) and (d) permanent dipole of the QD along the growth direction p_z, (e) and (f) the polarizability α of the emitter. The fitted normal distributions and the calculated mean values are also shown as solid curves and dashed lines, respectively.

wavelength λ, reads

$$\frac{hc}{\lambda} = \frac{hc}{\lambda_0} - p_z F + \alpha F^2, \tag{6.1}$$

where λ_0 is the QD emission wavelength at $F = 0\,\mathrm{kV/cm}$, p_z is the permanent dipole moment of the QD along the growth direction and parallel to the applied field direction, and α is the polarizability of the emitter. The applied field as a function of the bias voltage V is $F = (V - V_i)/t$, where $t = 70\,\mathrm{nm}$ is the nominal thickness of the intrinsic layer surrounding the QDs in the wafer under study and the built-in field V_i/t has been calculated from the difference between the Fermi levels of the p- and n-doped GaAs layers [14], which gives $V_i/t = 224.24\,\mathrm{kV/cm}$. Histograms of the fit parameters for all analysed QDs and the evaluated mean values and standard deviations are reported in Fig. 6.6 and Tab. 6.1, respectively. Overall, the quantities obtained by statistical

	X^0		X^+	
Parameter	**Bulk**	**PhCW**	**Bulk**	**PhCW**
λ_0 [nm]	906 (3)	905 (3)	908 (3)	908 (3)
p_z/e [nm]	0.42 (6)	0.35 (6)	0.27 (5)	0.34 (5)
α/e [nm^2/V]	-19 (3)	-16 (3)	-14 (2)	-15 (2)

Table 6.1: Summary of the mean values and standard deviations (in parentheses) for the fit parameters calculated from the normal distributions shown in Fig. 6.6.

analysis are comparable with values reported in literature [36, 37, 138, 139].

We analysed the difference between the fit parameters before and after nanofabrication for QDs located at different positions in the PhCW unit cell. The data are presented in Fig. 6.7. No correlation is visible between the Stark-shift parameters and the separation between QD and nearest hole, confirming once again our conclusion that a redistribution of internal strain and stress after the release of the GaAs membrane is responsible for the detected spectral shift, rather than effects due to charges trapped at the surface. We also note that the variations due to integration in nanostructures on the parameters for X^+ are generally smaller than the ones on X^0. This difference may be related to the smaller extension of the excitonic wavefunction associated with X^+ compared to the one describing the neutral exciton [36], which probably makes the former less susceptible to changes in the local environment.

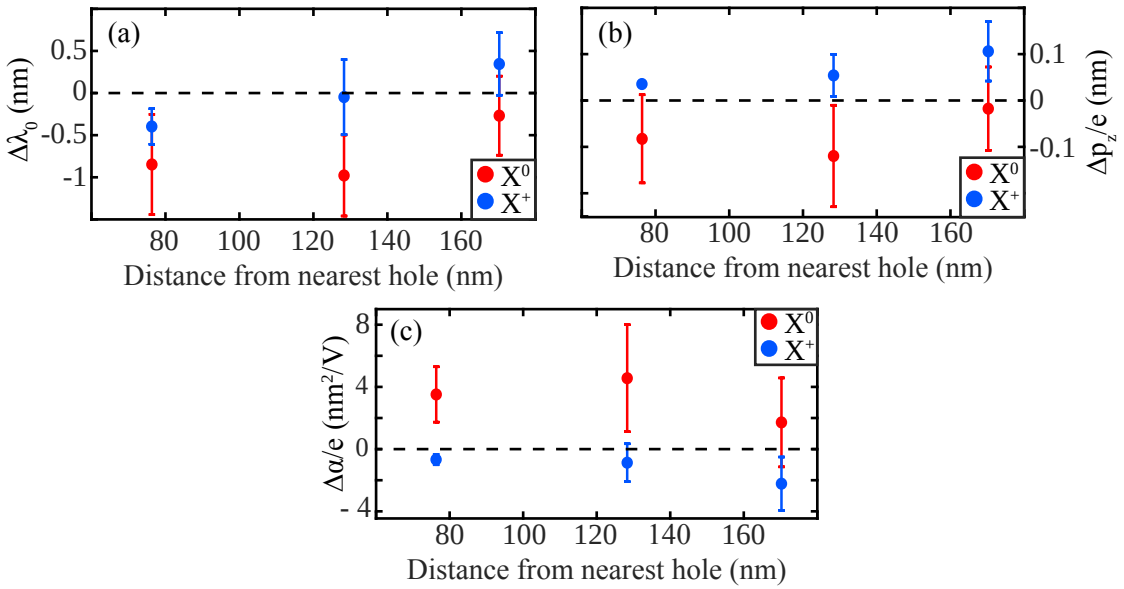

Figure 6.7: Fabrication-induced changes to the Stark-shift parameters as a function of the nominal distance from the closest hole: (a) emission wavelength at vanishing applied electric field λ_0, (b) permanent dipole of the QD along the growth direction p_z and (c) polarizability α of the emitter. Two to four emitters were measured at each position and the error bars represent the calculated standard deviations.

6.2 Deterministic control of the emission properties of QDs integrated in PhCWs

In Chap. 2 we presented how the light-matter interaction in photonic crystal waveguides affects the emission properties of embedded QDs, which experience an enhancement or a suppression of their decay rates when compared to the values in a homogenous material. The Purcell factor F_p is the parameter that quantifies such effects and in a PhCW we showed having the form of eq. 2.18

$$F_p(\omega,\mathbf{r}) = \frac{3\pi a c^2}{\omega^2\sqrt{\varepsilon(\mathbf{r})}} n_g(\omega)\,|\hat{\mathbf{e}}(\omega,\mathbf{r})\cdot\hat{\mathbf{e}}_\mathbf{d}|^2\,,$$

which explicitly shows its dependence on the emission frequency ω and the position $\mathbf{r}$ of the emitter. The periodic modulation of the dielectric constant in PhCWs, however, strongly confines the propagating mode, resulting in photonic-coupling efficiencies $\geq 96\%$ possible only if the emitter sits within 50 nm from the field maximum [50]. Furthermore, the dispersion relation of PhCWs strongly depends on the values of the lattice constant and the hole radius that are defined in the mask design, thus locking the frequency of the propagating modes once the devices are fabricated. In fact, a few options exist for tuning such a parameter (e.g. temperature tuning or nitrogen deposition), but changes of only 1-2 nm are possible [112, 140]. The lack of spatial and spectral knowledge that characterises QDs grown by Stranski-Krastanov method clearly hinders an optimal coupling between this type of emitters and PhCWs, forcing most quantum photonics experiments to rely on the fabrication of many devices at once and on the post-selection of the few structures where the QDs are at the desired spatial and spectral locations. The localisation technique we developed allows us to overcome these difficulties and helps unlocking the full power of the PhCWs platform; in the following pages we report on our investigations of such capabilities.[b]

We set out to study the spatial dependence of the radiative decay $\Gamma_{wg,r}$ in a PhCW by fabricating nanostructures with QDs placed at different locations within their unit cell, as shown in Fig 6.8. Furthermore, we exploited the ability to perform spectral characterisation of the QD emission before nanofabrication to design devices with lattice constants and hole radii in such a way that their band edges resulted within 10 nm from the emission of the selected emitter (about 915 nm, on average). The investigated devices were fabricated on the doped sample that was presented in the previous chapter and we therefore refer the reader to Sec. 5.4 for the list of chosen parameters.

The sample was mounted on the optical setup described in Sec. 6.1, where a half-wave plate and a polariser were introduced to the excitation and the collection path, respectively, in order to improve the polarisation control of excitation laser and collected signal. We measured the transmission through each fabricated photonic crystal waveguide by coupling a continuously tunable laser (by TOPTICA Photonics AG) into the nanostructures via a grating coupler and detecting the signal emitted from the second one (cf. Fig. 5.19c). An example of the collected data is reported in Fig. 6.9a, which presents the sharp transmission cut-off typical for PhCWs. In the same plot we report the normalised emission from the QD embedded in the nanostructure, obtained by exciting the emitter from the top and collecting the generated photoluminescence from one of the out-couplers of the devices. The analysis of spectra similar to those shown in Fig. 6.9a allowed us to calculate the detuning $\Delta\lambda_{be}$ from the band edge for each QD and build the histogram in Fig. 6.9b, which demonstrates that we were able to integrate QDs in PhCWs with a cut-off wavelength at about 10 nm from the spectral position of the emitter. The corresponding group index n_g to each $\Delta\lambda_{be}$ was also estimated and reported in the same histogram. These values have been estimated from

[b] The data collection and analysis presented in this section have been performed in close collaboration with Dr. Xiao-Liu Chu.

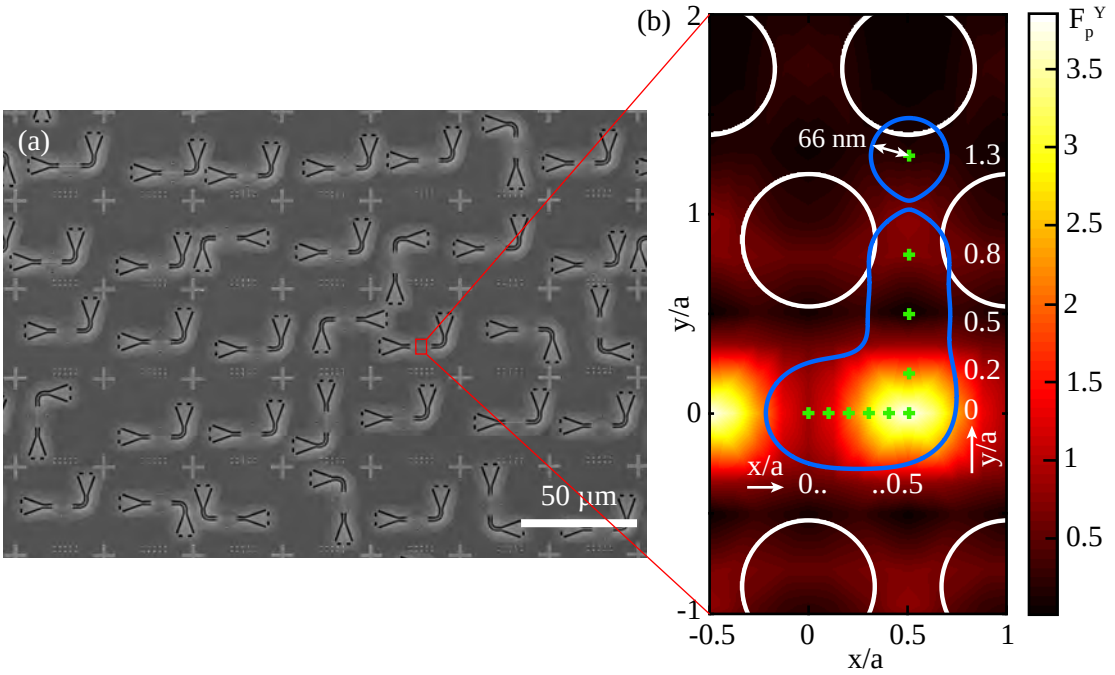

Figure 6.8: Deterministic fabrication of PhCWs about QDs. (a) A SEM image of the fabricated nanostructures placed at pre-selected QD positions. (b) Map of the simulated spatial dependence of F_p for a dipole oriented perpendicularly to the propagation direction. The selected positions within the unit cell are marked by green crosses. The blue line encloses the area corresponding to twice the standard deviation of the alignment error extrapolated for this sample (see Sec. 5.4).

finite-element (FE) simulations of the band structures for few of the fabricated PhCWs and hence represent only a rough indication of typical values for each $\Delta\lambda_{be}$, as the exact relationship between group index and distance from the bandedge depends on the exact geometry of each nanostructure.

Time-resolved measurements on the neutral exciton of 13 different QDs not embedded in nanostructures were performed in order to estimate the radiative decay rate in a homogeneous medium Γ_B for the emitters grown on the wafer under investigation. The lifetime measurements were performed by exciting the QDs with a pulsed Ti:sapphire laser (Tsunami, by Spectra-Physics), set to a wavelength of 860 nm and generating pulses of about 10 ps with a rate of 80 MHz. The collected signal was sent to the spectrometer for spectral filtering and detected by silicon avalanche photodiode with time resolution lower than 50 ps and detection efficiency of about 5% at 900 nm (by Micro Photon Devices). The decay curves were constructed by building histograms of the arrival times of single-photon detection events by means of a time tagging module (PicoQuant PicoHarp300), with 4 ps resolution and triggered by the signal of a photodiode (PicoQuant TDA200) that collects part of the beam from the excitation laser. Every lifetime was fitted with a single exponential and a histogram of the fitted rates is presented in Fig. 6.9c. By fitting a normal distribution to the data we obtain a mean decay rate of $3.9\,\mathrm{ns}^{-1}$ and a standard deviation of $0.7\,\mathrm{ns}^{-1}$, which is a quite large value if compared to the rates usually measured for this type of emitter [8, 40]. We explain such a discrepancy by assuming that the decay dynamics of the QDs under study is heavily affected by a non-radiative component $\gamma_{B,nr}$, as suggested also by the single-exponential nature of the collected decay curves. In fact, when $\gamma_{B,nr}$ is large, the square-root term in the fast and slow decay rates presented in Chap. 2 is small compared to the other parts and the

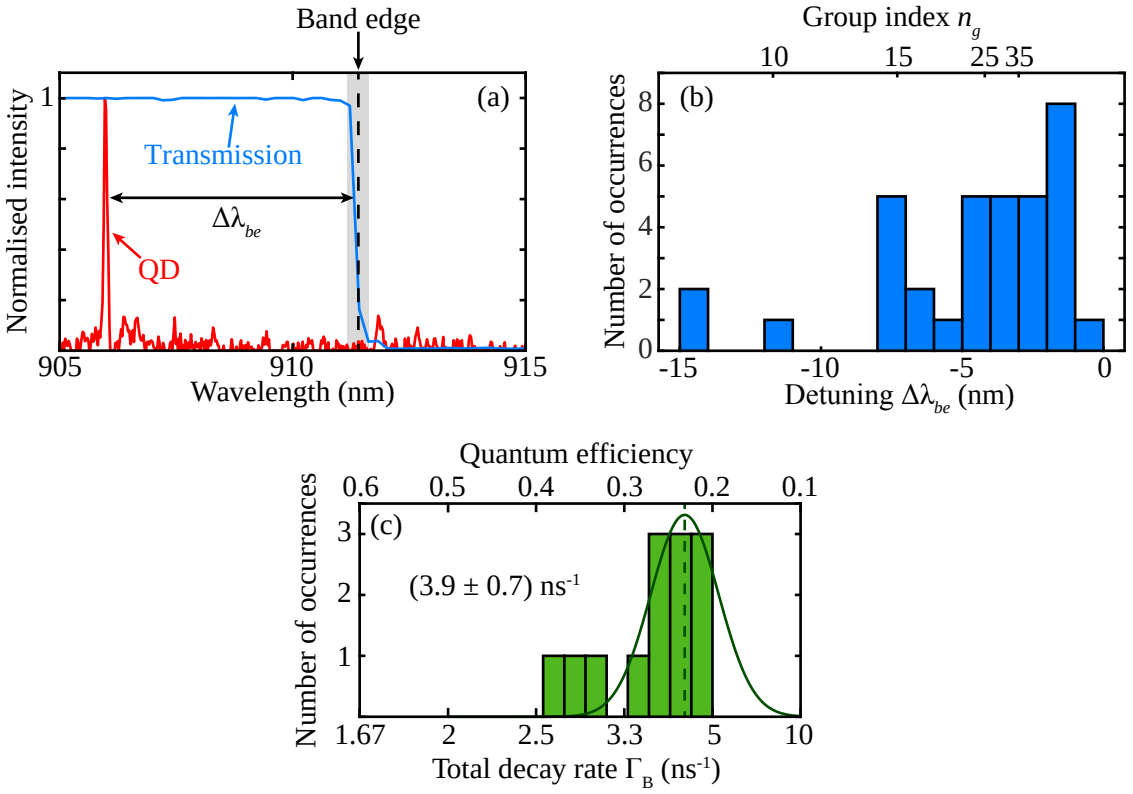

Figure 6.9: Initial characterisation of the fabricated sample. (a) Example of transmission (blue curve) and QD emission (red curve) spectra collected from the fabricated PhCWs, from which we obtain the difference between QD emission peak and the band edge $\Delta\lambda_{be}$. The grey area marked the uncertainty in the position of the band edge. (b) Histogram of the calculated $\Delta\lambda_{be}$. Typical values of the group index corresponding to reported detunings are also indicated. (c) Histogram of the total decay rate Γ_B of 13 QDs embedded in an area without nanostructures. The fitted normal distribution and the calculated mean value are also shown. The top x-axis reports the corresponding quantum efficiencies.

total decay rate therefore reads

$$\Gamma_B = \gamma_{B,r} + \gamma_{B,nr}\,, \tag{6.2}$$

where $\gamma_{B,r}$ identifies the radiative component in bulk. Our assumption is also confirmed by the low quantum efficiencies QE_B calculated from the values reported in Fig. 6.9c, where we assumed $\gamma_{B,r} \approx 1\,\text{ns}^{-1}$.

The total decay rate Γ_{wg} of QDs embedded in PhCWs can be written as

$$\begin{aligned}\Gamma_{wg}(\omega,\mathbf{r}) &= \gamma_{wg,r}(\omega,\mathbf{r}) + \gamma_{wg,nr} \\ &= F_p(\omega,\mathbf{r})\cdot\gamma_{B,r} + \gamma_{wg,nr} \approx A(\mathbf{r})\cdot n_g(\omega)\cdot\gamma_{B,r} + \gamma_{wg,nr},\end{aligned} \tag{6.3}$$

where we assume that the non-radiative component $\gamma_{wg,nr}$ is independent of the emission frequency ω of the emitter. In the second line of eq. (6.3) the radiative component $\gamma_{wg,r}$ has been rewritten in terms of Purcell factor F_p, which is subsequently decomposed into two factors: (i) the frequency-dependent group index $n_g(\omega)$ and (ii) a term $A(\mathbf{r})$ that is assumed only weakly affected by ω since determined by the pre-factor in eq. (2.18) and by the overlap between propagating mode and dipole. Such assumption arises from the minor changes of the mode field profile for different

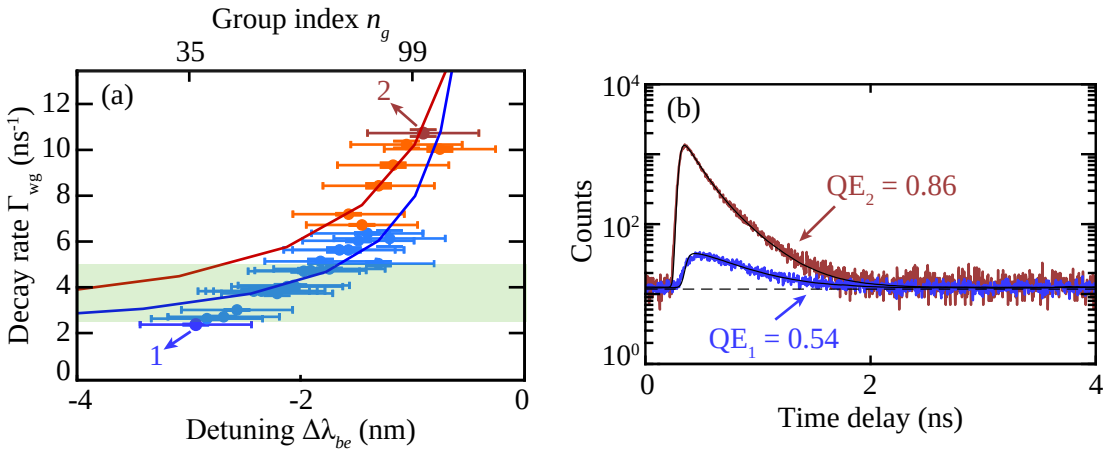

Figure 6.10: Decay rate enhancement when approaching the PhCW band edge. (a) Evaluated decay rates Γ_{wg} as a function of detuning $\Delta\lambda_{be}$ from the measured band edge. Datasets for two QDs placed at different position in the unit cell are shown: QD1 (light blue symbols) is at (0.2a,0), whereas the coordinates of QD2 (orange) are (0.4a,0). Both dataset are well fitted by eq. (6.3) (solid curves). (b) Examples of the acquired lifetimes, with the respective fits and background level (black solid and dashed lines, respectively). The curves correspond to the data points marked in (a). The extrapolated quantum efficiencies QE are also shown.

group indices and allowed us to independently study the effects of the spectral and spatial position on the emission properties.

We first studied the influence of $\Delta\lambda_{be}$ on the total decay rate Γ_{wg} and to do so we focused on 2 QDs that were situated spectrally closed to the photonic band gap, where we expected a large enhancement of the decay rate due to the high value of n_g. The emitters, denoted QD1 and QD2, were respectively located at (0.2a,0) and (0.4a,0) in the unit cell of PhCWs (cf. Fig. 6.8b) and showed $\Delta\lambda_{be} \approx -2\,\text{nm}$ at bias voltage $V = 0.3\,\text{V}$. Via electrical tuning, we modified the value of $\Delta\lambda_{be}$ for each QD and measured the decay rate at each spectral position; the measured values of Γ_{wg} are shown in Fig. 6.10a, whereas Fig. 6.10b reports the slowest (dark blue dataset) and the fastest (dark red) decay rates that were measured, indicated by numbers 1 and 2 in Fig. 6.10a, respectively. The plotted data clearly show a significant increase of Γ_{wg} when the detuning is reduced, as expected from the corresponding increase of n_g.

The behaviour of QD1 and QD2 reported in Fig. 6.10a presents some differences when related to the values of Γ_B measured in bulk (shown as a light green area in the same figure). In fact, although both emitters show similar trends, only QD2 demonstrates decay rates always faster than the values measured in bulk, whereas the measured lifetimes of QD1 move from being suppressed to slightly enhanced when the detuning is reduced. This difference can be explained by the spatial dependence of F_p depicted in Fig. 6.8b: QD1 is placed in a region of the unit cell where the Purcell factor is expected to be $F_p \leq 1$ and therefore causing a slight suppression. This is not the case for QD2, which sits close to a maximum of the mode profile and therefore always experiences an enhancement of the decay rate due to a better overlap between propagating field and emitter. Furthermore, the data can be fitted with eq. (6.3) (solid lines in Fig. 6.10a) and the values of radiative and non-radiative rates can be extracted, from which we can calculate the quantum efficiencies QE_{wg} for the QDs integrated in the nanostructures. As expected from the behaviour of Γ_{wg} vs. detuning, QD1 shows $QE_{wg,1} = 0.54$ when located at $\Delta\lambda_{be} \approx -2\,\text{nm}$, which increases to $QE_{wg,1} = 0.76$ for smaller detuning. Similarly, the quantum efficiency for QD2 changes from

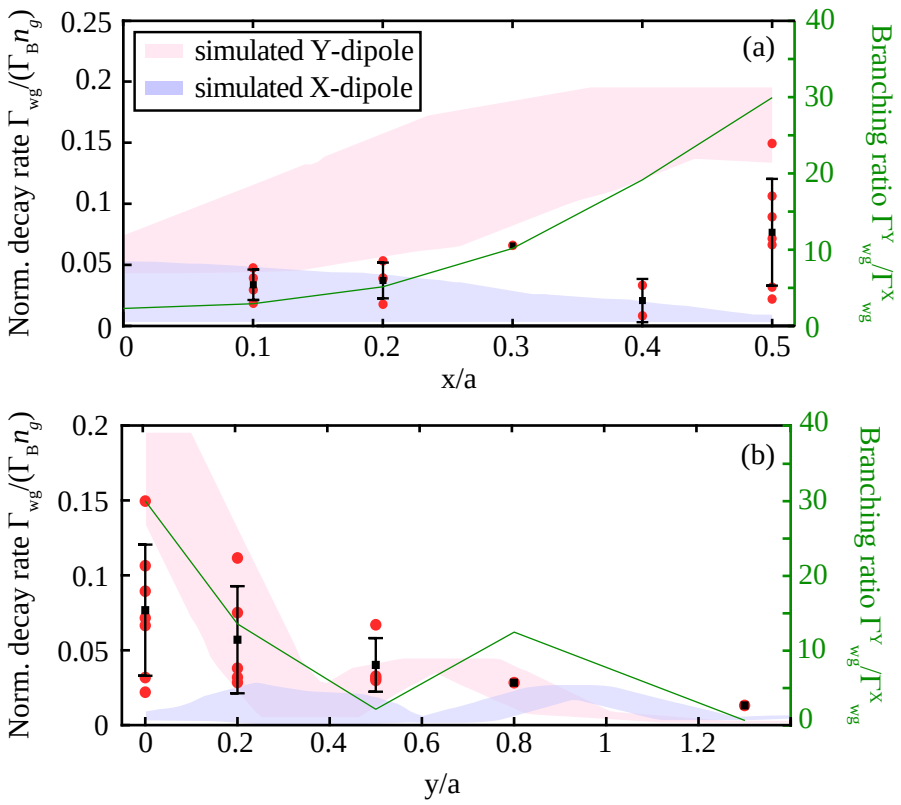

Figure 6.11: Normalised decay rate $\Gamma_{\mathrm{wg}}/(\Gamma_{\mathrm{B}} n_g)$ for QDs located at different positions in the PhCW unit cell. The QDs location varies (a) along the x-direction, at y/a = 0, or (b) along the y-direction, at x/a = 0.5 (cf. Fig. 6.8). The evaluated decay rates for each QD are shown as red circles, whereas the corresponding mean values and standard deviations (when possible to calculate) are depicted as black squares and error bars, respectively. The shaded regions indicates the values obtained from simulations (with $n_g = 20$) of the normalised $\Gamma_{\mathrm{wg}}/(\Gamma_{\mathrm{B}} n_g)$, for both $\hat{y}$-oriented (bright red) and $\hat{x}$-oriented (bright blue), and they are calculated for an area that represents twice the standard deviation of the alignment error of our localisation protocol. The calculated branching ratio $\Gamma^{\mathrm{Y}}_{\mathrm{wg}}/\Gamma^{\mathrm{X}}_{\mathrm{wg}}$ is also shown (green curve, right axis).

$QE_{\mathrm{wg},2} = 0.78$ to $QE_{\mathrm{wg},2} = 0.86$ for $\Delta\lambda_{be} \to 0$ nm. These results agree well with our model and demonstrate that electrical tuning of the QD emission can be used to successfully overcome the suppression caused by the spatial position and, more importantly, to improve the QE_{wg} of the emitters.

The spatial dependence of the QD emission properties is presented in Fig. 6.11, where the data are grouped by the position of the emitter within the unit cell, both along the x- and y-direction (Fig. 6.11a and b, respectively). Here, the evaluated decay rates Γ_{wg} are normalised by the mean rate obtained for QDs in bulk Γ_{B} and the value of n_g that each QD experiences. The individual measurements are depicted as red circles, whereas the mean and standard deviations calculated at each positions are shown as black squares and error bars, respectively. For comparison, we present in the same plots also the calculated values of the normalised $\Gamma_{\mathrm{wg}}/(\Gamma_{\mathrm{B}} n_g)$ (with $n_g = 20$) obtained from FE simulations of the structures under study [50]. Both the transverse ($\hat{y}$-oriented, bright red) and longitudinal ($\hat{x}$-oriented, bright blue) dipoles are shown and they are depicted as shaded areas containing all the values measured in a region delimited by 2 standard deviations of the alignment error measured for this sample (see Sec. 5.4). The plots demonstrate a qualitative agreement

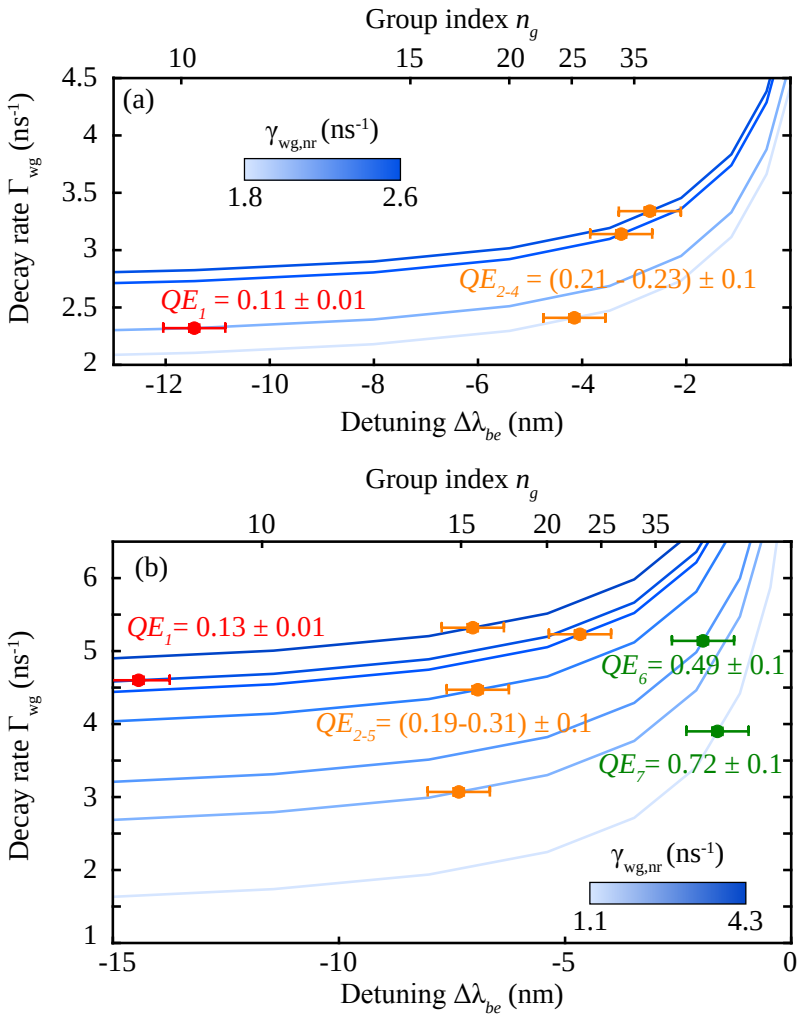

Figure 6.12: Decay rates as a function of detuning for QDs placed at locations of (a) minimum and (b) maximum of F_p. The corresponding values of group index n_g are also shown (top axis). The data of each plot is fitted by eq. (6.3) where the ratio Γ_{wg}/n_g is kept constant while varying $\gamma_{wg,nr}$. The range of values for $\gamma_{wg,nr}$ are indicated by the colour-coded curves in each plot. The fitting parameters are used to calculated the value of QE, revealing QDs with decay rates that are suppressed (red), enhanced (green) or comparable to the values measured in bulk (orange).

between the theory and the measured decay rates, with values increasing as the QDs move to the edge of the unit cell along the x-direction (Fig. 6.11a) and decreasing when the y-coordinate increases (Fig. 6.11b). The calculated branching ratio $\Gamma^{Y}_{wg}/\Gamma^{X}_{wg}$ is also reported in Fig. 6.11 (green curve, right axis) and its high values suggest that the detected signal is dominantly emitted by the transverse Y-dipole at most positions, an assumption that was confirmed by the fact that each collected decay curve was well-fitted by a single exponential.

We ascribe the discrepancy between the theoretical values and those extrapolated from our analysis to the lack of extensive statistic and to the large and variable non-radiative component that characterises the decay rates of the QDs in the investigated wafer. Assuming that QDs placed in the same position have an identical factor $A(\mathbf{r})$, every emitter in the same spatial group can be simultaneously fitted with eq. (6.3) and their values of $\gamma_{wg,r}$, $\gamma_{wg,nr}$ and the corresponding quantum

efficiencies can thus be evaluated. Fig. 6.12 reports the results of such analysis for QDs located at two different positions of the unit cell, namely (0.5a, 0.5a) (Fig. 6.12a) and (0.5a, 0) (Fig. 6.12b), i.e. respectively at the expected minimum and maximum of the simulated F_p (cf. Fig. 6.8b).

Similarly to what we saw already in Fig. 6.10, Fig. 6.12a demonstrates that QDs located spatially in regions where $F_p < 1$ and spectrally far from the band edge have slow radiative decay rates, resulting in low levels of quantum efficiency (red dot, $QE_1 = 0.11 \pm 0.01$). Higher values of QE can be obtained by fabricating PhCWs with smaller $\Delta\lambda_{be}$, so that when the group index is around $n_g = 25 - 35$ quantum efficiencies comparable to the quantities measured in bulk can be recovered, even in the case of large non-radiative rates as demonstrated for QDs 2 to 4 in Fig. 6.12a. Positioning the emitters at the maximum of the propagating mode improves the light-matter interaction and bulk QE_{B} values can be recovered already for $n_g = 15 - 25$, even in the cases of fairly large $\gamma_{\mathrm{wg,nr}}$ (cf. QD 2 to 5 in Fig. 6.12b). Further reduction of the detuning from the band edge enables higher enhancement of the radiative component of Γ_{wg}, unlocking QE values of 0.49 and 0.72 that are well above what we measured in bulk.

6.3 Conclusions

In this chapter we have presented two experiments that exploit the capabilities of the localisation protocol developed during this PhD project. In the first investigation, we characterised the nanofabrication-induced effects on the photoluminescence emission from single QDs. We detected a spectral shift in all the studied devices, which we believe being caused by the release of strain initially accumulated inside the GaAs membrane during the wafer growth. Even though the specific magnitude and direction of such shifts is found to be dependent on the fabricated structure and employed wafer, we showed that electrical tuning can be used to correct for these changes, as it allows to partially recover the emission collected before fabrication. Finally, the analysis of the Stark shift parameters as a function of the distance between QDs and the closest vertical surface has shown no clear correlation down to a separation of about 79 nm. In general, the results show that the two-steps imaging method is an efficient tool to systematically investigate fabrication-induced changes on the spectral properties of individual QDs and provide more insight on how self-assembled QDs are affected by nearby surfaces.

In the second reported experiment, we studied the temporal response and the quantum efficiency of QDs deterministically integrated in PhCWs. The small alignment error of our technique allowed us to study the spatial dependence of the measured decay rates over different positions of the unit cell. Furthermore, the spectral characterisation performed before the nanofabrication was employed to tailor the parameters of the designed nanostructures, in order to fabricate PhCWs with a band edge spectrally close to the emission of the integrated QD. The slow-light effect achieved at such small detunings has shown to enhance the radiative decay rate of the emitters and allowed us to overcome the suppression caused by a small overlap between the dipole and the photonic mode. Even though a large non-radiative component in the decay rate of the investigated QDs has hindered an extensive optical study of the fabricated samples, we showed that the localisation technique we developed enables a rigorous analysis of the emission properties of QDs embedded in PhCWs. The knowledge that such a study may provide, in combination with the ability of designing PhCWs with band edges at frequencies arbitrarily close to the emission of the emitters, can be exploited to fabricate efficient light-matter interfaces, which are key components for advanced quantum photonic chips.

Chapter 7

Conclusions and outlook

7.1 Summary of the thesis

In this thesis, our progress on the fabrication of complex quantum-photonic architectures has been reported.

In the first part, we presented nanofabrication protocols for the production of some of the building blocks that constitute the quantum-photonic platform. Suspended nanobeam waveguides and photonic crystal waveguides have been prepared by means of an optimised soft-mask process. The low level of structural imperfections and roughness that was achieved enabled the fabrication of nanostructures for coupling photonic chips to optical fibers. Single-photon source efficiencies as high as 15.5% in nanobeam waveguides were measured [94], which is twice as much as what was previously reported for similar structures [99].

A protocol for the deposition of ohmic contacts on thin p-i-n GaAs diodes was also developed. The improved control of the electrical properties of the fabricated nanostructures enabled the successful suppression of the decoherence mechanisms originated by charge noise, and emission of single-photons showing HOM visibility of 94% was reported [32]. Moreover, the reduction of spectral diffusion achieved on gated samples allowed for the detection of near-lifetime-limited transitions from a QD embedded in a nanobeam waveguide [33]. This proves that the procedures presented in this thesis can be employed for the fabrication of complex photonic components with the high level of coherence necessary to detect exotic quantum effects such as single-photon nonlinearities [141]. Finally, the electrical contacts have also been shown to provide the control of the QD spin-state to the single-electron level and with a fidelity of 96%. We were therefore able to fabricate nanostructures that could be employed as an efficient spin-photon interface [98], which is a fundamental component for the nodes of quantum networks [45].

In the second part of this thesis, we addressed the challenges posed by the random growth of self-assembled QDs. We presented a localisation method based on a modified photoluminescence imaging approach that allowed for precise detection of the emitter positions with respect to a reference frame fabricated on the sample. We reported final location uncertainties as low as $\approx$ 5 nm. Most importantly, the knowledge of the QD locations was exploited to fabricate suspended photonic nanostructures about the emitters. A statistical analysis revealed final alignment errors smaller than 50 nm, demonstrating that the proposed protocol has the capabilities to fabricate nanophotonic devices where the QDs are deterministically placed at pre-selected locations.

We made use of the newly acquired knowledge of the QD positions to investigate for the first time the fabrication-induced effects on the photoluminescence emission of single self-assembled QDs embedded in suspended nanostructures. From all the studied devices we found an averaged spectral shift of $\approx$ 1 nm, which we suggested being caused by the redistribution of the strain accu-

mulated in the GaAs membrane after its release from the sacrificial AlGaAs layer. Nonetheless, we showed that electrical tuning can be employed to partially recover the initial emission. Furthermore, the effects of the distance between QDs and nearest vertical surface on the Stark shift parameters have also been investigated, showing that no clear correlation is visible down to a separation of about 79 nm.

Finally, we combined the developed fabrication protocols with the localisation technique to integrate single QDs in gated photonic crystal waveguides. The small accuracy error allowed for the deterministic placing of the emitters at different positions within the unit cell of the nanostructures, whereas the spectral characterisation of the QDs before fabrication facilitated the engineering of the photonic crystals in such a way that their band edge would be within 10 nm from the spectral position of the embedded emitters. We employed time-resolved measurements to investigate the spatial and spectral dependence of the emission properties of these QDs and we reported how the slow-light effect can be exploited to enhance the radiative decay rate of the QDs and hence improve their quantum efficiencies.

7.2 Outlook

The deterministic control of the spatial and spectral positions of QDs embedded in photonic nanostructures reported in this work demonstrates the capability of the developed methods to produce chips for advanced quantum photonic experiments on this platform. The localisation technique could be employed to first map the locations of the emitters on the sample and then cherry-pick only those with properties that better fulfil the requirements for the specific experiment (e.g. high quantum efficiency or narrow linewidth). The list of collected coordinates could then be used to design and position complex nanostructures on the chip, which would be subsequently fabricated with high precision and low level of defects by the protocols reported in this thesis.

The demonstrated versatility of the developed processes facilitates the implementation of a variety of new functionalities: for example, QDs could be precisely placed in photonic nanostructures that are engineered to enhance the chirality of the light-matter interaction, thus improving the emission directionality required for advanced components of photonic circuits such as CNOT gates or quantum optical circulators [97, 142]. Alternatively, additional electrical gates with dif-

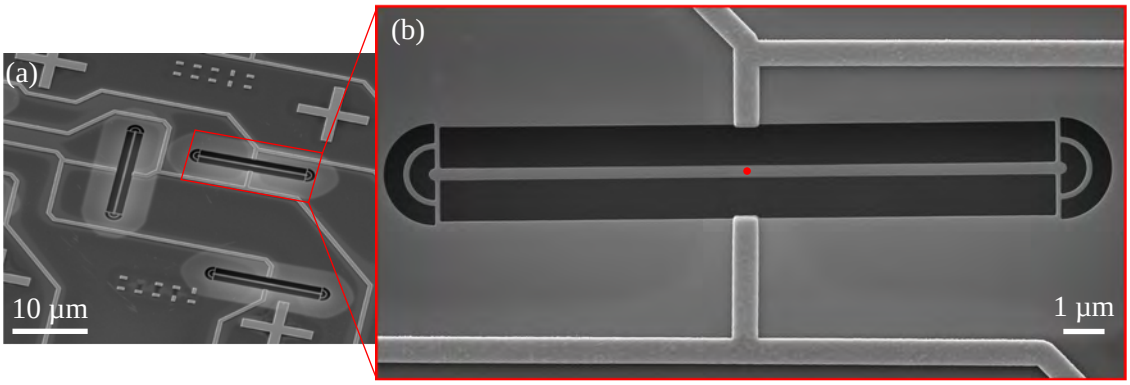

Figure 7.1: Implementation of planar electrodes in nanophotonic devices. (a) Tilted-view SEM image of planar metallic electrodes fabricated about the pre-selected positions of the QDs, which are integrated in suspended nanobeam waveguides. (b) Close-up view of one of the nanostructures. The embedded QD is marked by the red dot.

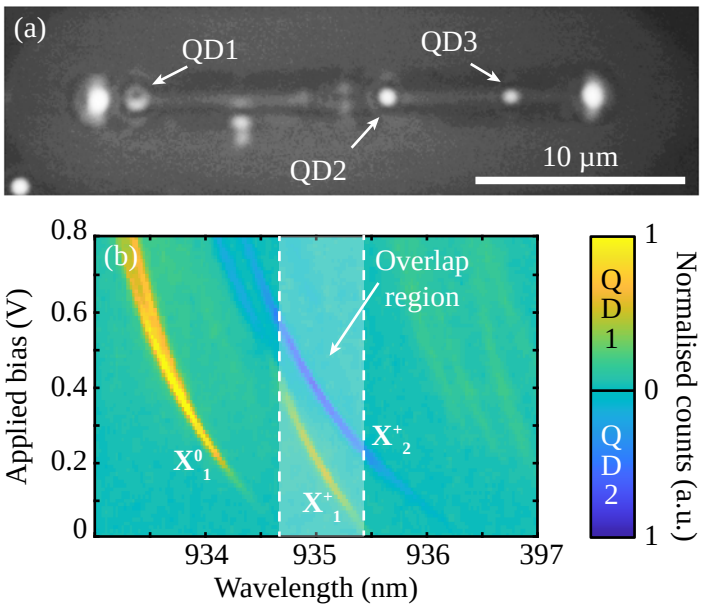

Figure 7.2: Photonic nanostructures with multiple emitters. (a) Photoluminescence image of a suspended nanobeam waveguides hosting three QDs coupled to it (indicated by white arrows). The two outermost bright spots correspond to the light emitted from two grating out-couplers. (b) Voltage-wavelength PL spectra for two QDs pre-selected by the developed localisation technique. By controlling the bias applied to each of the emitters, overlap (delimited by the white dashed lines) between the fluorescence signals of excitons generated in the different QDs can be achieved.

ferent geometries could be accurately deposited around the location of the emitters. An example of this type of device is shown in Fig. 7.1a, which reports an SEM image of our first attempt to fabricate planar electrodes around QDs embedded in nanobeam waveguides (red dot in Fig. 7.1b). This configuration allows for the application of a local electric field that is coplanar with the emitters, which has been shown to be effective in reducing the fine structure splitting in self-assembled QDs [143, 144] and hence may be employed for the generation of highly entangled photons [145]. Moreover, no doped layers are required for this type of electrodes and hence all the detrimental effects of the built-in field are avoided.

Finally, it is worth mentioning that all the considerations so far have been focused on a single QD per device. Excitingly, the technique presented in this thesis poses no limitations on the number of emitters that can be simultaneously located and hence readily provide all the necessary tools to fabricate nanostructures embedding multiple QDs, as shown in the photoluminescence image in Fig. 7.2a. Such a device is one of the most interesting elements of complex quantum photonic systems, as it may be employed to study nonlinear quantum effects in exotic states [141, 146]. The intrinsic randomness of self-assembled QDs has always hindered the fabrication of this type of component, as the emitters not only must be placed in the same nanostructure at precise locations, but also have to be on resonance with each other to be able to interact by exchanging photons. The localisation technique presented in this thesis offers the optimal tools for overcoming these issues, as it allows for the *a priori* selection of QDs that can be electrically tuned to emit light with the same frequency (cf. Fig. 7.2b). Such capability, in combination with the developed high-precision nanofabrication protocols, constitutes an important step towards the deterministic production of complex quantum circuits based on self-assembled QDs integrated in GaAs nanophotonic structures.

Appendix A

Layout of wafers

In this appendix the nominal values for the structure of the wafers used during the work for this thesis are reported.

Material	**Thickness (nm)**
GaAs	81
InAs QDs	
GaAs	79
$Al_{0.77}Ga_{0.23}As$	1371
GaAs (100)	substrate

Table A.1: Layers structure of the undoped sample.

Material	**Doping** (cm^{-3})	**Thickness (nm)**
p - GaAs	$1x10^{19}$	20
p - GaAs	$1x10^{18}$	14
GaAs	-	1
$Al_{0.3}Ga_{0.7}As$	-	45
GaAs	-	8
InAs QDs		
GaAs	-	2
$Al_{0.3}Ga_{0.7}As$	-	7
GaAs	-	7
n - GaAs	$2x10^{18}$	40
n - GaAs	$>2x10^{18}$	15
GaAs	-	14
$Al_{0.75}Ga_{0.25}As$	-	1371
GaAs (100)	-	substrate

Table A.2: Layers structure of the doped sample.

Appendix B

Developed recipes

During the work for this PhD project a number of fabrication recipes have been developed. This appendix reports a summary of them.

B.1 Recipes for the preparation of a mesa

B.1.1 Mesa layer

1. Cleave a chip of about 10 mm x 10 mm.
2. Clean the substrate by flushing it with Acetone and Isopropanol (IPA) and blow it dry with N_2.
3. Spin-coat AZ1505 at 4000 rpm for 45 s.
4. Bake the sample on hot plate at 115 °C for 45 s.
5. UV exposure of mask for mesa layer.
6. Develop in AZ developer:H_2O (1:1) at room temperature for 75 s. Rinse in MQ water and blow dry with N_2.
7. Descum in O_2 plasma (100W, 45 s).
8. RIE etching in BCl_3/Ar (5/10 sccm), RF power 43W, 20 mTorr. Time depends on the etch depth, but in general stop at 10-20 nm above the n-doped layer.
9. Remove the resist in NMP at $T = 70\,°C$ for 10 min, then NMP at room temperature for 2 min and finally rinse in IPA and N_2 blow dry.

B.1.2 n-type contact

1. Clean the substrate by flushing it with Acetone and Isopropanol and blow it dry with N_2.
2. Dehydrate the sample on a hot plate at $T = 185\,°C$ for 5 min.
3. Spin-coat negative resist man-N 1440 at 4000 rpm for 45 s.
4. Bake on hot plate at $T = 120\,°C$ for 3 min.

5. UV exposure of the n-metals layer.

6. Develop in ma-D 533S developer at room temperature for 125 min. Rinse for 1 min in MQ water and blow it dry with N_2.

7. Descum in O_2 plasma.

8. Flood exposure under mask aligner lamp (Karl Suss MJB-3) for 10 min. Do this right before evaporation.

9. Deoxidation in H_3PO_4:H_2O (1:5) for 2 min. Rinse in MQ water for 1 min and N_2 blow dry.

10. Evaporate Ni/Ge/Au/Ni/Au (5/40/60/27/150 nm) in e-beam evaporator.

11. Lift-off in hot NMP at $T = 80\,^{\circ}$C for 5 min. Then NMP at room temperature for 2 min and finally rinse in IPA and N_2 blow dry.

12. Rapid thermal annealing at $T = 420\,^{\circ}$C for 10 s.

B.1.3 p-type contact

1. Clean the substrate by flushing it with Acetone and Isopropanol and blow it dry with N_2.

2. Dehydrate the sample on a hot plate at $T = 185\,^{\circ}$C for 5 min.

3. Spin-coat negative resist man-N 1440 at 4000 rpm for 45 s.

4. Bake on hot plate at $T = 120\,^{\circ}$C for 3 min.

5. UV exposure of the p-metals layer.

6. Develop in ma-D 533S developer at room temperature for 125 s. Rinse for 1 min in MQ water and blow it dry with N_2. **IMPORTANT:** perform this step in the dark to avoid photochemical corrosion.

7. Descum in O_2 plasma.

8. Flood exposure under mask aligner lamp (Karl Suss MJB-3) for 10 min. Do this right before evaporation.

9. Deoxidation in H_3PO_4:H_2O (1:20) for 2 min. Rinse in MQ water for 1 min and N_2 blow dry. **IMPORTANT:** perform this step in the dark to avoid photochemical corrosion.

10. Evaporate Ti/Au (50/150 nm) in e-beam evaporator.

11. Lift-off in hot NMP at $T = 80\,^{\circ}$C for 5 min. Then NMP at room temperature for 2 min and finally rinse in IPA and N_2 blow dry.

B.1.4 Contact protection

1. Spin-coat resist mr-DWL 5 (6:4 dilution) at 5000 rpm for 60 s.
2. Pre-bake: on hot plate at $T = 60\,^{\circ}\mathrm{C}$ for 2 min, then set to $T = 75\,^{\circ}\mathrm{C}$ and finally $T = 90\,^{\circ}\mathrm{C}$ and wait for 4 min. The final thickness should be about 625 nm.
3. UV exposure of the metal-protection layer.
4. Repeat the same pre-bake procedure.
5. Wait at least 30 min.
6. Develop in mr-DEV 600 developer at room temperature for 90 s, then rinse in IPA for 30 s and finally in MQ water for 30 s. Use a strong agitation throughout the entire process, otherwise some residues might appear. If this happens, develop for 20 s more and repeat the rinsing steps.
7. Hard bake: 90 °C for 1 min, 100 °C for 2 min, 110 °C for 2 min, 120 °C for 5 min, 130 °C for 5 min, 140 °C for 20 min.

B.2 Recipes for fabrication of nanostructures on undoped material

B.2.1 Electron-beam lithography

1. Clean the substrate by flushing it with Acetone and Isopropanol and blow it dry with N_2.
2. Bake the substate at $T = 185\,^{\circ}\mathrm{C}$ for 5 min (dehydration).
3. Clean the substrate in NMP at $T = 60\,^{\circ}\mathrm{C}$ for 5 min and then flush it with IPA
4. Spin coat the sample with approx. 80 µL of the resist ZEP 520A for 60 s. For samples with size of about 10 mm x 10 mm, set the spin rate at 2000 rpm. For samples with size of about 5 mm x 5 mm, set the spin rate at 2400 rpm. Start the spinning after pouring the resist on the sample.
5. Clean any drops of resist from the bottom of the sample by sliding it on a piece of Si until it does not leave any traces (this prevents that the sample sticks to the Si holder after the bake).
6. Bake the sample at $T = 185\,^{\circ}\mathrm{C}$ for 5 min. If the colour of the resist is green, its thickness is correct.
7. Check the actual thickness of the resist: it must be $d \approx 550\,\mathrm{nm}$.
8. Exposed the pattern with a base dose of $D_0 = 336\,\mu\mathrm{C/cm^2}$.
9. Develop the sample in n-amylacetate at $T = -5\,^{\circ}\mathrm{C}$ for 60 s and then stop the process in IPA $T = -5\,^{\circ}\mathrm{C}$ for 10 s.
10. Blow it dry with N_2

Cleaning of the resist To remove the resist from the sample, dip it in NMP at $T = 70\,^{\circ}\mathrm{C}$ for 5 min and then flush it with IPA.

B.2.2 Dry-etching of nanostructures

The ICP system used for the etching is a PlasmlabSystem 100 ICP65, by Oxford Instruments.

1. Put a small drop of Fomblin oil on the Si carrier. The size of the drop has to be such that it does not come out from under the sample.
2. Load the Si carrier with the sample in the loadlock, evacuate it and start the process. The developed recipe is:
   - gas mixture: BCl_3/CL_2/Ar with respective flows 3/4/25 sccm
   - chamber pressure: 4.7 mTorr
   - ICP power: 300 W
   - DC bias: ≈ 310 V
   - table $T = 0\,^{\circ}\mathrm{C}$
3. When the process is over and the loadlock is vented, remove the carrier from the loadlock and remove the sample from the Si wafer.
4. Clean the Si wafer with IPA, blow it dry and put it back in the loadlock.
5. Remove the resist in NMP at $T = 70\,^{\circ}\mathrm{C}$ for 10 min, then NMP at room temperature for 2 min and finally rinse in IPA and N_2 blow dry.

B.2.3 Wet-etching of nanostructures

1. Prepare a solution of HF 10% by adding 5 ml of HF 40% to 15 ml of H_2O.
2. Dip the sample in the acid solution for the necessary time ($t = 45$ s gives $\approx 2\,\mu$m of undercut in photonic crystals). From now on it is important to always keep a drop of liquid on top of the chip while moving from an etchant to the other, in order to prevent any collapse due to capillary forces.
3. Stop the process by dipping the sample in MQ water for 10 min. Prepare multiple beakers with clean water and move the sample from one to another in order to progressively dilute the concentration of HF in the water.
4. Dip the sample in H_2O_2 30% w/w for 1 min (due to its high volatility, prepare this solution during the previous step in order to minimize the amount of lost reactant).
5. Stop the process in MQ water for 10 min as after the HF dip.
6. Dip the sample in H_3PO_4:H_2O (1:10) for 1 min.
7. Stop the process in MQ water for 10 min as before
8. Dip the sample in IPA for 3 min and then move it into the sample holder of the Critical Point Dryer (CPD).
9. Load the sample in the CPD and start the process.

10. When the process is over, unload the sample.

Note: In order to prevent any contamination between the used reactant, it is important to change the MQ water after every use.

B.3 Recipe for fabrication of nanostructures on doped material

The steps for e-beam lithography and dry etching are the same as for undoped samples.

B.3.1 Wet-etching of nanostructures

1. Prepare a solution of HF 10% by adding 5 ml of HF 40% to 15 ml of H_2O.
2. Dip the sample in the acid solution for the necessary time ($t = 45$ s gives $\sim 2\,\mu$m of undercut in photonic crystals). From now on it is important to always keep a drop of liquid on top of the chip while moving from an etchant to another, in order to prevent any collapse due to capillary forces.
3. Stop the process by dipping the sample in MQ water for 10 min. Prepare multiple beakers with clean water and move the sample from one to another in order to progressively dilute the concentration of HF in the water.
4. Dip the sample in IPA for 3 min and then move it into the sample holder of the Critical Point Dryer (CPD).
5. Load the sample in the CPD and start the process.
6. When the process is over, unload the sample.

B.4 Recipe for fabrication of reference frame for localisation technique

B.4.1 Electron-beam lithography

1. Clean the substrate by flushing it with Acetone and IPA and blow it dry with N_2.
2. Bake the substate at $T = 185\,^{\circ}$C for 5 min (dehydration).
3. Clean the substrate in NMP at $T = 60\,^{\circ}$C for 5 min and then flush it with IPA
4. Spin coat the sample with approx. 80 µL of the resist ZEP 520A for 60 s. For samples with size of about 10 mm x 10 mm, set the spin rate at 2000 rpm. For samples with size of about 5 mm x 5 mm, set the spin rate at 2400 rpm. Start the spinning right after pouring the resist on the sample.
5. Clean any drops of resist from the bottom of the sample by sliding it on a piece of Si until it does not leave any traces (this prevents that the sample sticks to the Si holder after the bake).
6. Bake the sample at $T = 185\,^{\circ}$C for 5 min. If the colour of the resist is green, its thickness is correct.

7. Check the actual thickness of the resist: it must be $d \approx 550 - 570\,\text{nm}$.
8. Exposed the pattern with a base dose of $D_0 = 336\,\mu\text{C}/\text{cm}^2$.
9. Develop the sample in n-amylacetate at $T = -5\,^\circ\text{C}$ for 70 s and then stop the process in IPA $T = -5\,^\circ\text{C}$ for 10 s.
10. Blow it dry with N_2

Cleaning of the resist To remove the resist from the sample, dip it in NMP at $T = 70\,^\circ\text{C}$ for 5 min and then flush it with IPA.

B.4.2 Metal deposition

1. Chemical descum: dip the sample in a solution of HCl:H_2O (1:10) for 30 s and then quickly rinse in MQ water. It can be performed in darkness to prevent any corrosion.
2. Load the sample in the e-beam evaporator and run one step of Ar sputtering (100 sccm, 20.5 W) for 60 s.
3. Metal deposition: evaporate Ti/Au (10/90 nm). Alternatively Cr/Au (10/90 nm) works too.
4. Lift-off in hot NMP ($T = 80\,^\circ\text{C}$) for 10 min. Then move the sample is a beaker with clean NMP and sonicate gently (i.e. plastic beaker, 80 kHz, 30% power). Flush the sample with IPA and then dip it in another beaker with IPA for inspection. If the pattern looks fine, flush with IPA again and blow dry with N_2.

Note: This recipe can be used for any metallic pattern with thickness of about 100 nm.

Bibliography

[1] B. Hensen, H. Bernien, A. E. Dréau, A. Reiserer, N. Kalb, M. S. Blok, J. Ruitenberg, R. F. L. Vermeulen, R. N. Schouten, C. Abellán, W. Amaya, V. Pruneri, M. W. Mitchell, M. Markham, D. J. Twitchen, D. Elkouss, S. Wehner, T. H. Taminiau, and R. Hanson, "Loophole-free Bell inequality violation using electron spins separated by 1.3 kilometres," Nature **526**, 682 (2015).

[2] C. B. Møller, R. A. Thomas, G. Vasilakis, E. Zeuthen, Y. Tsaturyan, M. Balabas, K. Jensen, A. Schliesser, K. Hammerer, and E. S. Polzik, "Quantum back-action-evading measurement of motion in a negative mass reference frame," Nature **547**, 191 (2017).

[3] J. P. Dowling and G. J. Milburn, "Quantum technology: the second quantum revolution," Philos. Trans. R. Soc. London. Ser. A Math. Phys. Eng. Sci. **361**, 1655 (2003).

[4] P. Lodahl, "Quantum-dot based photonic quantum networks," Quantum Sci. Technol. **3**, 013001 (2018).

[5] D. Buterakos, E. Barnes, and S. E. Economou, "Deterministic Generation of All-Photonic Quantum Repeaters from Solid-State Emitters," Phys. Rev. X **7**, 041023 (2017).

[6] P. Lodahl, S. Mahmoodian, and S. Stobbe, "Interfacing single photons and single quantum dots with photonic nanostructures," Rev. Mod. Phys. **87**, 347 (2015).

[7] R. J. Warburton, "Single spins in self-assembled quantum dots," Nat. Mater. **12**, 483 (2013).

[8] M. Arcari, I. Söllner, A. Javadi, S. Lindskov Hansen, S. Mahmoodian, J. Liu, H. Thyrrestrup, E. H. Lee, J. D. Song, S. Stobbe, and P. Lodahl, "Near-Unity Coupling Efficiency of a Quantum Emitter to a Photonic Crystal Waveguide," Phys. Rev. Lett. **113**, 093603 (2014).

[9] P. M. Petroff, A. Lorke, and A. Imamoglu, "Epitaxially self-assembled quantum dots," Phys. Today **54**, 46 (2001).

[10] C. Kittel, *Introduction to Solid State Physics*, 8th ed. (John Wiley & Sons, Inc., 2004).

[11] T. Ihn, *Semiconductor Nanostructures* (Oxford University Press, USA, 2010).

[12] A. Baca and C. Ashby, *Fabrication of GaAs Devices* (IET, The Institution of Engineering and Technology, Michael Faraday House, Six Hills Way, Stevenage SG1 2AY, UK, 2005).

[13] I. Vurgaftman, J. R. Meyer, and L. R. Ram-Mohan, "Band parameters for III-V compound semiconductors and their alloys," J. Appl. Phys. **89**, 5815 (2001).

[14] S. Sze and K. K. Ng, *Physics of Semiconductor Devices* (John Wiley & Sons, Inc., Hoboken, NJ, USA, 2006).

[15] S. C. Jain and D. Roulston, "A simple expression for band gap narrowing (BGN) in heavily doped Si, Ge, GaAs and Ge_xSi_{1-x} strained layers," Solid. State. Electron. **34**, 453 (1991).

[16] G. Borghs, K. Bhattacharyya, K. Deneffe, P. Van Mieghem, and R. Mertens, "Band-gap narrowing in highly doped n- and p-type GaAs studied by photoluminescence spectroscopy," J. Appl. Phys. **66**, 4381 (1989).

[17] T. Pregnolato, *Fabrication and Characterization of a Photonic-Crystal Cavity with Electrically Tuneable Quantum Dots*, MSc thesis, University of Copenhagen (2014).

[18] W. Mönch, *Semiconductor Surfaces and Interfaces*, Springer Series in Surface Sciences, Vol. 26 (Springer Berlin Heidelberg, Berlin, Heidelberg, 2001).

[19] M. D. Pashley, K. W. Haberern, R. M. Feenstra, and P. D. Kirchner, "Different Fermi-level pinning behaviour on n- and p-type GaAs(001)," Phys. Rev. B **48**, 4612 (1993).

[20] D. Yan, F. H. Pollak, T. P. Chin, and J. M. Woodall, "In situ study of Fermi-level pinning on n- and p-type GaAs (001) grown by molecular-beam epitaxy using photoreflectance," Phys. Rev. B **52**, 4674 (1995).

[21] P. H. L. Notten, *Electrochemical study of the etching of III-V semiconductors*, Ph.D. thesis, Technische Universiteit Eindhoven (1989).

[22] J. Márquez, L. Geelhaar, and K. Jacobi, "Atomically resolved structure of InAs quantum dots," Appl. Phys. Lett. **78**, 2309 (2001).

[23] D. Leonard, K. Pond, and P. M. Petroff, "Critical layer thickness for self-assembled InAs islands on GaAs," Phys. Rev. B **50**, 11687 (1994).

[24] K. Jacobi, "Atomic structure of InAs quantum dots on GaAs," Prog. Surf. Sci. **71**, 185 (2003).

[25] A. Gushterov, L. Lingys, and J. Reithmaier, "Control of dot geometry and photoluminescence linewidth of InGaAs/GaAs quantum dots by growth conditions," J. Cryst. Growth **311**, 1783 (2009).

[26] V. Dubrovskii, G. Cirlin, Y. Musikhin, Y. Samsonenko, A. Tonkikh, N. Polyakov, V. Egorov, A. Tsatsul'nikov, N. Krizhanovskaya, V. Ustinov, and P. Werner, "Effect of growth kinetics on the structural and optical properties of quantum dot ensembles," J. Cryst. Growth **267**, 47 (2004).

[27] P. Joyce, T. Krzyzewski, G. Bell, T. Jones, S. Malik, D. Childs, and R. Murray, "Growth rate effects on the size, composition and optical properties of InAs/GaAs quantum dots grown by molecular beam epitaxy," J. Cryst. Growth **227-228**, 1000 (2001).

[28] L. Novotny and B. Hecht, *Principles of Nano-Optics* (Cambridge University Press, Cambridge, 2012).

[29] S. Seidl, M. Kroner, P. A. Dalgarno, A. Högele, J. M. Smith, M. Ediger, B. D. Gerardot, J. M. Garcia, P. M. Petroff, K. Karrai, and R. J. Warburton, "Absorption and photoluminescence spectroscopy on a single self-assembled charge-tunable quantum dot," Phys. Rev. B **72**, 195339 (2005).

[30] P. A. Dalgarno, J. M. Smith, J. McFarlane, B. D. Gerardot, K. Karrai, A. Badolato, P. M. Petroff, and R. J. Warburton, "Coulomb interactions in single charged self-assembled quantum dots: Radiative lifetime and recombination energy," Phys. Rev. B **77**, 245311 (2008).

[31] M. C. Löbl, I. Söllner, A. Javadi, T. Pregnolato, R. Schott, L. Midolo, A. V. Kuhlmann, S. Stobbe, A. D. Wieck, P. Lodahl, A. Ludwig, and R. J. Warburton, "Narrow optical linewidths and spin pumping on charge-tunable close-to-surface self-assembled quantum dots in an ultrathin diode," Phys. Rev. B **96**, 165440 (2017).

[32] G. Kiršanskė, H. Thyrrestrup, R. S. Daveau, C. L. Dreeßen, T. Pregnolato, L. Midolo, P. Tighineanu, A. Javadi, S. Stobbe, R. Schott, A. Ludwig, A. D. Wieck, S. I. Park, J. D. Song, A. V. Kuhlmann, I. Söllner, M. C. Löbl, R. J. Warburton, and P. Lodahl, "Indistinguishable and efficient single photons from a quantum dot in a planar nanobeam waveguide," Phys. Rev. B **96**, 165306 (2017).

[33] H. Thyrrestrup, G. Kiršanskė, H. Le Jeannic, T. Pregnolato, L. Zhai, L. Raahauge, L. Midolo, N. Rotenberg, A. Javadi, R. Schott, A. D. Wieck, A. Ludwig, M. C. Löbl, I. Söllner, R. J. Warburton, and P. Lodahl, "Quantum Optics with Near-Lifetime-Limited Quantum-Dot Transitions in a Nanophotonic Waveguide," Nano Lett. **18**, 1801 (2018).

[34] D. Miller, D. Chemla, T. Damen, A. Gossard, W. Wiegmann, T. Wood, and C. Burrus, "Band-Edge Electroabsorption in Quantum Well Structures: The Quantum-Confined Stark Effect," Phys. Rev. Lett. **53**, 2173 (1984).

[35] P. Fry, I. Itskevich, D. Mowbray, M. Skolnick, J. Finley, J. Barker, E. O'Reilly, L. Wilson, I. Larkin, P. Maksym, M. Hopkinson, M. Al-Khafaji, J. David, A. Cullis, G. Hill, and J. Clark, "Inverted Electron-Hole Alignment in InAs-GaAs Self-Assembled Quantum Dots," Phys. Rev. Lett. **84**, 733 (2000).

[36] J. Finley, M. Sabathil, P. Vogl, G. Abstreiter, R. Oulton, A. Tartakovskii, D. Mowbray, M. Skolnick, S. Liew, A. Cullis, and M. Hopkinson, "Quantum-confined Stark shifts of charged exciton complexes in quantum dots," Phys. Rev. B **70**, 201308 (2004).

[37] A. J. Bennett, R. B. Patel, J. Skiba-Szymanska, C. A. Nicoll, I. Farrer, D. A. Ritchie, and A. J. Shields, "Giant Stark effect in the emission of single semiconductor quantum dots," Appl. Phys. Lett. **97**, 031104 (2010).

[38] Q. Wang, S. Stobbe, and P. Lodahl, "Mapping the Local Density of Optical States of a Photonic Crystal with Single Quantum Dots," Phys. Rev. Lett. **107**, 167404 (2011).

[39] J. Johansen, B. Julsgaard, S. Stobbe, J. M. Hvam, and P. Lodahl, "Probing long-lived dark excitons in self-assembled quantum dots," Phys. Rev. B **81**, 081304 (2010).

[40] S. Stobbe, J. Johansen, P. T. Kristensen, J. M. Hvam, and P. Lodahl, "Frequency dependence of the radiative decay rate of excitons in self-assembled quantum dots: Experiment and theory," Phys. Rev. B **80**, 155307 (2009).

[41] A. V. Kuhlmann, J. Houel, A. Ludwig, L. Greuter, D. Reuter, A. D. Wieck, M. Poggio, and R. J. Warburton, "Charge noise and spin noise in a semiconductor quantum device," Nat. Phys. **9**, 570 (2013).

[42] A. V. Kuhlmann, J. H. Prechtel, J. Houel, A. Ludwig, D. Reuter, A. D. Wieck, and R. J. Warburton, "Transform-limited single photons from a single quantum dot," Nat. Commun. **6**, 8204 (2015).

[43] P. Tighineanu, C. L. Dreeßen, C. Flindt, P. Lodahl, and A. S. Sørensen, "Phonon Decoherence of Quantum Dots in Photonic Structures: Broadening of the Zero-Phonon Line and the Role of Dimensionality," Phys. Rev. Lett. **120**, 257401 (2018).

[44] C. L. Dreeßen, C. Ouellet-Plamondon, P. Tighineanu, X. Zhou, L. Midolo, A. S. Sørensen, and P. Lodahl, "Suppressing phonon decoherence of high performance single-photon sources in nanophotonic waveguides," Quantum Sci. Technol. **4**, 015003 (2018).

[45] J. Borregaard, A. S. Sørensen, and P. Lodahl, "Quantum Networks with Deterministic Spin-Photon Interfaces," Adv. Quantum Technol. **2**, 1800091 (2019).

[46] B. Urbaszek, X. Marie, T. Amand, O. Krebs, P. Voisin, P. Maletinsky, A. Högele, and A. Imamoglu, "Nuclear spin physics in quantum dots: An optical investigation," Rev. Mod. Phys. **85**, 79 (2013).

[47] N. Somaschi, V. Giesz, L. De Santis, J. C. Loredo, M. P. Almeida, G. Hornecker, S. L. Portalupi, T. Grange, C. Antón, J. Demory, C. Gómez, I. Sagnes, N. D. Lanzillotti-Kimura, A. Lemaítre, A. Auffeves, A. G. White, L. Lanco, and P. Senellart, "Near-optimal single-photon sources in the solid state," Nat. Photonics **10**, 340 (2016).

[48] J. D. Joannopoulos, S. G. Johnson, J. N. Winn, and R. D. Meade, *Photonic Crystals: Molding the Flow of Light*, 2nd ed. (Princeton University Press, 2008).

[49] S. Hughes, "Enhanced single-photon emission from quantum dots in photonic crystal waveguides and nanocavities," Opt. Lett. **29**, 2659 (2004).

[50] A. Javadi, S. Mahmoodian, I. Söllner, and P. Lodahl, "Numerical modeling of the coupling efficiency of single quantum emitters in photonic-crystal waveguides," J. Opt. Soc. Am. B **35**, 514 (2018).

[51] K. Prindal-Nielsen, *Light Matter Interaction in Nanobeam Waveguides*, MSc thesis, University of Copenhagen (2017).

[52] C. Constancias, S. Landis, S. Manakli, L. Martin, L. Pain, and D. Rio, "Electron Beam Lithography," in *Lithography*, edited by S. Landis (John Wiley & Sons, Inc., Hoboken, NJ USA, 2013) Chap. 3.

[53] K. Koshelev, M. Ali Mohammad, T. Fito, K. L. Westra, S. K. Dew, and M. Stepanova, "Comparison between ZEP and PMMA resists for nanoscale electron beam lithography experimentally and by numerical modeling," J. Vac. Sci. Technol. B, Nanotechnol. Microelectron. Mater. Process. Meas. Phenom. **29**, 06F306 (2011).

[54] R. Kirchner, V. Guzenko, I. Vartiainen, N. Chidambaram, and H. Schift, "ZEP520A A resist for electron-beam grayscale lithography and thermal reflow," Microelectron. Eng. **153**, 71 (2016).

[55] L.-C. Chang, C. Nien, J.-H. Ye, C.-H. Chung, V.-C. Su, C.-H. Wu, and C.-H. Kuan, "A comprehensive model for sub-10 nm electron-beam patterning through the short-time and cold development," Nanotechnology **28**, 425301 (2017).

[56] R. Wüest, P. Strasser, M. Jungo, F. Robin, D. Erni, and H. Jäckel, "An efficient proximity-effect correction method for electron-beam patterning of photonic-crystal devices," Microelectron. Eng. **67-68**, 182 (2003).

[57] N. Jedidi, J.-H. Tortai, T. Figueiro, and P. Schiavone, "Application of cubic spline models in electron-beam lithography," J. Vac. Sci. Technol. B, Nanotechnol. Microelectron. Mater. Process. Meas. Phenom. **33**, 041602 (2015).

[58] T. Figueiro, M. Saib, J.-H. Tortai, and P. Schiavone, "PSF calibration patterns selection based on sensitivity analysis," Microelectron. Eng. **112**, 282 (2013).

[59] C.-H. Liu, P. C. W. Ng, Y.-T. Shen, S.-W. Chien, and K.-Y. Tsai, "Impacts of point spread function accuracy on patterning prediction and proximity effect correction in low-voltage electron-beam-direct-write lithography," J. Vac. Sci. Technol. B Microelectron. Nanom. Struct. **31**, 021605 (2013).

[60] L. Midolo, T. Pregnolato, G. Kiršanskė, and S. Stobbe, "Soft-mask fabrication of gallium arsenide nanomembranes for integrated quantum photonics," Nanotechnology **26**, 484002 (2015).

[61] X. Zhang, K. Takeuchi, X. Cong, Y. Xiong, M. Morifuji, A. Maruta, H. Kajii, and M. Kondow, "Dry etching of deep air holes in GaAs/AlGaAs-based epi-wafer having InAs quantum dots for fabrication of photonic crystal laser," Jpn. J. Appl. Phys. **56**, 126501 (2017).

[62] U. K. Khankhoje, S.-H. Kim, B. C. Richards, J. Hendrickson, J. Sweet, J. D. Olitzky, G. Khitrova, H. M. Gibbs, and A. Scherer, "Modelling and fabrication of GaAs photonic-crystal cavities for cavity quantum electrodynamics." Nanotechnology **21**, 065202 (2010).

[63] J. Liu, R. Su, Y. Wei, B. Yao, S. F. C. da Silva, Y. Yu, J. Iles-Smith, K. Srinivasan, A. Rastelli, J. Li, and X. Wang, "A solid-state source of strongly entangled photon pairs with high brightness and indistinguishability," Nat. Nanotechnol. **14**, 586 (2019).

[64] C.-W. Cheng, K.-T. Shiu, N. Li, S.-J. Han, L. Shi, and D. K. Sadana, "Epitaxial lift-off process for gallium arsenide substrate reuse and flexible electronics." Nat. Commun. **4**, 1577 (2013).

[65] J. Yoon, S. Jo, I. S. Chun, I. Jung, H.-S. Kim, M. Meitl, E. Menard, X. Li, J. J. Coleman, U. Paik, and J. A. Rogers, "GaAs photovoltaics and optoelectronics using releasable multilayer epitaxial assemblies." Nature **465**, 329 (2010).

[66] A. R. Clawson, "Guide to references on IIIV semiconductor chemical etching," Mater. Sci. Eng. R Reports **31**, 1 (2001).

[67] H. Gerischer and W. Mindt, "The mechanisms of the decomposition of semiconductors by electrochemical oxidation and reduction," Electrochim. Acta **13**, 1329 (1968).

[68] H. Gerischer, "The impact of semiconductors on the concepts of electrochemistry," Electrochim. Acta **35**, 1677 (1990).

[69] P. Atkins and J. de Paula, *Physical Chemistry*, 8th ed. (W.H. Freeman and Company, 2006).

[70] J. Li and L. Peter, "Surface recombination at semiconductor electrodes," J. Electroanal. Chem. Interfacial Electrochem. **199**, 1 (1986).

[71] G. S. Weng, J. L. Luo, and D. G. Ivey, "Galvanic corrosion behavior of GaAs in acid solutions," J. Vac. Sci. Technol. A Vacuum, Surfaces, Film. **20**, 1015 (2002).

[72] C. Steer, G. Weng, J. Luo, and D. Ivey, "Formation of As_2O_3 during anodic dissolution of GaAs," Electrochem. commun. **2**, 754 (2000).

[73] W. M. Haynes, *CRC Handbook of Chemistry and Physics*, 95th ed., edited by W. M. Haynes (CRC Press, 2014).

[74] I. P. González, L. E. Muñoz Camuñez, A. G. Taboada, C. Robles Urdiales, J. M. Ripalda Cobián, and P. A. Postigo Resa, "Fabrication of high quality factor GaAs/InAsSb photonic crystal microcavities by inductively coupled plasma etching and fast wet etching," J. Vac. Sci. Technol. B, Nanotechnol. Microelectron. Mater. Process. Meas. Phenom. **32**, 011204 (2014).

[75] O. Painter, R. K. Lee, A. Scherer, A. Yariv, J. D. O'Brien, P. D. Dapkus, and I. Kim, "Two-Dimensional Photonic Band-Gap Defect Mode Laser," Science **284**, 1819 (1999).

[76] G. T. Edwards, A. Sobiesierski, D. I. Westwood, and P. M. Smowton, "Fabrication of high-aspect-ratio, sub-micron gratings in AlGaInP/GaAs laser structures using a $BCl_3/Cl_2/Ar$ inductively coupled plasma," Semicond. Sci. Technol. **22**, 1010 (2007).

[77] L. Jalabert, P. Dubreuil, F. Carcenac, S. Pinaud, L. Salvagnac, H. Granier, and C. Fontaine, "High aspect ratio GaAs nanowires made by ICP-RIE etching using Cl_2/N_2 chemistry," Microelectron. Eng. **85**, 1173 (2008).

[78] G. Kiršanskė, *Electrical control of excitons in semiconductor nanostructures, from quantum dots in photonic-crystal devices to the exciton Mott transition in coupled quantum wells*, Ph.D. thesis, University of Copenhagen, Copenhagen (2016).

[79] A. Piotrowska and E. Kaminska, "Ohmic contacts to III-V compound semiconductors," Thin Solid Films **193-194**, 511 (1990).

[80] V. Rideout, "A review of the theory and technology for ohmic contacts to group III-V compound semiconductors," Solid. State. Electron. **18**, 541 (1975).

[81] A. Piotrowska, A. Guivarc'h, and G. Pelous, "Ohmic contacts to III-V compound semiconductors: A review of fabrication techniques," Solid. State. Electron. **26**, 179 (1983).

[82] N. Braslau, J. Gunn, and J. Staples, "Metal-semiconductor contacts for GaAs bulk effect devices," Solid. State. Electron. **10**, 381 (1967).

[83] Y.-C. Shih, M. Murakami, E. L. Wilkie, and A. C. Callegari, "Effects of interfacial microstructure on uniformity and thermal stability of AuNiGe ohmic contact to n-type GaAs," J. Appl. Phys. **62**, 582 (1987).

[84] A. Lochmann, E. Stock, O. Schulz, F. Hopfer, D. Bimberg, V. A. Haisler, A. I. Toropov, A. K. Bakarov, M. Scholz, S. Büttner, and O. Benson, "Electrically driven quantum dot single photon source," Phys. status solidi **4**, 547 (2007).

[85] F. Hofbauer, S. Grimminger, J. Angele, G. Bohm, R. Meyer, M. C. Amann, and J. J. Finley, "Electrically probing photonic bandgap phenomena in contacted defect nanocavities," Appl. Phys. Lett. **91**, 201111 (2007).

[86] B. Ellis, T. Sarmiento, M. Mayer, B. Zhang, J. Harris, E. Haller, and J. Vuckovic, "Electrically pumped photonic crystal nanocavity light sources using a laterally doped p-i-n junction," Appl. Phys. Lett. **96**, 181103 (2010).

[87] A. Piotrowska, E. Kamińska, A. Barcz, J. Adamczewska, and A. Turos, "Gold-based ohmic contacts on III-V compounds: Thermally induced reactions between metallization and the semiconductor compound," Thin Solid Films **130**, 231 (1985).

[88] T. Sanada and O. Wada, "Ohmic Contacts to p-GaAs with Au/Zn/Au Structure," Jpn. J. Appl. Phys. **19**, L491 (1980).

[89] Y. Lu, T. S. Kalkur, and C. A. Paz de Araujo, "Rapid Thermal Alloyed Ohmic Contacts to p-Type GaAs," J. Electrochem. Soc. **136**, 3123 (1989).

[90] G. C. DeSalvo, "Wet Chemical Digital Etching of GaAs at Room Temperature," J. Electrochem. Soc. **143**, 3652 (1996).

[91] J. Moore, H. Hendriks, and A. Morales, "Characterization and Control of Galvanic Corrosion During GaAs Wafer Photoresist Processing," in *2003 Int. Conf. Compd. Semicond. Manuf.*, 831 (2003).

[92] M. Dejarld, J. C. Shin, W. Chern, D. Chanda, K. Balasundaram, J. A. Rogers, and X. Li, "Formation of high aspect ratio GaAs nanostructures with metal-assisted chemical etching," Nano Lett. **11**, 5259 (2011).

[93] J. van de Ven and J. J. Kelly, "Galvanic Effects in the Etching of Semiconductor p/n Structures," J. Electrochem. Soc. **148**, G10 (2001).

[94] R. S. Daveau, K. C. Balram, T. Pregnolato, J. Liu, E. H. Lee, J. D. Song, V. Verma, R. Mirin, S. W. Nam, L. Midolo, S. Stobbe, K. Srinivasan, and P. Lodahl, "Efficient fiber-coupled single-photon source based on quantum dots in a photonic-crystal waveguide," Optica **4**, 178 (2017).

[95] R. S. Daveau, *Efficient fiber-coupled single-photon sources based on quantum dots*, Ph.D. thesis, University of Copenhagen, Copenhagen (2016).

[96] A. Javadi, I. Söllner, M. Arcari, S. L. L. Hansen, L. Midolo, S. Mahmoodian, G. Kiršanskė, T. Pregnolato, E. Lee, J. Song, S. Stobbe, and P. Lodahl, "Single-photon non-linear optics with a quantum dot in a waveguide," Nat. Commun. **6**, 8655 (2015).

[97] I. Söllner, S. Mahmoodian, S. L. Hansen, L. Midolo, A. Javadi, G. Kiršanskė, T. Pregnolato, H. El-Ella, E. H. Lee, J. D. Song, S. Stobbe, and P. Lodahl, "Deterministic photonemitter coupling in chiral photonic circuits," Nat. Nanotechnol. **10**, 775 (2015).

[98] A. Javadi, D. Ding, M. H. Appel, S. Mahmoodian, M. C. Löbl, I. Söllner, R. Schott, C. Papon, T. Pregnolato, S. Stobbe, L. Midolo, T. Schröder, A. D. Wieck, A. Ludwig, R. J. Warburton, and P. Lodahl, "Spinphoton interface and spin-controlled photon switching in a nanobeam waveguide," Nat. Nanotechnol. **13**, 398 (2018).

[99] M. Davanço, M. T. Rakher, W. Wegscheider, D. Schuh, A. Badolato, and K. Srinivasan, "Efficient quantum dot single photon extraction into an optical fiber using a nanophotonic directional coupler," Appl. Phys. Lett. **99**, 121101 (2011).

[100] X. Ding, Y. He, Z.-C. Duan, N. Gregersen, M.-C. Chen, S. Unsleber, S. Maier, C. Schneider, M. Kamp, S. Höfling, C.-Y. Lu, and J.-W. Pan, "On-Demand Single Photons with High Extraction Efficiency and Near-Unity Indistinguishability from a Resonantly Driven Quantum Dot in a Micropillar," Phys. Rev. Lett. **116**, 020401 (2016).

[101] B. M. D. Rigal, *Site-controlled quantum dots integrated with photonic crystal waveguides and cavities*, Ph.D. thesis, EPFL (2018).

[102] B. Rigal, C. Jarlov, P. Gallo, B. Dwir, A. Rudra, M. Calic, and E. Kapon, "Site-controlled quantum dots coupled to a photonic crystal molecule," Appl. Phys. Lett. **107**, 141103 (2015).

[103] C. Jarlov, A. Lyasota, L. Ferrier, P. Gallo, B. Dwir, A. Rudra, and E. Kapon, "Exciton dynamics in a site-controlled quantum dot coupled to a photonic crystal cavity," Appl. Phys. Lett. **107**, 191101 (2015).

[104] A. Huggenberger, C. Schneider, C. Drescher, S. Heckelmann, T. Heindel, S. Reitzenstein, M. Kamp, S. Höfling, L. Worschech, and A. Forchel, "Site-controlled In(Ga)As/GaAs quantum dots for integration into optically and electrically operated devices," J. Cryst. Growth **323**, 194 (2011).

[105] K. D. Jöns, P. Atkinson, M. Müller, M. Heldmaier, S. M. Ulrich, O. G. Schmidt, and P. Michler, "Triggered Indistinguishable Single Photons with Narrow Line Widths from Site-Controlled Quantum Dots," Nano Lett. **13**, 126 (2013).

[106] F. Albert, S. Stobbe, C. Schneider, T. Heindel, S. Reitzenstein, S. Höfling, P. Lodahl, L. Worschech, and A. Forchel, "Quantum efficiency and oscillator strength of site-controlled InAs quantum dots," Appl. Phys. Lett. **96**, 151102 (2010).

[107] A. Badolato, K. Hennessy, M. Atatüre, J. Dreiser, E. Hu, P. M. Petroff, and A. Imamoglu, "Deterministic coupling of single quantum dots to single nanocavity modes." Science **308**, 1158 (2005).

[108] K. Kuruma, Y. Ota, M. Kakuda, D. Takamiya, S. Iwamoto, and Y. Arakawa, "Position dependent optical coupling between single quantum dots and photonic crystal nanocavities," Appl. Phys. Lett. **109**, 071110 (2016).

[109] S. M. Thon, M. T. Rakher, H. Kim, J. Gudat, W. T. M. Irvine, P. M. Petroff, and D. Bouwmeester, "Strong coupling through optical positioning of a quantum dot in a photonic crystal cavity," Appl. Phys. Lett. **94**, 111115 (2009).

[110] R. J. Coles, D. M. Price, J. E. Dixon, B. Royall, E. Clarke, P. Kok, M. S. Skolnick, A. M. Fox, and M. N. Makhonin, "Chirality of nanophotonic waveguide with embedded quantum emitter for unidirectional spin transfer," Nat. Commun. **7**, 11183 (2016).

[111] L. Sapienza, J. Liu, J. D. Song, S. Fält, W. Wegscheider, A. Badolato, and K. Srinivasan, "Combined atomic force microscopy and photoluminescence imaging to select single InAs/GaAs quantum dots for quantum photonic devices," Sci. Rep. **7**, 6205 (2017).

[112] T. Kojima, K. Kojima, T. Asano, and S. Noda, "Accurate alignment of a photonic crystal nanocavity with an embedded quantum dot based on optical microscopic photoluminescence imaging," Appl. Phys. Lett. **102**, 011110 (2013).

[113] L. Sapienza, M. Davanço, A. Badolato, and K. Srinivasan, "Nanoscale optical positioning of single quantum dots for bright and pure single-photon emission," Nat. Commun. **6**, 7833 (2015).

[114] J. Liu, M. I. Davanço, L. Sapienza, K. Konthasinghe, J. V. De Miranda Cardoso, J. D. Song, A. Badolato, and K. Srinivasan, "Cryogenic photoluminescence imaging system for nanoscale positioning of single quantum emitters," Rev. Sci. Instrum. **88**, 023116 (2017).

[115] Y.-M. He, J. Liu, S. Maier, M. Emmerling, S. Gerhardt, M. Davanço, K. Srinivasan, C. Schneider, and S. Höfling, "Deterministic implementation of a bright, on-demand single-photon source with near-unity indistinguishability via quantum dot imaging," Optica **4**, 802 (2017).

[116] J. Liu, K. Konthasinghe, M. Davanço, J. Lawall, V. Anant, V. Verma, R. Mirin, S. W. Nam, J. D. Song, B. Ma, Z. S. Chen, H. Q. Ni, Z. C. Niu, and K. Srinivasan, "Single Self-Assembled InAs/GaAs Quantum Dots in Photonic Nanostructures: The Role of Nanofabrication," Phys. Rev. Appl. **9**, 064019 (2018).

[117] S. Liu, Y. Wei, R. Su, R. Su, B. Ma, Z. Chen, H. Ni, Z. Niu, Y. Yu, Y. Wei, X. Wang, and S. Yu, "A deterministic quantum dot micropillar single photon source with >65% extraction efficiency based on fluorescence imaging method," Sci. Rep. **7**, 13986 (2017).

[118] A. Dousse, J. Suffczyński, R. Braive, A. Miard, A. Lemaître, I. Sagnes, L. Lanco, J. Bloch, P. Voisin, and P. Senellart, "Scalable implementation of strongly coupled cavity-quantum dot devices," Appl. Phys. Lett. **94**, 121102 (2009).

[119] A. Dousse, L. Lanco, J. Suffczyński, E. Semenova, A. Miard, A. Lemaître, I. Sagnes, C. Roblin, J. Bloch, and P. Senellart, "Controlled Light-Matter Coupling for a Single Quantum Dot Embedded in a Pillar Microcavity Using Far-Field Optical Lithography," Phys. Rev. Lett. **101**, 267404 (2008).

[120] A. K. Nowak, S. L. Portalupi, V. Giesz, O. Gazzano, C. Dal Savio, P.-F. Braun, K. Karrai, C. Arnold, L. Lanco, I. Sagnes, A. Lemaître, and P. Senellart, "Deterministic and electrically tunable bright single-photon source," Nat. Commun. **5**, 3240 (2014).

[121] M. Sartison, S. L. Portalupi, T. Gissibl, M. Jetter, H. Giessen, and P. Michler, "Combining in-situ lithography with 3D printed solid immersion lenses for single quantum dot spectroscopy," Sci. Rep. **7**, 39916 (2017).

[122] M. Gschrey, F. Gericke, A. Schüßler, R. Schmidt, J.-H. Schulze, T. Heindel, S. Rodt, A. Strittmatter, and S. Reitzenstein, "In situ electron-beam lithography of deterministic single-quantum-dot mesa-structures using low-temperature cathodoluminescence spectroscopy," Appl. Phys. Lett. **102**, 251113 (2013).

[123] M. Gschrey, R. Schmidt, J.-H. Schulze, A. Strittmatter, S. Rodt, and S. Reitzenstein, "Resolution and alignment accuracy of low-temperature in situ electron beam lithography for nanophotonic device fabrication," J. Vac. Sci. Technol. B, Nanotechnol. Microelectron. Mater. Process. Meas. Phenom. **33**, 021603 (2015).

[124] S. Fischbach, M. V. Helversen, M. Schmidt, A. Kaganskiy, R. Schmidt, A. Schliwa, T. Heindel, S. Rodt, and S. Reitzenstein, "A deterministically fabricated spectrally-tunable quantum dot based single-photon source," (2018), arXiv:1805.10623 .

[125] P. Mrowiński, P. Schnauber, P. Gutsche, A. Kaganskiy, J. Schall, S. Burger, S. Rodt, and S. Reitzenstein, "Directional emission of a deterministically fabricated quantum dot - Bragg reflection multi-mode waveguide system," (2019), arXiv:1902.01905 .

[126] A. Kaganskiy, M. Gschrey, A. Schlehahn, R. Schmidt, J.-H. Schulze, T. Heindel, A. Strittmatter, S. Rodt, and S. Reitzenstein, "Advanced in-situ electron-beam lithography for deterministic nanophotonic device processing," Rev. Sci. Instrum. **86**, 073903 (2015).

[127] P. Schnauber, J. Schall, S. Bounouar, T. Höhne, S.-I. Park, G.-H. Ryu, T. Heindel, S. Burger, J.-D. Song, S. Rodt, and S. Reitzenstein, "Deterministic Integration of Quantum Dots into on-Chip Multimode Interference Beamsplitters Using in Situ Electron Beam Lithography," Nano Lett. **18**, 2336 (2018).

[128] M. C. Löbl, S. Scholz, I. Söllner, J. Ritzmann, T. Denneulin, A. Kovács, B. E. Kardynał, A. D. Wieck, A. Ludwig, and R. J. Warburton, "Excitons in InGaAs quantum dots without electron wetting layer states," Commun. Phys. **2**, 93 (2019).

[129] S. H. Ø. Madsen, *Deterministic positioning of nanostructures to spatially and spectrally pre-characterized self-assembled quantum dots in GaAs*, MSc thesis, University of Copenhagen (2018).

[130] P. W. Fry, J. J. Finley, L. R. Wilson, A. Lemaitre, D. J. Mowbray, M. S. Skolnick, M. Hopkinson, G. Hill, and J. C. Clark, "Electric-field-dependent carrier capture and escape in self-assembled InAs/GaAs quantum dots," Appl. Phys. Lett. **77**, 4344 (2000).

[131] M. J. R. Staunstrup, L. Svensen, and M. W. Thorning-Schmidt, *Towards Automation of Large-Scale Localization of Quantum Dots*, BSc thesis, University of Copenhagen (2018).

[132] R. C. Gonzalez, R. E. Woods, and S. L. Eddins, *Digital Image Processing Using MATLAB*, 2nd ed. (Gatesmark Publishing, 2009).

[133] K. I. Mortensen, L. S. Churchman, J. a. Spudich, and H. Flyvbjerg, "Optimized localization analysis for single-molecule tracking and super-resolution microscopy," Nat. Methods **7**, 377 (2010).

[134] A. Berrier, M. Mulot, G. Malm, M. Östling, and S. Anand, "Carrier transport through a dry-etched InP-based two-dimensional photonic crystal," J. Appl. Phys. **101**, 123101 (2007).

[135] T. Nakaoka, T. Kakitsuka, T. Saito, S. Kako, S. Ishida, M. Nishioka, Y. Yoshikuni, and Y. Arakawa, "Strain-induced modifications of the electronic states of InGaAs quantum dots embedded in bowed airbridge structures," J. Appl. Phys. **94**, 6812 (2003).

[136] K. D. Jöns, R. Hafenbrak, R. Singh, F. Ding, J. D. Plumhof, A. Rastelli, O. G. Schmidt, G. Bester, and P. Michler, "Dependence of the Redshifted and Blueshifted Photoluminescence Spectra of Single $In_xGa_{(1-x)}As$/GaAs Quantum Dots on the Applied Uniaxial Stress," Phys. Rev. Lett. **107**, 217402 (2011).

[137] T. Pregnolato, X.-L. Chu, T. Schröder, R. Schott, A. D. Wieck, A. Ludwig, P. Lodahl, and N. Rotenberg, "Deterministic positioning of quantum dots in nanophotonic waveguides," (2019), arXiv:1907.01426 .

[138] R. J. Warburton, C. Schulhauser, D. Haft, C. Schäflein, K. Karrai, J. M. Garcia, W. Schoenfeld, and P. M. Petroff, "Giant permanent dipole moments of excitons in semiconductor nanostructures," Phys. Rev. B **65**, 113303 (2002).

[139] T. M. Hsu, W.-H. Chang, C. C. Huang, N. T. Yeh, and J.-I. Chyi, "Quantum-confined Stark shift in electroreflectance of InAs/$In_xGa_{(1-x)}$As self-assembled quantum dots," Appl. Phys. Lett. **78**, 1760 (2001).

[140] H. Thyrrestrup, L. Sapienza, and P. Lodahl, "Extraction of the β-factor for single quantum dots coupled to a photonic crystal waveguide," Appl. Phys. Lett. **96**, 231106 (2010).

[141] P. Türschmann, H. L. Jeannic, S. F. Simonsen, H. R. Haakh, S. Götzinger, V. Sandoghdar, and N. Rotenberg, "Coherent nonlinear optics of quantum emitters in nanophotonic waveguides," (2019), arXiv:1906.08565 .

[142] P. Lodahl, S. Mahmoodian, S. Stobbe, A. Rauschenbeutel, P. Schneeweiss, J. Volz, H. Pichler, and P. Zoller, "Chiral quantum optics," Nature **541**, 473 (2017).

[143] M. M. Vogel, S. M. Ulrich, R. Hafenbrak, P. Michler, L. Wang, A. Rastelli, and O. G. Schmidt, "Influence of lateral electric fields on multiexcitonic transitions and fine structure of single quantum dots," Appl. Phys. Lett. **91**, 051904 (2007).

[144] M. Zeeshan, N. Sherlekar, A. Ahmadi, R. L. Williams, and M. E. Reimer, "Proposed Scheme to Generate Bright Entangled Photon Pairs by Application of a Quadrupole Field to a Single Quantum Dot," Phys. Rev. Lett. **122**, 227401 (2019).

[145] D. Huber, M. Reindl, Y. Huo, H. Huang, J. S. Wildmann, O. G. Schmidt, A. Rastelli, and R. Trotta, "Highly indistinguishable and strongly entangled photons from symmetric GaAs quantum dots," Nat. Commun. **8**, 15506 (2017).

[146] R. E. Evans, M. K. Bhaskar, D. D. Sukachev, C. T. Nguyen, A. Sipahigil, M. J. Burek, B. Machielse, G. H. Zhang, A. S. Zibrov, E. Bielejec, H. Park, M. Lončar, and M. D. Lukin, "Photon-mediated interactions between quantum emitters in a diamond nanocavity," Science **362**, 662 (2018).